PHOTOELECTRON SPECTROSCOPY STUDIES ON GROUP IV SEMICONDUCTOR CLUSTERS AND NOVEL BINARY CLUSTERS

By

LIFENG CUI

A dissertation submitted in partial fulfillment of
the requirements for the degree of

DOCTOR OF PHILOSOPHY

WASHINGTON STATE UNIVERSITY
Materials Science Program

MAY 2007

To the Faculty of Washington State University:

The members of the Committee appointed to examine the dissertation of LIFENG CUI find it satisfactory and recommend that it be accepted.

_____

Chair

_____

_____

ACKNOWLEDGEMENTS

I would like to express my sincere gratitude and appreciation to Prof. Lai-Sheng Wang for his guidance and support throughout my research.

I would also like to acknowledge my doctoral committee, Prof. J. Thomas Dickinson and Prof. Alexander D. Li, for their effort on examining the progress of my graduate study in Materials Science Program. Dr. Xi Li, Dr. Xuebin Wang and Dr. Hua-Jin Zhai generously provided valuable helps and advices in the early stage of my research. I gratefully thank Dr. Xi Li and Mr. Lei-Ming Wang, who have been my collaborators in many of the experimental works described in this dissertation. I am also grateful to Prof. Alexander I. Boldyrev (Utah State University), Prof. Xiao-Cheng Zeng (University of Nebraska-Lincoln), Prof**.** Xin Huang **(**Fuzhou University), Prof. Dage Sundholm (University of Helsinki), and Dr. Jun Li (Pacific Northwest National Laboratory) who have been our theoretical collaborators and carried out the calculations presented in this dissertation. My appreciations extend to the Chemical Structure and Dynamics division within the W. R. Wiley Environmental Molecular Sciences Laboratory (EMSL) at PNNL, where all the experiments were performed.

Finally, I am indebted to my mother Aiju and my sister Bianxiao for their hearty encouragement and consistent support.

PHOTOELECTRON SPECTROSCOPY STUDIES ON

GROUP IV SEMICONDUCTOR CLUSTERS

AND NOVEL BINARY CLUSTERS

Abstract

by LIFENG CUI, Ph.D.
Washington State University
May 2007

Chair: Lai-Sheng Wang

Clusters consisting of a few to a few hundred atoms (~ 2 nm) cover a critical size range, in which the finite-sized systems evolve from molecular-like species to nano-particles. Photoelectron spectroscopy of size-selected cluster anions in gas phase is a powerful technique to investigate their electronic structure and follow the evolution from discrete molecular features to bulk band structures. Advances in our laboratory to improve the photoelectron energy resolution and to control cluster temperatures have enabled us to obtain well-resolved photoelectron spectra for a wide range of gas-phase atomic clusters. This dissertation mainly focuses on studies of group IV semiconductor (Si, Ge, Sn) clusters. Several binary cluster systems, such as hydrogenated aluminum clusters and alkali and coinage metal alloy clusters were also investigated. We have confirmed a prolate-to-spherical structural transition with the increase of size for silicon clusters. A semiconductor-to-metal transition was elucidated for tin clusters as a function of size. More importantly, we discovered a stable 12-atom tin cluster Sn_{12}^{2-}, which has a highly symmetric icosahedral structure and is named stannashperene for its high stability,

high symmetry and π-bonding characters. This icosahedral cage has a size comparable to that of C_{60} and can be considered as an inorganic analog of the fullerenes. Subsequently, we have synthesized a series of endohedral cage clusters $M@Sn_{12}^{2-}$, where M is a transition metal atom. The doped atom in $M@Sn_{12}^{-}$ keeps its quasi-atomic nature with large magnetic moments. These endohedral cage clusters might thus be viewed as "superatoms", yielding a rich class of new building blocks for cluster-assembled materials with tunable magnetic, electronic, and chemical properties.

TABLE OF CONTENTS

Page

LIST OF TABLES

Page

LIST OF FIGURES

Page

CHAPTER ONE

INTRODUCTION

Materials reduced to the nanoscale exhibit different properties from those of bulk materials.[1-8] Nano-structures with controlled size and dimension ranging from clusters of a few atoms to nanostructures with thousands of atoms have been synthesized in both gaseous and condensed phases using a variety of techniques such as laser ablation, supersonic jet expansion, chemical vapor deposition, matrix isolation, and solid state reaction.[2-10] These nano-structures may serve as building blocks for an entirely new class of nano-materials with designed physical and chemical properties.

Clusters are aggregates of atoms or molecules, generally intermediate in size between individual atoms or molecules and aggregates large enough to be called bulk matter. Clusters consisting of a few to few hundred atoms cover a critical-size range, in which the finite-sized systems evolve from molecular-like species to nano-particles. Clusters exhibit novel geometries and properties and it has been found that many physical and chemical properties of nanomaterials depend strongly on their size and shape. Cluster science forms the foundation of nanoscience and nanotechnology, which concern with materials and systems whose structures and components exhibit novel and significantly improved physical and chemical properties due to their nano-scale size.

The study of atomic clusters as a function of size enables one to probe the manner in which size dependent properties change from molecular-like to the bulk-like. Clusters and nanostructured materials exhibit novel properties that are not found in bulk materials. As the length scales of materials are reduced, the properties of bulk materials change

monotonically until a critical length scale is reached. Below this length scale, the properties vary non-monotonically and are influenced more strongly by quantum phenomena. The critical length scale does depend on the properties being considered. For example, while the inter-atomic distances approach the bulk value with as few as a dozen atoms in a cluster, the evolution of their electronic, magnetic, and optical properties may not reach the asymptotic value until they contain hundreds or even thousands of atoms. This flexibility endows one with an unprecedented ability to design clusters and nanostructered materials with specific properties that are very different from bulk matter. Combining various experimental investigations with first principles calculations aided by powerful computers, one can obtain a fundamental understanding of the unique properties of these novel systems and design new materials from nano-scale to bulk.

1.1 Gas-Phase Atomic Clusters

Research described in this thesis concerns the investigation of atomic clusters in the gas phase and their dependence on size and composition. Studies of these atomic clusters provide fundamental understanding for nanoscience. The study of atomic clusters is an interdisciplinary field involving catalysis, surface science, condensed matter physics, and materials science. One can point to the discovery of a third form of carbon, after diamond and graphite, composed of 60 carbon atoms, as the best fruit yet born out of research on clusters. This C_{60} cluster was named Buckminsterfullerene, after the architect of the geodesic dome, Buckminster Fuller. Nicknamed "Buckyball", it is a chemically bonded cluster of sixty carbon atoms with each occupying the sixty vertices of a soccer ball.[11] Recent studies on gas-phase planar carbon molecules,[12-14] planar gold

clusters,[15-17] planar boron clusters,[18,19] all-metal aromatic molecules,[20,21] large band gap clusters such as Au_{20} and B_{20},[22,23] and the halogen-like magic cluster Al_{13} [24] have manifested that cluster science is still much an active and exciting field. The ability to create and assemble nano-sized atomic clusters with tailored properties surely will benefit the advancements of nanotechnology.

In the past two decades a fast growth has been seen in the literature on the study of atomic clusters.[25,26] It is mainly because small clusters have been found very useful in the study of intermolecular forces, hydrogen bonding, chemical dynamics, and novel nano-optical and magnetic materials while the study of large clusters is an essential step towards understanding heterogeneous catalysis, atmospheric chemistry, and several other phenomena whose study requires measurement of the behavior of matter in the transition between molecular and condensed bulk properties. It has become apparent that cluster beam technologies may offer increasingly new possibilities for the study of surface phenomena and nano-structure based functional materials such as physisorption, chemisorption, reactivity, biosensors, and nano-materials.

Cluster study can provide new understanding about the surface of bulk when clusters are used as models for surfaces. As we know, knowledge of the detailed surface electronic structure is critical in the understanding of the chemisorptive and catalytic properties of functional materials. Studies on surfaces have been concentrated on the detection of the electronic states not found in the bulk that are generated by the presence of surface defects. These states are called surface states. The energy of the surface states of interest in catalysis commonly lies near the Fermi Level of the solid (or valence states). These surface states are either partially filled with electrons so that they both donate and

accept electrons from the molecules interacting with the surface or close enough to the empty conduction band such that together, they provide a pair of states to accept and donate electrons to the interacting molecules simultaneously.

A cluster has a high surface-to-volume ratio, and its chemistry occurs essentially on its surface. Surface science is, at the same time, one of the most economically significant areas of chemistry and physics and one of the least understood. The capability for controlled experiments with clusters of a range of sizes combined with the future outlook for computational understanding of cluster properties gives real promise that we can ultimately develop a fundamental understanding of their surface chemistry and physics. This understanding will lead to some comprehension of the behavior of bulk surfaces.

Clusters carry out chemical reactions in new ways. One of the promising applications of clusters is in industrial catalysis, which is central in petroleum refining, in pollution control and in the synthesis of pharmaceuticals. The efficacy of a catalyst depends on its ability to attract reactants strongly enough for adsorption yet hold their end products weakly enough for desorption. Clusters are also the ideal laboratories for studying catalytic active sites because their unfilling bonding capacity makes them adsorb molecules readily and their small size limits the number of possible adsorption geometries. This constraint also makes them likely sources of highly specific catalysts, which do what they are intended to do and no more. That specificity is highly prized in industry, because many catalysts speed undesired reactions just as effectively as they speed desired ones.

Clusters are new kinds of materials with novel properties. Thin films of clusters possessing desired electronic qualities would be of great interest in microelectronics. We can envision the application in optical memories, image processing and superconductivity. Given the potential for constructing parts from networks of clusters, it may eventually be possible to make electronic devices in a molecular scale. Ultimately, a machine might be engineered that could serve as a link between solid-state electronics and biological system, such as systems of neurons. Surface science of magnetic media has been applied to improve the technology of magnetic storage devices. Many magnetic nano-structured materials have also been developed to write individual "bit" of information onto a tiny area of the surface of a disk used for electronic storage. Clusters with enhanced magnetic moments may provide the ideal medium for inexpensive multi-gigabyte electronic storage.

1.2 Photoelectron Spectroscopy Investigations of Clusters

Photoelectron spectroscopy (PES) is one of the most powerful techniques to probe the electronic structure of atomic clusters. Photoelectron Spectroscopy employs the photoelectric effect of matter, i.e., the emission of electrons upon the absorption of electromagnetic radiation. PES is the study of the energies, abundances, and angular distributions of the emitted photoelectrons. The radiation source can vary from X-ray to ultraviolet and visible light. X-Ray Photoelectron Spectroscopy (XPS) of solid surfaces was first developed at Uppsala University, Sweden in the 1960's by a group headed by Kai Siegbahn,[27] who in 1981 won the Nobel Prize for Physics for this contribution. Ultraviolet Photoelectron Spectroscopy (UPS) was developed by David W. Turner in late

1960's for the electronic structure investigation of gas-phase molecules.[27] Both X-ray and ultraviolet photoelectron spectroscopy have been extensively advanced and found numerous applications in chemistry and physics. PES has contributed tremendously to our detailed understanding of the electronic structure of matter. For the first time molecular orbital (energy levels) could be 'visible', and the prediction of quantum electronic structure calculations could be tested experimentally. PES directly probes the electronic structures of solid surfaces and individual molecules and yields the ionization potentials (IP's) of different energy levels.

In the application of PES to gas-phase atomic clusters, negative ions are often chosen since anions have lower electron binding energies, allowing commercial lasers to be used as radiation source. More importantly, PES on anions yields spectroscopic information about the neutral clusters, which are often of interest.

PES studies on cluster anions were pioneered by the groups of Lineberger,[28] Smalley,[29] and Meiwes-Broer.[30] The groups of Bowen,[31] Newmark,[32] Zewail,[33] Cheshnovsky,[34] Kaya,[35] Wang,[36] Haberland and Issendorff,[37,38] and Ganteför[39] have also made extensive contributions on the PES studies of cluster anions. PES of size-selected anions has become the most powerful technique to obtain electronic structure information for a wide range of clusters. It provides directly the valence electronic density of states of the neutral clusters. Information about the electronic states and chemical bonding of clusters can provide insight into their structural, physical, and chemical properties.

Figure 1.1 shows a schematic view of photodetachment transitions from the ground state of an anion to the ground and low-lying excited states of the corresponding

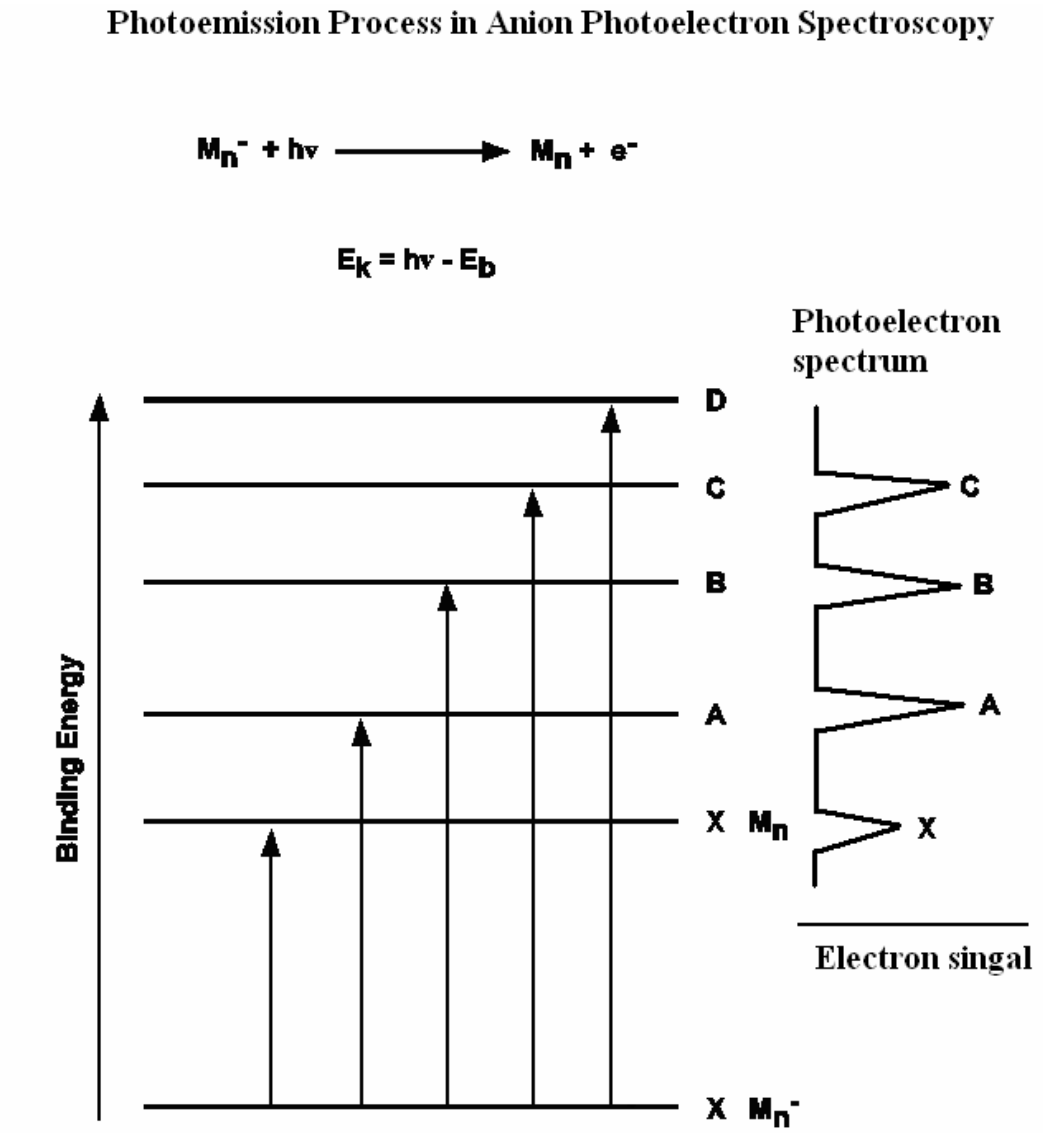

Figure 1.1 A schematic view of photodetachment transitions from the ground state of an anion to the ground and excited states of the corresponding neutral species. M_n^- is the size-selected cluster anion, hν is the photon energy, E_b is the binding energy of the electrons, and E_k is the kinetic energy of the electrons detached from the cluster anion.

neutral. In anion PES experiment, a size selected anion cluster is photodetached by fixed wavelength photons and the kinetic energies of the photoemitted electrons are measured.

The ejected photoelectrons are separated according to their kinetic energies in an electron energy analyzer and recorded as an energy spectrum. The photoelectron spectrum is a record of the number of electrons detected at each energy level. To understand the photoelectron spectrum, one needs to know the principles governing the photodetachment process. The exact quantum mechanical description assigns each feature to a transition from the electronic ground state of the anion to an electronic state of the neutral. At normal temperatures, the ground-state anion resides in the lowest vibrational level. However after photodetachment, the resulted neutral cluster can reside in any number of vibrational energy levels. Thus each electronic transition is governed by the Franck-Condon principle.[27] The transition of maximum intensity will occur to the vibrational level for which there is a maximum of overlap between the vibrational wave functions of the ground- and excited-state energy levels. The feature at the lowest binding energy (BE) corresponds to the transition to the ground state of the neutral. The time scale of the detachment process is very fast (~ 10^{-15} s) with respect to the movements of the nuclei (~ 10^{-13} s). Therefore, the observed features correspond to the electronic states of the neutral cluster having the ground state geometry of the anion. In a different view, a PES spectrum can be discussed using the molecular orbital theory (single particle picture). The observed features in a PES spectrum can be viewed qualitatively as photoemission from occupied molecular orbitals (see Figure 1.2). Within this approximation a PES spectrum represents a picture of the occupied molecular orbitals.

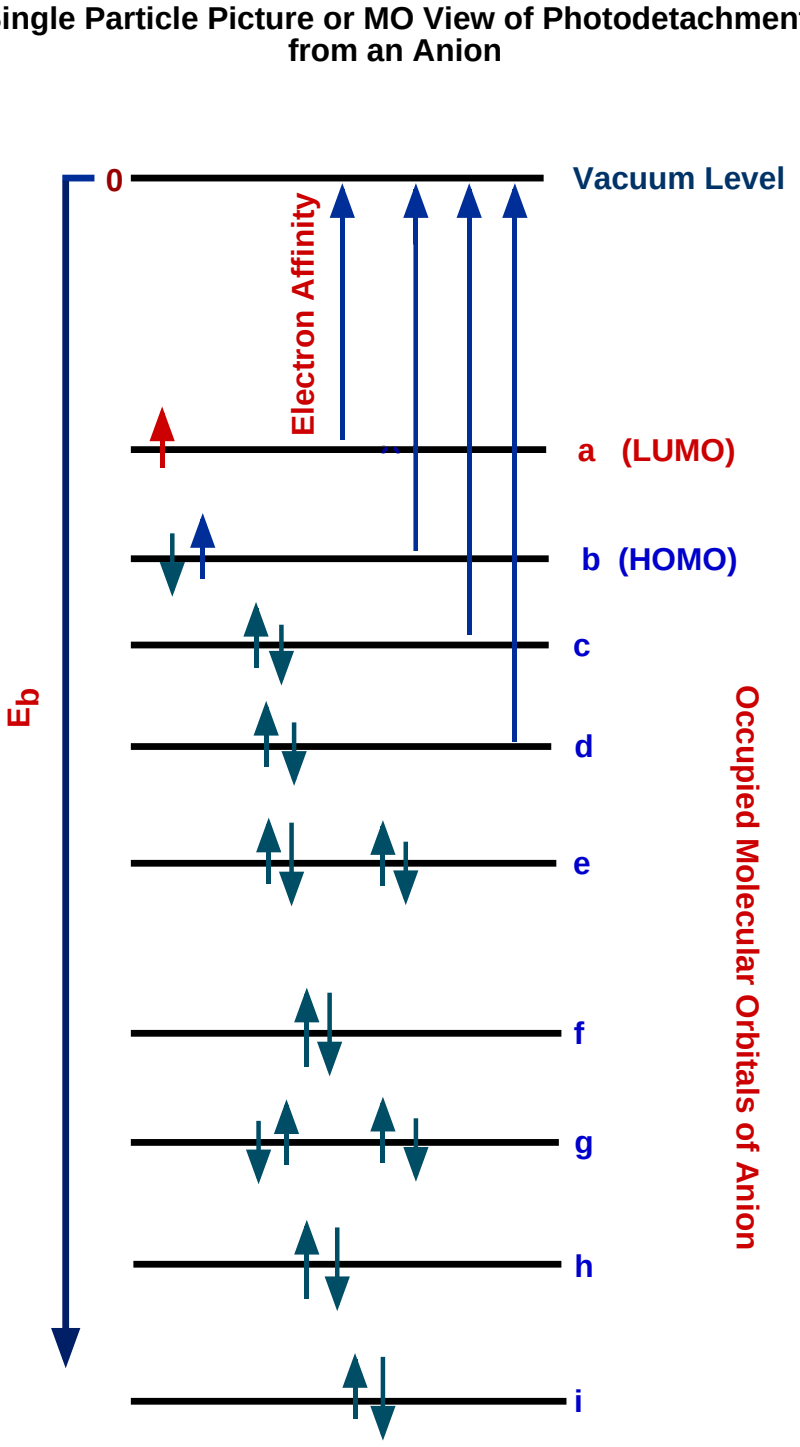

Figure 1.2 Single particle picture of photoemission processes.

However, this approach can only be used for a qualitative interpretation while the following effects must be considered.

First, the emission of an electron corresponds to a change of the charge state of the cluster. The remaining electrons adjust to the changed potential. Therefore, the calculated binding energy of a single particle orbital is smaller than that determined from a photoelectron spectrum. The energy difference is called the electronic relaxation energy. Second, if the anion has an unpaired electron, photoemission from one of the doubly occupied orbitals results in a neutral final state with two unpaired electrons. The two electrons can couple to a singlet or triplet state with different energies. Therefore, photoemission from one single particle orbital can yield more than one feature. In general this multiplicity splitting can be identified in the spectrum because it occurs for all occupied single particle orbitals of the cluster in a similar pattern, which has a characteristic intensity ratio equivalent to the degree of degeneracy (singlet/triplet = 1/3). Third, photoemission of one electron can induce the simultaneous excitation of other electrons. This is called a shake-up process. Usually the direct photoemission signals in a PES spectrum have significant higher intensity than the shake-up signals.

With the single particle picture in mind, the quantity measured directly in PES is the detachment energies for the removal of electrons in different molecular orbitals in a cluster. An approximation called Koopmans' theorem relates the orbital energies with the measured detachment energies.[27] This approximation states that, each detachment energy, I_i, i denotes a molecular orbital, is equal in magnitude to an orbital energy, $-E_i$. i.e. $I_i = -E_i$. Koopmans' theorem is only valid if the one-electron wavefunctions in the N-electron and the (N ± 1) -electron Slater determinants are the same, i.e. the single-particle orbitals do

not relax when an electron is added to or removed from the system. From the energy conservation, we know that, $I_i = h\nu - E_k$, if Koopmans' theorem applies, namely, $I_i = -E_i$, we have $-E_i = h\nu - E_k$. If we only concern the magnitude of the quantities, and we use a commonly used notation E_b for the electron binding energies, we have $E_b = h\nu - E_k$ (Figure 1.1 and 1.2). Therefore, by measuring the kinetic energies of the photoelectrons, one can obtain the information of the electronic binding energies of the clusters. PES experiments are able to provide direct measure of the electron affinity (EA) and electronic energy levels of the neutral clusters from the studied anion clusters.

The Koopman's theorem is only as an approximate model and can be used to qualitatively interpret PES spectra. To understand the PES spectra quantitatively, high level theoretical calculations are required. In this thesis many different theoretical methods and computational programs have been employed by our collaborators to calculate the energetics, electronic structures, and geometrical structures of various cluster systems. The chemical bonding and physical properties of the clusters are understood by combining PES spectra of the cluster anions with the theoretical calculations.

In order to obtain a well-resolved PES spectrum for various size of cluster anions, there are at least several requirements that must be met. First, a cluster source that can produce a broad size range of clusters; second, a cold cluster beam; third, a electron spectrometer with good energy resolution; last, a high photon energy source to be able to detach electrons with high binding energies.

Our experimental apparatus consists of a laser vaporization cluster source, a time-of-flight mass spectrometer, and a magnetic bottle TOF-PES analyzer.[40] The work was

carried out with several improvements on the experimental instruments (see details in Chapter two). The instrumental resolution was improved to ~ 2.5% ($\Delta E_k / E_k$), i.e., ~ 25 meV at 1 eV of electron kinetic energy as measured and calibrated from the known spectra of Cu^-, Au^-, Pt^-, and Rh^-. The PES data can be obtained under well-controlled temperature conditions at four different photon energies: 2.331(532 nm), 3.496 (355 nm), 4.661(266 nm) and 6.424 eV (193 nm). Low photon energy spectra yielded better-resolved data for low binding energy features, while the high photon energies allowed us to probe electronic features with high binding energies. In the second chapter of this dissertation, a detailed description of the experimental set-up employed in this work will be presented.

1.3 Other Experimental Studies on Atomic Clusters

Besides photoelectron spectroscopy, many other experimental techniques have been developed to investigate the electronic/geometric structure and other physical or chemical properties of gas-phase clusters. A brief summary of the principle and application of each technique will be discussed as follows.

1.3.1 Zero Electron Kinetic Energy (ZEKE) spectroscopy

ZEKE spectroscopy is a novel high-resolution electron spectroscopy technique. Instead of dispersing photoelectron kinetic energies, it detects electrons with close to zero kinetic energies, while the ionization laser wavelength is scanned. Typically it uses a delayed or pulsed electric field to extract the zero energy electrons, which are otherwise hidden in the much larger signals of high energy electrons. Schlag et al. first invented this

technique for neutral molecules. Neumark's group[41] has applied this technique to negative cluster ions with a laser vaporization source and has obtained interesting vibrationally resolved spectra for several small semiconductor clusters. Recently Yang's group[42] has studied many neutral metal cluster complexes using ZEKE. While this is unquestionably a high-resolution technique, it is nonetheless a laser spectroscopy rather than a photoelectron spectroscopy technique. The information is mostly about the ground state and perhaps a few low-lying excited states and it is difficult for it to probe deep into the inner electronic energy level of a cluster.

1.3.2 Time-resolved Photoelectron Spectroscopy

Time-resolved photoelectron spectroscopy (TRPES) was developed by Zewail *et al*.[43] and has become a powerful new tool in studying the dynamics of molecules and clusters. It has been applied to processes ranging from energy flow in electronically excited states of molecules to electron solvation dynamics in clusters. Most of the TRPES experiments involve a pump-probe configuration in which an ultrafast pump pulse initiates a reaction or, more generally, creates a nonstationary state, and the evolution of this state is monitored by means of a probe pulse. TRPES have been performed on mass-selected negative cluster ions by Neumark's group[44] and recently by Eberhardt's group.[45]

TRPES enables one to indeed monitor evolution of the excited state dynamics along the entire reaction coordinate. The probe laser does not have to be tuned, since the PES spectrum at each delay provides the full mapping of the evolving wave packet onto those electronic states accessible by photodetachment (or photoionization, in the case of neutrals).

1.3.3 Resonant Two Photon Ionization Spectroscopy

In this technique, neutral clusters in the electronic ground state are excited using laser radiation (e.g., of a dye laser) with tunable photon energies.[25,46,47] A second laser with fixed photon energy, usually operating in the UV, serves to ionize the excited clusters. The intensity of the ions is recorded as a function of the photon energy of the tunable laser. The spectra exhibit peaks at photon energies corresponding to resonant absorptions of the neutral cluster. Only dipole allowed transitions can be observed. This is a high resolution technique, but limited to very small clusters, such as dimers, and trimers, etc.

1.3.4 Photodissociation Spectroscopy

Infrared photodissociation spectroscopy[25,46] is usually performed on cluster-molecule complexes and probes cluster chemisorption interactions. A powerful infrared laser is used to excite the characteristic vibrations of molecules adsorbed on the surfaces of clusters, causing the complexes to dissociate. The resulting photodissociation spectrum reveals whether or not the adsorbed molecules have undergone a chemical reaction after sticking to the surface of the cluster. It is anticipated that these experiments will contribute to our understanding of particle size effects and their influence on reaction mechanisms and pathways in heterogeneous catalysis systems.

A caveat in photodissociation spectroscopy is that photoabsorption is only detected when the absorbed energy results in dissociation. Thus, single photon photodissociation spectra are a convolution of the absorption and dissociation events for each given cluster. These two events can be separated by using two different color

photons to perform resonant two-color photodissociation spectroscopy (RTPD). In RTPD, clusters are irradiated with the first photon, followed by the second photon. The first photon performs the spectroscopy and the second higher energy photons add additional energy so that the clusters can dissociate.

1.3.5 Magnetic Moment Measurement

It is well known that all transition metal atoms are magnetic, however, only the late 3d transition metals Fe, Co and Ni are known to be ferromagnetic in the bulk. Therefore, fascinating size-dependent magnetism is expected to exist in small transition metal clusters. The dependence of the magnetic properties on the cluster size can be determined in a Stern-Gerlach experiment in which the free magnetic clusters interact with an applied inhomogeneous magnetic field and are deflected from the original beam trajectory.

Cox and coworkers[48] conducted the first measurement of the magnetic properties of isolated Fe clusters ranging in size 2 to 17 atoms as well as the magnetic behavior of the monoxides and dioxides of smaller Fe clusters. Bloomfile and co-workers[49] later on studied the magnetic properties of cobalt clusters (up to 200 atoms) in a beam and found these cobalt clusters possess larger magnetic moments per atom than the bulk value. de Heer and co-workers[50] did extensive experiment on the magnetic moments of Fe, Co and Ni clusters with sizes ranging from about 20 to 700 atoms. Those experiments revealed that clusters of ferromagnetic elements (Fe, Co, and Ni) containing a few to hundreds of atoms all have larger magnetic moments than their corresponding bulk materials. More

recently, Knickelbein's group[51,52] did magnetic experiments on CO adsorbed Ni clusters and Mn clusters.

1.3.6 Chemisorption Experiments of Clusters

Chemisorption has been used extensively to probe the geometric structures of clusters by Riley's group.[53] This technique uses the adsorption of weakly bound non-invasive molecules to probe the morphology of a cluster's surface. Since most of the atoms of a cluster are on the cluster surface, the accessible surface sites contain information about the cluster structure. The measured size-dependent information of the number and strength of the surface's binding site can then be used to select structures consistent with the adsorbate binding patterns. Using this method, cluster structures for a number of species such as Co, Fe, Ni, and so on have been investigated.

1.3.7 Collision Induced Dissociation (CID)

CID experiments can yield quantitative thermodynamic stabilities of clusters in the form of bond dissociation energies. A positively charged cluster beam with a well-defined and variable kinetic energy (0-1000 eV) is injected into a radio frequency octopole ion beam guide. The octopole directs the beam through a gas cell that contains a neutral collision gas (Xe, for example). The octopole minimizes losses due to scattering of both reactant and product ions. Thus, the ions are collected with high efficiency and injected into a quadrupole mass filter for product mass analysis. The mass intensity is converted into reaction cross sections from the laboratory to center-of-mass frame. This kind of work has mainly been carried out by Armentrout group. [54]

1.3.8 Infrared Spectroscopy (IRS)

The infrared spectroscopy was first used to investigate gas-phase clusters by Gough and coworkers over two decades ago.[55] Nowadays IRS has been extended into studies on clusters trapped in low temperature matrices. The clusters produced from a target collide with argon atoms during the condensation process. The energetic product molecules are relaxed and trapped in the solid argon or other inert gas matrices for spectroscopic studies. This method usually only provides the spectroscopic information about the ground state of cluster species. Andrew's group[56] and Lindsay's group[57] have employed this technique to study metal oxides, metal hydrides, metal nitrides, and bare metal clusters. Recently a free electron laser with tunable IR light in the 5-250 μm region has been used to obtain the IR spectra of many clusters, including pure metal clusters (Al, V, Nb, Rh, and W), fullerenes (C_{60}) and small metal-carbide clusters (Ti_8C_{12} and V_8C_{12}).[58]

1.3.9 Ion Mobility Experiments

Ion mobility spectrometry (IMS) is a gas-phase electrophoretic technique that allows gas phase species to be distinguished on the basis of their size and shape (mobility). It has been proved that IMS can be used to study the structural characteristics of a wide range of chemical species, from atomic clusters to biomolecules. The ion mobility method as such has been developed long ago by Mason and McDaniel[59] and the combination of this technique with modern mass spectrometry has been pioneered by the Bowers' group.[60] In recent years, Jarrold and coworkers have developed high resolution drift cells. They applied this technique to a large variety of different ionic systems such as

fullerenes and fullerene derivatives, biopolymers, silicon clusters and a variety of metal clusters.[61,62] In another setup, Clemmer and co-workers have more recently used an ion trap to accumulate and concentrate the ions before injection into a drift cell. This is followed by a time-of-flight mass spectrometer (TOFMS).[63] This setup has been optimized for rapid data acquisition, i.e., time-of-flight mass spectra and drift time distributions are recorded simultaneously. It allows rapid screening of (for example) peptide libraries, the unfolding reactions of peptides and the analysis of the size parameters of the various amino acids in peptides.

1.4 Motivation and Objectives

Over the last decade, the structural elucidation of free atomic clusters has been an area of intense research effort. Most elements evolve from just a few atoms to nanoparticles simply by sequentially accruing new layers of atoms. These layers may form atomic (geometric) shells, such as in clusters of noble gas atoms[4], alkaline earths[64], and some transition metals, including Ni, Fe, and Co.[65-70] In clusters with atomic shells, these layers arrange to produce an ordered packing of hard spheres, most often icosahedral. Clusters of free electron metals with weakly directional bonding normally adopt an electronic shell structure, where the geometry adapts to minimize the total electronic energy. This is characteristic of the alkali and coinage metals,[4] and group 13 elements (Al,[71,72] Ga,[73] In,[74] and Th[75]). Species of group 12 metals (Zn, Cd, and Hg) undergo a transition to the electronic shell structure once the *s* and *p* electrons are hybridized.[76] Obviously, the clusters of all elements must eventually assume the bulk-like structure. The dominance of geometric or electronic shell structure for a particular cluster

may also depend on the temperature.[77] In any case, most elements including all previously studied metals form densely packed clusters that grow without gross deviations from near-spherical shape.

The only species found to assume noncompact geometries and thus experience major structural transitions are those of covalently bound nonmetals, in particular the group 14 elements: carbon,[78] silicon,[79] and germanium.[80] This dissertation is largely composed of investigations of group 14 semiconductor clusters, such as silicon, germanium and tin clusters. Semiconductor clusters are a special class of matter with sizes in between single atoms and semiconductor quantum dots. Small to medium-sized semiconductor clusters have received considerable attention since the 1980s, mainly because of their potential relevance to and applications in the nanoelectronics industry. It is known that geometric structures of semiconductor clusters generally bear little resemblance to those of their bulk counterparts. One of the key questions is to understand the growth pattern and bonding behavior of these clusters as a function of size. The trend going down the periodic table is fascinating for the group 14 elements, from the semi-metallic graphite (or wide band gap diamond) to the semiconductors Si and Ge to the metallic Sn and Pb. The cluster forms of group 14 elements also exhibit very intriguing properties. Carbon clusters have been found to undergo interesting structural variations with the increase of cluster size from linear chains to monocyclic rings to polycyclic rings to fullerenes and carbon nanotubes.[78] Small Si and Ge clusters seem to exhibit tetrahedral bonding feature found in the bulk semiconductors.[62,81-85] Ion mobility experiments have revealed that they form prolate structures in the smaller size regime and undergo a structural transition to more spherical geometries at the size of several dozen atoms.[80-82,85]

In this dissertation, I present the investigations of Si, Ge, and Sn clusters using photoelectron spectroscopy. One of the major motivations is to elucidate the evolution of electronic and geometrical structures of semiconductor clusters with the increase of size. In many cases, the electronic/geometric structures and chemical bonding of the clusters are understood by combining PES with high level calculations carried out by our collaborators. This thesis also covers my studies of several interesting binary cluster systems, such as hydrogenated aluminum clusters and alkali-coinage metal alloy clusters.

CHAPTER TWO

EXPERIMENTAL SETUP

The gas-phase atomic clusters in our studies were produced by a laser vaporization cluster source, then analyzed by a modified Wiley-McLaren time-of-flight (TOF) mass spectrometer.[86,87] After size selection and deceleration, the anion clusters were investigated by a magnetic-bottle TOF photoelectron analyzer.[40,88] A schematic diagram of the experimental apparatus is shown in Figure 2.1. The main parts are described in detail in the following sections.

2.1 Laser Vaporization Cluster Source

Our cluster source employs the laser vaporization technique, which was invented and developed mainly by Smally's group at Rice University.[11,89,90] As seen in the left part of Figure 2.1, a pulsed laser beam is focused down to a 1 mm diameter spot onto a target surface, which is controlled by two stepping motors, one for rotation movement and another for up-down movement. The vaporization laser is typically 10-20 mJ/Pulse at 10 Hz from the second harmonic (532 nm, green light) of a solid state Nd:YAG laser with 10 nanosecond pulse width. The intense laser beam produces a plasma of atoms and ions from the target surface. The electron temperature of the nascent plasma could reach as high as 10,000 K. To facilitate clustering, a very intense helium carrier gas is delivered into the plasma right after the vaporization laser pulse. Two pulsed high-pressure Jordan valves (produced by Jordan Co., CA) are symmetrically mounted to deliver a pulsed and

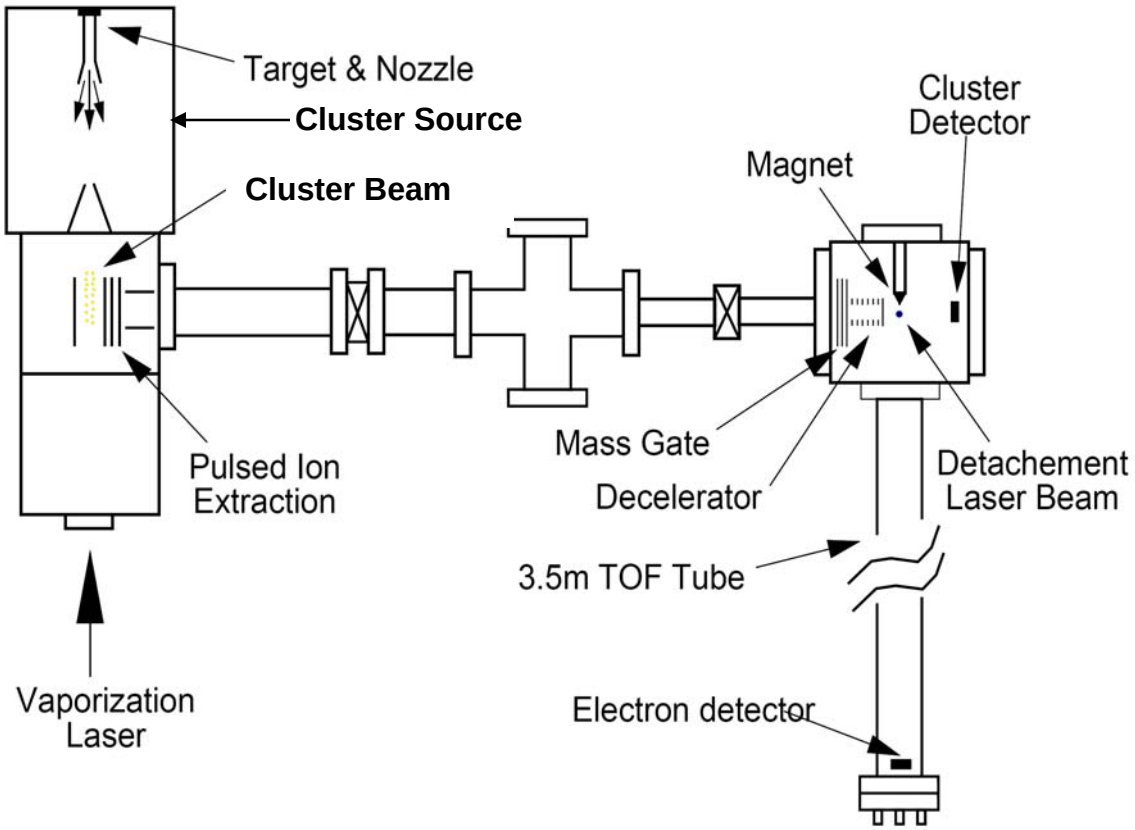

Figure 2.1 Schematic view of the laser vaporization magnetic-bottle photoelectron spectrometer.

intense carrier gas (usually helium gas). The stagnation pressure of the carrier gas is 10 atm at each valve. A nozzle with a clustering chamber (waiting room) and a small outlet orifice is used in the source. The intense pulsed carrier gas cools the laser-vaporized plasma to induce nucleation. The mixture of the carrier gas and the nascent clusters travels through the small outlet orifice and undergoes a supersonic expansion to a vacuum chamber and are skimmed to form a collimated beam into the ion extraction chamber. This supersonic expansion further cools down the formed clusters. The initial formation of clusters is primarily due to three body processes. When two atoms collide, they form a temporarily bound dimer. This activated dimer is very hot and must release its heat of formation to become stable. If it lives long enough to have a collision with a He atom, it can be stabilized by collisional deactivation. Once the dimers are formed, the process repeats for trimers and higher clusters. Larger clusters can live longer before needing a thermalizing collision than small clusters because they have more internal degrees of freedom. These big clusters are essentially molten droplets of metals. As they collide with He atoms, they slowly cool down and start to solidify. If this cooling process occurs slowly enough, the clusters should settle in their lowest energy structures.

The size and number densities of clusters produced are affected by many variables. The pressure of the carrier gas above the target will determine how quickly the plasma cools. The length and the shape of the nozzle determine the resident time of the clusters. If the carrier gas pressure is too low to provide sufficient cooling or if the plasma is too dilute, only atoms or small clusters will be produced. These variables are controlled experimentally in several ways. The carrier gas pressure can be readily adjusted. The time delay between the carrier gas pulse and the firing of the vaporization laser is

adjusted so that the laser fires right before the peak pressure. The plasma density can be adjusted by varying the laser power or by changing the size of the focused laser beam. If very large clusters are needed, the carrier gas pressure can be increased. Although different materials and cluster sizes require different clustering conditions, adjustment of the apparatus for the maximum signals can be usually done quickly by scanning the time delay between the He pulse and the firing of the vaporization laser.

2.2 Time-of-Flight Mass Spectrometer

The clusters generated from the source are mixtures of positive, negative, and neutral species of various sizes. In this work, only negative clusters are extracted perpendicularly from the beam by a 1.0 to 5.0 kV high-voltage pulse (repeller) and are subjected to a TOF mass analysis. Our mass spectrometer is a modified Wiley-McLaren type for large volume ion extraction and simultaneous high mass resolution.[86,87] The major modification is an addition of a short free-flight zone in between the two acceleration stages of the original Wiley-McLaren design. This modification allows us to achieve a mass resolution ($M/\Delta M$) of more than 300. The resolution deteriorates slightly at higher masses, mainly limited by the fringe field effect due to the ion steering optics to compensate for the transverse velocity of the clusters.

To obtain well-resolved mass spectrum for larger clusters, several experimental conditions need to be tuned. First, the repeller stack needs to be rotated to the right position that is favorable for heavier clusters. Secondly, the voltage on the repeller stack has to be increased to accelerate heavier clusters to a reasonable speed to obtain a compact mass packet. Finally the voltages on the first ion deflector and the focusing

Einzel lens have to be tuned accordingly to achieve the best mass resolution. The Einzel lens consists of three isolated copper cylinders. The two end cylinders are grounded while the middle one is biased at -400 V typically (for 1000 V extraction voltage). A set of stainless steel electrostatic deflectors is located behind the Einzel lens and can be used to adjust the cluster beam horizontally and vertically. This fine tuning of the ion beam is critical to align the ion beams and laser beam in the detachment zone. The time of flight mass spectra of the cluster ions are measured with a set of two micro-channel plates and a pre-amplifier.

Impurity (especially oxide contamination) is always a problem in laser vaporization source for metal clusters. There are three major oxygen sources: (1) oxide layer on the target surface; (2) trace amount of oxygen impurity in the carrier gas; and (3) adsorbed water and oxygen on the internal walls of the gas lines and the pulsed molecular beam valves. To minimize the problem, we use ultrahigh purity helium (99.9999%) as the carrier gas. Before each experiment, the gas line and the pulsed valves are fully baked with helium flushing to desorb any water and oxygen. The target surface oxide layer can be substantially reduced after the target is laser ablated several hours. Once the oxide contaminations are minimized or eliminated, clean mass spectra of clusters can be observed for most systems. Figure 2.2 shows a typical mass spectral pattern of $CrSn_n^-$ clusters for n = 6 - 12.

2.3 Mass Selection and Momentum Deceleration

In the PES experiment, only clusters of interest are selected to enter the photoelectron detachment zone. The cluster anions are selected by a mass gate and

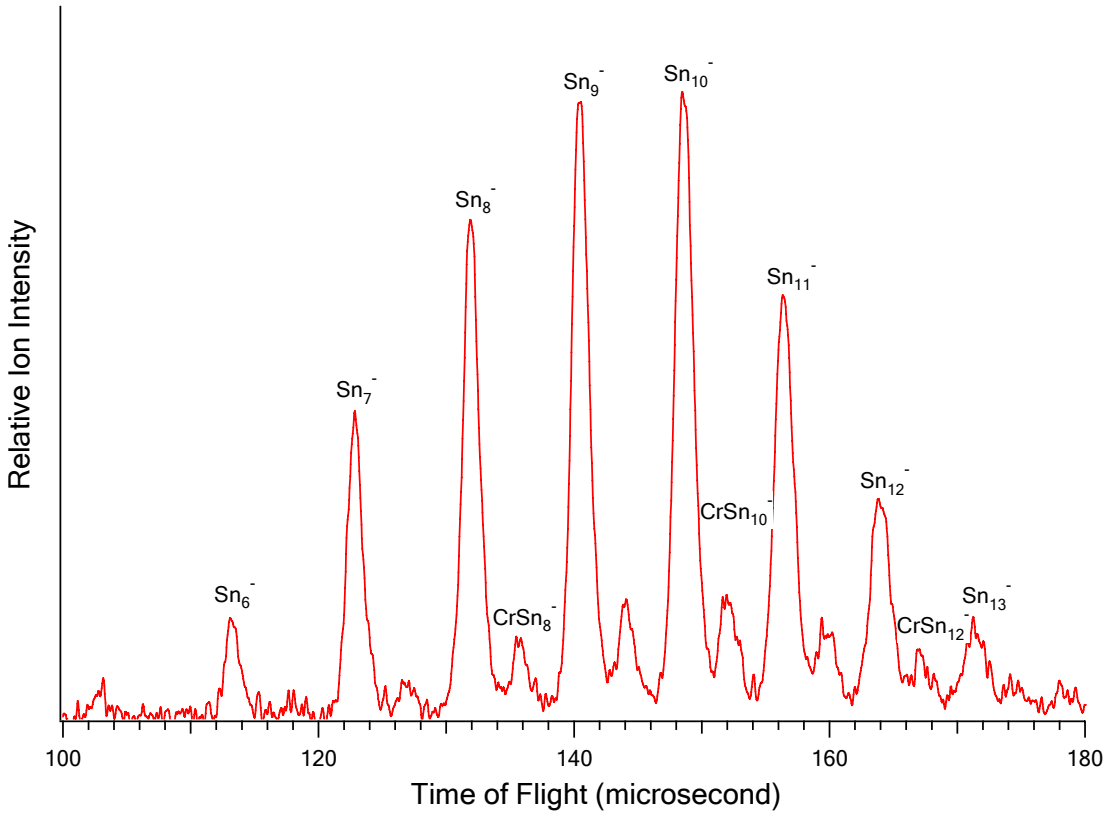

Figure 2.2 A time-of-flight mass spectrum of $CrSn_n^-$ clusters for n = 6 - 13 using a Sn/Cr target pressed from Sn and Cr powerders.

decelerated by a momentum decelerator. A schematic view of the mass gate and momentum decelerator is shown in Figure 2.3. A three-grid mass gate is used for mass selection. The first and third grids are grounded, and the middle grid is at a negative high voltage (-1kV to -5kV) so that no negative clusters are able to pass. Once the desired clusters arrive at the first grid, the high voltage is pulsed to ground for a short period of time (this period of time can be tuned from a few hundred nanoseconds to microseconds depending on the cluster size). After the selected cluster anions pass, the high voltage is engaged again to block the anions with different masses. A fast transistor switch is used to deliver sharp and variable width pulses for the mass gate.

After passing through the mass gate, the selected cluster anion packet enters a momentum deceleration[91] zone as shown in Figure 2.3. Once the cluster anion packet passes the third grid of the mass gate, a positive square high-voltage pulse is applied to this grid for the momentum deceleration. The high voltage is pulsed to ground before the ion packet leaves the deceleration stack, which consists of 10 guarded rings to ensure a uniform deceleration electrical field. Both the pulse amplitude and the pulse width can be varied to achieve the best deceleration effect. During the momentum deceleration, all ions experience the same decelerating force within the same period of time, thus will be decelerated by the same amount of linear momentum. The initial ion energy spread is decreased after the deceleration. The deceleration step is crucial to improve the electron energy resolution due to the minimization of the Doppler-broadening caused by the anion beam velocity. The momentum decelerator allows us to decelerate a given cluster ion packet down to such low kinetic energies that the Doppler-broadening is no longer a factor in most experiments.

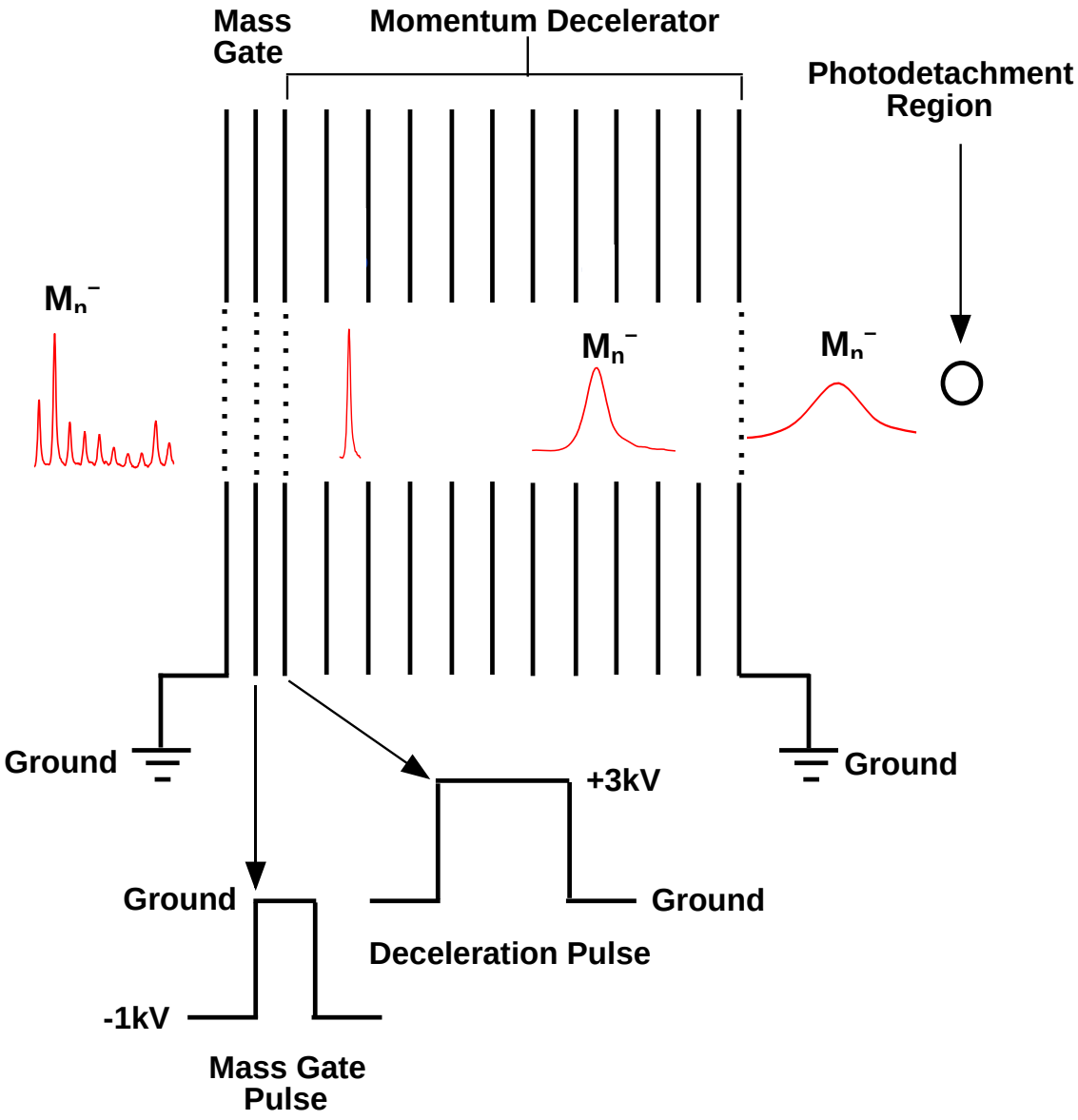

Figure 2.3 Schematic view of the mass gate and momentum decelerator.

For large clusters, although the mass peaks could not be separated to the base line the PES spectra from such mass spectra were still insured to be from pure clusters by applying narrow mass gate timing. By applying a mass gate voltage in a narrower period of time, only the middle part of the mass packet was selected to enter the deceleration zone. On the other hand, to make sure the PES spectra are from a pure cluster, one has to take PES spectra from the front part of a mass peak and rear part of the same peak, and see if any difference is found in the spectra.

2.4 Magnetic-bottle Time-of-Flight Photoelectron Analyzer

Photoelectron spectroscopy measures the kinetic energy distribution of photon-emitted electrons of an underlying system (atoms, molecules, clusters, and surfaces, etc.) at fixed photon energies. The magnetic-bottle type TOF photoelectron spectrometer (MTOF) first described by Kruit and Read is ideal for the study of clusters due to its high collecting efficiency (2π solid angle).[92] In this work, the apparatus is a modified version of the MTOF with a 4π solid angle. [40,88,93]

As shown in Figure 2.1, the MTOF is located at the end of the TOF mass spectrometer. The strong magnetic field is generated by a permanent magnet tip with a V shape head of 75 degree and magnetic flux intensity of about 5000 Gauss at the tip surface machined from a magnetic rod with 3/4 inch in both diameter and length. The distance between the magnet and the detachment laser beam can be varied depending on photon energies (532, 355, 266, 193 nm). A short distance is used for 532 and 355 nm experiments to achieve optimal PES resolution. The distance is increased for photon energies higher than 266 nm to minimize background electrons emitted from the magnet

tip by scattered photons. To reduce the background electron emission, the surface of the magnet tip is coated with graphite (Aquadag E layer). This coating has two purposes: (1) To reduce the noise, because the worker function of graphite is higher than the materials of the magnet. (2) To achieve a relatively uniform electric field around the detachment zone. From our experience, the photoelectron resolution is very sensitive to the variation of work functions in the detachment chamber. The weak uniform magnetic field along the TOF tube (3.5 m long) is generated by a solenoid on the outside wall of the flight tube.

We use two detachment lasers including four harmonics of a Nd:YAG laser (1064 nm, 532 nm, 355 nm, 266 nm), and an ArF excimer laser (193 nm). Accurate energy measurements also depend on the proper calibration of the instrumental energy scale. TOF spectra of the electrons detached from the clusters are measured, and then converted to kinetic energy distributions. The kinetic energy of an electron is related to its time of flight in a following relationship: $E_k = a + b/(c+t)^2$, where t is the time of flight, and a, b and c are parameters related to individual experimental conditions of the whole system. There are a number of sources that cause some change of these parameters. For example, slight changes of surface potentials in the detachment chamber or in the 3.5 meter "*e* tube" due to variation of vaccum conditions may induce a change of parameter a. Different electron trajectories induced by a slight non-uniformity of the electric field or magnetic field in the photoelectron detachment zone may cause a change of parameter b. Small changes of the detachment laser position may induce a change of parameter c. The known PES spectra of Cu^-, Rh^-, Au^-, and Pt^- atomic anions are used as the spectrometer calibration to obtain the calibration parameters (a, b, and c) for each experiment. The

binding energy spectra are obtained by subtracting the kinetic energy spectra from the corresponding photon energies.

TOF spectra of the electrons are measured with a set of three micro-channel plates (the Z stack from Jordon company), and then the TOF spectra are recorded with a 200MHz transient digitizer. A PC through a Computer Aided Measurement and Control (CAMAC) interface controls this experiment. The computer originates a sequence of commands to generate timing pulses and delays through the CAMAC interface to initiate the experiment and acquire the data.

2.5 Performance of the Photoelectron Spectrometer

Figure 2.4 shows the typical PES spectra of Cu^- at three photon energies 3.496, 4.661 and 6.424 eV. At 355 and 266 nm, we observe transitions from the ground state of Cu^- (^1S, $3d^{10}4s^2$) to the ground state ($^2S_{1/2}$, $3d^{10}4s^1$) and two excited states ($^2D_{5/2,\ 3/2}$, $3d^9 4s^2$) of Cu , which give three PES peaks. The 355 nm (3.496 eV) spectrum represents the best resolution of our PES spectrometer with very large momentum deceleration. The photoelectron spectrometer has an electron energy resolution of $\Delta E/E \approx 2.5\%$, i.e., about 25 meV for 1 eV electrons. In Figure 2.4 , the peak widths (FWHM) for the $^2S_{1/2}$, $^2D_{5/2}$, and $^2D_{3/2}$ states are 47, 21, and 17 meV, respectively, indicating the dependence of the energy resolution on the electron kinetic energies. This dependence is also shown clearly by the increasing peak widths for the 266 nm and 193 nm spectra. The bandwidth of the excimer laser (~30 meV) also contributes to the broadening of the 193 nm spectrum.

From Figure 2.4, it can be seen that noise begins to show up at the high BE side of the 266 and 193 nm spectra above ~3.5 eV. The 193 nm spectrum indicates that the 266

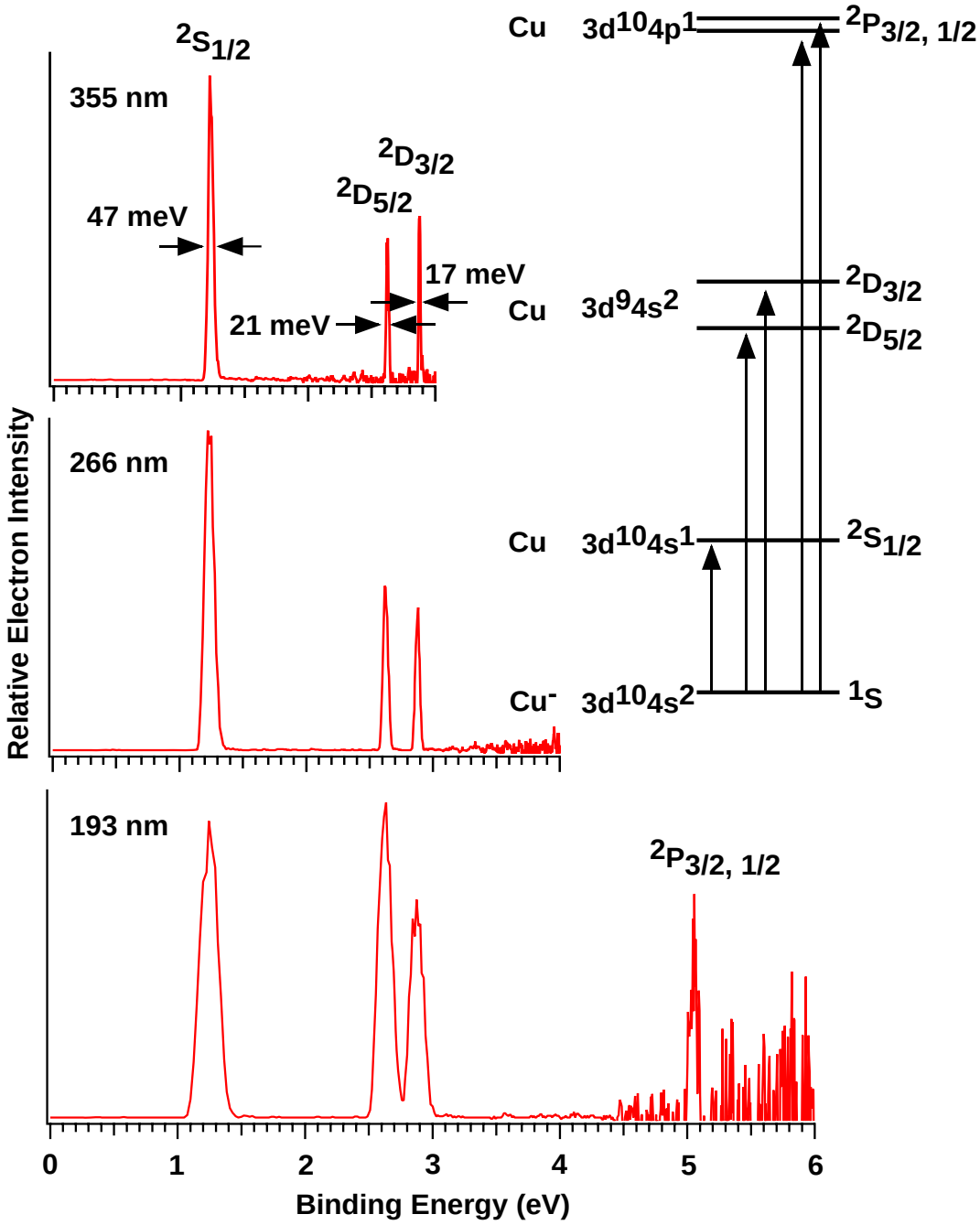

Figure 2.4 Photoelectron spectra of Cu^- spectra at three photo energies 3.496, 4.661 and 6.424 eV.

and 193 nm spectra above ~3.5 eV. The 193 nm spectrum indicates that the noise becomes significant above 4 eV and thus often low photon fluences have to be used at the higher photon energies to reduce the noise problem.

One other new observation shows up in Figure 2.4: The photon energy dependence of detachment cross-sections for different transitions. Since our spectrometer collects nearly 90% of the photoelectrons the relative peak intensities represent the relative total detachment cross-sections. It is easily noted that the cross section for the ^{2}D states increases with photon energies relative to that for the ^{2}S state. This is consistent with the general observation in PES that cross sections for emitting electrons from higher angular momentum states increase with photon energies. The variation of the detachment cross section with photon energy depends on the symmetry of the orbital and provides useful information for spectral assignments.

A new peak near 5 eV BE at 193 nm in Figure 2.4 is due to a two-electron transition. This peak can be assigned from the Cu atomic energy levels.[94] It is due to the ^{2}P excited state of Cu atom with an $3d^{10}4p^1$ electron configuration. There is a small spin-orbit splitting (30 meV), that is not resolved in the 193 nm spectrum. Cu^- has a $3d^{10}4s^2$ configuration. Thus, the ^{2}P state is resulted from detaching a 4s electron and at the same time exciting another 4s electron to the 4p orbital. These transitions due to electron correlation effects are usually called satellites (or shake-up) and exhibit very weak intensities. It is surprising that the intensity of the ^{2}P state observed here are almost comparable to the main transitions. This suggests very strong electron correlation effects between the two 4s electrons in Cu^-.

2.6 Temperature Effect and Control

There are several conditions that determine if the intrinsically separated electronic energy levels could be resolved in the PES experiment. First, the instrumental resolution is the basic factor to resolve the electronic energy levels. The best achieved energy resolution of our apparatus is about 25 meV for a photoelectron with 1.0 eV kinetic energy. The resolution deteriorates with the increase of photoelectron kinetic energies. Second, the temperatures of the clusters play an important role in the quality of the PES spectra. Hot clusters, in general, result in severe spectral broadening that smears out discrete electronic transitions even under a high instrumental resolution, which is due to "hot band" transition from vibrationally excited anions. Spectra from cold clusters render a definitive spectroscopic signature of the electronic structures of the clusters. Third, high photon fluence can result in "heating" effects for the cluster anions due to multiple photon absorption and electronic to vibrational energy transfer in the parent anions. Thus, the photon fluence is usually controlled to the lowest possible value during PES experiment.

Previous study on Al_n^- clusters[95] suggested that the cluster temperature from our vaporization source spans a wide range, depending on the residence time of the clusters in the nozzle and the firing timing of the vaporization laser. To obtain stable and cold clusters, the optimal vaporization laser firing timing was at the leading edge of the carrier gas pulse, typically 420 to 435 μs later after the triggering of the pulsed Jordan valves. Firing the laser too early often produces hot clusters because there is not enough carrier gas to quench the plasma, whereas firing the laser too late often leads to unstable cluster formation. The waiting room allows the nascent clusters to stay inside the nozzle longer,

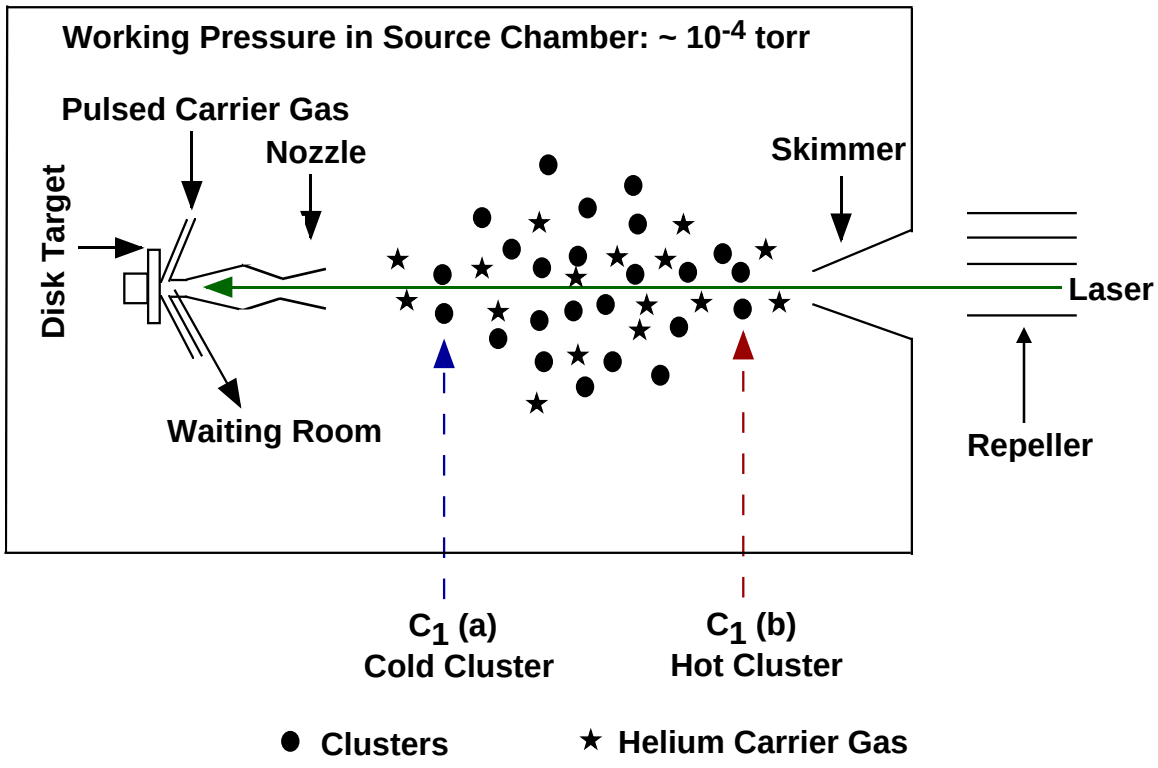

Figure 2.5 Schematics illustrating the cluster temperature distribution from the laser vaporization cluster source.

thus experiencing more collisions with the He carrier gas to be thermalized and cooled. Coupled with such a firing point, clusters coming out of the nozzle late tend to be colder (longer resident time). We refer F_3 as the time delay between the firing time of the vaporization laser and the arrival time of the cluster to the repeller. F_3 timing can be scanned by our PC control. By choosing larger F_3, we can get relatively colder clusters.

Figure 2.5 shows a schematic view of the mass distribution of clusters produced from one single shot of the vaporization laser pulse. This ensemble of clusters is experiencing a supersonic expansion out of the orifice. In the cluster beam from a single laser shot, cluster C_1(a) is flying behind C_1(b), which means that C_1(a) resides in the nozzle for a longer time and experiences more thermalizing collisions with the carrier gas, while C_1(b) resides in the nozzle for a shorter time and experiences fewer collisions to dissipate its internal energies. Therefore, C_1(a) is colder than C_1(b). By measuring the PES spectra of the same cluster size with different F_3 timing [i.e. either C_1(a) or C_1(b)], we confirmed that the above explanation on the cluster temperature is valid although the exact temperatures of clusters are not known.[95] The F_3 timing provides an important parameter to control the temperatures of the clusters, which determine the quality of the obtained PES spectra.

CHAPTER THREE

STRUCTURAL EVOLUTION OF SILICON CLUSTER ANIONS

3.1 Introduction

Silicon is the backbone of the electronics industry. As miniaturization of electronic devices is approaching the nanoscale, it is important to understand the electronic and structural properties of Si_n nanoclusters. Indeed, extensive experimental and theoretical work have been carried out on silicon clusters.[37,79,81-83,85,96-116] Experimentally, the structures of very small silicon clusters ($n < 8$) have been inferred from molecular spectroscopy[82] and high-resolution photoelectron spectroscop[116] measurements. For larger Si clusters, structural shape information has been obtained on basis of ion mobility data by Jarrold and co-workers.[79,112] It has been found that medium-sized low-lying clusters are mostly prolate in shape for $n < 27$ and become near spherical for $n > 27$. A computational study based on a genetic algorithm search procedure[85] uncovered a generic structural feature in low-lying neutral clusters Si_n, $n = 10 – 18$, that is, nearly all clusters contain the tricapped-trigonal-prism (TTP) Si_9 motif. The most compelling evidence was later provided by Müller et al.[83] who both measured and simulated anion PES spectra in the size range $8 \leq n \leq 20$ and validated the presence of the TTP structural motif in many medium-sized low-lying Si_n^- clusters. Indeed, the combined experimental and theoretical PES approach has become a very effective method to identify cluster structures.[6,22,83,102-104,117,118]

However, the combined theoretical/experimental approach is most effective when the following two conditions are met: (1) Well-resolved PES spectra can be obtained,

particularly for the first two or three PES peaks near the threshold as they are directly related to the frontier orbitals of the cluster (because of congested electronic transitions, multiple low-energy isomers, or high cluster temperatures, well-resolved PES spectra are rather difficult to measure). (2) A large database on low-energy clusters is available, typically obtained using various global optimization techniques, e.g., genetic algorithms,[85] basinhopping method,[119] or minima-hopping method,[120] combined with first-principles calculations.[121-123] We have obtained well resolved PES spectra for Si_n^- (n = 5 – 45) at a photon energy of 6.424 eV controlling cluster temperatures from a laser vaporization supersonic cluster source (see chapter two). On the other hand, in density functional theory (DFT) calculations carried out by our collaboraters, many candidate structures (or database of low-lying clusters) have been reported in the literature.[106-111] On the basis of the calculated electron binding energies along with the measured PES spectra, we are able to identify some new generic structural features in low-lying prolate-shaped Si_n^- clusters and to provide spectroscopic corroboration of the prolate-to-spherical shape transition at n = 27.

3.2 Results and Discussion

A. Photoelectron Spectra and Calculated Structures of Si_n^- (n = 4 – 19). Figure 3.1 displays the spectra of Si_n^- (n = 4 − 19) using 6.424 eV phonton energy. Except for the very small ones (n ≤ 7), whose spectra were vibrationally resolved by Neumark and co-workers,[124,125] our spectra display the best resolution compared with previously published results.[37,83,101,126] As seen in Figure 3.1, Si_4^-, Si_6^-, Si_7^- and Si_{10}^- exhibit very large band gaps, indicating their neutral species are stable cluster units with

closed-shell electronic structure. However, only Si_7^- and Si_{10}^- display band gaps that are larger than crystalline silicon.

PES of Si_n^- (n = 3 − 12) was first performed by Smalley and co-workers.[126] They found that Si_4^-, Si_7^- and Si_{10}^- show very large band gaps. Vibrationally resolved photoelectron spectra of Si_n^- (n = 3 − 7) have been obtained by Neumark and co-workers.[124,125] Accurate electron affinities, term energies, and vibrational frequencies for the ground and excited electronic states of the neutral clusters were extracted from these well resolved spectra. Aided by *ab initio* calculations and photoelectron angular distributions, they also made the electronic assignments for the excited states. Their PES experiments and previous IR/Raman spectroscopy[82,127] have consistently established the geometries of Si_n (n = 3 − 7): an isosceles triangle for Si_3, a rhombus for Si_4, and trigonal, tetragonal, and pentagonal bi-pyramids for Si_5, Si_6, Si_7, respectively.

Gantefor and co-workers[101] performed the PES study for a wide range of silicon clusters Si_n^- (n = 3 − 45). They estimated the HOMO−LUMO gaps of neutral clusters from the anion PES spectra. Contrary to expectations of quantum confinement, almost all clusters (except for n = 7 and 10) in this size range have a band gap smaller than that of crystalline Si or even display a continuous density of states. They suggested this is due to covalent bond formation analogous to the reconstructions observed on single-crystal surfaces. The group of Gantefor and the theoretical group of Chelikowsky[83] have collaborated to elucidate the growth pattern of Si cluster anions with up to 20 atoms. Spectra for an extensive set of low-energy isomers found by a global search have been simulated using density functional theory (DFT) and pseudopotentials. Good agreements have been obtained between simulated and experimental spectra for n = 8−20, confirming

the theoretical prediction of tricapped trigonal prism (TTP) Si_9 motif in this size rage. The optimized structures of Si clusters up to 20 atoms by Shvartsburg and co-workers[128] are displayed in Figure 3.2.

B. Photoelectron Spectra and Calculated Structures of Si_n^- (n = 20 – 45). The PES of Si_n^- (n = 20 – 26) measured at 193 nm are shown in column a of Figure 3.3, where X and A (peaks) mark the first two electronic levels of the primary isomer and X' and A' denote the first two electronic levels of a secondary isomer. Here the "primary isomer" refers to the isomer that gives rise to the most conspicuous peaks in the PES. Some weak features in the spectra, however, are presumably due to one or a few secondary isomers. The spectra are consistent with the results of a previous PES study[37] that had a somewhat lower resolution. For Si_n^- (n = 20 – 26), we observed fairly large gaps between the binding energies of the two most external electrons (0.5-1.0 eV) for the primary anion isomers, implying that the corresponding neutral Si_n clusters are all closed-shell systems with a reasonably large HOMO-lowest-unoccupied molecular orbital (LUMO) gap. Among these clusters, Si_{25}^- exhibited the largest gap (1.0 eV), which is already quite close to that of bulk silicon (1.12eV). The VDEs of both the primary and secondary isomers are listed in Table 3.2.

The searches for low-energy neutral and anion cluster structures generated a large database. For prolate-shaped clusters (in the size range of $12 \leq n \leq 30$), our collaborators adopted the basin-hopping (BH) method[119] combined with DFT.[121] In the DFT-BH search,[111] the Monte Carlo scheme is used to explore the potential-energy surface. The potential energy and energy gradient-driven optimizations were computed by using the

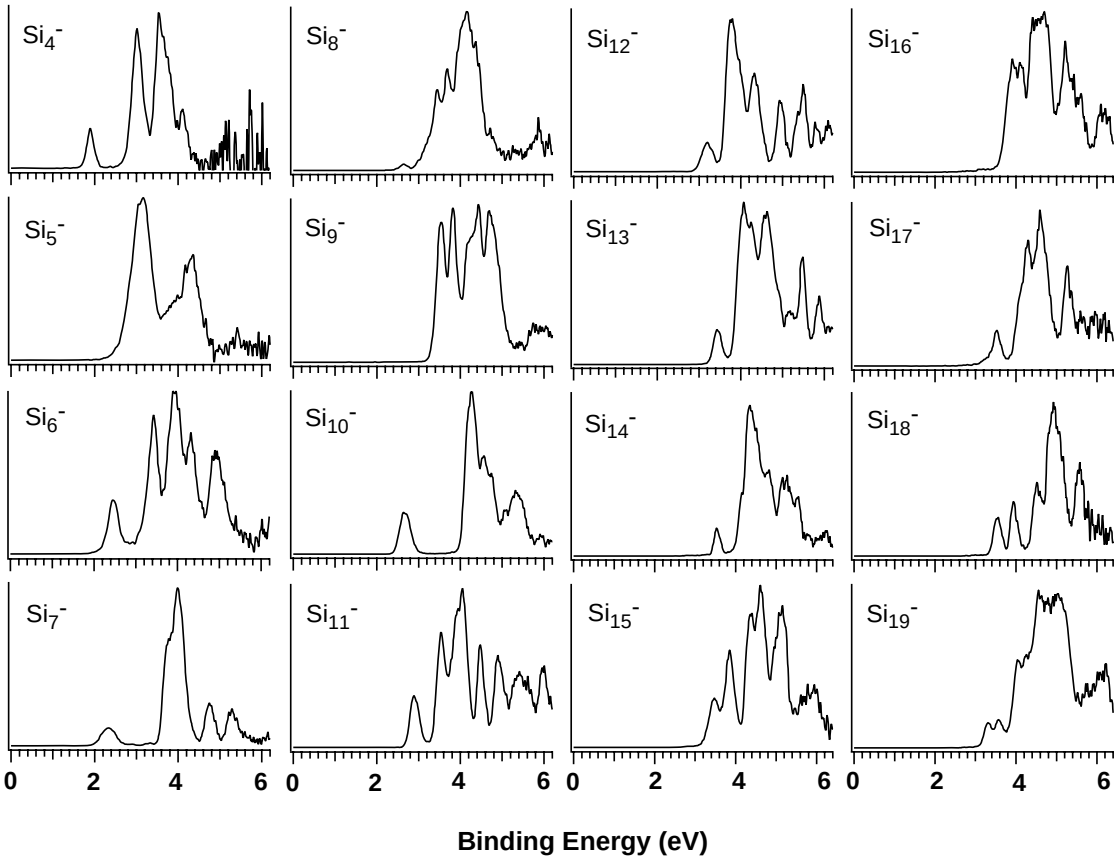

Figure 3.1 Photoelectron spectra of Si_n^- (n = 4 − 19) at 193nm (6.424 eV)

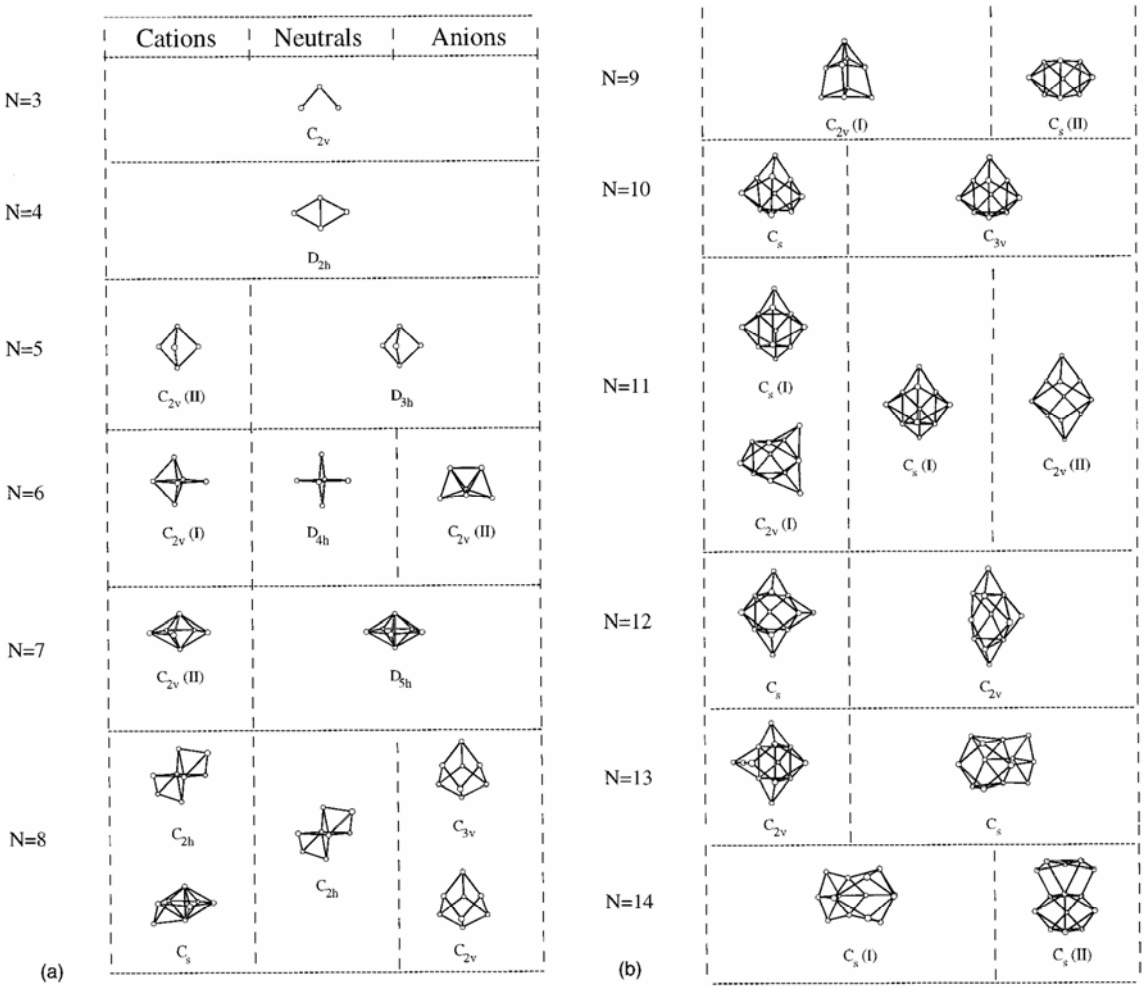

Figure 3.2 Optimized structures of Si_n cations, neutrals, and anions (n = 3 − 20) clusters from Ref. [128].

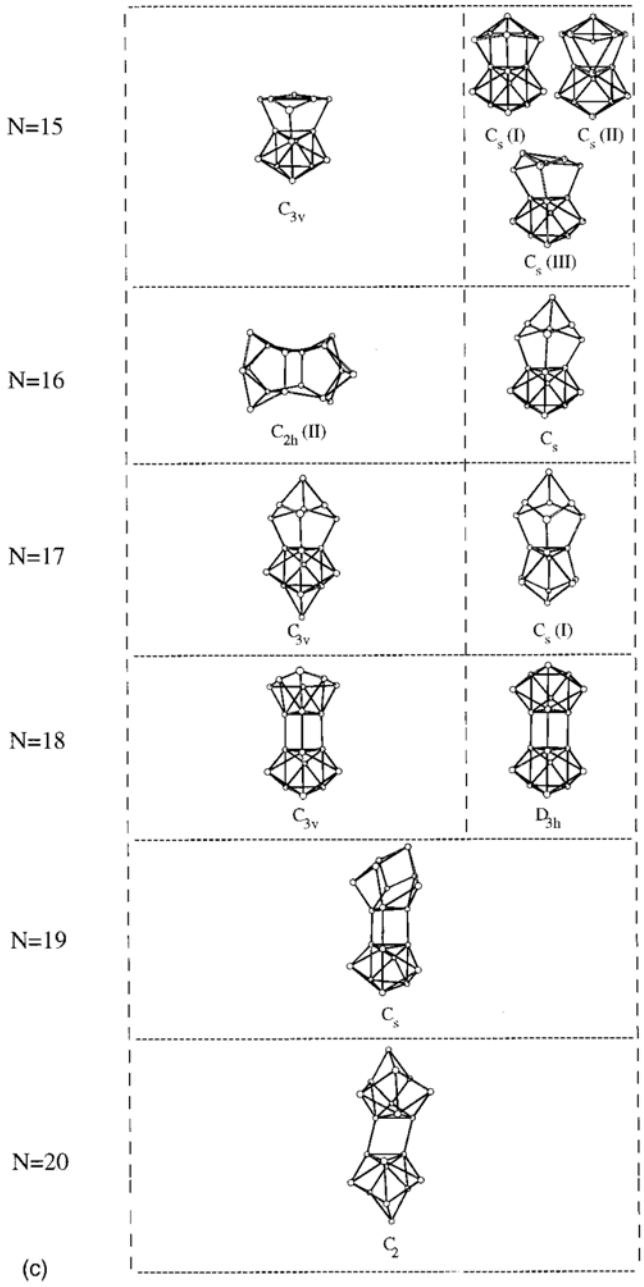

Figure 3.2 (*Continued*.)

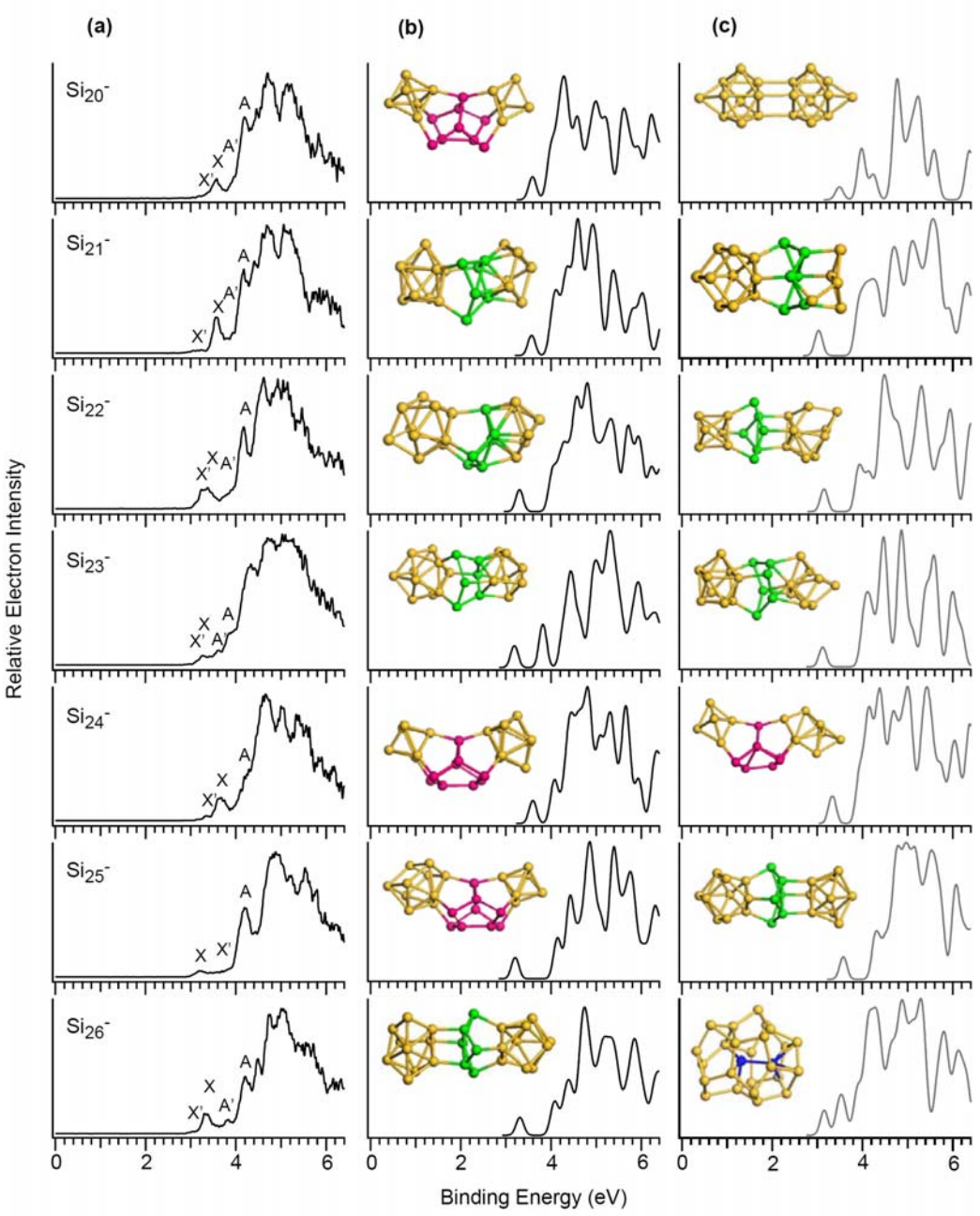

Figure 3.3 Comparison of measured and simulated PES spectra for Si_{20}^- – Si_{26}^-. (a) Spectra measured at 193 nm (6.424 eV). X and A (X' and A') denote the first and second photoelectron peaks for the primary (secondary) isomers. (b) Simulated spectra for the primary isomers. (c) Simulated spectra for the secondary isomers. The simulated spectra were obtained by convoluting the discrete DFT energy eigenvalues with Gaussians of width 0.08 eV. The primary isomer provides the best comparison with the measured spectra (e.g., the location of the threshold peak X as well as the separation between the first and the second major peak A). The secondary isomer is intended to compare with certain weak features in the spectra (e.g., the X' and A' peaks).

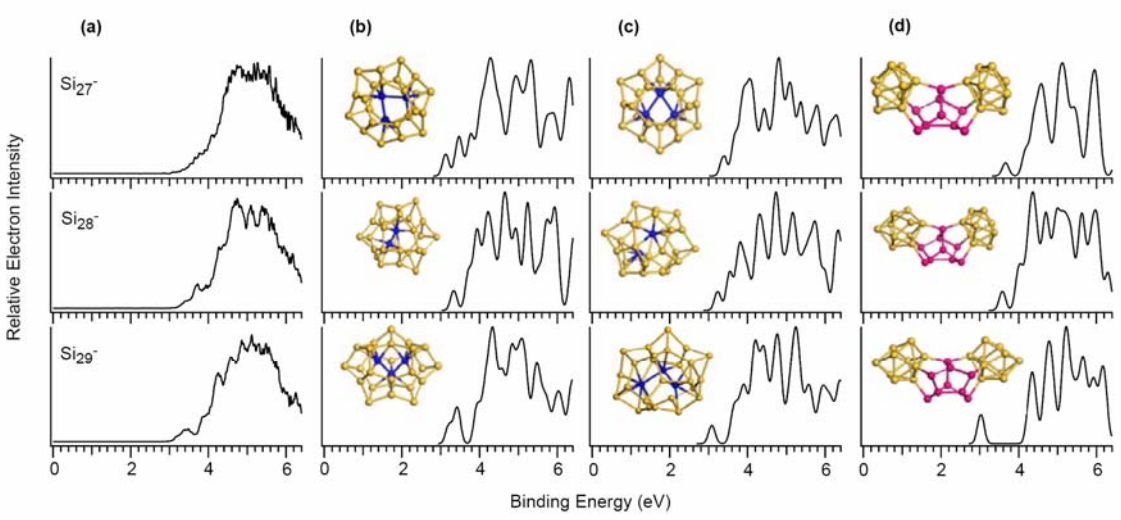

Figure 3.4 The same as Figure 3.3 for Si_{27}^{-} – Si_{29}^{-}. Here simulated spectra from the three lowlying isomers are presented.

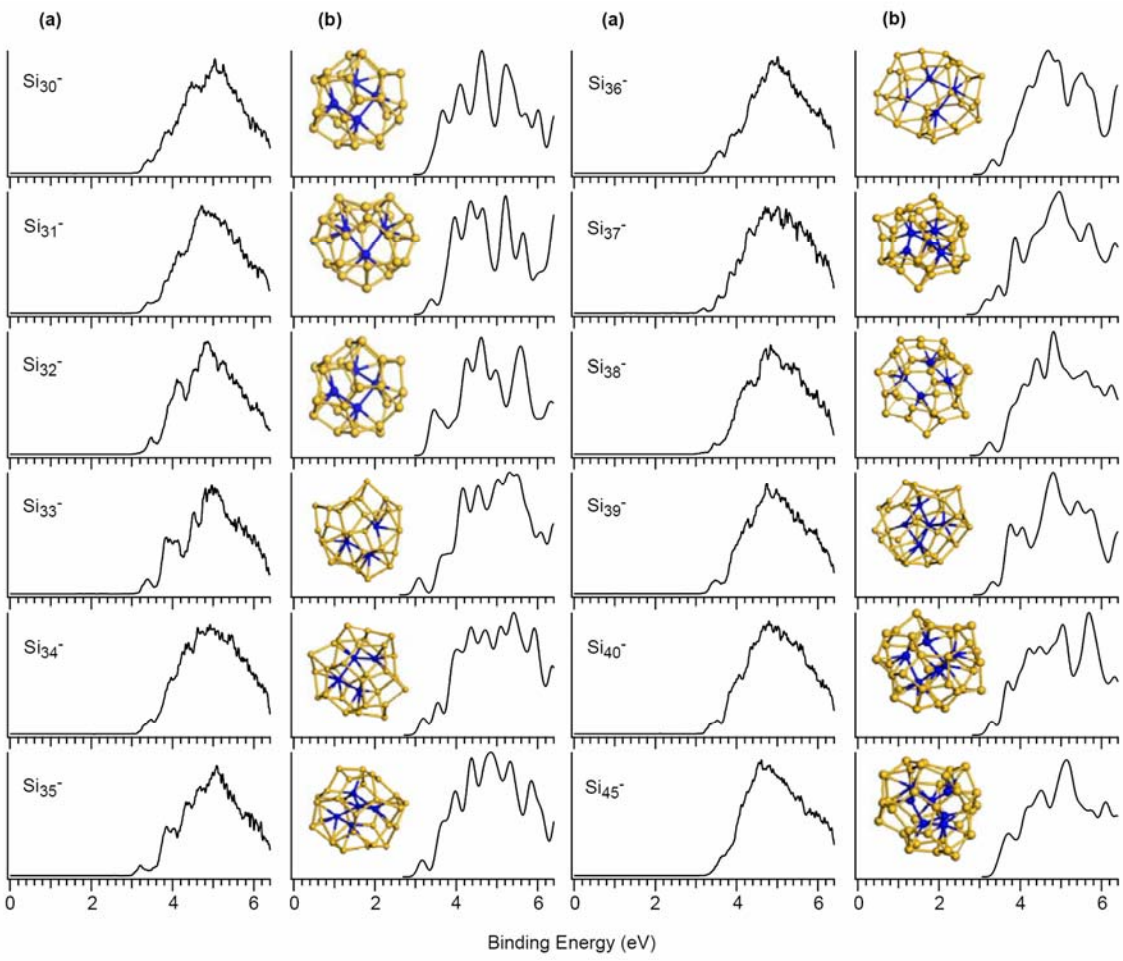

Figure 3.5 The same as Figure 3.4 but for Si_{30}^- – Si_{40}^- and Si_{45}^-.

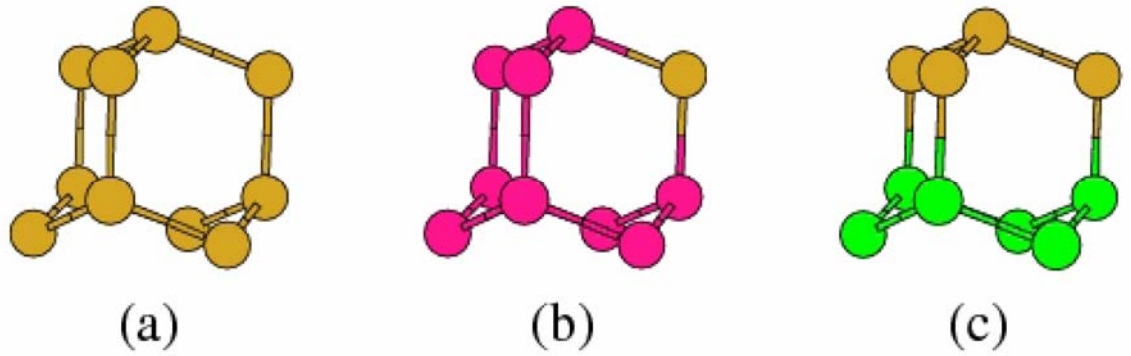

Figure 3.6 (a) A bulk fragment of the cubic diamond silicon, "adamantane" Si_{10}. (b) A nine-atom subunit of the Si_{10}, two fused puckered hexagonal rings, highlighted in pink color. (c) A six-atom subunit of the Si_{10}, a puckered hexagonal ring, highlighted in green color.

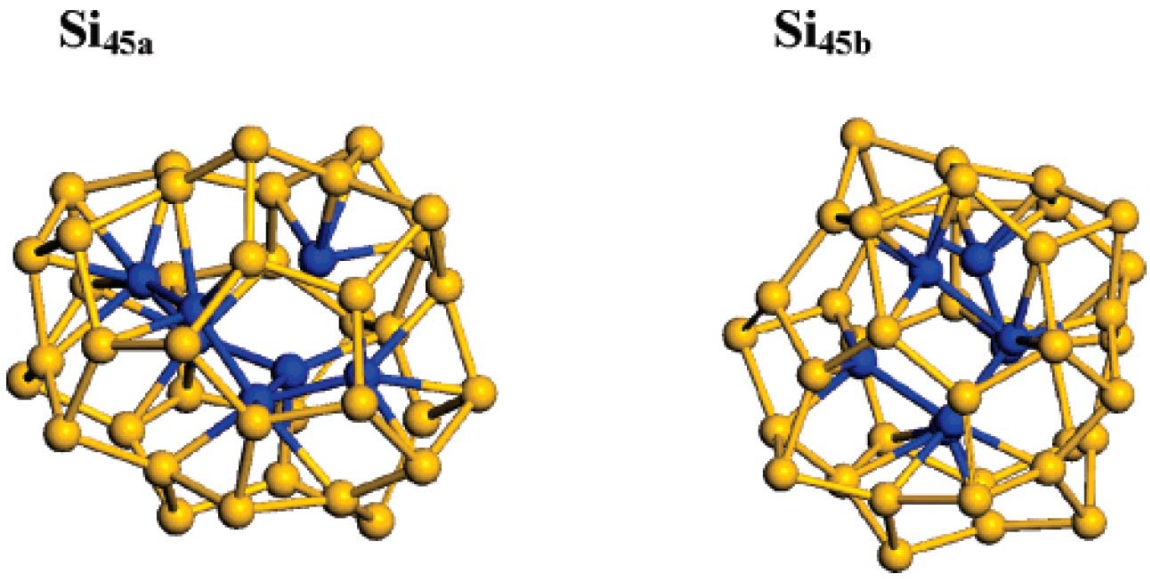

Figure 3.7 Two low-energy Si_{45} isomers obtained respectively from two potential-energy-surface searches. The Si_{45a} isomer has the lowest energy. The endohedral core-filling Si atoms are highlighted in blue color.

Table 3.1: Calculated total energy differences (eV) with respect to the isomer with the lowest energy for $Si_{20}^{-} - Si_{29}^{-}$ shown in figures 3.3 and 3.4.

anion	energy difference (primary isomer)	energy difference (secondary isomer)	energy difference (tertiary isomer)
Si_{20}^{-}	0.0	0.011	
Si_{21}^{-}	0.0	0.303	
Si_{22}^{-}	0.0	0.411	
Si_{23}^{-}	0.0	0.326	
Si_{24}^{-}	0.0	1.004	
Si_{25}^{-}	0.0	0.022	
Si_{26}^{-}	0.008	0.0	
Si_{27}^{-}	0.0	0.104	0.252
Si_{28}^{-}	0.127	0.0	0.093
Si_{29}^{-}	0.279	0.0	0.301

Table 3.2: Measured and computed VDEs of primary and secondary isomers of Si_{20}^- – Si_{26}^- shown in figures 3.3.

anions		VDE (eV)	
		experimental	theoretical
Si_{20}^-	X	3.57	3.587
	X'	3.38	3.491
Si_{21}^-	X	3.57	3.564
	X'	3.16	3.031
Si_{22}^-	X	3.37	3.299
	X'	3.23	3.155
Si_{23}^-	X	3.26	3.194
	X'	3.12	3.124
Si_{24}^-	X	3.66	3.597
	X'	3.34	3.336
Si_{25}^-	X	3.21	3.206
	X'	3.60	3.571
Si_{26}^-	X	3.34	3.311
	X'	3.02	3.153

CPMD code.[121] For larger near-spherical clusters (in the size range $25 \leq n \leq 45$), our collaborators took a two-step approach.[109,110] The first step is a global search of the potential-energy surface by using a genetic algorithm[85] coupled with the tight-binding model.[129] The second step is an augmented search using the DFTBH method or the minima-hopping method coupled with the density-functional tight-binding (DFTB) theory,[122] based on those low-energy structures obtained in the first step. For all clusters, after the low-energy anion isomers were identified, all-electron DFT optimizations at the PBEPBE/6-31G(d) level of theory and basis set, as implemented in the Gaussian 03 code,[123] were performed. Total energy differences with respect to the lowest-energy anion isomers (for $20 \leq n \leq 29$) are listed in the Table 3.1. Finally, simulated PES spectra of low-energy isomers were obtained from the negatives of the Kohn-Sham (KS) eigenenergies by shifting them so that the negative of the highest-occupied molecular orbital (HOMO) KS eigenenergy coincides with the computed value of the vertical detachment energy (VDE). The one or two cases that provide the best fit to the measured PES spectra are shown in Figures 3.3–3.5.

In columns b and c of Figure 3.3, our collaborators plot the simulated PES spectra of the primary and the most plausible secondary isomer. As is shown from the figure, the simulated spectra of the primary isomers are in very good agreement with the experimental PES data. The computed spectra for the leading secondary isomers can account for many weak PES features. We found that the primary isomers of Si_{20}^- – Si_{26}^- and the leading secondary isomers of Si_{20}^- – Si_{26}^- are all prolate in shape. Moreover, these clusters contain a bulklike fragment, either a six-atom (the puckered hexagonal ring highlighted in green color) or a nineatom (two fused hexagonal rings highlighted in pink

color) subunit of the "adamantane" Si_{10} (Figure 3.6).[81,113] Note that the six-atom subunit has been identified earlier in smaller anion clusters (Si_{16}^- and Si_{17}^-)[83] as well as in neutral clusters (Si_{16} – Si_{20}),[111] and these two subunits are always coupled with one or two magic-number cluster (Si_6, Si_7, Si_{10})[97,107,108,111] or the TTP Si_9. It should be noted that the leading secondary isomer of Si_{26}^- is no longer prolate in shape, and it is more compact and near spherical.

A dramatic spectral change is observed at Si_{27}^- (Figure 3.4a), whose PES spectrum is featureless while the spectra for many clusters larger than Si_{27}^- again exhibit resolvable features up to Si_{45}^- (Figures 3.4 and 3.5). This observation suggests that there must be several coexisting isomers for Si_{27}^- and many clusters larger than Si_{27}^-, which contribute to the spectrum more or less equally. In other words the prolate isomer does not dominate any more. This observation is in complete agreement with the ion mobility experiments by Jarrold and co-workers,[79,112] who found a structural transition from prolate to near-spherical shapes for Si_n^- clusters in the size range n = 27 – 29. Our study shows that indeed for n < 26 both the primary and the leading secondary isomer of Si_n^- are of prolate shape (Figure 3.3), whereas for Si_{26}^- the primary isomer is prolate, but the leading secondary isomer is near spherical. It is natural then that for Si_{27}^- the prolate and some near-spherical isomers coexist and that, for clusters larger than n = 27, the near-spherical isomers are expected to become more and more competitive energetically than the prolate isomers (Table 3.1).

Two questions arise: (1) What are the structures of the nearspherical clusters? (2) Are there any generic structural features in these near-spherical clusters? Numerous candidates for the near-spherical clusters have been reported recently[109,110] for n >26. In

Figure 3.4, we compare experimental PES for Si_{27}^- – Si_{29}^- to simulated spectra with three low-energy isomers: two nearspherical (panels b and c) and one prolate (panel d). Each of the three simulated spectra of Si_{27}^- is highly structured. The measured spectrum of this cluster however is largely featureless. This suggests that all these three isomers of Si_{27}^- contribute about equally to the measured spectrum. The same can be said about Si_{28}^-. However, for Si_{29}^- only the simulated spectra of the primary and one secondary isomer (panel b) appear to agree with the measured spectrum (panel a), suggesting that the prolate isomer of Si_{29}^- (panel d) has a negligible contribution.

In Figure 3.5, we compare the experimental PES with the simulated spectra for the leading candidate of the lowest-energy isomer of Si_n^-, n = 30 – 45. For most sizes, there are certain degrees of agreement between the experiment and the computations, for example, the location of the first peak and for some clusters, even the location of the second peak. For Si_{30}^-, our collaborators computed PES of a prolate isomer that has the lowest energy in previous database, and we found that the simulated PES entails a large energy gap between the first and second peak (like Figure 3.4d for Si_{29}^-). We therefore conclude that the low-lying isomers of Si_{30}^- – Si_{45}^- are most likely near spherical in shape and exhibit "stuffed-cage"-like structures. Interestingly, theoretical calculations indicate that the cages of these candidate low-lying isomers are all homologous to the carbon fullerene cages in the sense that they are composed of only pentagonal and hexagonal rings and have even numbers of Si atoms. In Figures 3.4 and 3.5, we highlight the core-filling ("stuffing") atoms inside the cages with blue color. If these core-filling atoms were removed and the cage atoms were replaced by carbon atoms, one would obtain the fullerene cages after structural relaxation.[109,110] The reasonable match between the

measured and simulated PES spectra provides additional spectroscopic support to the view that the near-spherical low-lying silicon clusters all exhibit a "stuffed-fullerene"-like structural feature. Figure 3.7 displays two low-energy isomers of Si_{45} obtained in two different studies.[109,115] One can see that both isomers have "stuffed-fullerene"-like structures with seven core-filling atoms. The core-filling subunits however do not exhibit diamond-like tetrahedral packing characteristic of bulk silicon with diamond structure.

3.3 Conclusion

Well resolved photoelectron spectra of Si_n^- clusters ($4 \leq n \leq 45$) at 193nm are reported. Combined photoelectron spectroscopy and first-principles density-functional study of Si_n^- clusters in the size range $20 \leq n \leq 45$ are performed and discussed. Evidence for a prolate-to-near-spherical shape transition at $n = 27$ is presented. It is shown that the tricapped-trigonal-prism (TTP) structural motif Si_9 found in most low-lying clusters Si_n^-, $9 \leq n \leq 19$, is replaced or augmented by a series of structural motifs consisting of a bulklike "adamantane" fragment plus a magic-number cluster (Si_6, Si_7, Si_{10}) or TTP Si_9 in low-lying prolate clusters Si_n^-, $n \geq 20$. For $28 \leq n \leq 45$, almost all low-lying near-spherical clusters Si_n^- adopt "stuffed-cage"-like structures where the cages are homologous to carbon fullerenes in the sense that they are composed of only five- and six-membered rings. However the arrangement of the "stuffing" atoms is not yet diamondlike.

CHAPTER FOUR

DOUBLY CHARGED SILICON CLUSTERS

4.1 Chemical Bonding in Si_5^{2-} and $NaSi_5^-$ via Photoelectron Spectroscopy and Ab Initio Calculations

4.1.1 Introduction

The discovery of the C_{60} buckyball[11] has induced a great deal of interest in cagelike clusters, particularly in silicon clusters. However the obvious valence isoelectronic Si_{60} analogue does not have the same structure as C_{60}.[130,131] Instead of a beautiful soccer-ball shape, Si_{60} seems to adopt a rather low symmetry structure.[131] An alternative approach to searching for cagelike silicon clusters is to use the isolobal analogy between an HB unit and a Si atom[132] and the known fact that boranes, such as $B_{12}H_{12}^{2-}$, have cagelike deltahedral structures.[133] However, preliminary calculations of the Si_{12}^{2-} cluster[134] indicate indeed that an icosohedral Si_{12}^{2-} cage is only a local minimum, but not the global minimum. Preliminary results on other Si_n^{2-} clusters[134] also demonstrate that many doubly charged silicon anionic clusters adopt low-symmetry structures rather than the beautiful deltahedral structures. We are interested in developing a unified chemical bonding picture for silicon clusters and understanding the deviation of the geometric structures of doubly charged silicon cluster anions from the isolobal deltahedral $B_nH_n^{2-}$ analogues.[133]

We begin this endeavor with the Si_5^{2-} dianionic cluster, which has been recently synthesized and characterized in the solid state.[135] The Si_5^{2-} cluster was synthesized in the

(Rb-crypt)$_2$Si$_5$-4NH$_3$ crystal and was shown to be a trigonal-bipyramidal cluster with equatorial distances $d_{eq\text{-}eq}$ = 2.535 Å and axial distances $d_{ax\text{-}eq}$ = 2.350 Å. An isolated Si_5^{2-} dianion is expected to be metastable toward autodetachment in the gas phase, but it may be stabilized by an alkali metal cation (M^+) in MSi_5^-. Kishi et al.[136] reported experimental observation of $NaSi_5^-$, as well as its photoelectron spectrum at 355 nm, which displayed one broad spectral band. They also presented theoretical calculations for $NaSi_5^-$ and Si_5^{2-} at the MP2/6-31G* level of theory and found a trigonal-bipyramidal structure for Si_5^{2-} and two isomers for $NaSi_5^-$: a C_{2v} ($^1A_1$) structure and a C_{3v} ($^1A_1$) structure. The C_{2v} structure with the Na^+ cation coordinated to the edge of the triangular base was found to be more stable by 0.823 eV (at MP4/6-31G*//MP2/6-31G*) than the C_{3v} isomer, in which the Na^+ cation was coordinated to one apex Si atom of the trigonal-bipyramidal Si_5^{2-} structure. The series of ME_5^- (M = Li, Na, K, and E = Si and Ge) anions have been studied by Li and co-workers,[137,138] who optimized the geometry for the trigonal-bipyramidal Si_5^{2-} structure using six different levels of theory. At their best density functional level of theory (B3PW91/6-311+G(3d2f)), they obtained $d_{ax\text{-}eq}$ = 2.53 Å and $d_{eq\text{-}eq}$ = 2.75 Å, and at their best ab initio level of theory (MP2/6-311G*) they got $d_{ax\text{-}eq}$ = 2.57 Å and $d_{eq\text{-}eq}$ = 2.76 Å. Both are in reasonable agreement with the Si_5^{2-} structure in the solid state: $d_{ax\text{-}eq}$ = 2.48 Å and $d_{eq\text{-}eq}$ = 2.69 Å.

In this chapter, we present a systematic and comprehensive study of Si_5^{2-} and $NaSi_5^-$ using a combined experimental and theoretical approach. Photoelectron spectra of $NaSi_5^-$ have been obtained at three photon energies: 355, 266, and 193 nm. The higher photon energy spectra yielded higher binding energy detachment features, which are better suited for comparison with the theoretical results. Molecular orbital analyses have

been carried out to understand the detailed chemical bonding in the Si_5^{2-} species, which are compared with $B_5H_5^{2-}$. We also included Si_5 and Si_5^- in the current study for completeness and for better evaluation of the theoretical methods, which will be used to investigate larger multiply charged silicon clusters in the future.

4.1.2 Experimental Results

A. Photoelectron Spectroscopy of Si_5^-. Figure 4.1 shows the photoelectron spectra of Si_5^- at three photon energies (355, 266, and 193 nm). The photoelectron spectra of Si_5^- have been reported in a number of previous studies.[37,125,126,139] In particular, vibrationally resolved spectra have been obtained by Xu et al.[125] The current spectra agree with the previous data, but they provide better resolved features beyond 3.5 eV binding energies. The 355 nm spectrum (Figure 4.1a) displays a broad band with a low binding energy tail. From their vibrationally resolved spectra and angular dependent studies, Xu et al. showed that the 355 nm spectrum contained two electronic transitions, with the low-energy tail (X) corresponding to the ground-state transition. A long vibrational progression with an average spacing of 233 ±10 cm^{-1} was observed in ref 49, suggesting a significant geometry change between the ground state of Si_5^- and Si_5. An adiabatic electron detachment energy (ADE) of 2.59 eV was estimated by Xu et al. from their Franck-Condon simulation. Thus the spectral onset at ~2.7 eV in the 355 nm spectrum only represents an upper limit for the ADE due to the large geometry changes between the anion and neutral ground state. The VDE of the X band is estimated to be around 3.0 eV, which is consistent with the Franck-Condon simulation by Xu et al. The intense part of the 355 nm spectrum at the high binding energy side (A) corresponds to

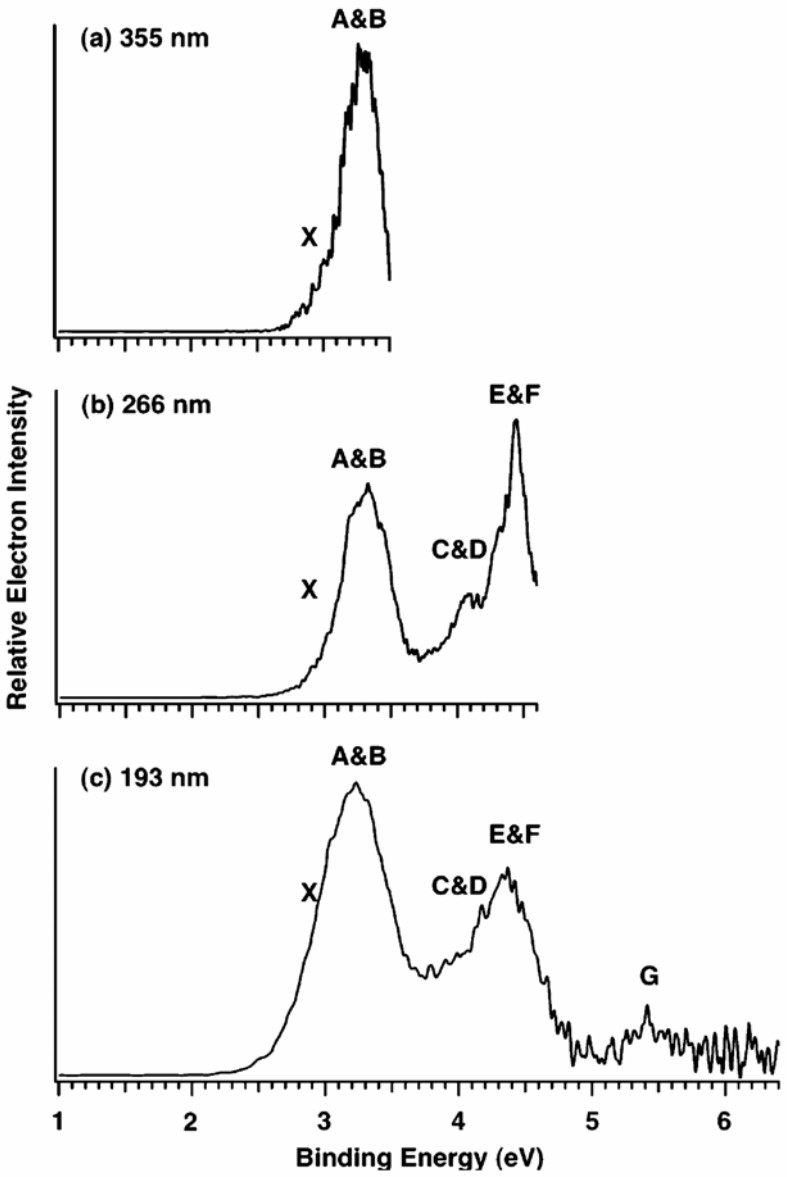

Figure 4.1 Photoelectron spectra of Si_5^- at (a) 355 nm (3.496 eV), (b) 266 nm (4.661 eV), and (c) 193 nm (6.424 eV).

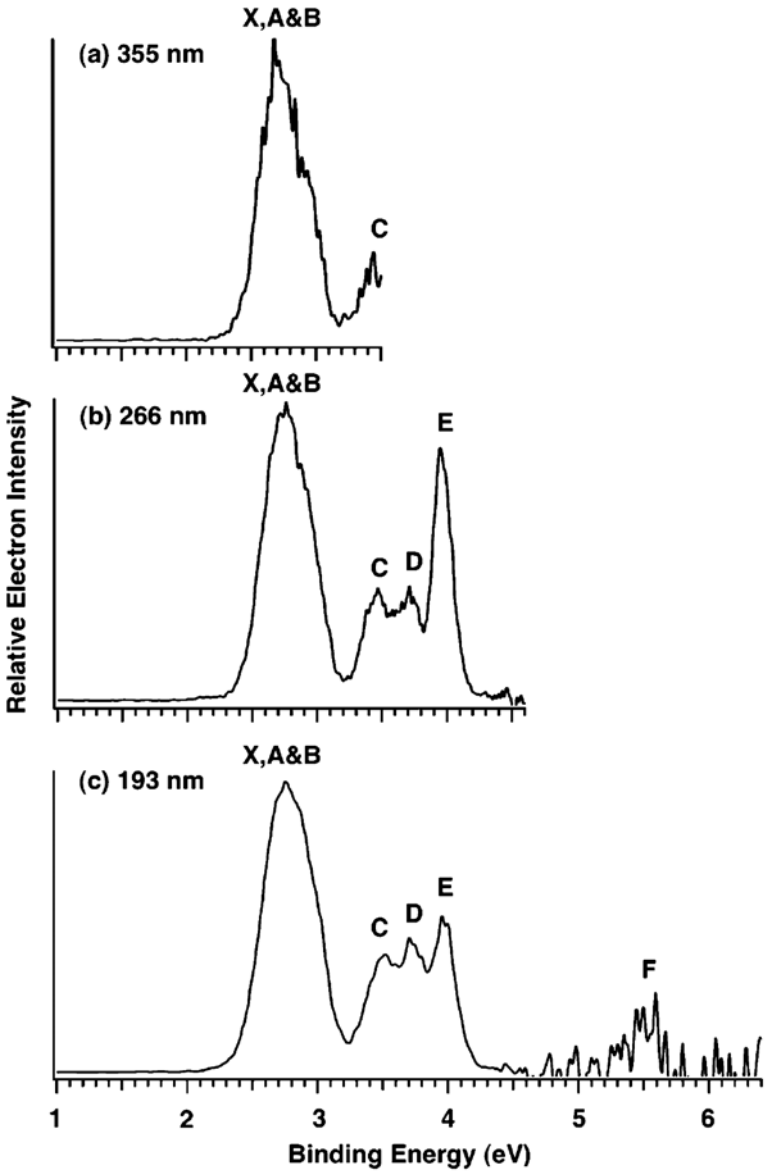

Figure 4.2 Photoelectron spectra of $NaSi_5^-$ at (a) 355 nm (3.496 eV), (b) 266 nm (4.661 eV), and (c)193 nm (6.424 eV).

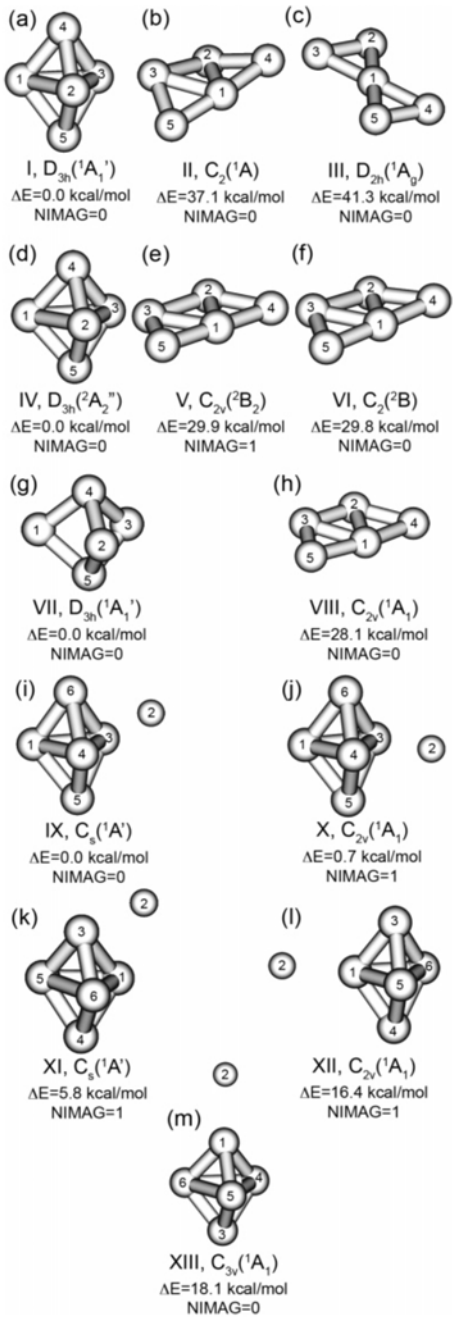

Figure 4.3 Optimized geometries (B3LYP/6-311+G*) of Si_5^{2-} (a-c), Si_5^- (d-f), Si_5 (g, h), and $NaSi_5^-$ (i-m). Relative energies are given at CCSD(T)/6-311+G(2df)//B3LYP/6-311+G*+ZPE. NIMAG, number of imaginary frequencies.

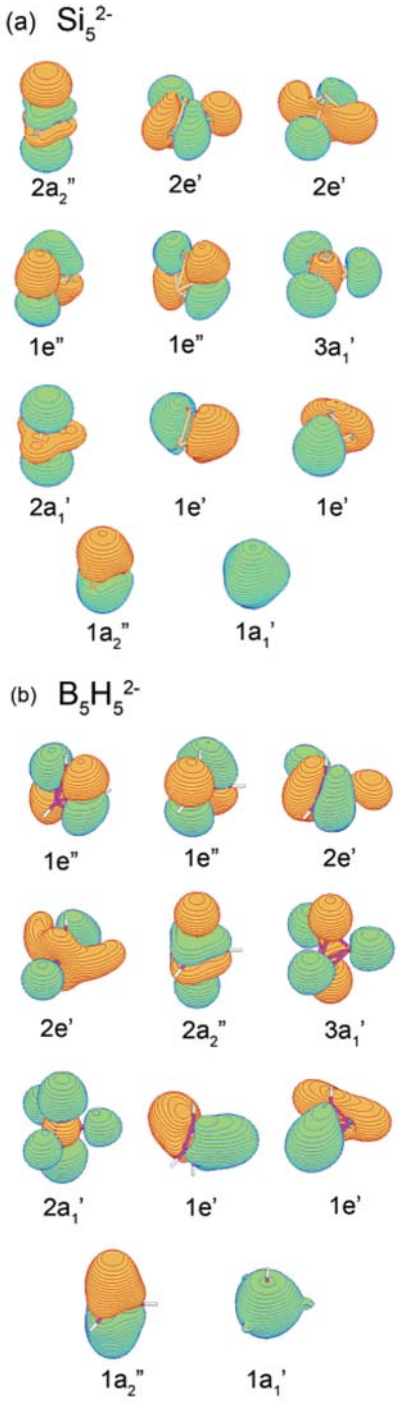

Figure 4.4 Valence molecular orbitals of (a) Si_5^{2-} (D_{3h}, $^1A_1'$) and (b) $B_5H_5^{2-}$ (D_{3h}, $^1A_1'$) at the RHF/6-311+G* level of theory.

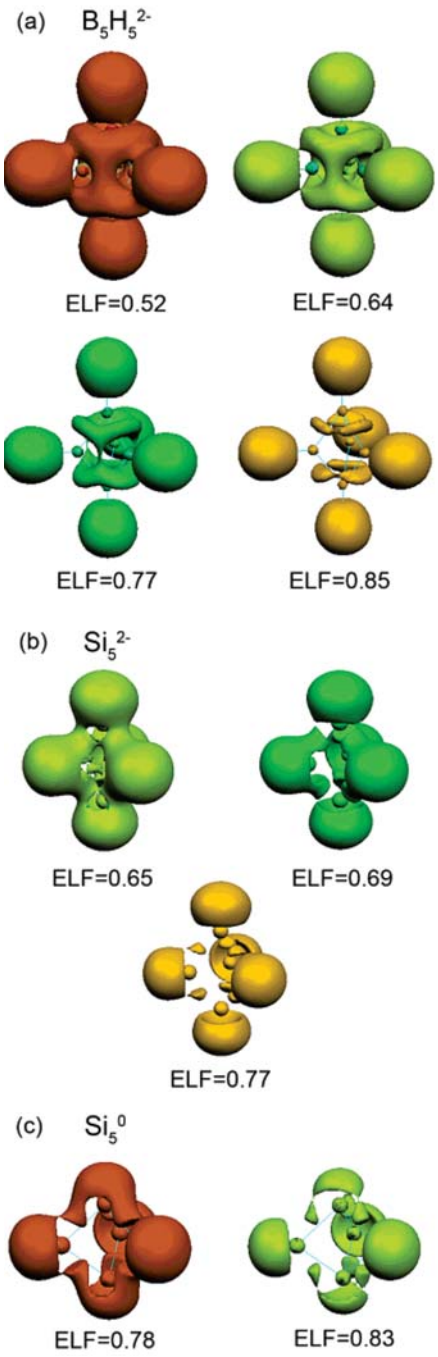

Figure 4.5 ELF bifurcations for (a) $B_5H_5^{2-}$ (D_{3h}, $^1A_1'$), (b) Si_5^{2-} (D_{3h}, $^1A_1'$), and (c) Si_5 (D_{3h}, $^1A_1'$) calculated at the B3LYP/6-311+G* level of theory.

Table 4.1: Experimental Compared with Calculated VDEs (eV) for D_{3h} ($^2A_2''$) Si_5^-

final state	expt	TD-B3LYP[a]	UOVGF[b]	CCSD(T)[c]	EOM[d]
$^1A_1'$ ($2a_1'^2 3a_1'^2 1e''^4 2e'^4 2a_2'^0$)	~3.0 (X)	3.06	2.99 (0.91)	3.01	3.01
$^3E''$ ($2a_1'^2 3a_1'^2 1e''^4 2e'^3 2a_2''^1$)	~3.2 (A)	3.13	2.95 (0.90)	3.24	*g*
$^1E''$ ($2a_1'^2 3a_1'^2 1e''^4 2e'^3 2a_2''^1$)	~3.4 (B)	3.52	*e*	*f*	3.26
$^3E'$ ($2a_1'^2 3a_1'^2 1e''^3 2e'^4 2a_2''^1$)	~4.1 (C)	4.03	3.87 (0.91)	*f*	*g*
$^1E'$ ($2a_1'^2 3a_1'^2 1e''^3 2e'^4 2a_2''^1$)	~4.3 (D)	4.36	*e*	*f*	4.50
$^3A_2''$ ($2a_1'^2 3a_1'^1 1e'^4 2e'^4 2a_2''^1$)	4.47 ± 0.03 (E)	4.29	4.31 (0.90)	*f*	*g*
$^1A_2''$ ($2a_1'^2 3a_1'^1 1e''^4 2e'^4 2a_2''^1$)	~4.6 (F)	4.52	*e*	*f*	4.81
$^3A_2''$ ($2a_1'^1 3a_1'^2 1e''^4 2e'^4 2a_2''^1$)	~5.4 (G)	5.27	4.92 (0.88)	*f*	*g*
$^1A_2''$ ($2a_1'^1 3a_1'^2 1e'^4 2e'^4 2a_2''^1$)		6.80	*e*	*f*	6.82

[a] The VDEs were calculated at the TD-B3LYP/6-311+G(2df)//B3LYP/6-311+G* level of theory. [b] The VDEs were calculated at the UOVGF/6-311+G(2df)//CCSD(T)/6-311+G* level of theory. The numbers in parentheses indicate the pole strength, which characterizes the validity of the one-electron-detachment picture. [c] The VDEs were calculated at the CCSD(T)/6-311+G(2df)//CCSD(T)/6-311+G* level of theory. [d] The VDEs were calculated at the CCSD(T)/6-311+G(2df)//CCSD(T)/6-311+G* level of theory. [e] The VDEs into the final singlet states were not calculated because of the multiconfigurational nature of the final singlet states. [f] The VDEs into these excited states cannot be calculated at this level of theory. [g] The VDEs into the final triplet states cannot be calculated using MOLPRO-2000-1.

Table 4.2: Experimental Compared with Calculated VDEs (eV) for C_s (^{1}A') $NaSi_5^-$

final state	expt	ROVGF[a]	TD-B3LYP[b]	UCCSD(T)[c]
^{2}A' ($4a'^2 5a'^2 2a''^2 6a'^2 3a'^2 7a'^2 8a'^1$)	~2.55 (X)	2.47 (0.88)	2.52	2.54
^{2}A' ($4a'^2 5a'^2 2a'^2 6a'^2 3a''^2 7a'^1 8a'^2$)	2.67 ± 0.04 (A)	2.68 (0.88)	2.59	*e*
^{2}A'' ($4a'^2 5a'^2 2a'^2 6a'^2 3a''^1 7a'^2 8a'^2$)	~2.9 (B)	2.90 (0.88)	2.74	*e*
^{2}A' ($4a'^2 5a'^2 2a''^2 6a'^1 3a''^2 7a'^2 8a'^2$)	3.47 ± 0.04 (C)	3.29 (0.88)	3.40	*e*
^{2}A'' ($4a'^2 5a'^2 2a''^1 6a'^2 3a''^2 7a'^2 8a'^2$)	3.71 ± 0.04 (D)	3.73 (0.88)	3.43	*e*
^{2}A' ($4a'^2 5a'^1 2a'^2 6a'^2 3a'^2 7a'^2 8a'^2$)	3.95 ± 0.03 (E)	3.83 (0.87)	3.74	*e*
^{2}A' ($4a'^1 5a'^2 2a''^2 6a'^2 3a''^2 7a'^2 8a'^2$)	5.50 ± 0.06 (F)	5.83 (0.83)	5.66[d]	*e*

[a] The VDEs were calculated at the ROVGF/6-311+G(2df)//B3LYP6-311+G* level of theory. The numbers in parentheses indicate the pole strength, which characterizes the validity of the one-electron-detachment picture. [b] The VDEs were calculated at the TD-B3LYP/6-311+G(2df)//B3LYP/6-311+* level of theory. [c] The VDEs were calculated at the TD-CCSD(T)/6-311+G(2df)//B3LYP/6-311+G* level of theory. [d] The electron detachment becomes a strongly multiconfigurational process. [e] The VDEs into these excited states cannot be calculated at this level of theory.

Table 4.3: Calculated Molecular Properties of Si_5^{2-} D_{3h} ($^1A_1'$)

method	B3LYP/ 6-311+G*	CASSCF(10,8)/ 6-311+G*	CCSD(T)/ 6-311+G*
-*E*, au	1447.524 931	1444.582 724	1445.075 619
R(Si_2-Si_5), Å	2.400	2.387	2.389
R(Si_2-Si_3), Å	2.606	2.634	2.591
$\omega_1(a_1')$, cm^{-1}	432 (0.0)[a]	464	452
$\omega_2(a_1')$, cm^{-1}	332 (0.0)[a]	342	338
$\omega_3(a_2'')$, cm^{-1}	445 (1.3)[a]	485	457
$\omega_4(e')$, cm^{-1}	330 (0.0)[a]	341	336
$\omega_5(e')$, cm^{-1}	180 (0.9)[a]	190	176
$\omega_6(e'')$, cm^{-1}	301 (0.0)[a]	317	311

[a] Infrared intensities (km/mol) are given in parentheses.

Table 4.4: Calculated Molecular Properties of Si_5^- D_{3h} ($^2A_2''$)

method	B3LYP/ 6-311+G*	CASSCF(9,7)/ 6-311+G*	CCSD(T)/ 6-311+G*
-*E*, au	1447.581 738	1444.639 338	1445.139 672
R(Si_2-Si_5), Å	2.356	2.348	2.346
R(Si_2-Si_3), Å	2.778	2.730	2.751
$\omega_1(a_1')$, cm^{-1}	450 (0.0)[a]	480	467
$\omega_2(a_1')$, cm^{-1}	292 (0.0)[a]	310	306
$\omega_3(a_2'')$, cm^{-1}	428 (2.6)[a]	422	445
$\omega_4(e')$, cm^{-1}	360 (0.6)[a]	388	366
$\omega_5(e')$, cm^{-1}	192 (0.7)[a]	200	193
$\omega_6(e'')$, cm^{-1}	328 (0.0)[a]	333	345

[a] Infrared intensities (km/mol) are given in parentheses.

Table 4.5: Calculated Molecular Properties of Si_5 D_{3h} ($^1A_1'$)

method	B3LYP/ 6-311+G*	CASSCF(8,7)/ 6-311+G*	CCSD(T)/ 6-311+G*
-*E*, au	1447.492 144	1444.580 865	1445.060 178
R(Si_2-Si_5), Å	2.330	2.330	2.316
R(Si_2-Si_3), Å	3.125	3.173	3.073
$\omega_1(a_1')$, cm^{-1}	456 (0.0)[a]	474	477
$\omega_2(a_1')$, cm^{-1}	228 (0.0)[a]	216	239
$\omega_3(a_2'')$, cm^{-1}	375 (4.6)[a]	369	404
$\omega_4(e')$, cm^{-1}	432 (4.5)[a]	457	435
$\omega_5(e')$, cm^{-1}	170 (0.6)[a]	161	164
$\omega_6(e'')$, cm^{-1}	338 (0.0)[a]	323	364

[a] Infrared intensities (km/mol) are given in parentheses.

Table 4.6: Calculated Molecular Properties of $NaSi_5^-$ C_s (^{1}A')

method	B3LYP/6-311+G*	MP2/6-311+G*
-*E*, au	1609.923 210	1607.003 523
$R(Si_1\text{-}Si_{3,4})$, Å	2.519	2.487
$R(Si_1\text{-}Si_5)$, Å	2.438	2.400
$R(Si_1\text{-}Si_6)$, Å	2.353	2.344
$R(Si_3\text{-}Si_4)$, Å	2.698	2.638
$R(Si_5\text{-}Si_{3,4})$, Å	2.389	2.384
$R(Si_6\text{-}Si_{3,4})$, Å	2.456	2.439
$R(Na\text{-}Si_{3,4})$, Å	2.831	2.842
$R(Na\text{-}Si_5)$, Å	4.167	4.251
$R(Na\text{-}Si_6)$, Å	2.959	2.914
ω_1(a'), cm^{-1}	446 (0.4)[a]	465 (2.4)[a]
ω_2(a'), cm^{-1}	440 (1.1)[a]	459 (1.1)[a]
ω_3(a'), cm^{-1}	344 (1.9)[a]	358 (0.7)[a]
ω_4(a'), cm^{-1}	305 (5.9)[a]	342 (0.8)[a]
ω_5(a'), cm^{-1}	294 (1.1)[a]	325 (3.6)[a]
ω_6(a'), cm^{-1}	236 (24.9)[a]	244 (34.9)[a]
ω_7(a'), cm^{-1}	185 (0.9)[a]	205 (1.3)[a]
ω_8(a'), cm^{-1}	65 (7.0)[a]	87 (7.4)[a]
ω_9(a''), cm^{-1}	346 (1.7)[a]	365 (0.4)[a]
ω_{10}(a''), cm^{-1}	302 (0.1)[a]	336 (0.9)[a]
ω_{11}(a''), cm^{-1}	195 (5.4)[a]	193 (5.6)[a]
ω_{12}(a''), cm^{-1}	97 (1.1)[a]	89 (0.8)[a]

[a] Infrared intensities (km/mol) are given in parentheses.

Table 4.7: Calculated NICS (ppm) Indices for Si_5^{2-}, Si_5^{-}, and Si_5 at B3LYP/6-311+G*

position[a]	Si_5^{2-} (D_{3h}, $^1A_1'$)	Si_5^{-} (D_{3h}, $^2A_2''$)	Si_5 (D_{3h}, $^1A_1'$)
0	-37.0	-48.9	-49.0
1	-37.9	-49.1	-48.8
2	-40.0	-49.4	-47.8
3[b]	-41.9	-48.2	-45.5
4	-41.4	-44.4	-41.0
5	-37.6	-37.9	-34.3

[a] NICS values are calculated along the normal to the triangular face of the trigonal bipyramid starting from the center of the cage. Increments are 0.233 Å for Si_5^{2-}, 0.242 Å for Si_5^{-}, and 0.256 Å for Si_5 clusters, respectively. [b] This point in the case of all three clusters corresponds to the intersection of the normal and the triangular face of the trigonal bipyramid.

the detachment transition to the first excited state of Si_5. The broad nature of the A band makes it difficult to evaluate its VDE, which should be approximately 3.2 eV. The 266 nm spectrum (Figure 4.1b) indicates that the A band is cut off at 355 nm. This band in fact is shown to extent to around 3.6 eV, suggesting that there is likely to be another detachment transition. This is labeled as band B with a VDE at approximately 3.4 eV. As will be shown below, this band is borne out in the current theoretical calculations. Although it was not recognized at the time, the 299 nm spectrum in the paper by Xu et al[125] resolved this band more clearly. The 266 nm spectrum (Figure 4.1b) reveals two more broad bands: a weak and broad band centered around 4 eV (C) and a more intense and sharper band at 4.47 eV (E). A shoulder can be discerned at the lower binding energy side of the intense band around 4.3 eV (D). At 193 nm (Figure 4.1c), band E becomes broad, suggesting an additional band around 4.6 eV, which is cut off in the 266 nm spectrum. A very weak band is also observed around 5.4 eV (G). We also took the spectrum of Si_5^- at 157 nm (not shown), but no new detachment transitions were observed because of the poor signal-to-noise ratio in the high binding energy side.

The VDEs of all the observed detachment channels for Si_5^- are summarized in Table 4.1, where the calculated VDEs at various levels of theory are also listed.

B. Photoelectron Spectroscopy of $NaSi_5^-$. The photoelectron spectra of $NaSi_5^-$ are shown in Figure 4.2 at three photon energies (355, 266, and 193 nm). The electron binding energies of $NaSi_5^-$ are lower than those of Si_5^-, but the overall spectral patterns for the two species are quite similar. The low binding energy part of the $NaSi_5^-$ spectra shows a very broad band, which also contains three overlapping detachment transitions (X, A, B) similar to the Si_5^- spectra. The VDE of the A band is assigned to be the most

intense feature in this band at 2.67 eV in the 355 nm spectrum (Figure 4.2a). The X and B bands are assigned to be on the lower and higher binding energy sides of this broad band, and their binding energies are estimated to be ~2.55 and ~2.9 eV, respectively. The onset of the X band is relatively sharp for $NaSi_5^-$, allowing us to evaluate an ADE of 2.42 ± 0.04 eV, which agrees with the value of 2.45 ± 0.05 eV reported previously by Kishi et al. at 355 nm.[136] Following the broad band, three well-resolved bands are observed (C, D, E). Bands C and D with VDEs of 3.47 and 3.71 eV, respectively, are relatively weak, whereas band E at 3.95 eV is quite sharp and intense in the 266 nm spectrum (Figure 4.2b). At 193 nm (Figure 4.2c), the intensity of the E band is significantly reduced and a very weak band with a relatively poor signal-to-noise ratio is observed at ~5.5 eV (F). Overall the spectral features of $NaSi_5^-$ appear to be slightly sharper and better resolved than the Si_5^- counterparts, suggesting that the geometry changes between $NaSi_5^-$ and $NaSi_5$ are relatively small. All the observed VDEs for $NaSi_5^-$ are given in Table 4.2, where they are compared with theoretical calculations.

It has been demonstrated previously that PES combined with ab initio calculations is a powerful tool for elucidating the electronic structure and chemical bonding of novel clusters.[74] In the following, different levels of theory are employed to investigate the detailed structures and underlying chemical bonding of Si_5^- and $NaSi_5^-$ (Si_5^{2-}) and to assist the assignment of the observed photoelectron spectra.

4.1.3. Theoretical Results

The geometric structures of Si_5^{2-}, Si_5^-, and Si_5 are well established in the literature.[136,140-143] Our collaborators performed the search for the global minimum

structures for these species primarily to test the gradient embedded genetic algorithm (GEGA) program. While the GEGA search could potentially be performed for these species at the B3LYP/3-21G level of theory, our collaborators used the semiempirical PM3 method for the energy, gradient, and force calculations. They plan to use the same level of theory for large silicon clusters, for which the B3LYP/3-21G GEGA calculations would not be possible with their computer resources.

A. Si_5^{2-}. The PM3 GEGA search yielded the bipyramidal D3h (1A1', 1a1'21a2"2 1e'42a1'23a1'21e"42e'42a2"2) global minimum structure I (Figure 4.3a). Two quasiplanar and planar isomers were also obtained: II, C_2 (^{1}A), and III, D_{2h} (^1A_g). Our collaborators then performed B3LYP/6-311+G* geometry optimization and frequency calculations for structures I, II, and III. Again the global minimum structure at this level of theory was found to be structure I. They also performed CCSD(T)/6-311+G* calculations for structure I. Both geometric parameters and frequencies are in good agreement between the two methods, as shown in Table 4.3. The optimized d_{eq-eq} (2.606 Å at B3LYP/6-311+G* and 2.591 Å at CCSD(T)/6-311+G*) and d_{ax-eq} (2.400 Å at B3LYP/6-311+G* and 2.389 Å at CCSD(T)/6-311+G*) values are slightly longer than the corresponding experimental values of d_{eq-eq} = 2.535 Å and d_{ax-eq} = 2.350 Å obtained in solid,[44] but they agree well with the ab initio calculations reported by Kishi et al.[136] The isomers II, C_{2v} ($^1A_1$), and III, D_{2h} (^1A_g), were found to be higher in energy than the global minimum structure by 37.0 and 41.3 kcal/mol (all at CCSD(T)/6-311+G(2df)//B3LYP/6-311+G*+ZPE correction at B3LYP/6-311+G*), respectively. Optimized geometry and harmonic frequencies calculated at the CASSCF(10,8)/6-311+G* level of theory are in good agreement with the results at B3LYP/6-311+G* and CCSD(T)/6-311+G* (Table

4.3). The Hartree-Fock configuration was found to be dominant (C_{HF} = 0.943) among 1176 configurations in the CASSCF wave function, thus confirming the applicability of the used one-electron configuration based methods. Our collaborators also performed a single-point calculation with the extended active space CASSCF(12,9)/6-311+G*. The Hartree-Fock configuration was found to be almost the same (C_{HF} = 0.943) among 3570 configurations in the CASSCF wave function.

B. Si_5^- and Si_5. The similar PM3 GEGA search also yielded a bipyramidal D_{3h} ($^2A_2"$, $1a_1'^2 1a_2"^2 1e'^4 2a_1'^2 3a_1'^2 1e"^4 2e'^4 2a_2"^1$) global minimum structure for Si_5^- (IV, Figure 4.3d), with the lowest planar isomer VI being C_2 (^2B) (Figure 4.3f). Subsequent B3LYP/6-311+G* geometry optimization and frequency calculations for structures IV, V, and VI confirmed that structure IV (Table 4.4) is the global minimum. Our collaborators also performed CCSD(T)/6-311+G* calculations for structure IV (Table 4.4). The D_{3h} ($^2A_2"$) global minimum structure was first predicted by Raghavachari[144] and has been confirmed in numerous calculations later.[98,136,145] The PM3 GEGA findings and the more sophisticated calculations are in excellent agreement with the previous results. The lowest C_2 (^2B) isomer VI (Figure 4.3f) for Si_5^- found in the calculations is substantially higher in energy (by 30 kcal/mol at CCSD(T)/6-311+G(2df)//B3LYP/6-311+G*+ZPE corrections at B3LYP/6-311+G*) and thus should not be significantly populated in the Si_5^- ion beam.

For Si_5, the PM3 GEGA search revealed the bipyramidal D_{3h} ($^1A_1'$, $1a_1'^2 1a_2"^2$ $1e'^4 2a_1'^2 3a_1'^2 1e"^4 2e'^4 2a_2"^0$) global minimum structure VII (Figure 4.3g, Table 4.5) with a low-lying singlet C_{2v} ($^1A_1$) planar isomer VIII (Figure 4.3h). The bipyramidal D_{3h} global minimum for Si_5 was also first predicted by Raghavachari and Logovinsky[146] and has been confirmed by numerous subsequent calculations.[98,136,140-143] The lowest C_{2v} ($^1A_1$)

isomer VIII (Figure 4.3h) for Si_5 was found to be substantially (28 kcal/mol at CCSD(T)/6-311+G(2df)//B3LYP/6-311+G*+ZPE corrections at B3LYP/6-311+G*) higher in energy. Our collaborators also optimized geometry and calculated harmonic frequencies at the CASSCF(9,7)/6-311+G* (Si_5^-) and CASSCF(8,7)/6-311+G* (Si_5) levels of theory (Tables 4.4 and 4.5). The CASSCF results are in good agreement with the results at B3LYP/6-311+G* and CCSD(T)/6-311+G*. The Hartree-Fock configurations were found to be dominant (C_{HF} = 0.969) among 490 configurations in the CASSCF wave function for Si_5^- and (C_{HF} = 0.953) among 490 configurations in the CASSCF wave function for Si_5, thus confirming the applicability of the one-electron configuration based methods.

C. $NaSi_5^-$. For the $NaSi_5^-$ anion it was expected that the global minimum structure should be related to the trigonal-bipyramidal structure I of Si_5^{2-} (Figure 4.3a), because alternative structures for the dianion are substantially higher in energy. They placed a Na^+ cation at different positions around the D_{3h} Si_5^{2-}: (1) above a triangular face (Figure 4.3i), (2) above an edge between two equatorial Si atoms (Figure 4.3j), (3) above an edge between one axial and one equatorial Si atom (Figure 4.3k), (4) above an equatorial silicon atom (Figure 4.3l), and (5) above an axial Si atom (Figure 4.3m). Geometry optimization and frequency calculations for these structures were performed at the B3LYP/6-311+G* level of theory. The lowest energy structure among those is structure IX (C_s, ^{1}A'). This structure was reoptimized at the MP2/6-311+G* level of theory, and the results agree well with the B3LYP/6-311+G* results (Table 4.6). They were not able to converge geometry optimization at CCSD(T)/6-311+G* because of the numerical calculation procedure for gradients at the CCSD(T) level of theory and because of a very

shallow potential energy surface. Structure X (C_{2v}, $^1A_1$), with the Na^+ cation located above the edge, was found to be a first-order saddle point at just 0.7 kcal/mol (CCSD(T)/6-311+G(2df)//B3LYP/6-311+G*+ZPE corrections at B3LYP/6-311+G*) above the global minimum. Thus, the $NaSi_5^-$ potential energy surface is very flat and the Na^+ cation can almost freely move from a position over the upper face to a position over the lower face in the Si_5^{2-} trigonal bipyramid. Structure XI (C_s, $^1A'$) is also a first-order saddle point corresponding to internal motion of Na^+ around the upper or lower part of the Si_5^{2-} trigonal bipyramid. The barrier for this motion is appreciably higher (5.8 kcal/mol (CCSD(T)/6-311+G(2df)//B3LYP/6-311+G*+ZPE corrections at B3LYP/6-311+G*). Two other optimized structures with Na^+ coordinated to just one Si atom were found to be much higher in energy. Structure XII (C_{2v}, $^1A_1$) is a saddle point at B3LYP/6-311+G*, being 16.4 kcal/mol (CCSD(T)/6-311+G(2df)//B3LYP/6-311+G*+ZPE corrections at B3LYP/6-311+G*) higher in energy than the global minimum, and structure XIII (C_{3v}, $^1A_1$) is a local minimum, being 18.1 kcal/mol (CCSD(T)/6-311+G(2df)//B3LYP/6-311+G*+ZPE corrections at B3LYP/6-311+G*) above the global minimum.

Even though the potential energy surface is very flat, the finding that the C_s ($^1A'$) structure IX is the global minimum for $NaSi_5^-$ disagrees with the conclusion of Kishi et al.,[136] who reported structure X with Na^+ coordinated to an equatorial edge as the global minimum.

4.1.4. Interpretation of the Photoelectron Spectra of Si_5^- and $NaSi_5^-$

A. Si_5^-. The VDEs of Si_5^- were calculated at four levels of theory (TD-B3LYP, UOVGF, CCSD(T), and EOM, all with 6-311+G(2df) basis sets), as summarized in Table 4.1. The VDEs calculated at the different levels of theory are surprisingly close to each other and agree with the experimental data very well. The ground-state transition corresponds to the electron detachment from the singly occupied $2a_2$" HOMO, which is the same $2a_2$" orbital in Si_5^{2-}, as shown in Figure 4.4a. This orbital is bonding within the equatorial atoms, but antibonding between the equatorial atoms and the axial atoms. Thus detachment of the $2a_2$" electron leads to a considerable geometry change in neutral Si_5. It turns out that the largest change is in the equatorial Si-Si distances, which increase from 2.751 Å in Si_5^- to 3.073 Å in Si_5 accompanied by a very small contraction of the Si-Si distances between the equatorial and axial atoms (see Tables 4.2 and 4.5). The huge geometry changes lead to a very broad band for the ground-state transition. Xu et al. resolved a long vibrational progression for this transition with an average spacing of 233 cm^{-1}, which is in excellent agreement with the calculated frequency for the ν_1 mode (239 cm^{-1}, Table 4.5). The calculated ADE, i.e., the adiabatic electron affinity of neutral Si_5, is 2.35 eV at B3LYP/6-311+G(2df) and 2.37 eV at CCSD(T)/6-311+G(2df), which is significantly lower than the calculated VDE (Table 4.1), consistent with the large geometry changes between the anion and neutral. The large geometry changes between Si_5^- and Si_5 mean that the ADE may not be obtained from the PES spectra because the Franck-Condon factor for the 0-0 transition may be negligible. Xu et al. estimated an ADE of 2.59 ± 0.02 eV from their Franck-Condon simulation.[125] The observed detachment threshold in the 355 nm spectrum (Figure 4.1a) is around 2.7 eV. All of these should be viewed as upper limits for the ADE.

The next detachment is from the 2e' HOMO-1 orbital, which can result in two detachment channels, a triplet and a singlet final state. These states are Jahn-Teller active and are expected to give very complicated spectral features. As given in Table 4.1, the calculated VDE for the triplet state ranges from 2.95 to 3.24 eV, whereas that for the singlet state ranges from 3.26 to 3.52 eV. These VDEs are in good agreement with the estimated VDEs for the overlapping A and B bands. Thus, the first broad feature (X, A, B) in the photoelectron spectra of Si_5^- contains three detachment transitions. From their vibrationally resolved data and angular dependent study, Xu et al. clearly resolved the A band. However, they did not recognize the third detachment channel corresponding to the singlet state (^{1}E"), even though they resolved it more clearly. The complex vibrational structures observed in their spectra agree with the Jahn-Teller effects expected for these final states.

The HOMO-2 orbital (1e") is also a doubly degenerate MO. Detachment from this MO will again yield a triplet and a singlet state, which are Jahn-Teller active. The calculated VDE for the triplet state ranges from 3.87 to 4.03 eV, whereas that for the singlet state ranges from 4.36 to 4.50 eV. These calculated VDEs are in good agreement with the estimated VDEs for the C and D bands. The HOMO-3 is a nondegenerate orbital ($3a_1$'). Detachment from this orbital will also lead to a triplet state ($^3A_2$") and a singlet state ($^1A_2$"). The calculated VDEs for these two states agree well with the estimated VDEs for the E and F bands, respectively.

Finally, the highest binding energy feature observed in the photoelectron spectra is the weak band G with an estimated VDE of ~5.4 eV, which is in good agreement with the calculated VDE for the triplet final state from detachment from the $2a_1$' HOMO-4

(Table 4.1). The calculated VDE for the corresponding singlet final state is about 6.8 eV. However, the intensity for this detachment channel is expected to be very low, considering the weak intensity for the triplet channel (G), and is not observed in the 157 nm spectrum, which also has very poor signal-to-noise ratios in the higher binding energy part. Overall, the calculated VDEs for the D_{3h} Si_5^- are in excellent agreement with the photoelectron spectra, confirming the D_{3h} structure for Si_5^- and lending credence for the TD-B3LYP and the UOVGF methods used to compute VDEs.

B. $NaSi_5^-$. The C_s $NaSi_5^-$ IX (Figure 4.3i) can be viewed as a D_{3h} Si_5^{2-} stabilized by a Na^+ cation. Si_5^{2-} is closed shell, and its 11 fully occupied valence MOs are shown in Figure 4.4a. Thus $NaSi_5^-$ is also closed shell and should give simpler photoelectron spectra because detachment from each occupied MO can only yield one doublet final state (Table 4.2). The HOMO of $NaSi_5^-$ is the 8a' MO, which corresponds to the $2a_2$" HOMO in Si_5^{2-} (Figure 4.4a). This is also the same HOMO in Si_5^-, albeit it is singly occupied in the latter. Detachment from the 8a' HOMO of $NaSi_5^-$ yields the ground state of $NaSi_5$ [$Na^+(Si_5^-)$]. Even though the equatorial Si-Si bond lengths are shorter in Si_5^{2-} (Table 4.3) than in Si_5^- (Table 4.4), the change between Si_5^{2-} and Si_5^- (2.591 vs 2.751 Å) is only half that between Si_5^- and Si_5 (2.751 vs 3.073 Å). Thus the X band of $NaSi_5^-$ is sharper than that in the Si_5^- spectra. The calculated VDE for the ground-state transition at all three levels of theory (ROVGF, TD-B3LYP, and CCSD(T), all with 6-311+G(2df)) is in good agreement with the experiment.

The next two detachment channels correspond to the 7a' and 3a" orbitals, which can be traced to the pair of doubly degenerate 2e' MO in Si_5^{2-} (Figure 4.4a). The Na^+ coordination to Si_5^{2-} splits the degeneracy of the 2e' orbitals. However, the calculated

VDEs for these two MOs are fairly close to each other and they are also very close to the ground-state detachment channel. These three closely spaced detachment channels give rise to the broad band at the lower binding energies in the photoelectron spectra (X, A, and B in Figure 3.2 and Table 4.2). The photoelectron spectra of $NaSi_5^-$ at higher binding energies exhibit four well-separated bands (C, D, E, and F), which correspond to detachment from the 6a', 2a", 5a', and 4a' MOs, respectively. The calculated VDEs are all in excellent agreement with the experimental values (Table 4.2). The 6a' and 2a" MOs correspond to the 1e" MO in Si_5^{2-}, whereas the 5a' and 4a' correspond to the $3a_1$' and $2a_1$' MOs of Si_5^{2-}, respectively (Figure 4.4a).

The overall agreement between the experimental spectral pattern and the calculated VDEs is very good, confirming the global minimum structure for $NaSi_5^-$ (C_s, ^{1}A'), in which the Na^+ counterion is coordinated to the face of the trigonal-bipyramidal Si_5^{2-} (Figure 4.3i). Again, the two theoretical methods, ROVGF and TD-B3LYP, performed well for $NaSi_5^-$ and are shown reliable to be used in the future for large sodium coordinated silicon clusters.

4.1.5. Chemical Bonding in Si_5, Si_5^-, and Si_5^{2-}

Chemical bonding in Si_5 and Si_5^{2-} has been previously discussed[147-149] In particular, Wang and Messmer,[147] and Patterson and Messmer,[148] have interpreted chemical bonding in Si_5 using the valence bond model, a key feature of which is that each atom is surrounded by a tetrahedrally oriented set of orbitals. Then, pairs of occupied orbitals are singlet spin coupled into electron pairs, which are spatially separated from one another due to the Pauli exclusion principle. For the Si_5 cluster they obtained six

symmetry-equivalent bent bonds that arise from the overlap of two orbitals, one from each of two atoms. These six bonds describe 2e-2c bonding between axial and equatorial Si atoms. Every equatorial atom possesses a lone pair, and the two axial Si atoms form a long bond. According to this valence bond picture, the long bond is formed by two collinear tetrahedral orbitals on the two axial silicon atoms, which are pointing away from each other, but nevertheless overlap enough to form a bond. King et al.[149] pointed out that the trigonal-bipyramidal Si_5^{2-} is a three-dimensional aromatic cluster similar to the valence isoelectronic $B_5H_5^{2-}$ cluster on the basis of diatropic NICS(0) values: NICS(0) = -38.5 for Si_5^{2-} and NICS(0) = -25.9 for $B_5H_5^{2-}$. These dianions are also aromatic according to the *styx* Lipscomb rule,[150,151] and they also satisfy Wade's $2n + 2$ skeletal electron rule[152] for aromatic deltahedral systems. However, they do not obey Hirsch's $2(N + 1)^2$ rule[153,154] for three-dimensional aromaticity.

In consideration of the chemical bonding in Si_5, Si_5^-, Si_5^{2-}, and $B_5H_5^{2-}$, our collaborators used the natural population analysis (NPA), molecular orbital analysis, electron localization functions (ELFs), and nuclear independent chemical shifts (NICS).

A. NPA Analysis. According to the NPA, an electron density change upon an electron detachment from Si_5^{2-} [$Q(Si_{eq})$ = -0.40 |e| (hybridization $3s^{1.63}3p^{2.71}$) and $Q(Si_{ax})$ = -0.40 |e| ($3s^{1.65}3p^{2.70}$)] to Si_5^- [$Q(Si_{eq})$ = -0.20 |e| ($3s^{1.68}3p^{2.48}$) and $Q(Si_{ax})$ = -0.20 |e| ($3s^{1.59}3p^{2.56}$)] occurs on all five atoms, while upon an electron detachment from Si_5^- to Si_5 [$Q(Si_{eq})$ = +0.16 |e| ($3s^{1.74}3p^{2.08}$) and $Q(Si_{ax})$ = -0.24 e ($3s^{1.59}3p^{2.60}$)] it occurs primarily on the equatorial Si atoms.

B. Molecular Orbital Analysis. The valence molecular orbital picture for $B_5H_5^{2-}$ is quite similar to that for Si_5^{2-} (Figure 4.4), although the order of their occupied MOs is

somewhat different. This similarity at first glance indicates that the chemical skeletal bonding in the trigonal B_5 or Si_5 units should be quite similar. Indeed, King et al. calculated NICS(0) indices at the center of both dianions and reported that they are highly negative (-25.9 ppm for $B_5H_5^{2-}$ and -38.5 ppm for Si_5^{2-}), showing significant aromaticity in both species. The aromatic nature of deltahedral boranes has been previously discussed by King and Rouvray[155] and Aihara.[156]

C. ELF Analysis. The ELFs calculated for $B_5H_5^{2-}$, Si_5^{2-}, and Si_5 are presented in Figure 4.5. The local maxima of the ELFs define "localization attractors", of which there are only three basic types: bonding, nonbonding, and core. Bonding attractors lie between the core attractors (which themselves surround the atomic nuclei) and characterize the shared-electron interactions. The spatial organization of localization attractors provides a basis for a well-defined classification of bonds. From any point in space the ELF gradient is followed to an attractor in that region, and this point is then attributed to this attractor. The collection of all the points in the space that is assigned to a given attractor is called its basin. The criterion of discrimination between basins is provided by the reduction of reducible (containing more than one attractor) domains. The reduction of a reducible localization domain occurs at critical values (saddle points) of the bonding isosurface, over which the domain is split into domains containing fewer attractors. The localization domains are then ordered with respect to the ELF critical values, yielding bifurcations.

The ELF pictures calculated for $B_5H_5^{2-}$ (Figure 4.5a) reveal that the protonated attractor domains (spherelike areas) are separated as a result of bifurcations at ELF = 0.52 (axial domains separated) and ELF = 0.64 (equatorial domains separated). These domains correspond to the 2e-2c B-H bonds. Two more bifurcations can be seen in Figure 4.5a at

ELF = 0.77 and ELF = 0.85. The first bifurcation yields two reducible domains in the region of boron-boron bonding, and the second bifurcation reveals the six irreducible domains corresponding to six B_{ax}-B_{eq} bonds. According to the ELF analysis, there is no B_{eq}-B_{eq} bonding. This chemical bonding picture is consistent with the *styx* Lipscomb's description of chemical bonding in $B_5H_5^{2-}$.

The ELF pictures calculated for the valence isoelectronic Si_5^{2-} (Figure 4.5b) are somewhat different from those for the $B_5H_5^{2-}$ dianion. First, at ELF = 0.65 one can see the system of three attractors in the equatorial plane, which can be tentatively attributed to a pair of electrons delocalized in the equatorial area. At ELF = 0.69 one can see the separation of the two lone pairs corresponding to the axial Si atoms. Finally, at ELF = 0.77 one can see the separation of the three nonbonding domains corresponding to the equatorial Si atoms. Simultaneously, the six bonding domains corresponding to the Si_{eq}-Si_{ax} bonds are revealed. Thus, in Si_5^{2-}, if compared to $B_5H_5^{2-}$, one can see that some electrons, which are supposed to belong to Si equatorial lone pairs, are actually participating in chemical skeletal bonding.

The bifurcations corresponding to the Si_5 neutral species are shown in Figure 4.5c. The major difference in the ELF analysis between Si_5 and Si_5^{2-} is the absence of the system of the three equatorial attractors in the neutral system and the significant alternation of the nonbonding domains corresponding to the axial Si atoms. It also should be pointed out that the interaction between the bonding Si_{ax}-Si_{eq} domains and the axial nonbonding domains is appreciably stronger, because the bifurcation occurs at relatively high ELF values (0.69 for Si_5^{2-} and 0.83 for Si_5). Thus, the change in the electron density accompanying the removal of an electron pair from $Si_5^{2-} \rightarrow Si_5$ corresponds to the loss of

electron density in the area primarily belonging to the equatorial Si atoms, and that is consistent with the NPA analysis discussed above.

D. NICS Analysis. Our collabrators also performed calculations of the NICS indices (at B3LYP/6-311+G*) for Si_5^{2-}, Si_5^-, and Si_5 along the normal to the triangular face of the trigonal bipyramid starting from the center of the cluster. Calculated results are summarized in Table 4.7. They found that the NICS(0) values at the center of the cluster are highly negative for all the Si_5^{2-}, Si_5^-, and Si_5 species, clearly showing the presence of aromaticity in these clusters. The NICS(0) value increases along the Si_5^{2-}, Si_5^-, and Si_5 series. The NICS(0) value for the Si_5^{2-} dianion reported by King at al.[149] is very similar to the cuurent value. They found that the NICS value is growing along the normal for the Si_5^{2-} dianion and reaching the maximum value (-41.9 ppm) at the point of crossing the triangular face. That could be a manifestation of the additional contribution from the ¤ -aromaticity (aromaticity originated from the perpendicular $3p_x$ and $3p_y$ atomic orbitals of Si) in the triangular face of the trigonal bipyramid. When one electron is detached from the $2a_2$" HOMO in Si_5^{2-}, the NICS values are substantially higher for almost all calculated points, but the NICS value at the point of crossing the triangular face is no longer the highest. Finally, when the second electron is removed from the $2a_2$" HOMO in Si_5^{2-}, the NICS values are similar to those for Si_5^-, but now they are steadily decreasing from the center. These results show that, upon detachment of an electron pair from the $2a_2$" HOMO in Si_5^{2-}, the contribution from ¤-aromaticity in the neutral Si_5 is diminished.

4.1.6. Conclusions

We obtained photoelectron spectra for Si_5^- and $NaSi_5^-$ at several photon energies. The experimental spectra were interpreted by comparing with calculated VDEs at four different levels of theory (TD-B3LYP, R(U)OVGF, UCCSD(T), and EOM-CCSD(T), all with 6-311+G(2df) basis sets). Excellent agreement was found between the experiment and calculations for both anions, confirming their global minimum structures for Si_5^- (D_{3h}) and $NaSi_5^-$ (C_s). In the latter, Na^+ is coordinated to the face of a trigonal-pyramidal Si_5^{2-}. Chemical bonding in Si_5^{2-}, Si_5^-, Si_5, and $B_5H_5^{2-}$ was analyzed using NPA, molecular orbitals, ELF, and NICS indices. On the basis of these analyses we concluded that Si_5^{2-} differs from $B_5H_5^{2-}$ by involvement of the electron density, which is supposed to be "lone pairs" in the skeletal bonding in Si_5^{2-}. The NICS indices indicated that all Si_5^{2-}, Si_5^-, and Si_5 clusters are highly aromatic. According to the higher negative NICS(0) value, the neutral and singly charged clusters are more aromatic than the doubly charged one.

4.2 On the Structure and Chemical Bonding of Si_6^{2-} and Si_6^{2-} in $NaSi_6^-$ upon Na^+ Coordination

4.2.1 Introduction

The Si_6^{2-} cluster is the first system, which can be expected to have highly a highly symmetric octahedral structure, similar to the borane $B_6H_6^{2-}$. However, a previous attempt to characterize the aromaticity of the octahedral Si_6^{2-} led to the conclusion that it is antiaromatic[149] and thus totally different from the corresponding aromatic $B_6H_6^{2-}$ closo-borane. The difference was explained to be due to the mixing of the terminal hydrogen orbitals with the symmetry adapted skeletal MOs of $B_6H_6^{2-}$, which lower their energies

relative to the corresponding lone pair-dominated Si_6^{2-} MOs, where such mixing is not possible.[149]

The hexasilicon cluster (neutral or with a negative charge) has been studied in numerous works with different theoretical methods.[102,144,145,157,158] It has also been extensively studied experimentally by mass spectretry,[159-161] IR and Raman spectroscopy,[127,162] and photoelectron spectroscopy.[37,125,126,136,139] The vertical detachment energies of Si_6^- have also been computed.[103,163] Of particular interest to the present work was the report by Kishi et al.[136] about the photoelectron spectrum of $NaSi_6^-$ at 355 nm, which contained two broad spectral bands approximately at 2.1 and 3.0 eV. Theoretical analyses of the relative stability of several Si_6^{2-} and $NaSi_6^-$ isomers at MP2/6-31G* and MP4(SDTQ)/6-31G* levels of theory were also carried out by the same authors, who concluded that the most stable structure of $NaSi_6^-$ is based on a C_{2v} Si_6^{2-} fragment, rather than the O_h motif. However, the experimentally determined VDE (2.10 ± 0.04 eV) and ADE (1.90 ± 0.06 eV) for $NaSi_6^-$ differ significantly from the calculated VDE (1.518 eV) and ADE (1.446 eV) at MP4/6-31G*. Li and co-workers[138] reported that according to their calculations, The $LiSi_6^-$, $NaSi_6^-$ and KSi_6^- clusters have also been calculated at the B3PW91/6-311G* and MP2(full)/6-311+G* levels, which give a C_{3v} ($^1A_1$) structure for all three species with a cation coordinated to one face of an octahedral Si_6^{2-}. Thus, the global minimum structure of the $NaSi_6^-$ cluster is not yet definitely established.

In the current study, we present a systematic investigation of Si_6^{2-} and $NaSi_6^-$ both experimentally and theoretically focusing on elucidating structures and chemical bonding. Well resolved photoelectron spectra were obtained for $NaSi_6^-$ at three photon energies

(355, 266, 193 nm), which allow quantitative comparisons with the accompanying *ab initio* calculations. The ground state structure of $NaSi_6^-$ was established on the basis of good agreement between the photoelectron spectra and theoretical VDEs, calculated at several levels of theory: CCSD(T)/6-311+G(2d), ROVGF/6-311+G(2df), TD-B3LYP/6-311+G(2df), all at the B3LYP/6-311+G* geometry. Our collaborators further investigated the chemical bonding in the most stable isomer of $NaSi_6^-$ and its silicon kernel Si_6^{2-}. Results of MO, natural bond orbital (NBO), and electron localization function (ELF) analyses were compared with those for the octahedral Si_6^{2-} and $B_6H_6^{2-}$ species. We also included photoelectron spectroscopic results on Si_6^- primarily to test theoretical methods used for $NaSi_6^-$.

4.2.2 Experimental Results

A. Photoelectron Spectroscopy of Si_6^-. Figure 4.6 displays the photoelectron spectra of Si_6^- at three photon energies (355, 266, and 193 nm). Five distinct and intense spectral bands (X, A, B, C, D) were observed at 193 nm (Figure 4.6c) and their VDEs measured from the peak maxima are given in Table 4.8. At 355 nm, the X band was better resolved with a well-defined onset, which yielded an ADE of 2.23 ± 0.3 eV and VDE of 2.35 ± 0.05 eV. Since no vibrational structures were resolved, the ADE, which also represents the electron affinity (EA) of neutral Si_6, was measured by drawing a straight line at the leading edge of the X band and then adding the spectral resolution to the intersection with the binding energy axis. The X band was quite broad, suggesting significant geometry changes between the ground state of Si_6^- and the corresponding neutral state. Weak and broad signals were observed in between bands X and A, in

particular, the feature labeled "IS" was shown as a shoulder on the A band. These weak features could be either due to isomers or impurities. Since our mass resolution was high enough to resolve the isotopic pattern of Si_6^-, we could rule out the possibility of impurity contamination. Thus, these features were most likely due to another structural isomer, consistent with previous theoretical calculations.[103,139] The X-A band separation defines a HOMO-LUMO gap for the neutral Si_6 as 1.05 eV. All the higher energy bands were all rather broad, due to either large geometry changes upon photodetachment or overlapping electronic transitions.

The photoelectron spectra of Si_6^- have been reported in a number of previous studies.[37,125,126,136,139] The current study presents a more systematic data set at different photon energies and are in general slightly better than or consistent with the previous measurements. The best resolved spectrum for Si_6^- was by Xu *et al*. at 355 nm.[125] Our obtained ADE (2.23 eV) and VDE (2.35 eV) are in good agreement with their corresponding values at 2.22 and 2.36 eV, respectively. However, the shoulder labeled as "IS" in Figure 4.6 was resolved as a vibrational progression by Xu et al., who assigned it as the transition to the first excited state of Si_6. As discussed below, this weak feature is most likely due to the D_{4h} isomer of Si_6^- as shown via the molecular dynamics simulation by Binggeli and Chelikowsky.[103]

B. Photoelectron Spectroscopy of $NaSi_6^-$. The photoelectron spectra of $NaSi_6^-$ are shown in Figure 4.7 at three photon energies (355, 266, and 193 nm). The electron binding energies of $NaSi_6^-$ are lower than those of Si_6^-, but the overall spectral patterns for the two species are quite similar. Again five distinct and intense spectral bands (X, A, B, C, D) were observed for $NaSi_6^-$, which were slightly better spaced than those of Si_6^-.

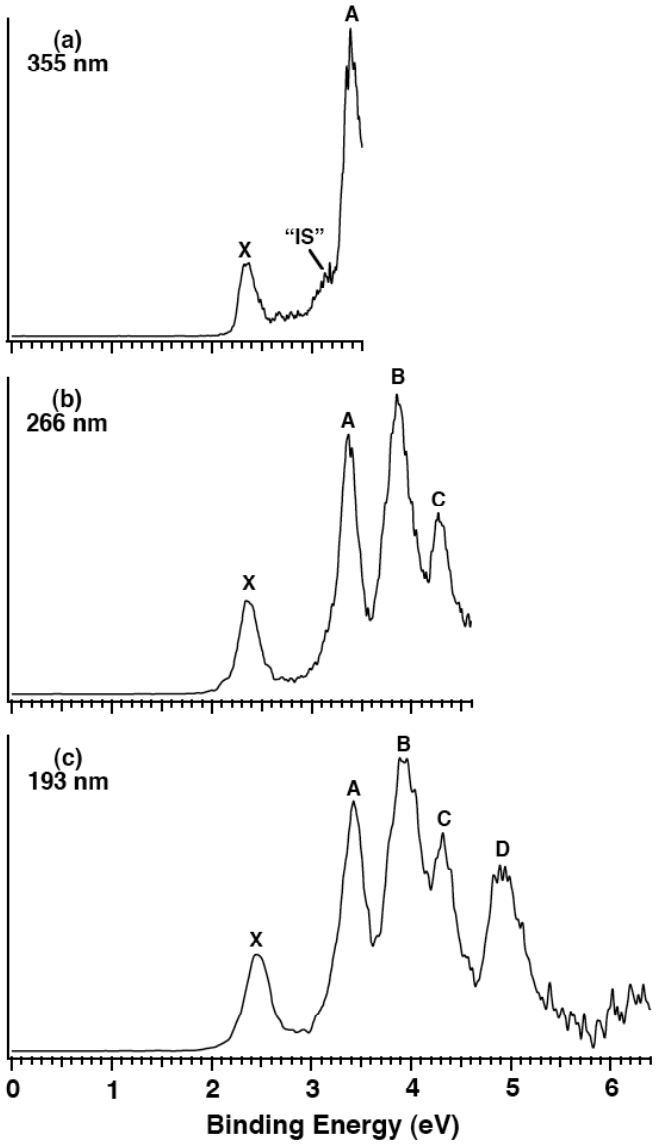

Figure 4.6 Photoelectron spectra of Si_6^- at (a) 355nm (3.496 eV), (b) 266 nm (4.661 eV), and (c) 193 nm (6.424 eV).

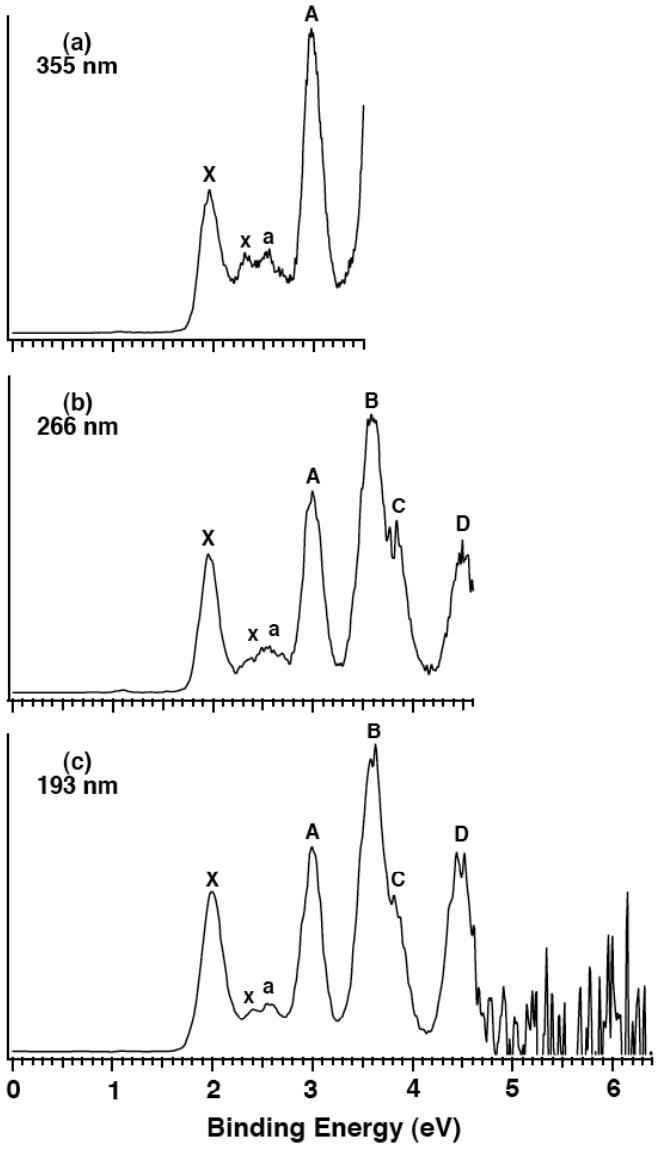

Figure 4.7 Photoelectron spectra of $NaSi_6^-$ at (a) 355nm (3.496 eV), (b) 266 nm (4.661 eV), and (c) 193 nm (6.424 eV).

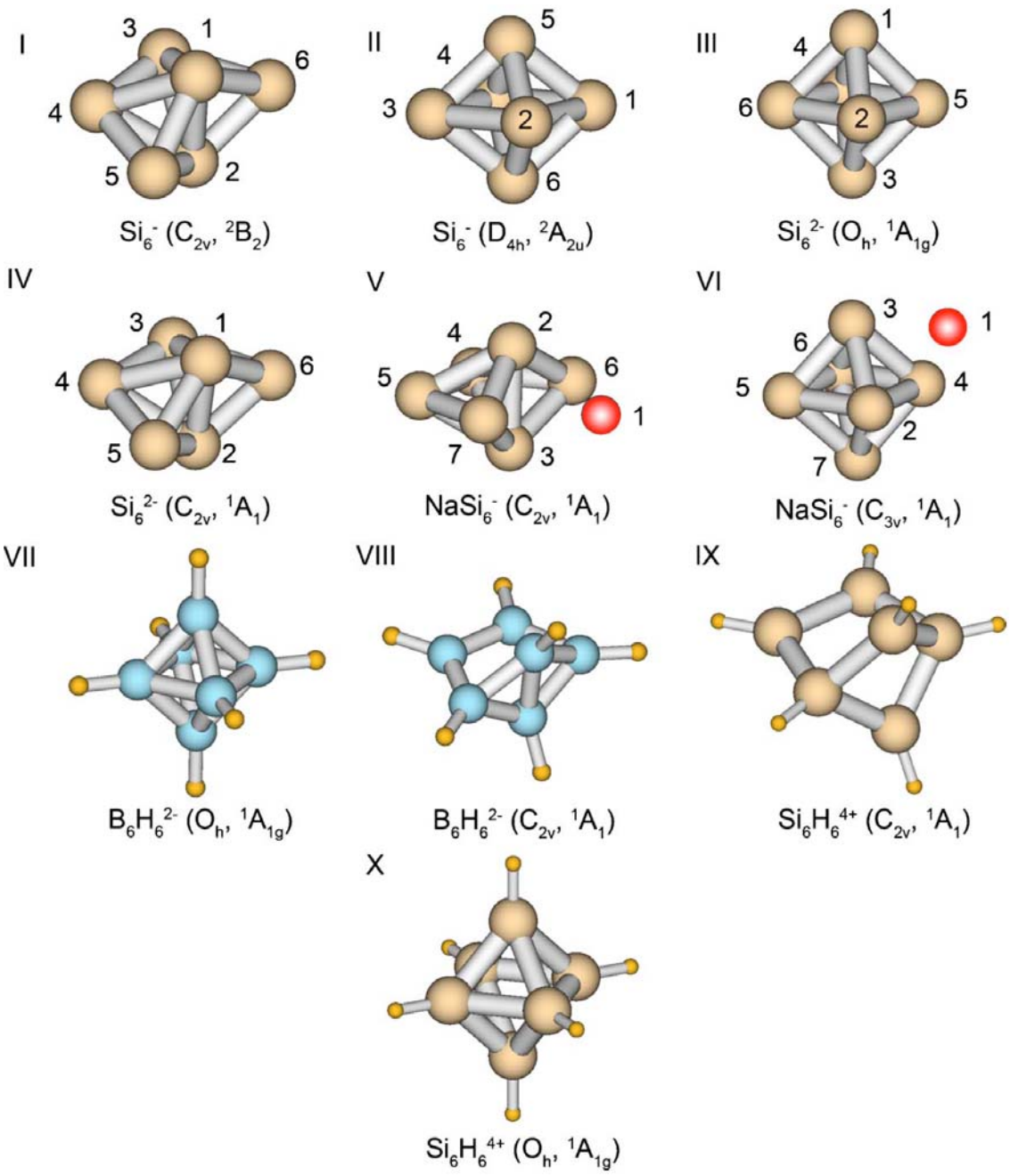

Figure 4.8 Structures of isomers for Si_6^- (I, II), Si_6^{2-} (III, IV), $NaSi_6^-$ (V, VI), $B_6H_6^{2-}$ (VII, VIII), and $Si_6H_6^{4+}$ (IX, X).

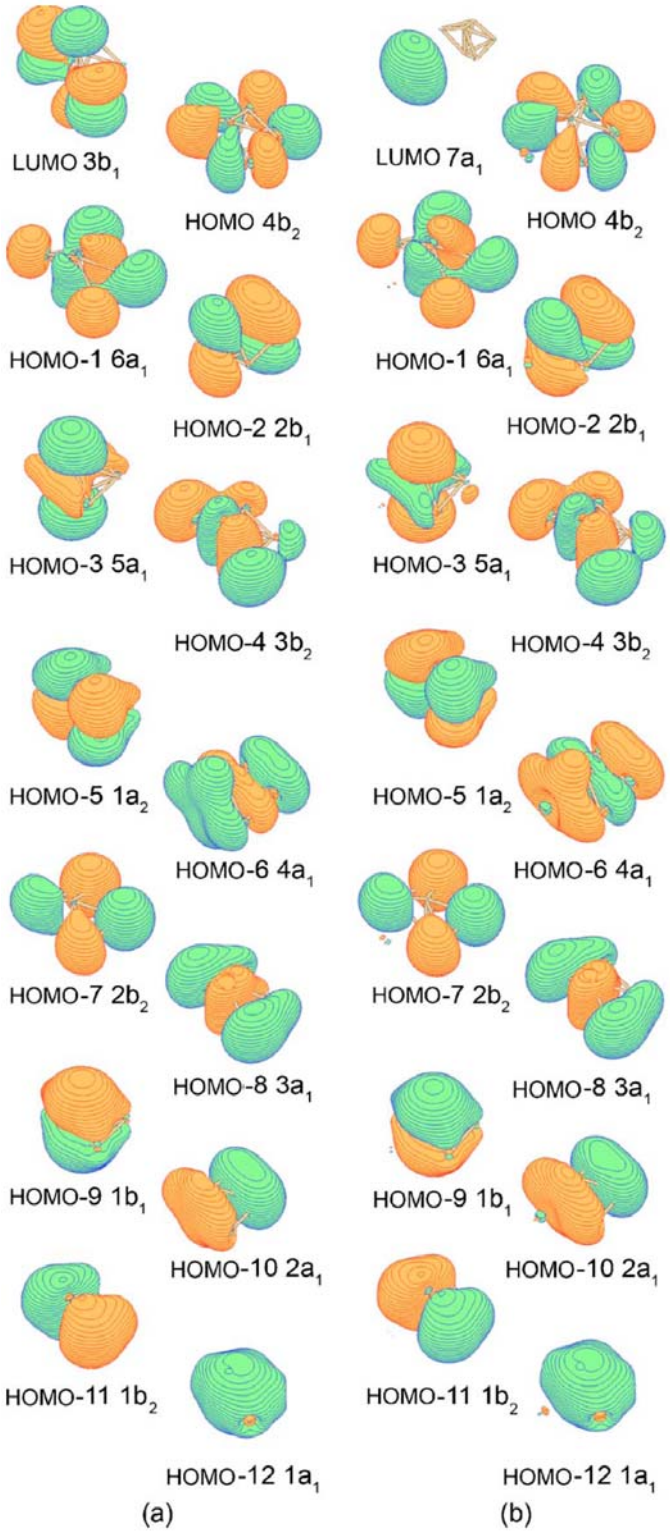

Figure 4.9 Molecular orbitals Si_6^{2-} $C_{2v}(^1A_1)$ and $NaSi_6^-$ $C_{2v}(^1A_1)$.

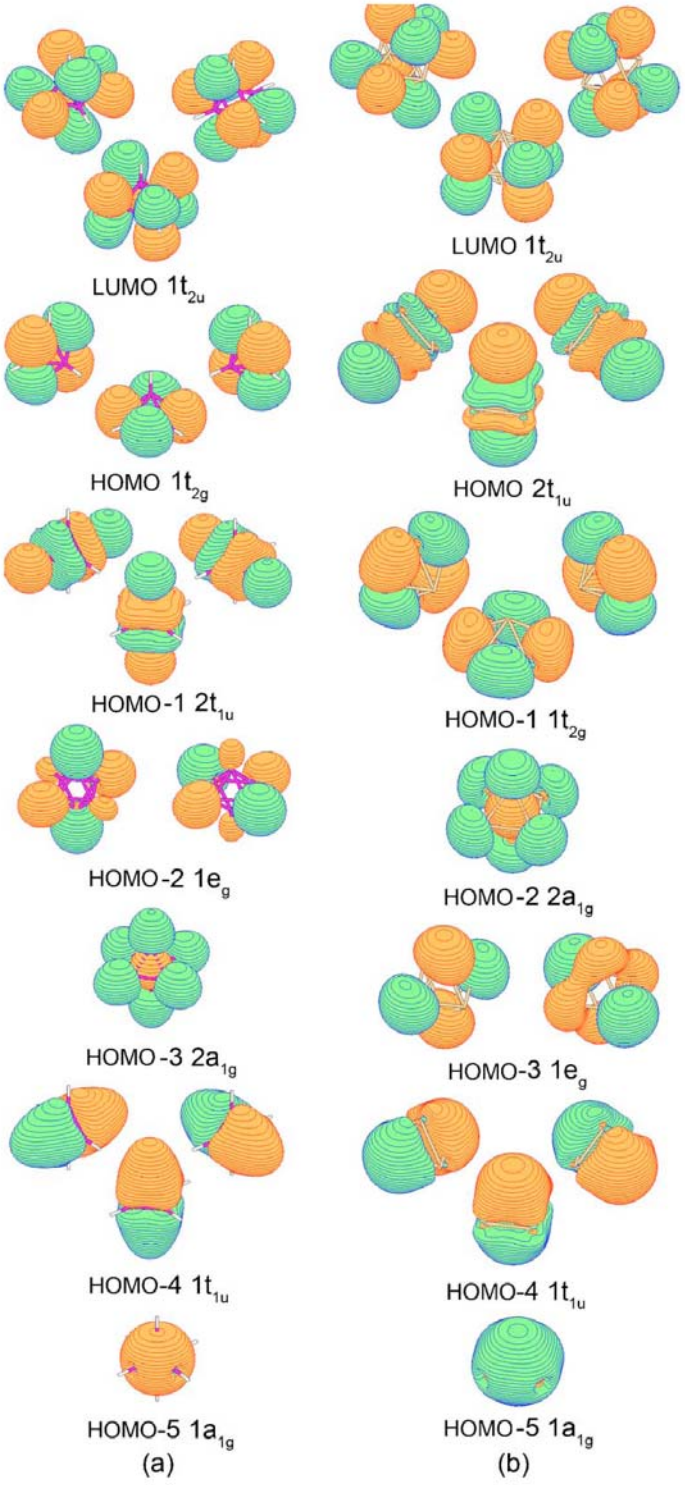

Figure 4.10 Molecular orbitals of $B_6H_6^{2-}$ $O_h(^1A_{1g})$ and Si_6^{2-} $O_h(^1A_{1g})$.

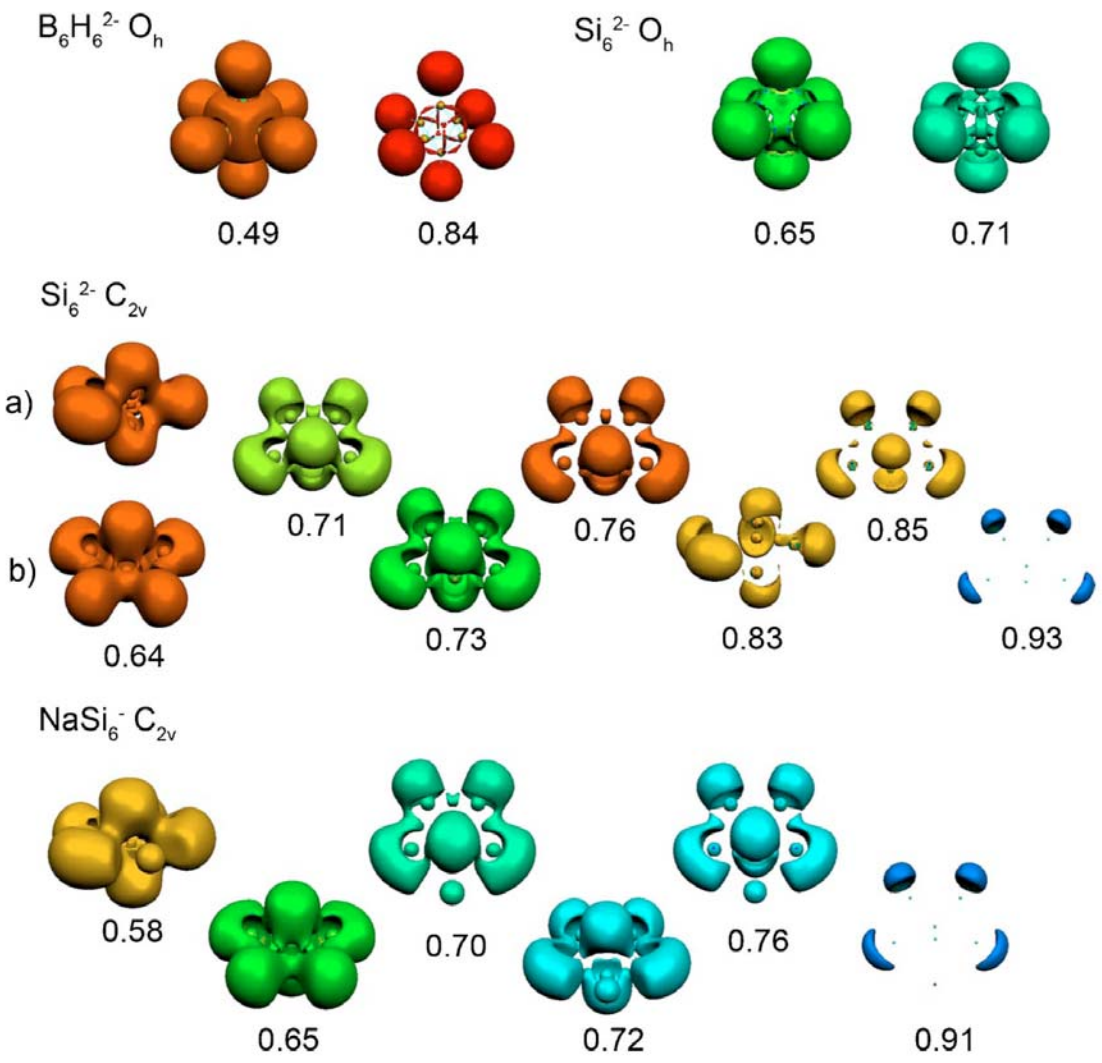

Figure 4.11 Bifurcations of ELF for $B_6H_6^{2-}$ (O_h,$^1A_{1g}$), Si_6^{2-} (O_h,$^1A_{1g}$), Si_6^{2-} (C_{2v},$^1A_1$), and $NaSi_6^-$ (C_{2v},$^1A_1$).

Table 4.8 Experimental and theoretical vertical detachment energies for Si_6^-. All energies are in eV.

Final configuration		Expt. VDE[a]	TD-B3LYP/ 6-311+G(2*df*)	UOVGF/ 6-311+G(2*d*)	EOM/ 6-311+G(2*df*)	CCSD(*T*)/ 6-311+G(2*df*)
			Si_6^- $C_{2v}(^2B_2)$			
$^1A_1$ ($4a_1^2 1a_2^2 5a_1^2 3b_2^2 2b_1^2 6a_1^2 4b_2^0$)	*X*	2.35±0.03	2.38	2.17 (0.84)[b]	2.31	2.29
$^3B_2$ ($4a_1^2 1a_2^2 5a_1^2 3b_2^2 2b_1^2 6a_1^1 4b_2^1$)	*A*	3.38±0.03	3.23	3.15 (0.84)[b]	[c]	3.30
$^1B_2$ ($4a_1^2 1a_2^2 5a_1^2 3b_2^2 2b_1^2 6a_1^1 4b_2^1$)	*B*	3.85±0.03	3.65	[d]	3.78	[e]
$^3A_1$ ($4a_1^2 1a_2^2 5a_1^2 3b_2^1 2b_1^2 6a_1^2 4b_2^1$)			3.75	3.61 (0.84)[b]	[c]	3.78
$^3A_2$ ($4a_1^2 1a_2^2 5a_1^2 3b_2^2 2b_1^1 6a_1^2 4b_2^1$)			3.80	3.67 (0.83)[b]	[c]	3.94
$^1A_2$ ($4a_1^2 1a_2^2 5a_1^2 3b_2^2 2b_1^1 6a_1^2 4b_2^1$)			3.96	[d]	4.14	[e]
$^3B_2$ ($4a_1^2 1a_2^2 5a_1^1 3b_2^2 2b_1^2 6a_1^2 4b_2^1$)			4.05	3.93 (0.83)[b]	[c]	[e]
$^1B_2$ ($4a_1^2 1a_2^2 5a_1^1 3b_2^2 2b_1^2 6a_1^2 4b_2^1$)	*C*	4.26±0.03	4.21	[d]	4.44	[e]
$^1A_1$ ($4a_1^2 1a_2^2 5a_1^2 3b_2^1 2b_1^2 6a_1^2 4b_2^1$)			4.23	[d]	4.42	[e]
$^3B_1$ ($4a_1^2 1a_2^1 5a_1^2 3b_2^2 2b_1^2 6a_1^2 4b_2^1$)	*D*	4.89±0.03	4.69	4.61 (0.83)[b]	[c]	4.86
$^3B_2$ ($4a_1^1 1a_2^2 5a_1^2 3b_2^2 2b_1^2 6a_1^2 4b_2^1$)			4.69	4.59 (0.83)[b]	[c]	[e]
$^1B_1$ ($4a_1^2 1a_2^1 5a_1^2 3b_2^2 2b_1^2 6a_1^2 4b_2^1$)			4.92	[d]	5.11	[e]
$^1B_2$ ($4a_1^1 1a_2^2 5a_1^2 3b_2^2 2b_1^2 6a_1^2 4b_2^1$)			5.32	[d]	5.49	[e]
			Si_6^- $D_{4h}(^2A_{2u})$			
$^1A_{1g}$ ($3a_{1g}^2 1e_g^4 1b_{2g}^2 2e_u^4 2a_{2u}^0$)		~2.7[f]	2.74	2.61 (0.92)[b]	[g]	2.63
^3E_g ($3a_{1g}^2 1e_g^4 1b_{2g}^2 2e_u^3 2a_{2u}^1$)		~3.1[f]	3.04	3.05 (0.91)[b]	[g]	3.17
^1E_g ($3a_{1g}^2 1e_g^4 1b_{2g}^2 2e_u^3 2a_{2u}^1$)			3.08	[d]	[g]	[e]
$^3B_{1u}$ ($3a_{1g}^2 1e_g^4 1b_{2g}^1 2e_u^4 2a_{2u}^1$)			4.49	4.53 (0.91)[b]	[g]	4.77
$^3A_{2u}$ ($3a_{1g}^1 1e_g^4 1b_{2g}^2 2e_u^4 2a_{2u}^1$)			4.60	4.63 (0.90)[b]	[g]	4.91
$^1B_{1u}$ ($3a_{1g}^2 1e_g^4 1b_{2g}^1 2e_u^4 2a_{2u}^1$)			4.61	[d]	[g]	[e]
^3E_u ($3a_{1g}^2 1e_g^3 1b_{2g}^2 2e_u^4 2a_{2u}^1$)			4.68	4.71 (0.91)[b]	[g]	4.92
^1E_u ($3a_{1g}^2 1e_g^3 1b_{2g}^2 2e_u^4 2a_{2u}^1$)			5.09	[d]	[g]	[e]
$^1A_{2u}$ ($3a_{1g}^1 1e_g^4 1b_{2g}^2 2e_u^4 2a_{2u}^1$)			5.58	[d]	[g]	[e]

[a] The adiabatic detachment energy or the electron affinity of Si_6 is measured to be 2.23±0.03 eV.
[b] The numbers in the parentheses indicate the pole strength, which characterizes the validity of the one-electron detachment picture.
[c] EOM-CCSD(T) calculations for triplet excited states cannot be performed within the MOLPRO program.
[d] Singlet excited states have two-configurational character and therefore are not reported.
[e] These states cannot be calculated using the CCSD(T) method implemented in Gaussian.
[f] Broad features in Figure 4.6(a) between bands *X* and *A*.
[g] These computations were not performed.

Table 4.9 Experimental and theoretical Vertical Detachment Energies for $NaSi_6^-$. All energies are in eV.

Feature	VDE (Exp.)	$NaSi_6^-$ (C_{2v}, $^1A_1$) MO	ROVGF/ 6-311+G(2*df*)[a]	TD-B3LYP/ 6-311+G(2*df*)[a]	CCSD(T)/ 6311+G(2*df*) [a]
X[b]	1.96 ±0.05	$4b_2$	1.96 (0.88)[c]	1.88	1.92
A	3.00 ±0.05	$6a_1$	2.78 (0.89)	2.90	2.94
B	3.60 ±0.05	$2b_1$	3.46 (0.88)	3.32	3.45
		$3b_2$	3.45 (0.88)	3.46	d
C	3.83 ±0.05	$5a_1$	3.64 (0.88)	3.65	d
D	4.50 ±0.05	$1a_2$	4.42 (0.87)	4.26	4.39
		$4a_1$	4.48 (0.88)	4.32	d

Feature	VDE (Exp.)	$NaSi_6^-$ (C_{3v}, $^1A_1$) MO	ROVGF/ 6-311+G(2*df*)[b]	TD-B3LYP/ 6-311+G(2*df*)[b]
x	2.32 ±0.03	$5a_1$	2.29 (0.88)[c]	2.26
a	2.55±0.03	4e	2.45 (0.88) [c]	2.48
		3e	4.30 (0.88) [c]	4.32
		$4a_1$	4.35 (0.88) [c]	4.32

[a.] The adiabatic detachment energy or the electron affinity of $NaSi_6$ is measured to be 1.80 ± 0.05 eV.
[b] At B3LYP//6-311+G*.
[c] The numbers in the parentheses indicate the pole strength, which characterizes the validity of the one-electron detachment picture.

Table 4.10 Calculated molecular properties of $C_{2v}(^2B_2)$ and $D_{4h}(^2A_{2u})$ isomers of Si_6^-.

$C_{2v}(^2B_2)$ method	B3LYP/ 6-311+G*	MP2/ 6-311+G*	CCSD(T)/ 6-311+G*[a,b]	$D_{4h}(^2A_{2u})$ method	B3LYP/ 6-311+G*	CCSD(T)/ 6-311+G*[c,d]
$-E$, a.u.	1737.1074	1734.1283	1734.1849	$-E$, a.u.	1737.1032	1734.1795
ΔE, kcal/mol	0	0	0	ΔE, kcal/mol	2.7	3.4
$R(Si_1–Si_2)$, Å	2.547	2.525	2.536	$R(Si_1–Si_5)$, Å	2.433	2.414
$R(Si_1–Si_3)$, Å	2.541	2.492	2.527	$R(Si_1–Si_2)$, Å	2.607	2.594
$R(Si_1–Si_6)$, Å	2.402	2.381	2.394	$\omega_1(a_{1g})$, cm^{-1}	313 (0.0)[e]	
$R(Si_3–Si_6)$, Å	2.497	2.471	2.484	$\omega_2(a_{1g})$, cm^{-1}	424 (0.0)[e]	
$R(Si_3–Si_4)$, Å	2.329	2.359	2.328	$\omega_3(a_{2u})$, cm^{-1}	342 (0.2)[e]	
$\omega_1(a_1)$, cm^{-1}	148 (0.1)[e]	163 (0.2)[e]		$\omega_4(b_{1g})$, cm^{-1}	367 (0.0)[e]	
$\omega_2(a_1)$, cm^{-1}	304 (0.2)[e]	332 (0.2)[e]		$\omega_5(b_{2g})$, cm^{-1}	287 (0.0)[e]	
$\omega_3(a_1)$, cm^{-1}	340 (0.0)[e]	355 (0.1)[e]		$\omega_6(b_{2u})$, cm^{-1}	139 (0.0)[e]	
$\omega_4(a_1)$, cm^{-1}	418 (0.5)[e]	427 (0.3)[e]		$\omega_7(e_u)$, cm^{-1}	95 (0.1)[e]	
$\omega_5(a_1)$, cm^{-1}	433 (0.0)[e]	458 (0.7)[e]		$\omega_8(e_u)$, cm^{-1}	391 (10.3)[e]	
$\omega_6(a_2)$, cm^{-1}	110 (0.0)[e]	111 (0.0)[e]		$\omega_9(e_g)$, cm^{-1}	359 (0.0)[e]	
$\omega_7(a_2)$, cm^{-1}	340 (0.0)[e]	406 (0.0)[e]				
$\omega_8(b_1)$, cm^{-1}	207 (3.4)[e]	320 (2.7)[e]				
$\omega_9(b_1)$, cm^{-1}	287 (0.1)[e]	6915[f]				
$\omega_{10}(b_2)$, cm^{-1}	235 (4.0)[e]	255 (1.2)[e]				
$\omega_{11}(b_2)$, cm^{-1}	273 (1.5)[e]	306 (1.7)[e]				
$\omega_{12}(b_2)$, cm^{-1}	436 (4.1)[e]	465 (0.6)[e]				

[a] E_{tot}=1734.367 370 a.u. at CCSD(T)/6-311+G(2*df*)//CCSD(T)/6-311+G*, $\langle S^2\rangle$=0.85.
[b] $\langle S^2\rangle$=0.83.
[c] E_{tot}=–1734.368 752 a.u. at CCSD(T)/6-311+G(2*df*)//CCSD(T)/6-311+G*, $\langle S^2\rangle$=0.80.
[d] $\langle S^2\rangle$=0.78
[e] Infrared intensities (km/mol) are given in parentheses.
[f] Symmetry broken problem.

Table 4.11 Calculated molecular properties of $O_h(^1A_{1g})$ and $C_{2v}(^1A_1)$ isomers of Si_6^{2-}

Method	B3LYP/6-311+G*	MP2/6-311+G*	CCSD(T)/6-311+G*
	Si_6^{2-} $O_h(^1A_{1g})$		
$-E$, a.u.	1737.0441 00	1734.0542 45	1734.112 726[a]
ΔE, kcal/mol	0	0	0
R(Si–Si), Å	2.498	2.464	2.475
$\omega_1(a_{1g})$, cm^{-1}	405 (0.0)[b]	438 (0.0)[b]	431
$\omega_2(e_g)$, cm^{-1}	334 (0.0)[b]	322 (0.0)[b]	332
$\omega_3(t_{1u})$, cm^{-1}	364 (7.4)[b]	379 (9.7)[b]	378
$\omega_4(t_{2g})$, cm^{-1}	333 (0.0)[b]	330 (0.0)[b]	328
$\omega_5(t_{2u})$, cm^{-1}	137 (0.0)[b]	168 (0.0)[b]	146
	Si_6^{2-} $C_{2v}(^1A_1)$		
$-E$, a.u.	1737.031 182	1734.045 549	1734.099 297[c]
ΔE, kcal/mol	8.1	5.5	8.4
R(Si_1–Si_2), Å	2.496	2.461	2.484
R(Si_1–Si_6), Å	2.400	2.384	2.392
R(Si_1–Si_3), Å	2.662	2.595	2.637
R(Si_3–Si_6), Å	2.456	2.453	2.447
R(Si_3–Si_4), Å	2.420	2.407	2.412
$\omega_1(a_1)$, cm^{-1}	158 (4.5)[b]	177 (2.9)[b]	168
$\omega_2(a_1)$, cm^{-1}	287 (4.7)[b]	312 (2.9)[b]	297
$\omega_3(a_1)$, cm^{-1}	343 (2.1)[b]	346 (5.9)[b]	347
$\omega_4(a_1)$, cm^{-1}	355 (0.1)[b]	375 (2.2)[b]	367
$\omega_5(a_1)$, cm^{-1}	419 (2.4)[b]	449 (2.5)[b]	437
$\omega_6(a_2)$, cm^{-1}	129 (0.0)[b]	132 (0.0)[b]	122
$\omega_7(a_2)$, cm^{-1}	332 (0.0)[b]	375 (0.0)[b]	344
$\omega_8(b_1)$, cm^{-1}	151 (6.7)[b]	182 (3.0)[b]	158
$\omega_9(b_1)$, cm^{-1}	236 (0.0)[b]	260 (0.3)[b]	247
$\omega_{10}(b_2)$, cm^{-1}	217 (0.2)[b]	227 (0.1)[b]	221
$\omega_{11}(b_2)$, cm^{-1}	348 (0.2)[b]	345 (0.2)[b]	350
$\omega_{12}(b_2)$, cm^{-1}	436 (3.7)[b]	461 (10.7)[b]	450

[a] E_{tot}=–1734.309 096 a.u. at CCSD(T)/6-311+G(2*df*)//CCSD(T)/6-311+G*.
[b] Infrared intensities (km/mol) are given in parentheses.
[c] E_{tot}=–1734.289 598 a.u. at CCSD(T)/6-311+G(2*df*)//CCSD(T)/6-311+G*.

Table 4.12 Calculated molecular properties of the $C_{2v}(^1A_1)$ and $C_{3v}(^1A_1)$ isomers of $NaSi_6^-$.

$C_{2v}(^1A_1)$ method	B3LYP/ 6-311+G*	MP2/ 6-311+G*	$C_{3v}(^1A_1)$ method	B3LYP/ 6-311+G*	MP2/ 6-311+G*
$-E$, a.u.	1899.429907[a]	1896.020071	$-E$, a.u.	1899.424291[b]	1896.009937
ΔE, kcal/mol	0.0	0.0	ΔE, kcal/mol	3.5	6.4
$R(Na_1–Si_2)$, Å	2.875	2.887	$R(Na_1–Si_2)$	2.861	2.864
$R(Na_1–Si_6)$, Å	2.915	2.913	$R(Na_1–Si_5)$	4.705	4.693
$R(Na_1–Si_4)$, Å	4.578	4.582	$R(Si_2–Si_3)$, Å	2.495	2.471
$R(Si_2–Si_3)$, Å	2.544	2.505	$R(Si_5–Si_6)$, Å	2.548	2.512
$R(Si_2–Si_6)$, Å	2.447	2.428	$R(Si_2–Si_5)$, Å	2.472	2.447
$R(Si_2–Si_4)$, Å	2.553	2.524	$\omega_1(a_1)$, cm^{-1}	213 (7.4)[c]	224 (19.0)[c]
$R(Si_4–Si_6)$, Å	2.443	2.444	$\omega_2(a_1)$, cm^{-1}	328 (5.7)[c]	342 (6.4)[c]
$R(Si_4–Si_5)$, Å	2.504	2.463	$\omega_3(a_1)$, cm^{-1}	359 (31.6)[c]	377 (28.1)[c]
$\omega_1(a_1)$, cm^{-1}	188 (6.9)[c]	203 (5.0)[c]	$\omega_4(a_1)$, cm^{-1}	410 (0.0)[c]	435 (1.7)[c]
$\omega_2(a_1)$, cm^{-1}	230 (19.1)[c]	235 (23.2)[c]	$\omega_5(a_2)$, cm^{-1}	140 (0.0)[c]	186 (0.0)[c]
$\omega_3(a_1)$, cm^{-1}	292 (4.0)[c]	314 (4.2)[c]	$\omega_6(e)$, cm^{-1}	74 (4.2)[c]	92 (4.9)[c]
$\omega_4(a_1)$, cm^{-1}	339 (0.4)[c]	346 (8.1)[c]	$\omega_7(e)$, cm^{-1}	162 (0.0)[c]	197 (0.0)[c]
$\omega_5(a_1)$, cm^{-1}	350 (3.0)[c]	368 (0.2)[c]	$\omega_8(e)$, cm^{-1}	321 (0.3)[c]	316 (0.4)[c]
$\omega_6(a_1)$, cm^{-1}	414 (4.5)[c]	441 (3.2)[c]	$\omega_9(e)$, cm^{-1}	342 (0.0)[c]	360 (0.0)[c]
$\omega_7(a_2)$, cm^{-1}	139 (0.0)[c]	142 (0.0)[c]	$\omega_{10}(e)$, cm^{-1}	375 (9.9)[c]	384 (11.4)[c]
$\omega_8(a_2)$, cm^{-1}	325 (0.0)[c]	360 (0.0)[c]			
$\omega_9(b_1)$, cm^{-1}	90 (2.1)[c]	94 (3.4)[c]			
$\omega_{10}(b_1)$, cm^{-1}	180 (6.2)[c]	204 (2.5)[c]			
$\omega_{11}(b_1)$, cm^{-1}	280 (0.0)[c]	290 (0.5)[c]			
$\omega_{12}(b_2)$, cm^{-1}	143 (3.4)[c]	154 (3.9)[c]			
$\omega_{13}(b_2)$, cm^{-1}	235 (11.6)[c]	247 (8.8)[c]			
$\omega_{14}(b_2)$, cm^{-1}	338 (0.1)[c]	339 (0.1)[c]			
$\omega_{15}(b_2)$, cm^{-1}	414 (1.8)[c]	435 (5.9)[c]			

[a] E_{tot}=–1896.261 806 a.u. at CCSD(T)/6-311+G(2*df*)//B3LYP/6-311+G*.
[b] E_{tot}=–1896.259 976 a.u. at CCSD(T)/6-311+G(2*df*)//B3LYP/6-311+G*.
[c] Infrared intensities (km/mol) are given in parentheses.

The VDEs of these bands were given in Table 4.9. There appeared two weak features, labeled as x and a, between bands X and A in the spectra of $NaSi_6^-$, similar to the weak features observed between the X and A bands in the spectra of Si_6^-. These two weak features are assigned to be due to a low-lying isomer, analogous to Si_6^- (Table 4.9) (*vide infra*). The EA of $NaSi_6$ was measured from the onset of the X band of the 355 nm spectrum to be 1.80 ± 0.05 eV, which is 0.43 eV smaller that that of Si_6. The X-A band separation of 1.04 eV for $NaSi_6^-$ is identical to that for Si_6^-. In fact, all the five main spectral features of $NaSi_6^-$ line up well with those of Si_6^- with a shift of about 0.4 eV, suggesting that the geometrical and electronic structure of the Si_6 motif in $NaSi_6^-$ is similar to that in Si_6^-.

A very broad and diffuse photoelectron spectrum of $NaSi_6^-$ at 355 nm was reported previously by Kishi *et al*.[136] The current spectra were considerably better resolved, making it possible to quantitatively compare with theoretical calculations (*vide infra*). As shown previously, PES combining with *ab initio* calculations is a powerful tool for elucidating the electronic structure and chemical bonding of novel clusters.[117,164] In the following, different levels of theories are employed to assist the interpretation of the observed photoelectron spectra and to elucidate the detailed structures and the underlying chemical bonding of Si_6^- and $NaSi_6^-$ (Si_6^{2-}).

4.2.3 Theoretical Results

A. Si_6^-. The two lowest energy structures of Si_6^-, $C_{2v}(^2B_2)$ I and $D_{4h}(^2A_{2u})$ II, (Figure 4.8 and Table 4.10) have been identified in the literature.[102,144,145,157,158] According to the calculations the $C_{2v}(^2B_2)$ I and the $D_{4h}(^2A_{2u})$ II structures are almost

degenerate. At CCSD(T)/6-311+G(2*df*)//CCSD(T)/6-311+G* level of theory the D_{4h} ($^2A_{2u}$) II structure is slightly more stable (by 0.9 kcal/mol) than the C_{2v}($^2B_2$) I structure. Our collaborators also performed additional calculations for these structures using the CCSD(T) level of theory and three aug-cc-*p*vDZ, aug-cc-*p*vTZ, and aug-cc-*p*vQZ basis sets at the CCSD(T)/6-311+G* geometry. The calculated relative energies for two structures were found to be: 1.41 kcal/mol (DZ), 0.34 kcal/mol (TZ), and 0.13 kcal/mol (QZ) with the D_{4h} ($^2A_{2u}$) structure being more stable. Extrapolation to the infinite basis set showed that the C_{2v}($^2B_2$) structure was more stable by 0.02 kcal/mol. Thus, our collaborators used both of these structures for the theoretical calculations of VDEs to help interpret the main PES spectral features of Si_6^- (Table 4.8).

B. Si_6^{2-}. For Si_6^{2-} our collaborators performed the GEGA search at the semiempirical PM3 level of theory, followed by geometry reoptimization and frequency calculations at higher levels of theory. Two isomers with close energies were obtained: O_h($^1A_{1g}$) III and C_{2v}($^1A_1$) IV (Table 4.11), as shown in Figure 4.8 The octahedral structure consistently remains the global minimum at the B3LYP, MP2, and CCSD(T) levels of the theory (all at 6-311+G* basis set). At the highest level of theory [CCSD(T)/6-311+G(2*df*)//CCSD(T)/6-311+G*] the O_h($^1A_{1g}$) isomer is 12.2 kcal/mol more stable than the C_{2v}($^1A_1$) isomer. The C_{2v}($^1A_1$) isomer IV can be considered as a result of a distortion of the O_h($^1A_{1g}$) isomer III, leading to the cleavage of an "equatorial" Si–Si bond and the formation of a Si–Si bond between the two axial atoms. Alternation of other bond lengths occurs as well, the most noticeable is the increase of the distance between the axial ($Si_{1,2}$) and bridging-equatorial ($Si_{3,4}$) atoms and the decrease of the distance between the axial ($Si_{1,2}$) and the non-bridging-equatorial ($Si_{5,6}$) atoms.

C. $LiSi_6^-$ and $NaSi_6^-$. Due to technical reasons semiempirical GEGA computations could be performed only for the $LiSi_6^-$ system, whose isomers were then taken as starting geometries for higher-level calculations for $NaSi_6^-$. The low-lying $LiSi_6^-$ isomers from the GEGA search contained Si_6^- kernels with both the O_h and C_{2v} structures. Substitution of Li by Na and reoptimization of the obtained structures at the B3LYP/6-311+G* level of theory gave again two low-lying $NaSi_6^-$ isomers (Figure 4.8). Geometric parameters as well as harmonic frequencies for structures V and VI are summarized in Table 4.12, where total energies obtained in single-point calculations at CCSD(T)/6-311+G(2*df*) are also given. It was found that while for bare Si_6^- the $O_h(^1A_{1g})$ structure III is more stable than the $C_{2v}(^1A_1)$ isomer IV, for $NaSi_6^-$ the $C_{3v}(^1A_1)$ isomer VI with the O_h motif is energetically less favorable than structure V with the C_{2v} motif. At the highest level of theory [CCSD(T)/6-311+G(2*df*)//B3LYP/6-311+G*] the $C_{2v}(^1A_1)$ isomer V of $NaSi_6^-$ is only 1.2 kcal/mol more stable than the $C_{3v}(^1A_1)$ isomer VI. It was noted that Kishi *et al.* obtained a similar ground state isomer for $NaSi_6^-$.[136] But they did not obtain the C_{3v} isomer; they considered two much higher energy isomers instead, in which the Na^+ is coordinated to either an axial Si atom or to two equatorial Si atoms of O_h Si_6^-.

Comparison of the C_{2v} and O_h structures for the bare Si_6^- with the corresponding fragments in the two $NaSi_6^-$ isomers reveals relatively minor structural changes due to the Na^+ coordination, suggesting the robustness of the silicon kernel as a solid building block. In the global minimum $C_{2v}(^1A_1)$ $NaSi_6^-$, the effect of the Na^+ coordination appears to slightly increase the Si–Si bond length between the two axial atoms (Table 4.12). In the $C_{3v}(^1A_1)$ $NaSi_6^-$ isomer, the Na^+ coordination has little effect on the three proximate Si

atoms, but seems to increase the Si–Si bond distances for the three distal Si atoms (Table 4.12).

4.2.4. Interpretation of The Photoelectron Spectra

A.Si_6^-. Binggeli and Chelikowsky[103] first computed the PES spectra of Si_6^- using molecular dynamics simulation and compared them with the slightly lower resolution PES spectra reported by Chesnovsky *et al.*[126] They found that the simulated spectrum of the C_{2v} Si_6^- structure was in excellent agreement with the experimental data, whereas a low-lying isomer with a distorted octahedral structure might also make minor contributions to the experimental data. Their study firmly established the C_{2v} ground state structure for Si_6^-. However, a quantitative interpretation of the PES spectra requires detailed calculations for each photodetachment transition from the C_{2v} and D_{4h} ground state structures to the neutral final states. In particular, since the ground state of Si_6^- is a doublet with an unpaired electron, both singlet and triplet final states are possible and they need to be computed in order to make a quantitative comparison with the experimental PES spectra. In the current study, our collaborators calculated the VDEs for Si_6^- (C_{2v},$^2B_2$) at the following levels of theory: CCSD(T)/6-311+G(2*df*)||CCSD(T)/6-311+G*, EOM/6-311+G(2*df*)||CCSD(T)/6-311+G*, TD B3LYP/6-311+G(2*df*)||B3LYP/6-311+G*, and UOVGF/6-311+G(2*d*)||CCSD(T)/6-311+G*. The final electron configurations and the corresponding detachment energies are given in Table 4.8, compared with the experimental VDEs. The results at the different levels of theory generally agree well with each other and with the experiment.

As shown in Table 4.8, the LUMO of neutral Si_6 is $4b_2$, which is singly occupied in Si_6^-. Detachment of the $4b_2$ electron produces a singlet state ($^1A_1$) for the neutral Si_6. There is a very good agreement between the calculated VDE values among the different theoretical methods (Table 4.8). The next detachment channel involves the $6a_1$ orbital, which is the HOMO of the neutral Si_6. Detachment from this fully occupied MO produces both a triplet and a singlet final state. The calculated VDEs for the triplet final state ($^3B_2$) are in good agreement with the VDE of the *A* band observed experimentally. The *A*-*X* separation, which represents the excitation energy from the ground state of Si_6 ($^1A_1$) to the first excited triplet state ($^3B_2$), is an experimental measure of the HOMO-LUMO gap of neutral Si_6. It was noted that the TD-B3LYP method underestimates the HOMO-LUMO gap, whereas the CCSD(T) method yields a HOMO-LUMO gap which is in excellent agreement with the experimental measurement.

The next five detachment channels, including the singlet final state ($^1B_2$) obtained by removing the $6a_1$ electron, are congested within a narrow energy range from 3.65 to 4.05 eV from the TD-B3LYP calculations. All these detachment channels contributed to the *B* band, giving rise to the broad PES band. The next two detachment channels ($^1B_2$ and $^1A_1$) are nearly degenerate and their calculated VDEs are in good agreement with that of the *C* band. The next three detachment channels involve removal of an electron from the $1a_2$ orbital and $4a_1$ β orbital. The calculated VDEs to the triplet and singlet states are in the range of the *D* band. The last detachment channel calculated was from the $4a_1$ α orbital with a VDE of 5.32 eV, which could correspond to the tail part of the *D* band, although the signal-to-noise ratio was poor at the high binding energy part.

Overall, the computed VDEs from the C_{2v} Si_6^- are in excellent agreement with the experimental PES spectral pattern, consistent with the previous molecular dynamics simulations by Binggeli and Chelikowsky. These authors were able to obtain simulated spectral patterns very similar to the experimental PES spectra, even though they did not do state-to-state calculations. This was because of the congested nature of the PES spectra and the limited spectral resolution. The current study represents the most quantitative interpretation of the PES spectra of Si_6^-. The spectrum for the low-lying isomer which is a distorted octahedral structure (D_{4h}) was simulated by Binggeli and Chelikowsky. Our collaborators also obtained theoretical spectra for D_{4h} ($^2A_{2u}$) at the CCSD(T)/6-311+G(2*df*)||CCSD(T)/6-311+G*, TD-B3LYP/6-311+G(2*df*)||B3LYP-6-311+G*, and UOVGF/6311+G(2*d*)|| CCSD(T)/6-311+G* levels of theory (Table 4.8). The theoretical VDE for the ground state transition was ~2.61–2.74 eV, consistent with weak signals in the same energy range in Figure 4.6. One main feature from this isomer (triplet final state ^3E_g) is in good agreement with the weak feature labeled as IS in Figure 4.6, with the rest of the simulated features buried in the features from the C_{2v} ground state of Si_6^-. The calculations show effective degeneracy of the D_{4h} ($^2A_{2u}$) and C_{2v} ($^2B_2$) isomers; presence of the D_{4h} ($^2A_{2u}$) structure is revealed in all the PES spectra of Si_6^- reported so far, including the current data. The feature labeled IS in Figure 4.6 was vibrationally resolved by Xu *et al.*, who did not recognize it as a contribution from a low-lying isomer and attributed it incorrectly to the first excited state transition from the main Si_6^- isomer. The analysis showed that the theoretical spectrum of Si_6^- C_{2v} ($^2B_2$) was more consistent with the experimental data, demonstrating that under the experimental conditions the C_{2v} structure was more abundant in the molecular beam than the D_{4h} one.

B.$NaSi_6^-$. The ground state of $NaSi_6^-$ can be viewed as adding a Na atom to the C_{2v} ground state of Si_6^-, with an electron transfer from Na to the Si_6 motif to produce the C_{2v} Si_6^{2-} coordinated by a Na^+. The extra electron enters the $4b_2$ singly occupied molecular orbital (SOMO) of Si_6^-, producing a closed shell ground state of $NaSi_6^-$ with a nearly identical MO ordering. The closed shell nature of $NaSi_6^-$ means that the PES spectrum would be simpler because only doublet final states are produced and each occupied MO only yields one detachment channel, in contrast to Si_6^-, where both singlet and triplet final states can be produced after detachment from a fully occupied MO. Table 4.9 summarizes the calculated VDEs at several levels of theory for the C_{2v} ground state of $NaSi_6^-$, as well as those for the C_{3v} isomer, compared with the experimental values.

(1) $NaSi_6^-$ (C_{2v},$^1A_1$). The ground state transition corresponds to an electron detachment from the $4b_2$ HOMO. The ROVGF and CCSD(T) methods yielded VDEs for the ground state transition in exact agreement with the experimental values within the experimental uncertainty (Table 4.9). The second detachment channel is from the $6a_1$ HOMO-1. We note again that the CCSD(T) method yielded a VDE in quantitative agreement with the experimental value of the *A* band. The *X*-*A* separation measured to be 1.04 eV is also well reproduced by both the TD-B3LYP and CCSD(T) methods. It should be pointed out that the *X*-*A* separation measured in the spectra of $NaSi_6^-$ is identical to that of Si_6^- (Figure 4.6 and Table 4.8), suggesting that the Na^+ coordination has little electronic effect on these MOs. As can be clearly seen from Table 4.9, the next five detachment channels are in excellent agreement with the experimental pattern for the *B*, *C*, and *D* bands, with the *B* and *D* bands each containing two detachment channels. Comparison between the spectra of Si_6^- and $NaSi_6^-$ suggests that the detachment channels

of both species are similar. If all the excited singlet states were removed from Si_6^-, one would obtain almost identical spectra for these two species, which is why the spectra of $NaSi_6^-$ were simpler and less congested. The excellent agreement between the calculated VDEs and the experimental PES data confirms unequivocally that the ground state of $NaSi_6^-$ is the C_{2v} ($^1A_1$) structure V.

(2) $NaSi_6^-$ (C_{3v},$^1A_1$). The weak features in between the *X* and *A* bands clearly do not belong to the C_{2v} ground state isomer of $NaSi_6^-$. The low-lying C_{3v} ($^1A_1$) isomer VI of $NaSi_6^-$ (Figure 4.8) is only 1.2 kcal/mol higher in energy [at CCSD(T)/6-311+G(2*df*)||B3LYP/6-311+G*] than the global minimum C_{2v} structure and thus could be populated experimentally. As shown in Table 4.9, the calculated VDEs for the first two detachment channels for the C_{3v} isomer are in excellent agreement with the observed weak features (*x* and *a*). The ground state transition from the C_{3v} isomer corresponds to electron detachment from the $5a_1$ HOMO. The computed VDEs from both ROVGF and TD-B3LYP are in very good agreement with the experimental VDE from the *x* feature. The calculated VDE from the 4*e* HOMO-1 gives rise to feature *a*. The two higher binding energy transitions from the C_{3v} isomer have similar binding energies with the *D* band of the main isomer and might be obscured.

Comparisons of the experimental PES data of $NaSi_6^-$ with the theoretical calculations lead to several conclusions. First, two isomers were indeed observed experimentally for $NaSi_6^-$, similarly to Si_6^-. Second, good agreement between the experimental and theoretical VDEs confirms the global minimum (C_{2v},$^1A_1$) structure V for $NaSi_6^-$ and the low-lying (C_{3v},$^1A_1$) isomer VI. Third, the Si_6 moiety in $NaSi_6^-$ is very similar electronically and structurally to Si_6^-. Fourth, ROVGF/6-311+G(2*df*), TD

B3LYP/6-311+G(2*df*), and CCSD(T)/6-311+G(2*df*) levels of theory, used to calculate VDEs, show good agreement with each other and with experiment. Thus, the first two methods, which do not require as much computer resources as CCSD(T), can be reliably implemented in the future in analyzing PES of larger Na–Si clusters. We note that the poor agreement (>0.5 eV) between the calculated and experimental first VDEs and ADEs of $NaSi_6^-$ reported by Kishi *et al.*[136] was most probably caused by the small basis sets used in their calculations.

4.2.5 Chemical Bonding in Si_6^{2-} and $NaSi_6^-$

A.NBO analysis. Our collaborators performed NBO analysis for the Si_6^{2-} $O_h(^1A_{1g})$, Si_6^{2-} $C_{2v}(^1A_1)$, $NaSi_6^-$ $C_{3v}(^1A_1)$, and $NaSi_6^-$ $C_{2v}(^1A_1)$ species. Tables with the NBO data are available from the authors upon request.

The Si atoms in Si_6^{2-} $O_h(^1A_{1g})$ each carry an effective charge Q(Si)=–0.333 $|e|$ and their hybridization is $3s^{1.65}3p^{2.62}$. Thus, the $3s^2$ lone pairs on Si show some hybridization with the 3*p* atomic orbitals (AOs) in spite of the excessive –2 charge on the cluster. From $Si_6^{2-}O_h(^1A_{1g})$ to $Si_6^{2-}C_{2v}(^1A_1)$ some charge redistribution occurs. The two axial atoms with $Q(Si_{1,2})$=–0.305 $|e|$ (hybridization $3s^{1.55}3p^{2.70}$) lose some electron density and some *s*-*p* promotion also occurs. The two bridging-equatorial atoms with $Q(Si_{3,4})$=–0.324 $|e|$ (hybridization $3s^{1.66}3p^{2.60}$) are almost the same as in the octahedral structure. The other two non-bridging-equatorial atoms gain some extra negative charge with $Q(Si_{5,6})$=–0.371 $|e|$ and hybridization $3s^{1.67}3p^{2.67}$.

The major difference between the $O_h(^1A_{1g})$ and $C_{2v}(^1A_1)$ structures is the transfer of electron density from lone pairs to Si–Si bonds. The occupation numbers in the six

lone pairs in the $O_h(^1A_{1g})$ isomer are 1.965 $|e|$ and 1.964 $|e|$, compared to two lone pairs (Si_1 and Si_2) with occupation numbers 1.703 $|e|$, two lone pairs (Si_3 and Si_4) with occupation numbers 1.914 $|e|$, and two lone pairs (Si_5 and Si_6) with occupation numbers 1.931 $|e|$ in the $C_{2v}(^1A_1)$ isomer. Thus, about 0.5 $|e|$ was transferred from lone pairs in the O_h structure to Si–Si bonds (primarily to Si_3–Si_6 and Si_4–Si_5) in the C_{2v} structure. NBO analysis of $NaSi_6^-C_{3v}(^1A_1)$ and $C_{2v}(^1A_1)$ revealed that chemical bonding between Na^+ and Si_6^{2-} is highly ionic. The NBO charge for Na is +0.823 $|e|$ in $NaSi_6^-C_{2v}(^1A_1)$ and +0.709 $|e|$ in $NaSi_6^-C_{3v}(^1A_1)$. In both isomers there is some charge redistribution in the corresponding Si_6^{2-} kernels due to the coordination of Na^+. In the C_{2v} structure the axial atoms become more negatively charged [$Q(Si_{2,3})$=–0.419 $|e|$; hybridization $3s^{1.55}3p^{2.82}$], the bridging-equatorial atoms lose some negative charge [$Q(Si_{4,5})$=–0.103 $|e|$; hybridization $3s^{1.69}3p^{2.37}$], and there is almost no change of the charge on the two non-bridging-equatorial atoms [$Q(Si_{6,7})$=–0.391 $|e|$; hybridization $3s^{1.68}3p^{2.68}$]. In the C_{3v} structure, the Si atoms located at the face closest to Na^+ gained some negative charge [$Q(Si_{2,3,4})$=–0.402 $|e|$; hybridization $3s^{1.61}3p^{2.74}$], and the other three atoms become less negatively charged [$Q(Si_{5,6,7})$=–0.168 $|e|$; hybridization $3s^{1.68}3p^{2.44}$].

B.MO analysis. Figure 4.9 displays the MOs of Si_6^{2-} C_{2v} ($^1A_1$) IV and $NaSi_6^-C_{2v}$ ($^1A_1$) V. Comparison of these two systems shows that the identical sets of orbitals are occupied. From this point of view the chemical bonding in $Si_6^{2-}C_{2v}$ ($^1A_1$) and $NaSi_6^-C_{2v}$ ($^1A_1$) can be assumed to be similar. The same is true for Si_6^{2-} (O_h,$^1A_{1g}$) III and $NaSi_6^-$ (C_{3v},$^1A_1$) VI.

Upon transition from the O_h ($^1A_{1g}$) isomer of Si_6^{2-} to the C_{2v} ($^1A_1$) isomer a HOMO-LUMO switch occurs, namely, one of the $2t_{1u}$ triply degenerate HOMOs ($3b_1$ in

the C_{2v} notation) switches with one of the $1t_{2u}$ triply degenerate LUMOs ($4b_2$ in the C_{2v} notations). One can see from Figure 4.10 that the $2t_{1u}$ MO has a significant contribution from the 3*s* AOs of the Si atoms, while the $1t_{2u}$ MO is primarily composed of 3*p* AOs of Si. Thus, the $2t_{1u}$ MO ($3b_1$) to $1t_{2u}$ MO ($4b_2$) switch in the C_{2v} structure should result in decreasing 3*s* AO and increasing 3*p* AO occupations. That is consistent with the observation from the NBO analysis. One can see from Figure 4.9 that the sodium cation can interact more favorably with the $4b_2$ MO rather than with the $3b_1$ MO and that makes the $NaSi_6^-$ (C_{2v},$^1A_1$) V structure more stable than the $NaSi_6^-$ (C_{3v},$^1A_1$) VI structure. Molecular orbitals of $B_6H_6^{2-}$ O_h ($^1A_{1g}$) VII and Si_6^{2-} O_h ($^1A_{1g}$) III are shown in Figure 4.10. The sets of the occupied MOs are identical for both systems, but the ordering is slightly different: the HOMO of $B_6H_6^{2-}$ O_h is a triply degenerate $1t_{2g}$ orbital while in Si_6^{2-} it is $2t_{1u}$. Also, $1e_g$ and $2a_{1g}$ orbitals switch their positions.

C.ELF analysis. ELF analysis is a popular modern technique which reveals the regions within a chemical system where pairs of electrons with antiparallel spin can be localized. The local maxima of the ELFs define "localization attractors," of which there are only three basic types: bonding, nonbonding, and core. Bonding attractors lie between the core attractors (which themselves surround the atomic nuclei) and characterize the shared-electron interactions. The spatial organization of localization attractors provides a basis for a well-defined classification of bonds. From any point in space the ELF gradient is followed to an attractor in that region, and this point is then attributed to this attractor. The collection of all the points in space which are assigned to a given attractor is called its basin. The synaptic order of a basin is determined as the number of atomic cores it is connected with. The criterion of discrimination between basins is provided by the

reduction of reducible (containing more than one attractor) domains. The reduction of a reducible localization domain occurs at critical values (saddle points) of the bonding isosurface, over which the domain is split into domains containing fewer attractors. The localization domains are then ordered with respect to the ELF critical values, yielding bifurcations.

Our collaborators studied the ELF of $B_6H_6^{2-}$ O_h ($^1A_{1g}$), Si_6^{2-} O_h ($^1A_{1g}$), Si_6^{2-} C_{2v} ($^1A_1$), and $NaSi_6^-$ C_{2v} ($^1A_1$). The ELF bifurcations, leading to the separation of regions with chemical significance, are shown in Figure 4.11. Let us start with the comparison of the two octahedral isoelectronic species, $B_6H_6^{2-}$ O_h ($^1A_{1g}$) and Si_6^{2-} O_h ($^1A_{1g}$), which are expected to have similar chemical bonding. The first bifurcation in $B_6H_6^{2-}$ occurs at 0.49 and leads to the separation of six protonated basins (spherelike regions), which correspond to 2*e*-2*c* B–H bonds. There is a similar bifurcation in Si_6^{2-}, but it occurs at a higher ELF value (0.65), and the separated spherelike domains correspond to six lone pairs of the silicon atoms. This means that the interaction of the lone pairs and the skeletal bonds in O_h Si_6^{2-} is stronger than the interaction of the B–H bonds and the skeletal bonds in $O_h B_6H_6^{2-}$. The regions of skeletal bonds are different as well. Bifurcation, separating localization domains in the regions of B–B bonds, occurs at 0.84, revealing 8 domains over the center of each of the octahedron faces and 12 domains connecting these central domains with each other. The bifurcational value is very close to the maximum value of ELF for these domains (0.85). Thus, there is a very strong interaction between basins of the corresponding attractors, and effectively one six-synaptic basin exists around a single gridlike attractor, covering the entire boron cage. In Si_6^{2-} a similar bifurcation occurs at 0.71 and gives rise to 12 separated localization domains. There are no domains over the

centers of the triangular faces of the cluster, the maximum ELF value at the attractors within 12 disynaptic basins, corresponding to the skeletal Si–Si bonds, is 0.78. Thus, the skeletal bonding in O_h Si_6^{2-} is more "localizable" than in O_h $B_6H_6^{2-}$.

In the C_{2v} Si_6^{2-} the first bifurcation occurs at 0.64 and reveals a small bonding domain between the two axial atoms [scheme 0.64(a)], which can be tracked down to the ELF features of σ-antiaromatic Si_4^0 C_{2v} ($^1A_1$) cluster.[165] At 0.71 bonding domain between bridgelike Si atoms is separated. Bifurcation at 0.73 produces irreducible localization domains, corresponding to the lone pairs of the axial atoms, and the one at 0.76 finally separates lone pairs of the bridge-equatorial atoms. There are two bonding domains in the regions of Si–Si bonding between equatorial atoms, and two more lone pairs, which can be seen after domain reduction at 0.85. So, the interaction between the lone pair domains and the bonding domains is stronger in C_{2v} than in the O_h isomer, which is consistent with the conclusions from the NBO and MO analyses. The last scheme demonstrates that maximal ELF values within the basins corresponding to the axial lone pairs are lower (0.93) than those of equatorial lone pairs (0.98). In other words, the axial lone pairs are less localizable, than the equatorial ones. Scheme 0.64(b) shows ELF saddle points characterizing interaction of the axial lone pairs with the bond between bridge-equatorial atoms. In the O_h Si_6^{2-} isomer ELF maxima (attractors) can be found in the same regions, since irreducible domains exist there. These domains could have disappeared due to the strong interaction with the lone-pair domains as the O_h structure transforms into C_{2v}. The same can be true for bonding domains between the axial and non-bridge-equatorial atoms, since they merge with axial lone pairs at 0.83, but the maximum ELF value for them is between 0.83 and 0.84.

The pattern of chemical bonding in Si_6^{2-} C_{2v} somewhat changes after introduction of Na^+ into the system according to the ELF bifurcational sequence for the $NaSi_6^-C_{2v}$ isomer. The bonding domain between the axial atoms separates at 0.58 (versus 0.64); the bonding domain between bridge-equatorial atoms-separates at 0.70 (versus 0.71). Separation of the axial and two equatorial lone pairs occurs at 0.72 (versus 0.72) and 0.76 (versus 0.76) correspondingly. But there are no bonding domains between bridge and non-bridge-equatorial atoms anymore (which appeared at 0.85 in $Si_6^{2-}C_{2v}$); they merge with lone pair domains of the non-bridge-equatorial atoms. Finally, axial lone pairs have lower maximal ELF values (0.91) than the equatorial ones (0.98).

Chemical bonding analysis of the O_h ($^1A_{1g}$) isomer of Si_6^{2-} and O_h ($^1A_{1g}$) isomer of $B_6H_6^{2-}$ revealed that like in our previous study of Si_5^{2-} and $B_5H_5^{2-}$ species,[166] Si_6^{2-} differs from $B_6H_6^{2-}$ by involvement of the electron density, which is supposed to be "lone pairs" of the six silicon atoms in the skeletal bonding in Si_6^{2-}. This tendency of Si atoms in silicon clusters to favor *s-p* hybridization rather than $3s^2$ lone pairs is also responsible for Si_6^{2-} having two low-lying O_h ($^1A_{1g}$)and C_{2v} ($^1A_1$) isomers. When sodium atom is attached to Si_6^{2-} the alteration in stability occurs. The most stable isomer of $NaSi_6^{2-}$ is based on the Si_6^{2-} kernel with the C_{2v} symmetry. The second most stable isomers of $NaSi_6^{2-}$ is based on the Si_6^{2-} kernel with O_h symmetry.

The two low-lying O_h ($^1A_{1g}$) and C_{2v} ($^1A_1$) isomers of Si_6^{2-} inspired us to test the C_{2v} ($^1A_1$) isomer of $B_6H_6^{2-}$. It was found that the C_{2v} ($^1A_1$) isomer VIII of $B_6H_6^{2-}$ (Figure 4.8) with the same electronic configuration is not a minimum, but a first order saddle point with the relative energy [compared to the O_h ($^1A_{1g}$) isomer VII] of 65 kcal/mol (at

B3LYP/6-311++G**). Thus, even though Si_6^{2-} and $B_6H_6^{2-}$ are valence isoelectronic, they have somewhat different chemical bonding.

D. Protonation as a Way to Increase the Relative Stability of the Octahedral Si_6^{2-}? From the above discussion our collaborators inferred that in order to stabilize the high symmetry O_h ($^1A_{1g}$) structure of Si_6^{2-} over the C_{2v} ($^1A_1$) structure one has to enforce sp^3 hybridization on Si. In the isoelectronic $B_6H_6^{2-}$ dianion, the external hydrogen atoms enforce almost sp^3 hybridization on boron atoms. Our collaborators tested if a similar approach will work for silicon by calculating the C_{2v} ($^1A_1$) IX and O_h ($^1A_{1g}$) X structures of $Si_6H_6^{4+}$ at the B3LYP/6-311++G** level of theory (Figure 4.8). They checked that both structures have the same electronic configurations as the O_h ($^1A_{1g}$) and C_{2v} ($^1A_1$) structures of Si_6^{2-}. They found that both the C_{2v} ($^1A_1$) IX and O_h ($^1A_{1g}$) X structures of $Si_6H_6^{4+}$ are true local minima at our level of theory, but the C_{2v} ($^1A_1$) IX structure of $Si_6H_6^{4+}$ was found to be significantly more stable (by 19 kcal/mol at B3LYP/6-311++G**) than the O_h ($^1A_{1g}$) X of $Si_6H_6^{4+}$ and that is different from Si_6^{2-} where the O_h ($^1A_{1g}$) III structure is more stable than the C_{2v} ($^1A_1$) IV structure. Thus, protonation is not a solution for stabilization of high symmetric Si_n^{2-} clusters.

4.2.6 Conclusion

Well-resolved photoelectron spectra were obtained for Si_6^- and $NaSi_6^-$ at three photon energies (355, 266, and 193 nm) and compared with theoretical calculations to elucidate the structure and bonding in Si_6^- and Si_6^{2-} in $NaSi_6^-$. Global minimum structures of Si_6^{2-} and $NaSi_6^-$ were identified first by using gradient embedded genetic algorithm followed by the B3LYP/6-311+G*, MP2/6-311+G*, and CCSD(T)/6-311+G* (except

$NaSi_6^-$) geometry and frequency calculations. By comparing the theoretical VDEs with the experimental data we established the ground state structure for $NaSi_6^-$ to be C_{2v} ($^1A_1$), in which the Na^+ is coordinated to a C_{2v} Si_6^{2-}. Though the octahedral Si_6^{2-}, analogous to the closo form of borane $B_6H_6^{2-}$, is the most stable form for the bare dianion, it is not the kernel of the $NaSi_6^-$ global minimum geometry. However, the octahedral Si_6^{2-} coordinated by a Na^+ with C_{3v} ($^1A_1$) symmetry is a low-lying isomer only 1.2 kcal/mol higher in energy and it was observed experimentally.

Chemical bonding analysis of the two low-lying $O_h(^1A_{1g})$ and $C_{2v}(^1A_1)$ isomers of Si_6^{2-} revealed that they differ by switching one of the $2t_{1u}$ triply degenerate HOMOs ($3b_1$ in the C_{2v} notation) with one of the $1t_{2u}$ triply degenerate LUMOs ($4b_2$ in the C_{2v} notations). Because the $2t_{1u}$ triply degenerate HOMO in the $O_h(^1A_{1g})$ isomer contains significant contribution from 3*s* AOs of Si and the $1t_{2u}$ triply degenerate LUMO is composed of primarily 3*p* AOs of Si, such MO exchange resulted in *s*-*p* promotion with increasing *sp* hybridization and increase in Si–Si chemical bonding in the $C_{2v}(^1A_1)$ isomer. When the Na^+ is attached to the Si_6^{2-} cluster in $NaSi_6^-$ it more strongly stabilizes the $4b_2$ MO than the $3b_1$ MO, making the $C_{2v}(^1A_1)$ isomer of $NaSi_6^-$ with the $C_{2v}(^1A_1)Si_6^{2-}$ kernel somewhat more stable than the $C_{3v}(^1A_1)$ isomer of $NaSi_6^-$ with the $O_h(^1A_{1g})Si_6^{2-}$ kernel.

CHAPTER FIVE

PHOTOELECTRON SPECTROSCOPY STUDY OF GERMANIUM CLUSTER ANIONS

5.1 Introduction

Study of small atomic clusters is greatly beneficial to the understanding of evolution of materials from the molecular to macroscopic regimes. Small to medium-sized semiconductor clusters, such as Si and Ge clusters, have received considerable attention since the 1980s, largely because of their potential relevance to and applications in the nanoelectronics industry. Semiconductor clusters are a special class of matter with sizes in between single atoms and semiconductor quantum dots. Extensive studies have been carried out for silicon and germanium clusters.[37,62,79-85,96-116,126,167-185, 186-190] Much understanding has been obtained, for example, their stability, reactivity and the evolution of their electronic and geometrical structures toward bulk. Quantum confinement in nano-structured silicon, such as thin films or porous silicon, results in a renormalization of the band gap.[191] The continuous electronic bands in bulk semiconductors become discrete energy levels in these finite-sized clusters. Energy gaps more than three times the size of crystalline silicon have been reported for these systems.[192,193] The band gaps and band structures of semiconductor clusters are also expected to be greatly altered compared with those in the bulk due to the quantum confinement effect. However, most previous studies[37,62,79-85,96-116,126,167-185] have suggested that small Si and Ge clusters are highly coordinated and compact, bearing little resemblance to the tetrahedral lattice of the bulk. An interesting phenomenon of prolate-to-spherical structural transition with increase of

size has also been observed for both Si and Ge clusters by ion mobility measurements.[62,80,85,167]

Like silicon clusters that were extensively studied, Ge_n clusters also received various experimental investigations. As early as 1954, the Ge_n clusters containing two to eight atoms were experimentally studied for the first time by Kohl.[168] The atomization energies of small Ge clusters were first determined by Kant and Strauss[169] using mass spectrometry. Adopting a slightly modified technique, Gingerich *et al.*[170,171] determined the stabilities of the Ge_n (n = 2–5) clusters with higher accuracy. Other studies of Ge_n clusters include laser photofragmentation,[97,172] mass spectrometry,[173,174] Raman spectra,[194] photoelectron spectroscopy,[84,126,175-180] photodetachment thresholds and infrared spectroscopy.[181-184]

Numerous theoretical calculations[167,185-190] have been performed on small germanium clusters. Structures of very small germanium clusters up to 10 atoms have been well established. [167,185-188] Zeng and co-workers have employed the basin-hoping global optimization method to search for the low-lying structures for neutral Ge_n clusters up to 30 atoms.[189,190]

Photoelectron spectroscopy has been proven to be a powerful technique to study the electronic and geometric structures of atomic clusters in gas phase as a function of size,[126,195] due to its ability to combine size selectivity with quantitative spectral sensitivity. Since photodetachment is a process of transition from the ground state of anions into the ground state or electronic excited states of the corresponding neutrals, the electronic properties of the neutral clusters are readily observed from the photoelectron

spectra. Information on the atomic bonding and thus the geometry of the clusters has been generally derived from the analysis of photoelectron spectra.

Compared to the wealth of spectroscopic data for silicon clusters,[37,82,83,101,196] there are much less spectroscopy studies of germanium clusters. Froben and Schulze[194] measured Raman and fluorescence spectra from Ge molecules deposited onto a cryogenic matrix and assigned various vibrational frequencies to Ge_2, Ge_3, and Ge_4, but the absence of mass separation makes these assignments problematic. Low-lying states of Ge_2 and Ge_2^- have been probed and assigned in details by Neumark and co-workers using ZEKE spectroscopy.[176] The anion photoelectron spectroscopy study on Ge_n^- (n = 3 – 12), by Smalley and co-workers[126] represents the first spectroscopic work on mass-selected germanium clusters. These spectra were taken using detachment photon energy of 6.424 eV at a resolution of about 150 meV, yielding electron affinities and the first glimpse of the electronic complexity of small germanium clusters. Neumark and co-workers have recorded the photoelectron spectra of Ge_n^- (n = 2 – 15) at several photon energies up to 4.661 eV (266 nm).[84,177] Kaya and co-workers have also studied the germanium anion clusters Ge_n^- (n up to 32) using photoelectron spectroscopy.[178-180] The HOMO-LUMO gaps of the neutral Ge_n clusters were determined by them with a halogen atom doping method.

In the present work, we report a systematic photoelectron spectroscopy investigation of germanium anion clusters Ge_n^- (n = 4 – 38) at two photon energies, 6.424 eV (193 nm) and 4.661 eV (266 nm). Compared to previous recorded PES spectra, much better resolved spectra have been obtained, enabling more accurate measurements of the HOMO-LUMO gaps and the electron affinities of the neural germanium clusters. These

well defined PES spectra may serve as a good reference for future theoretical calculations for germanium clusters.

5.2 Experimental Results

A. The 193 nm spectra of Ge_n^- (n = 4 – 38). The 193 nm spectra of Ge_n^- are shown in Figure 5.1 for n = 4 – 38. Generally, our spectra are consistent with the previous PES results but much better resolved.[126] For $n \leq 8$, spectral features appeared only below 5 eV, but for larger clusters high binding energy features were observed, which could only be accessed at 193 nm. All spectra were well resolved for $n \leq 26$ and the PES spectra in this size range showed strong size dependence, where adding or removing one Ge atom produced major changes to the PES spectrum. Relatively simple spectra with well-resolved features were observed for clusters with $n \leq 11$. For $n \geq 12$, the spectral features became more congested. A clear energy gap was observed in most of the PES spectra, where a relatively weak threshold band was followed by an energy gap and more intense transitions at higher binding energies. This observation suggests that the neutral Ge clusters are closed shell and the extra electron in the anion occupies the lowest unoccupied molecular orbital (LUMO) of the neutral system, giving rise to the relatively weak threshold feature. Ge_4^- and Ge_7^- exhibited very large energy gaps of 1.01 and 1.55 eV, respectively, suggesting that neutral Ge_4 and Ge_7 are highly stable clusters. Several clusters were observed to have relatively small gaps, including n = 5, 8 and 15 in the size range below n = 26. For Ge_{17}^-, a weak feature (labeled * in Figure 5.1) seemed to be observed in the band gap range, which suggested the existence of a secondary isomer. For Ge_{25}^-, the intensity of the peak in the band gap range (labeled *) is even

higher than the first weak peak, suggesting this isomer is more populated than the one which gives the first peak in the spectra.

For the cluster size range of $n \geq 27$, the PES spectra were relatively poorly resolved due to the congested electronic transitions and/or the existence of isomers. Ge_{27}^- displays an almost continuous spectral pattern, indicating the existence of multiple isomers. Starting from Ge_{28}^-, all the spectra exhibit a similar pattern, in which a small peak is followed by an unresolved big hump. For Ge_{30}^-, a peak with intensity higher than the first peak appears in the gap region, suggesting the existence of a competitive isomer.

B. The 266 nm spectra of Ge_n^- (n = 4–28). Figure 5.2 shows the 266 nm spectra of Ge_n^- for n = 4–28. The PES spectra of small Ge_n^- clusters (n = 2–15) at 266 nm have been reported previously by Neumark and co-workers.[84,177] Kaya and co-workers[178-180] have also reported the 266 nm PES spectra of Ge_n^- for n = 4 – 32. Generally, the current PES spectra are consistent with the previous results, but significantly improved. In all the spectra reported by Neumark and Kaya, a low energy tail was present likely due to hotter clusters and poor resolution, which led to much lower adiabatic detachment energies (ADEs). For example, the well resolved threshold feature in the current spectra for Ge_{12}^- yielded an ADE of 2.82 ± 0.04 eV, which also defines a relatively accurate EA for neutral Ge_{12}. This is in contrast to the value of 2.40 ± 0.2 eV reported by Neumark and co-workers (see Table 5.1). All the EA values reported by Kaya and co-workers for Ge_n clusters (n = 4 – 9) are also significantly underestimated because of the low energy tails (Table 5.1).

Compared with the 193 nm spectra, the data at 266 nm were better resolved for the low binding energy features accessible at this photon energy. The 266 nm spectra of

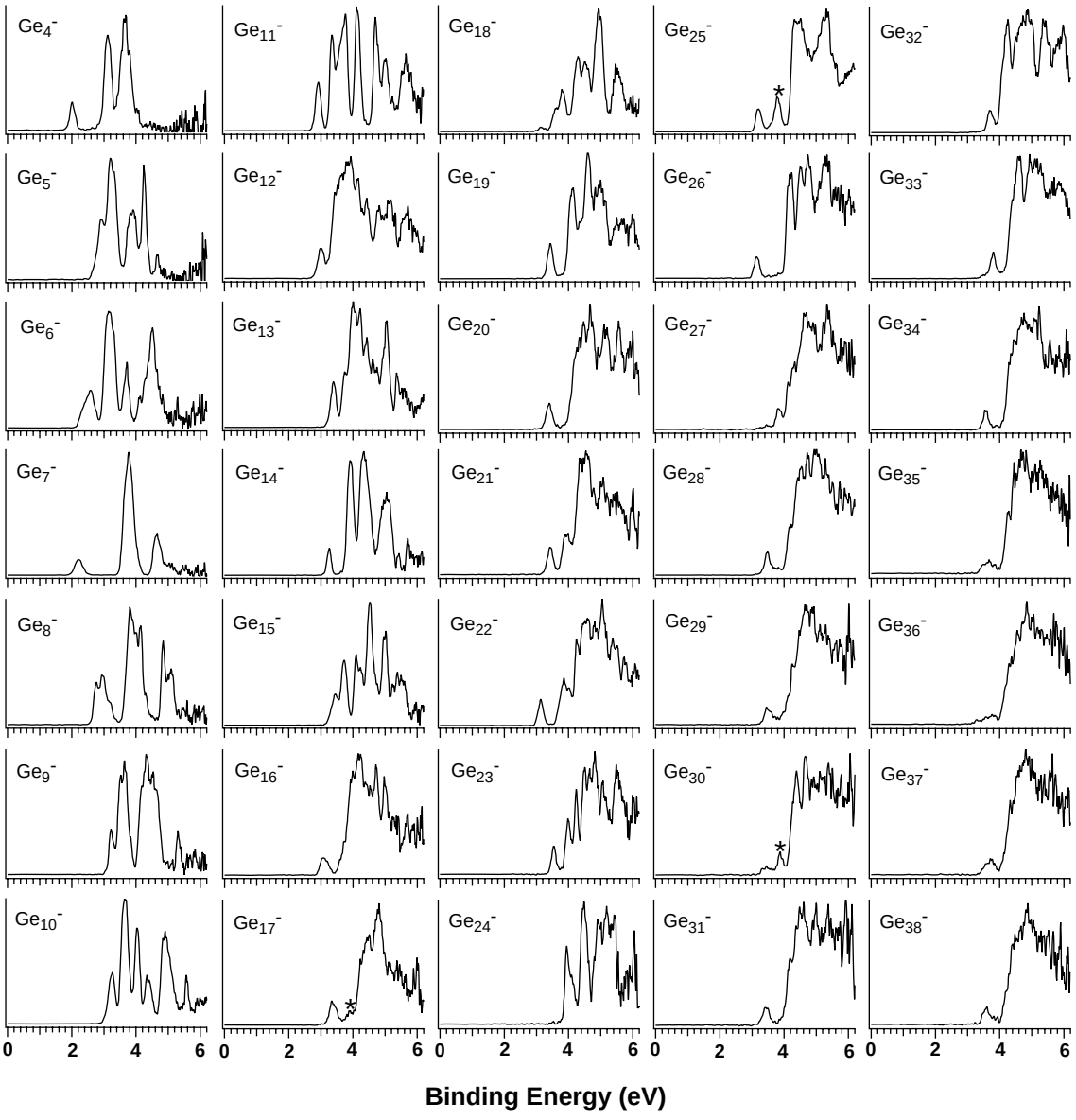

Figure 5.1 Photoelectron spectra of Ge_n^- (n = 4–38) at 193 nm (6.424 eV). "*" denotes contributions from a secondary isomer.

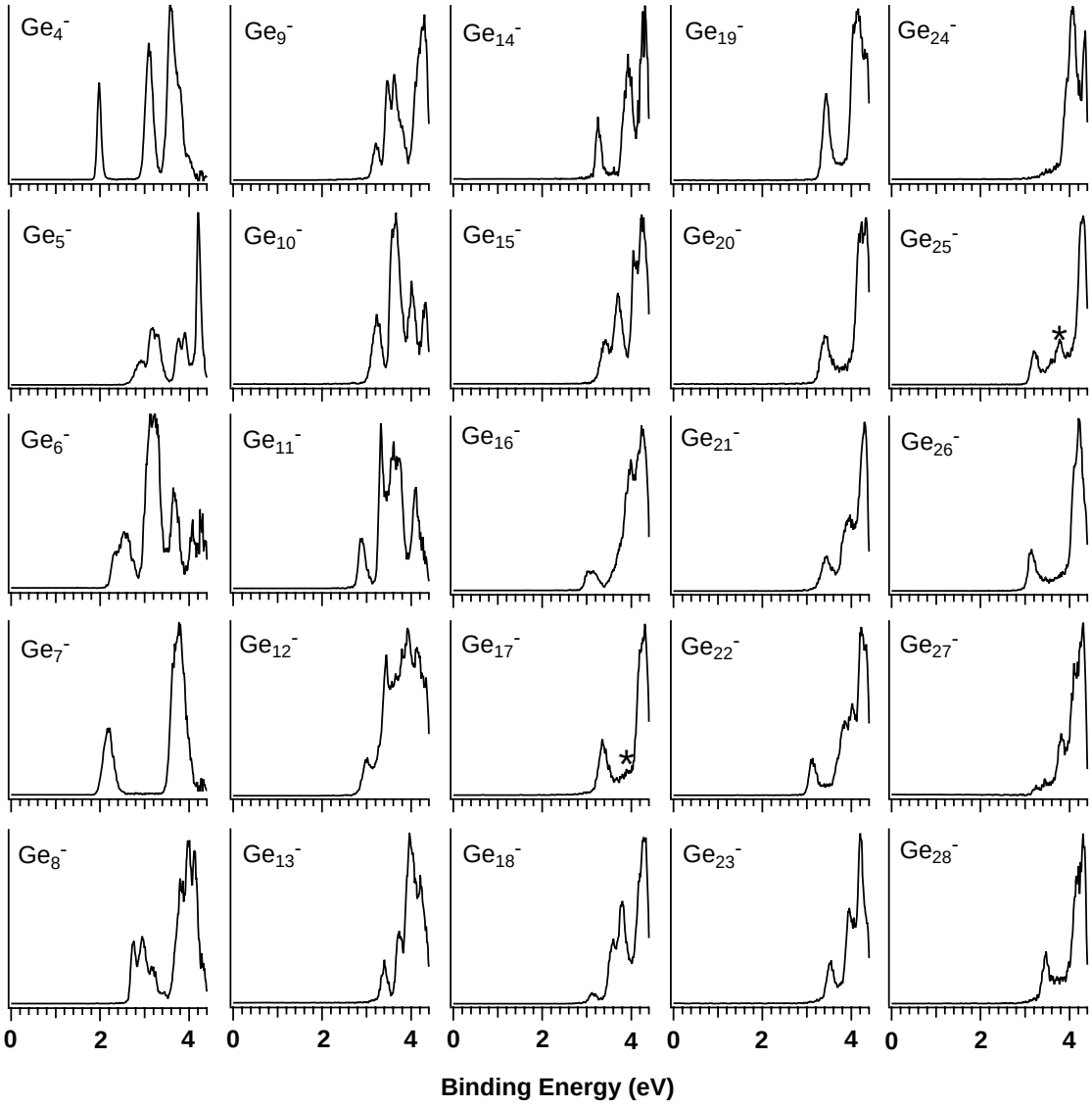

Figure 5.2 Photoelectron spectra of Ge_n^- (n = 4–28) at 266 nm (4.661 eV). "*" denotes contributions from a secondary isomer.

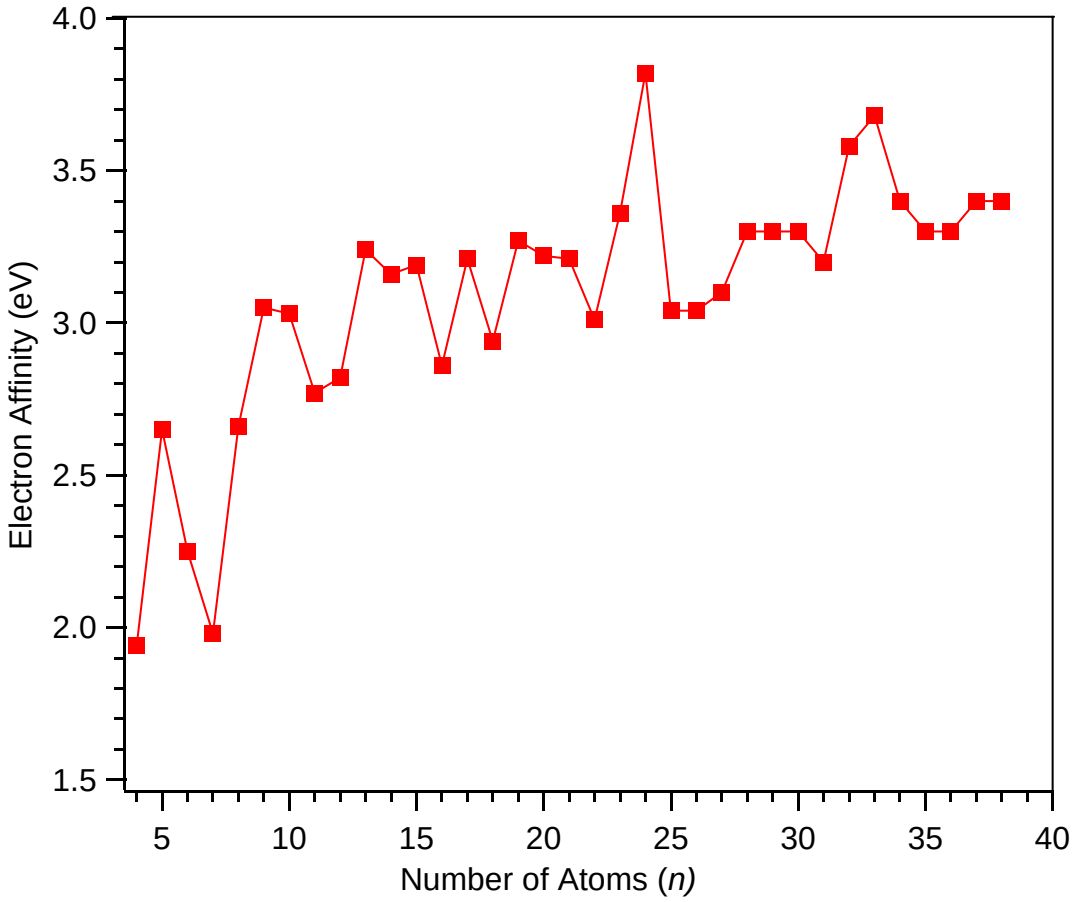

Figure 5.3 Electron affinities (EA) of Ge_n (n = 4–38) as a function of size n.

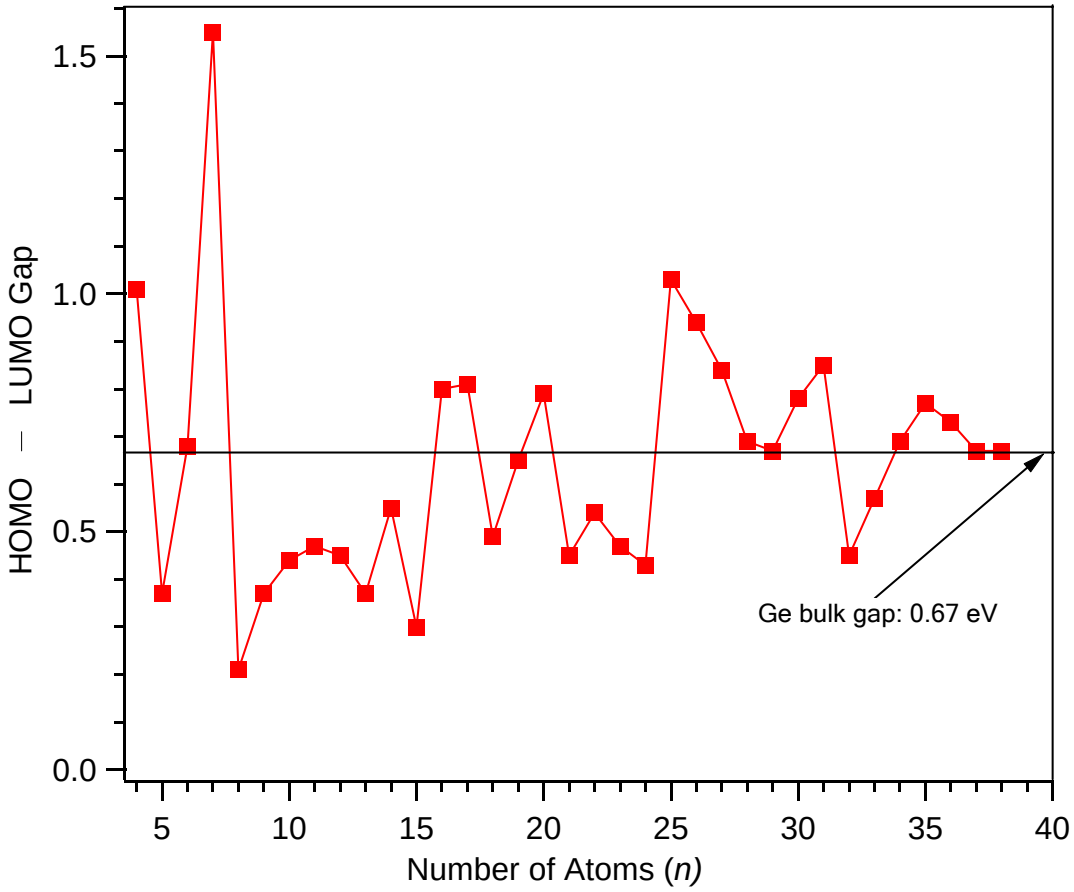

Figure 5.4 HOMO–LUMO gaps of Ge_n (n = 4–38) clusters as a function of size n. A line at 0.67 eV indicates the energy gap in bulk Ge.

Table 5.1 Electron affinities and HOMO–LUMO gaps of Ge_n clusters. All energies are in eV.[a]

	Electron Affinity			Gaps		Electron Affinity	Gaps
n	Current Results	Ref. [177]	Ref.[178]		*n*	Current Results	
4	1.94(7)	1.94(10)	1.81(9)	1.01(7)	22	3.01(4)	0.54(4)
5	2.65(5)	2.51(10)	2.67(17)	0.37(5)	23	3.36(4)	0.47(4)
6	2.25(6)	2.06(10)	2.04(8)	0.68(6)	24	3.82(3)	0.43(3)
7	1.98(7)	1.80(10)	1.79(6)	1.55(7)	25	3.04(4)	1.03(4)
8	2.66(5)	2.41(10)	2.47(11)	0.21(5)	26	3.04(4)	0.94(4)
9	3.05(4)	2.86(10)	2.92(11)	0.37(4)	27	3.10(4)	0.84(4)
10	3.03(4)	2.5(20)	2.52(8)	0.44(4)	28	3.30(4)	0.69(4)
11	2.77(4)	2.5(20)	2.40(35)	0.47(4)	29	3.32(10)	0.67(10)
12	2.82(4)	2.4(20)		0.45(4)	30	3.30(10)	0.78(10)
13	3.24(4)	2.9(20)		0.37(4)	31	3.22(10)	0.85(10)
14	3.16(4)	2.8(20)		0.55(4)	32	3.58(10)	0.45(10)
15	3.19(4)	2.7(20)		0.3(4)	33	3.68(10)	0.57(10)
16	2.86(5)			0.8(5)	34	3.42(10)	0.69(10)
17	3.21(4)			0.81(4)	35	3.30(10)	0.77(10)
18	2.94(4)			0.49(4)	36	3.32(10)	0.73(10)
19	3.27(4)			0.65(4)	37	3.42(10)	0.67(10)
20	3.22(4)			0.79(4)	38	3.40(10)	0.67(10)
21	3.21(4)			0.45(4)			

[a] Numbers in parentheses represent the uncertainty in the last digits.

Ge_n^- clusters were only taken up to Ge_{28}^- in the current study because of weak photoelectron signals for large size clusters, which led to deterioration of spectral qualities, as can be seen in Figure 5.2 for n = 27 and 28 already.

C. Adiabatic detachment energies and HOMO-LUMO gaps. The adiabatic detachment energies, which also represent the electron affinities of the corresponding neutral clusters, were difficult to measure in general without vibrationally resolved PES spectra. We estimated the EAs by drawing a straight line at the leading edge of the ground-state feature and then adding the appropriate instrumental resolution to the intersections with the binding energy axis. Although this is an approximate procedure, we have been able to obtain consistent EAs from well resolved spectra taken at different photon energies, in particular for spectra with a sharp onset. The relatively cold clusters in the current study resulted in better resolved spectra with sharp onsets, which were important in obtaining accurate EAs. All the reported EAs were determined from the 266 nm spectra wherever available. More accurate EAs were obtained in the lower photon energy spectra because of the better spectral resolution. The obtained EAs are compared with previous measurements in Table 5.1 and plotted as a function of size (n) in Figure 5.3.

If a neutral cluster is closed shell, then in the anion the extra electron occupies the LUMO of the corresponding neutral cluster. This extra electron usually yields a weak threshold PES band followed by an energy gap, which represents the experimental measure of the HOMO–LUMO gap in the neutral cluster. This energy gap carries important information about the electronic structure information in the germanium clusters. It was measured from the binding energy difference between the ADEs of the

first and second PES bands. In cases where the two bands were not well resolved, we estimated the energy gaps using the peak maxima, i.e. VDEs. The obtained values for the HOMO–LUMO gap are also given in Table 5.1 and plotted in Figure 5.4.

5.3 Discussion

A. Ge_4^- – Ge_{11}^- and Comparisons to Si_n^- Clusters. In chapter five, we made a complete comparison of the PES spectra for Si_n^-, Ge_n^- and Sn_n^- for n = 4–13.[197] We have found that the spectra of the three cluster systems exhibit remarkable similarities for n = 4–7, suggesting Si, Ge, and Sn clusters possess similar structures in this size range. A number of theoretical calculations have been reported for the structures of small neutral and anion germanium clusters.[167,185-190] The consensus is that the global minima of neutral Ge_n clusters for $n \leq 7$ are indeed identical to those previously established for Si_n species by PES and IR/Raman spectroscopy in matrices.[82,127] The relatively large energy gaps observed for n = 4 and 7 (Figure 5.4) are consistent with their high structural symmetries, a D_{2h} rhombus for n = 4 and a D_{5h} pentagonal bipyramid for n = 7. The structures for n = 5 and 6 have been determined to be trigonal and tetragonal bi-pyramids, respectively.

Compared to the PES spectra of Si_n^-, the spectra of Ge_n^- (n = 8, 9 and 10) appear very different.[197] Previous ion mobility measurements[167] suggested that very small silicon clusters and germanium clusters share similar structures and start to differentiate around 15 atoms. However, our PES results indicate that the growth pattern of silicon clusters and germanium clusters start to diverge as small as 8 atoms. Theoretical calculations also confirmed this observation. Ge_8^- has been predicted to be a bicapped octahedron,[167,187]

whereas Si_8^- has been confirmed to be a distorted cube.[128] Ge_9^- was predicted to be to bicaped pentagonal bipyramids,[167,187] which is also different from the confirmed tri-capped prism structure for Si_9^-.[83,128] For Ge_{10}^-, the lowest energy structure is a bicapped tetragonal antiprism,[167,187] whereas Si_{10}^- is a distorted tetra-capped prism.[83] Spectrum of Ge_{11}^- displays some similarity with that of Si_{11}^-, suggesting Ge_{11}^- may have a similar low symmetry C_s compact structure that was found for Si_{11}^-.[83,128]

B. Ge_{12}^- – Ge_{26}^-. The PES spectra of Ge_n^- in the size range of n = 12–26 became increasingly complicated, but were still well resolved at both 193 and 266 nm (Figures 5.1 and 5.2). Ion mobility measurements of Jarrold and co-workers[80,167] have suggested that germanium clusters of medium size ($13 \leq n \leq 35$) adopt prolate geometries, which are similar to those found for Si_n. Theoretical calculations on Ge_n ($n < 30$)[167,185-190] showed that the structures of small germanium clusters in the size range of n = 14–20 are similar to those of Si clusters, all exhibiting prolate shapes with a Tricapped Trigonal Prism (TTP) motif. The PES spectra of Ge_n^- in the size range of n = 14–25 display some similarity to those of Si_n^-, providing additional support for their structural resemblance.

In this size range, the PES spectra for Ge_{17}^- and Ge_{25}^- showed evidence of possible isomeric contributions. For Ge_{17}^-, a weak feature (labeled *) was to be observed in the band gap range, suggesting the existence of a secondary isomer. For Ge_{25}^-, the peak at 3.8 eV in the band gap region (labeled *) is even higher in intensity than the first weak peak. This suggests that the isomer which has a ground state transition at 3.8 eV is energetically more stable than the one which gives the first peak around 3.2 eV in the spectra. The current data on the Ge_n^- clusters in the size range of n = 12 – 26 are

sufficiently well reserved and can be used to compare with more detailed theoretical calculations to elucidate the structures of germanium clusters in the medium size range.

C. Ge_{27}^- – Ge_{38}^-. For Ge_n^- clusters with $n \geq 27$, the PES spectra became more congested and poorly resolved. For most species in this size range, only the ground state transition was resolved. For Ge_{30}^-, the peak at 3.9 eV ("*") in the gap region was likely due to a very competitive isomer, since its intensity is even high than the first small peak. Ion mobility experiments by Jarrold and co-workers[80,167] suggest that germanium clusters gradually rearrange from elongated structures towards near-spherical structures in the size range of $n \sim 20 – 30$. In Figure 5.1, we can see evidently that a new spectral pattern, which features a small peak followed by a big hump, starts to emerge at $n = 28$, and persists till Ge_{38}^-. This spectral pattern may be the electronic characteristics of near-spherical compact structures. The spectrum of Ge_{27}^- is rather complicated compared with all the other spectra, suggesting the co-existence of elongated isomers and spherical compact isomers. Beyond Ge_{27}^-, the spherical structures are energetically more stable and become the dominant species. So our PES spectra clearly indicate that the elongated-to-spherical structural transition may indeed occur at Ge_{27}.

D. EA and HOMO – LUMO Gap. The EAs obtained for Ge_n from the current work are given in Table 5.1 and compared with previously reported values. For $n = 4–9$, our data are consistent with those by Neumark and co-workers, but Neumark and co-workers gave a large uncertainty of 0.2 eV. In the size range of $n = 10–15$, their measured EAs are significantly underestimated by 0.3 –0.5 eV (see Table 5.1) because of the long low-binding-energy tail. Kaya and co-workers reported EAs for Ge_n clusters for $n = 4–9$, and their EA values were also underestimated because of the poor resolution and the hot

band transitions that led to low binding energy tails. Their EAs were generally by 0.2–0.4 eV too low. Our EAs are plotted as a function of size in Figure 5.3. Large size variations are observed for small clusters of $n \leq 12$. Distinct minima are seen in the EA vs. n curve at n = 4, 7, 11, 16, 25, 31, and 36. Interestingly, these EA minima correspond to maxima in the HOMO–LUMO gaps (Figure 5.4), suggesting that the corresponding neutral clusters exhibit pronounced stability. Ge_{24} displays the highest EA value of 3.82 eV, which suggests that neutral Ge_{24} might have a triplet state ground state structure and Ge_{24}^{2-} should be a stable cluster with a high symmetry.

In Figure 5.4 we plotted the HOMO–HUMO gaps of Ge_n clusters as a function of size. Most clusters display a significant HOMO–LUMO gap, suggesting the neutral germanium clusters have closed shell electronic configuration. The HOMO–LUMO gaps are strongly dependent on the cluster size. For n = 4, 7, 16, 17, 20, 25, 26, 30, 31 and 35, Ge_n display a HOMO–LUMO gap that is large than the bulk gap value of 0.67 eV. In addition to the unusually large gaps shown by Ge_4 and Ge_7, there are other pronounced maxima at n = 16, 25, 31, and 36, which correspond to the EA minima, as mentioned above.

5.4 Conclusion

A photoelectron spectroscopy study was carried out for Ge_n^- (n = 4 – 38) clusters at two detachment photon energies, 193 and 266 nm. Under well controlled experimental conditions to produce relatively cold cluster anions, well resolved PES spectra were obtained for small clusters with n = 4–26. The well resolved spectra can be used to compare with future theoretical calculations to elucidate the detailed structures of the

germanium clusters. More accurate electron affinities for germanium clusters were obtained and the evolution of their electronic structure was systematically investigated. A significant HOMO–LUMO gap was observed in the PES spectra for almost all of clusters, indicating the semiconductor nature of small germanium clusters. For many species, the measured HOMO–LUMO gap is considerably larger than the bulk gap value. A structural transition occurred around Ge_{27} was clearly reflected in the spectral pattern, confirming the prolate-to-shperical structural transition of germanium clusters found by ion mobility measurements.

CHAPTER SIX

EVOLUTION OF ELECTRONIC PROPERTIES OF TIN CLUSTER ANIONS

6.1 Introduction

Atomic clusters of the group 14 elements have been the topic of intensive studies in cluster science because of their major scientific and technological importance. One of the key questions concerns the growth pattern and bonding behavior of these clusters as a function of size. The trend going down the periodic table is fascinating for the group 14 elements, from the semi-metallic graphite (or wide band gap diamond) to the semiconductors Si and Ge to the metallic Sn and Pb. Carbon clusters have been found to undergo interesting structural variations with the increase of cluster size from linear chains to monocyclic rings to polycyclic rings to fullerenes and carbon nanotubes. Small Si and Ge clusters seem to exhibit tetrahedral bonding feature found in the bulk semiconductors.[37,79-83,85,96-116,126,167,180,186,189] Ion mobility experiments have revealed that they form prolate structures in the smaller size regime and undergo a structural transition to more spherical geometries at the size of several dozen atoms.[62,80,85,128,167] Relative to its lighter congeners, clusters of tin have attracted less attention. The growth behavior of tin clusters has been suggested in general to resemble those of Ge and Si clusters on the basis of ion mobility data.[198,199] Interestingly, the melting temperatures of tin clusters have been reported to be abnormally high relative to that of the bulk.[200] This finding has drawn significant recent attention to tin clusters,[201-207] although the nature of the abnormal melting temperature has not been fully elucidated. It is clear that knowledge of the electronic and atomic structures and the nature of the chemical bonding in these

clusters would be essential for a proper understanding of their melting behavior or other physical and chemical properties.

Bulk tin possesses two allotropes. Besides the metallic form (β-Sn) under ambient conditions, there also exists a semiconducting form (α-Sn) below 286 K.[208] Crystalline α-Sn has the same tetrahedral diamond lattice as Si and Ge with a very small band gap. Therefore, the nature of the chemical bonding in tin clusters is of great interest. Are tin clusters metallic- or semiconductor-like? How do they evolve as a function of size?

The mass spectra of tin clusters produced by various techniques have been compared with those of Si_n, Ge_n, and Pb_n by several groups.[173,209,210] But the arguments regarding the resemblance between the mass abundance spectra of Sn_n and those of Si_n, Ge_n, and Pb_n have not been very informative, because it is well known that mass abundances are strongly dependent on source conditions or methods of production. The size dependence of ionization potentials has been shown to be similar between Sn_n and Si_n/Ge_n clusters for $n \leq 12$, but it displays different behavior in the medium size range of $n = 15–41$.[211] Studies of Jarrold and co-workers[198,199] suggested that tin clusters, similar to silicon and germanium clusters, gradually rearrange from prolate to near spherical structures at the size range of $n = 35 – 65$, passing through several intermediate structural transitions.

A number of theoretical studies have also been carried out to investigate the electronic and atomic structures of small neutral and anion tin clusters.[201-205,212-216] The prior studies all predicted the lowest energy structures for neutral Sn_n clusters with $n \leq 7$ to be identical to those for Si_n and Ge_n clusters. Lu *et al.*[216] found that for $n \leq 7$, and $n =$

10 and 12, Si_n, Ge_n, and Sn_n clusters share similar structures, whereas Sn_8 and Sn_9 have different structures compared with those of the corresponding Si and Ge clusters. A more extensive study of the low lying isomers of neutral Sn_n clusters up to $n = 20$ has been carried out by Majumder *et al.*,[201,202] who suggested deviations from the growth behavior of Si and Ge clusters in the size range of $n \geq 8$.

Photoelectron spectroscopy (PES) of size-selected anion clusters is a powerful technique to probe the electronic structures of atomic clusters. PES studies of tin clusters have been performed by several groups previously.[217-219] The prior PES results[218,219] suggest that the photoelectron spectra of Sn_n^- clusters are similar to those of Si_n^- and Ge_n^-, consistent with the ion mobility studies concerning the structural similarity between Sn and Si/Ge clusters. In particular, Kaya and co-workers[219] reported an extensive set of PES data on Sn_n^- clusters and used halogen-doping to probe the nature of the electronic structure in Sn_n and Pb_n clusters. Their PES data suggested that a small band gap exists in small Sn_n clusters. But the semiconductor-to-metal transition was not conclusively observed due to the limited size range and/or spectral resolution.

All the previous PES works on Sn_n^- clusters have been done with photon energies at 4.661 eV (266 nm) or less and at relatively poor spectral resolution. We are interested in probing the electronic structure evolution of Sn_n^- clusters, in particular, the semiconductor to metal transition, at higher photon energies and improved spectral resolution. High photon energies allow more valence transitions to be observed, whereas the improved spectral resolution would allow more definitive observation of the energy gap. Our improved data immediately revealed that the spectra of Sn_{12}^- are unusual relative to those of its neighbors and are totally different from those of Si_{12}^- and Ge_{12}^-.

That let to the recent discovery of stannaspherene (Sn_{12}^{2-})[207] and subsequently plumbaspherene (Pb_{12}^{2-}),[220] which are highly stable icosahedral cages with large empty interiors analogous to the fullerene C_{60}. The chemical bonding in stannaspherene and plumbaspherene is similar to the well-known $B_{12}H_{12}^{2-}$ molecule. The stannaspherene and plumbaspherene cages have diameters larger than 6 Å and can host all transition metal atoms to form a class of stable endohedral cage clusters,[221] even more advantageous than endohedral fullerenes, which cannot entrap transition metal atoms other than the rare earth elements.[222]

In the current chapter, we report the details of our PES study on Sn_n^- (n = 4 – 45) at 193 nm (6.424 eV) and 266 nm (4.661 eV) under well controlled experimental conditions and with improved spectral resolution. The new data allow us to obtain more accurate electron affinities (EAs), as well better defined spectral features. The energy gap is also better determined, showing a clear closing at n = 42, which defines the cluster size of semiconductor-to-metal transition. The trend of the EAs as a function of size also indicates that for n > 41 it follows the metallic droplet model, consistent with the nonmetal to metal transition at n = 42.

6.2 Experimental Results

A. The 193 nm Spectra of Sn_n^- (n = 4 – 45). The 193 nm spectra of Sn_n^- are shown in Figure 6.1 for n = 4 – 45. For n < 10, spectral features appeared only below 5 eV, but for larger clusters high binding energy features were observed, which could only be accessed at 193 nm. All spectra were well resolved for $n \leq 25$ and the PES spectra in this size range showed strong size dependence, where adding or removing one Sn atom

produced major changes to the PES spectrum. Relatively simple spectra with well-resolved features were observed for clusters with $n < 10$. For $n \geq 10$, the spectral features became more congested, except for Sn_{12}^-, which exhibited a relatively simple spectrum with only five resolved features. It was this observation that led to our discovery of stannaspherene previously (see next chapter).

A clear energy gap was observed in most of the PES spectra, where a relatively weak threshold band was followed by an energy gap and more intense transitions at higher binding energies. This observation suggests that the neutral Sn clusters are closed shell and the extra electron in the anion occupies the lowest unoccupied molecular orbital (LUMO) of the neutral system, giving rise to the relatively weak threshold feature. Sn_4^- and Sn_7^- exhibited the largest energy gaps of 0.93 and 1.25 eV, respectively, suggesting that neutral Sn_4 and Sn_7 are highly stable clusters. A number of clusters were observed to have relatively small gaps, including n = 5, 8, 10, and 12 in the size range below n = 25. For Sn_{19}^- and Sn_{22}^-, a weak feature (labeled as * in Figure 6.1) seemed to be observed in the band gap range, which suggested the existence of potential isomers.

For the cluster size range of $n \geq 26$, the PES spectra were relatively poorly resolved due to the congested electronic transitions and/or the existence of isomers. The threshold transition and a small band gap could still be resolved for all the species up to n = 41, beyond which no spectral features could be resolved and the PES spectra became essentially continuous abruptly for n = 42 – 45. The spectrum of Sn_{29}^- was relatively well resolved and showed the largest band gap of 0.73 eV in this size range, indicating that neutral Sn_{29} should be an electronically stable cluster. Weak spectral features near

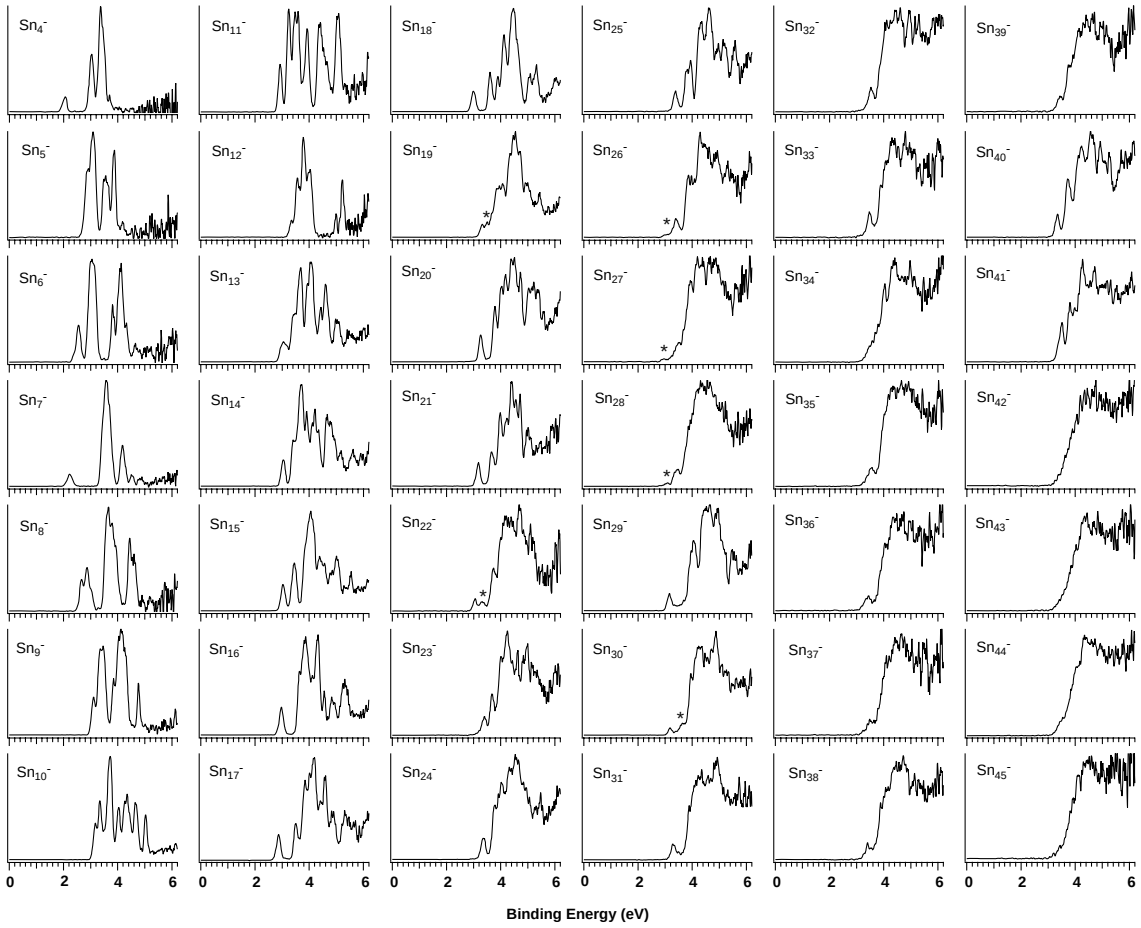

Figure 6.1 Photoelectron spectra of Sn_n^- (n = 4–45) at 193 nm (6.424 eV). "*" denotes contributions from a secondary isomer

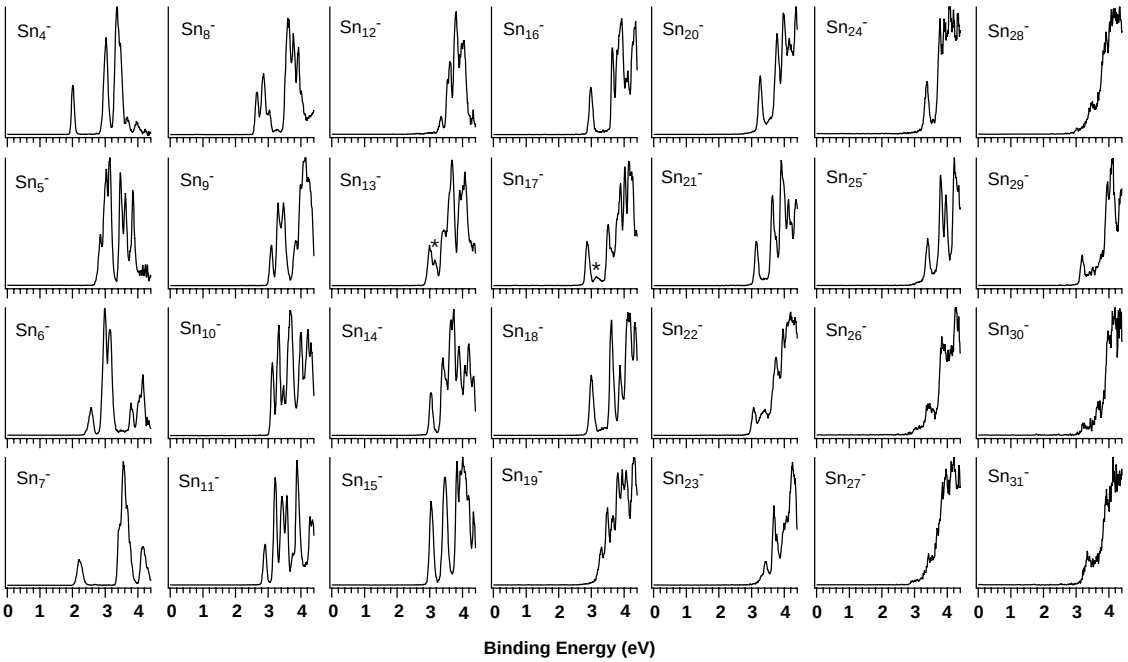

Figure 6.2 Photoelectron spectra of Sn_n^- (n = 4–31) at 266 nm (4.661 eV). "*" denotes contributions from a secondary isomer.

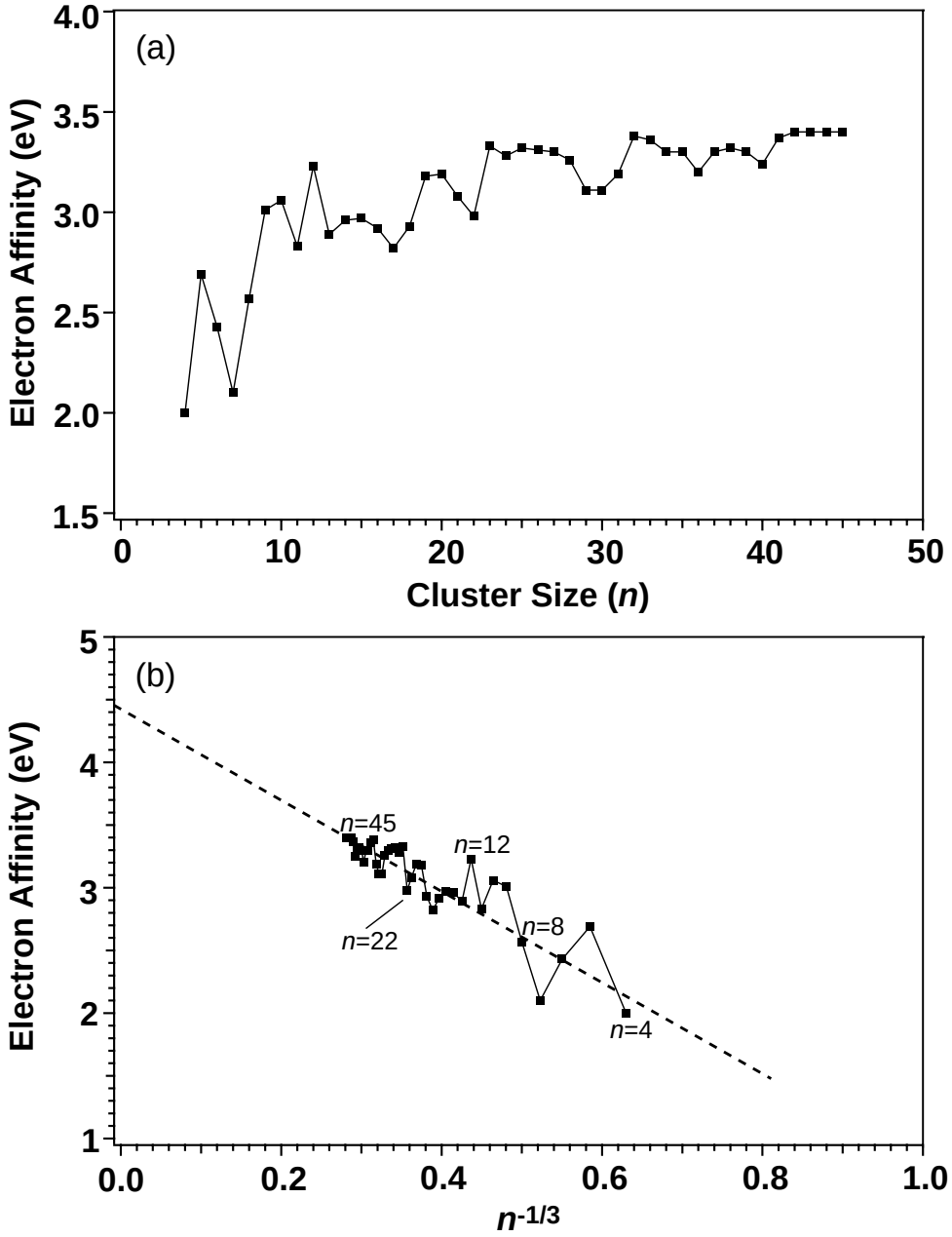

Figure 6.3 (a) Electron affinities (EA) of Sn_n (n = 4–45) as a function of size n. (b) EA vs. $n^{-1/3}$ ($n^{-1/3}$ is proportional to $1/r$, r being the cluster radius).

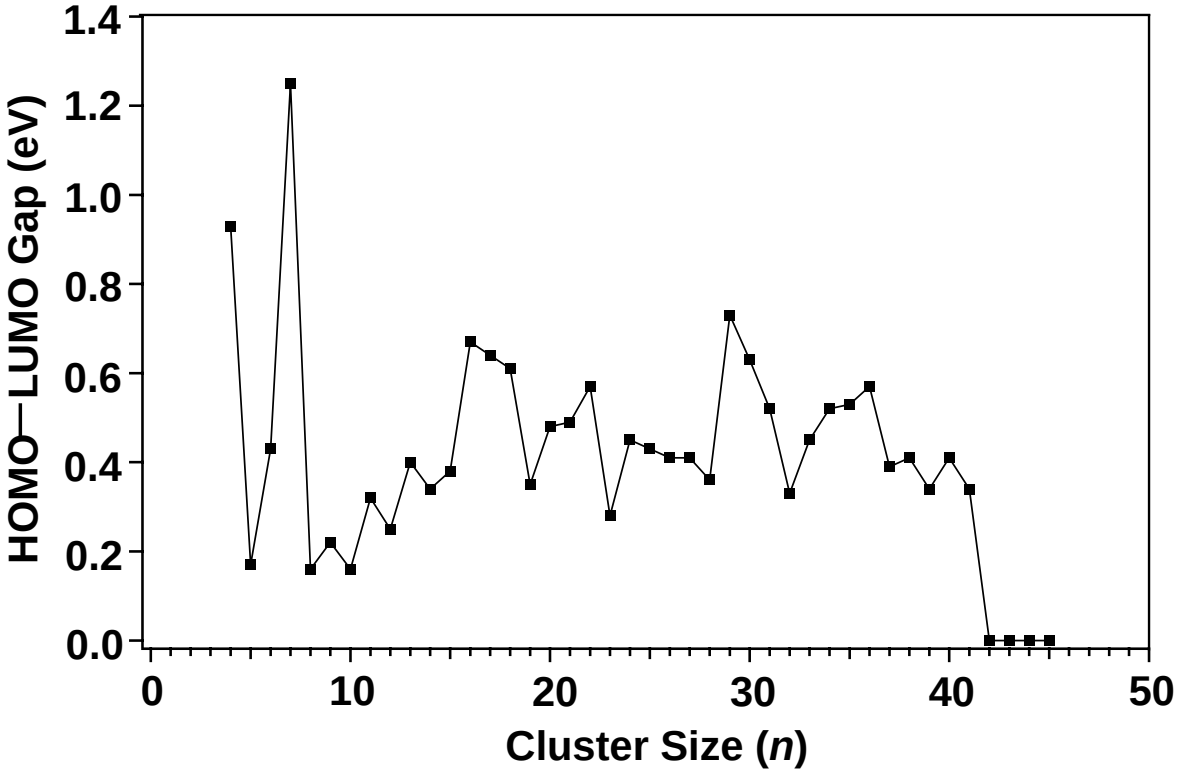

Figure 6.4 HOMO–LUMO gaps of Sn_n (n = 4–45) clusters as a function of size n.

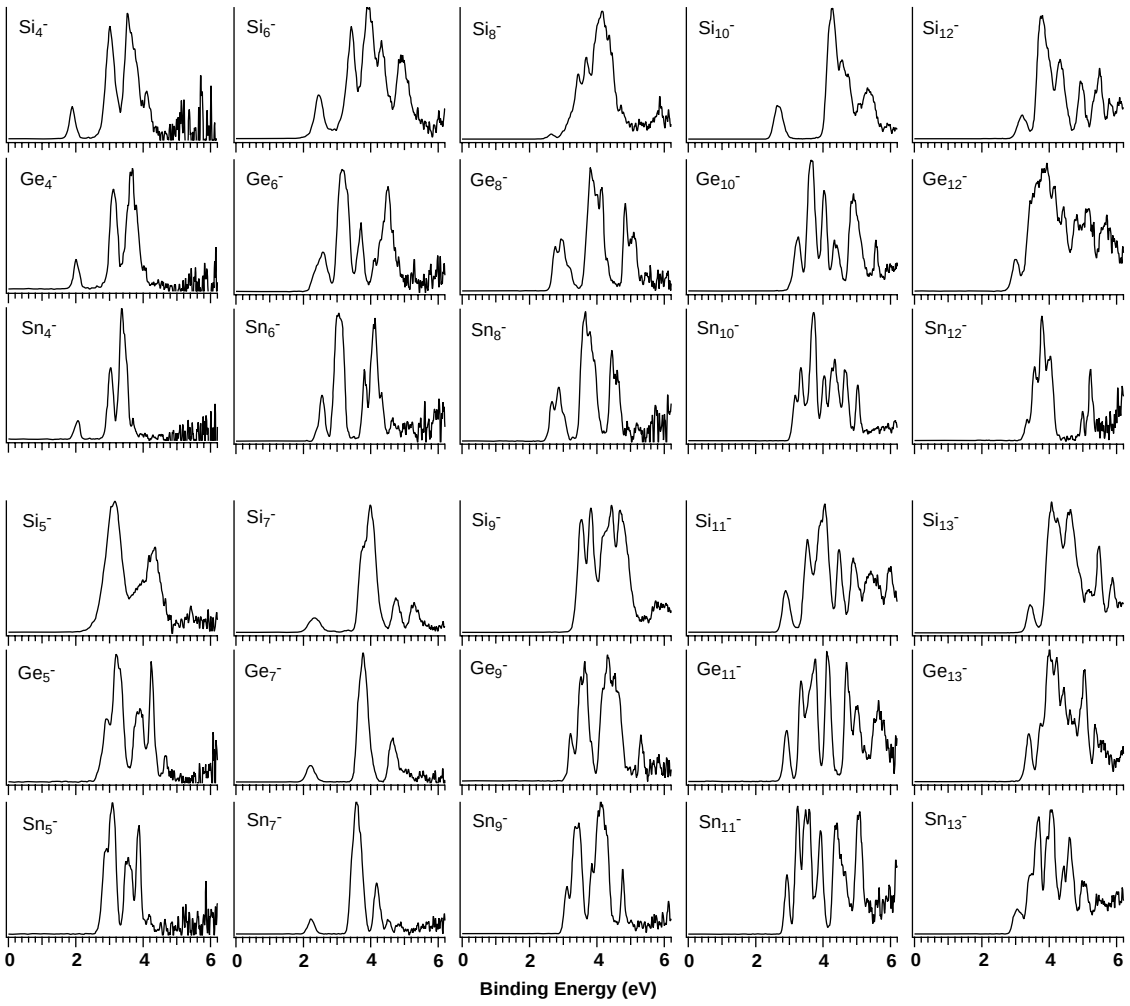

Figure 6.5 Photoelectron spectra of Sn_n^- (n = 4–13) at 193 nm compared to those of Si_n^- and Ge_n^-.

Table 6.1 Electron affinities and HOMO–LUMO gaps of Sn_n clusters. All energies are in eV.[a]

	Electron Affinity			Gaps		Electron Affinity		Gaps
n	Current Results	Ref. 51	Ref. 50		*n*	Current Results	Ref. 15	
4	2.00(7)	1.79(11)	2.04(1)	0.93(7)	25	3.32(6)	2.98(12)	0.43(6)
5	2.69(6)	2.51(32)	2.65(1)	0.17(6)	26	3.31(8)	2.86(12)	0.41(8)
6	2.43(6)	2.07(13)	2.28(1)	0.43(6)	27	3.30(10)	2.80(8)	0.41(10)
7	2.10(7)	1.87(7)	1.95(10)	1.25(7)	28	3.26(8)	2.92(15)	0.36(8)
8	2.57(6)	2.39(32)	2.48(10)	0.16(6)	29	3.11(4)	2.92(7)	0.73(4)
9	3.01(5)	2.74(5)	2.5–3.1	0.22(5)	30	3.11(8)	3.00(8)	0.63(8)
10	3.06(5)	2.76(11)	3.0–3.15	0.16(5)	31	3.19(8)	2.97(11)	0.52(8)
11	2.83(5)	2.47(5)	2.7–2.95	0.32(5)	32	3.38(8)	2.98(15)	0.33(8)
12	3.23(6)[b]	2.35(15)	3.0–3.6	0.25(6)	33	3.36(8)	2.92(13)	0.45(8)
13	2.89(5)	2.63(9)		0.40(5)	34	3.3(1)	2.96(18)	0.52(10)
14	2.96(5)	2.68(12)		0.34(5)	35	3.3(1)	2.85(9)	0.53(10)
15	2.97(5)	2.66(4)		0.38(5)	36	3.2(1)	2.88(11)	0.57(10)
16	2.92(5)	2.62(10)		0.67(5)	37	3.3(1)	2.90(13)	0.39(10)
17	2.82(5)	2.58(4)		0.64(5)	38	3.32(8)	2.96(10)	0.41(8)
18	2.93(5)	2.68(12)		0.61(5)	39	3.30(8)	2.97(12)	0.34(8)
19	3.18(6)	2.80(18)		0.35(6)	40	3.24(8)	3.04(8)	0.41(8)
20	3.19(5)	2.82(16)		0.48(5)	41	3.37(8)	3.04(7)	0.34(8)
21	3.08(5)	2.81(9)		0.49(5)	42	3.4(1)	2.93(6)	0
22	2.98(5)	2.72(13)		0.57(5)	43	3.4(1)	2.98(12)	0
23	3.33(7)	2.94(14)		0.28(7)	44	3.4(1)	2.97(18)	0
24	3.28(6)	3.04(12)		0.45(6)	45	3.4(1)	3.01(9)	0

[a] Numbers in parentheses represent the uncertainty in the last digits.
[b] From ref. [207].

the threshold (labeled * in Figure 6.1), which could be due to minor structural isomers, were observed in the spectra of Sn_{26}^-, Sn_{27}^-, Sn_{28}^-, and Sn_{30}^-. The threshold feature in Sn_{34}^- was not well resolved, possibly also due to the presence of isomers. However, the spectra of Sn_{40}^- and Sn_{41}^- were surprisingly well resolved compared to other species in this size range.

B. The 266 nm Spectra of Sn_n^- (n = 4–31). Figure 6.2 shows the 266 nm spectra of Sn_n^- for n = 4–31. The PES spectra of small Sn_n^- clusters (n = 1–12) at 266 nm have been reported previously by Moravec *et al*.[218] Kaya and co-workers[219] have reported the 266 nm PES spectra of Sn_n^- for n = 4 – 45. Generally, the current PES spectra are consistent with the previous results, but significantly improved. The spectral resolution of the current study is comparable to that of Moravec *et al*., but the signal to noise ratios were much improved, in particular, in the higher binding energy side. In all the spectra by Kaya and co-workers, a low energy tail was present likely due to hotter clusters and poor resolution, which led to much lower adiabatic detachment energies (ADEs). For example, the well resolved threshold feature in the current spectra for Sn_{12}^- yielded an ADE of 3.23 ± 0.05 eV,[207] which also defines a relatively accurate EA for neutral Sn_{12}. This is in contrast to the 3.0–3.6 eV range reported by Moravec *et al*. and the much smaller value of 2.35 ± 0.15 eV reported by Kaya and co-workers (see Table 6.1).

The 266 nm spectra of Sn_n^- clusters were only taken up to Sn_{31}^- in the current study because of weak photoelectron signals for large Sn_n^- clusters, which led to significant deterioration of spectral qualities, as can be seen in Figure 6.2 for n = 30 and 31 already. Compared with the 193 nm spectra, the data at 266 nm were better resolved for the low binding energy features accessible at this photon energy. The first band of

Sn_{13}^- at 193 nm was resolved into two peaks in the 266 nm spectrum, where the second weaker peak (labeled * in Figure 6.2) might be due to an isomer. A weak feature was also observed in the HOMO–LUMO gap region in the 266 nm spectrum of Sn_{17}^-, which was not resolved in the 193 nm spectrum and could also be due to a minor isomer. It is also worth pointing out that even though the spectrum of Sn_{12}^- was better resolved at 266 nm (Figure 6.2) the uniqueness of this spectrum in comparison to that of its neighbors was not quite obvious because of the limited spectral range, suggesting the importance of obtaining PES spectra at high photon energies or in general at various photon energies.

C. Adiabatic Detachment Energies and HOMO-LUMO Gaps. The adiabatic detachment energies, which also represent the electron affinities of the corresponding neutral clusters, were difficult to measure in general without vibrationally resolved PES spectra. We estimated the EAs by drawing a straight line at the leading edge of the ground-state feature and then adding the appropriate instrumental resolution to the intersections with the binding energy axis. Although this is an approximate procedure, we have been able to obtain consistent EAs from well resolved spectra taken at different photon energies, in particular for spectra with a sharp onset. The relatively cold clusters in the current study resulted in better resolved spectra with sharp onsets, which were important in obtaining accurate EAs. All the reported EAs were determined from the 266 nm spectra wherever available. More accurate EAs were obtained in the lower photon energy spectra because of the better spectral resolution. The obtained EAs are compared with previous measurements in Table 6.1 and plotted as a function of size (n) and $n^{-1/3}$ in Figure 6.3.

If a neutral cluster is closed shell, then in the anion the extra electron occupies the LUMO of the corresponding neutral cluster. This extra electron usually yields a weak threshold PES band followed by an energy gap, which represents the experimental measure of the HOMO–LUMO gap in the neutral cluster. This energy gap carries important information about the non-metal to metal transition in the tin clusters. It was measured from the binding energy difference between the ADEs of the first and second PES bands. In cases where the two bands were not well resolved, we estimated the energy gaps using the peak maxima, i.e. VDEs. The obtained values for the HOMO–LUMO gap are also given in Table 6.1 and plotted in Figure 6.4.

6.3 Discussion

A. Sn_4^- – Sn_{10}^- and Comparisons to Si_n^- and Ge_n^- Clusters. In Figure 6.5, we compare the PES spectra of Sn_n^- for n = 4–13 to those of Si_n^- and Ge_n^- in the same size range. PES of Si_n^- and Ge_n^- has been studied extensively previously.[37,101,126,177,180,196,223] The current data are slightly better resolved, but otherwise consistent with the previous reports. Clearly, the spectra of the three cluster systems exhibit remarkable similarities for n = 4–7, suggesting Si, Ge, and Sn clusters possess similar structures in this size range. A number of theoretical calculations have been reported for the structures of small neutral and anion tin clusters. [201-205,212-216] The consensus is that the global minima of neutral Sn_n clusters for $n \leq 7$ are indeed identical to those previously established for Si_n and Ge_n species by PES and IR/Raman spectroscopy in matrices.[82,127] The relatively large energy gaps observed for n = 4 and 7 (Figure 6.4) are consistent with their high structural symmetries, a D_{2h} rhombus for n = 4 and a D_{5h} pentagonal bipyramid for n = 7. The

structures for n = 5 and 6 have been determined to be trigonal and tetragonal bi-pyramids, respectively.[201,202,214-216]

The spectra of Sn_8^- – Sn_{10}^- are similar to those of the corresponding Ge_n^- clusters, but quite different from those of the Si_n^- clusters (Figure 6.5), suggesting Sn cluster anions in this size range have similar structures to those of Ge_n^- clusters, but different from those of Si_n^-. Indeed, Sn_8 has been predicted to be a capped pentagonal bi-pyramid,[201] whereas Si_8 is predicted to be a distorted bi-capped octohedron (C_{2h}) and Si_8^- has been confirmed to be a distorted cube (C_{2v}/C_{3v}).[128] Our PES spectral pattern for Sn_8^- displays some similarity to that of Sn_7^- (Figure 6.5), providing indirect support for a capped pentagonal bi-pyramidal structure for Sn_8^-. Sn_9 has been predicted to be a tetra-capped trigonal bi-pyramid,[201] which is also very different from the confirmed tri-capped prism structure for Si_9^-.[83,128] For Sn_{10}, two structures with very close energies have been predicted,[201] the lowest energy structure (10a) is a distorted tetra-capped prism, similar to that of Si_{10} and Si_{10}^-,[128] whereas another isomer (10b) with near C_{3v} symmetry is predicted to be only 0.09 eV higher in energy.[201] The tetra-capped prism structure for Si_{10} gives the large HOMO–LUMO and has been confirmed to be the ground state also for Si_{10}^-.[12] Thus, the very different PES spectra for Sn_{10}^- can easily rule out the (10a) structure for Sn_{10}, suggesting that the near C_{3v} (10b) isomer is likely to be the ground state for Sn_{10}^-.

B. Sn_{11}^- – Sn_{13}^-: the Unique PES Spectra of Sn_{12}^- and the Discovery of Stannaspherene. PES spectra of Sn_n^- (n = 11 – 13) at 193 nm have been reported and compared to those of Ge_n^- (n = 11 – 13) by us prviously.[207] In Figure 6.5, we compare the spectra of Si_n^-, Ge_n^-, and Sn_n^- in the same size range. The similarities among the

spectra for the 11-mer and 13-mer are obvious, suggesting these clusters should all have similar ground state structures. The previous theoretical calculations predicting different structures for Sn_{11} and Sn_{13} from the corresponding Si_n clusters are questionable.[201] Both Si_{11}^- and Si_{13}^- have been confirmed to possess low symmetry C_s structures.[83,128] However, the PES spectrum of Sn_{12}^- is totally different from those of Sn_{12}^- and Ge_{12}^- and is also surprisingly simple compared to those of its neighbors, Sn_{11}^- and Sn_{13}^-. The relatively simple and characteristic spectrum of Sn_{12}^- immediately suggested that it should possess a high-symmetry structure, which led to our recent discovery of stannaspherene.[207] Our prior theoretical calculations showed that Sn_{12}^- is a slightly distorted icosahedral cage due to the Jahn-Teller effect. Adding an electron to Sn_{12}^- led to a perfect icosahedral cage Sn_{12}^{2-}, which possesses a large empty interior (6.1 Å diameter) and spherical π bonding similar to C_{60} and was named "stannaspherene" for its near spherical symmetry and π bonding character.[207] The stannaspherene cage is highly stable and it has been shown to be able to trap all transition metal atoms, as well as rare earth atoms, to form a whole new class of stable endohedral clusters.[221]

C. Sn_{14}^- – Sn_{25}^-. The PES spectra of Sn_n^- in the size range of n = 14–25 became increasingly complicated, but were still well resolved at both 193 and 266 nm (Figures 5.1 and 5.2). Ion mobility measurements of Jarrold and co-workers[198,199] have suggested that tin clusters of medium size ($13 \leq n \leq 35$) adopt prolate geometries, which are similar to those found for Si_n and Ge_n. Theoretical calculations on Sn_n ($n \leq 20$)[201] showed that the structures of small tin clusters in the size range of n = 14–20 are similar to those of Si and Ge clusters, all exhibiting prolate shapes. The PES spectra of Sn_n^- in the size range of n =

14–25 display some similarity to those of Si_n^-, providing additional support for their structural similarities.

In this size range, the PES spectra for several clusters, namely, Sn_{13}^-, Sn_{17}^-, Sn_{19}^- and Sn_{22}^-, showed evidence of possible isomeric contributions. In the 266 nm spectrum of Sn_{13}^- (Figure 6.2), the second weak peak around 3.2 eV (labeled "*"), which was not resolved in the 193 nm spectrum, was likely due to an isomer. Similarly, a weak feature (*) was also resolved in the energy gap region in the 266 nm spectrum of Sn_{17}^- (Figure 6.2) and in both the 193 and 266 nm spectra of Sn_{19}^- and Sn_{22}^-. For Sn_{19}^- and Sn_{22}^-, this feature was fairly intense and in the 266 nm spectrum of Sn_{19}^- the second feature was even more intense than the first feature, suggesting the existence of two nearly degenerate isomers. The current data on the Sn_n^- clusters in the size range of n = 14–25 are sufficiently well reserved and can be used to compare with more detailed theoretical calculations to elucidate the structures of tin clusters in the medium size range.

D. Sn_{26}^- – Sn_{45}^-. For Sn_n^- clusters with $n > 25$, the PES spectra became more congested and poorly resolved. In a number of cases, the existence of possible isomers ("*") was evident, further aggravating the problem. For many species in this size range, only the ground state transition was resolved for $n \leq 41$. For $n > 41$, no features were resolved and the PES spectra became essentially continuous. Ion mobility experiments by Jarrold and co-workers[198,199] suggest that tin clusters gradually rearrange towards near-spherical geometries in the size range of $n \sim 35$–65. Our PES spectra indicate that this structural transition may occur around Sn_{42}, since continuous spectra were suddenly observed beyond n = 42. The featureless PES spectra may result from the metallic-like behavior of the large tin clusters, as will be discussed below.

In the larger cluster size range, the spectrum of Sn_{29}^- was somewhat special with well resolved spectral features and an unusually large energy gap. The most surprising observation was the spectrum of Sn_{40}^-, which was well resolved in sharp contrast to the nearly continuous spectra in this size range. These observations suggested that Sn_{29}^- and Sn_{40}^- were likely to have relatively stable and high symmetry structures. The spectrum of Sn_{41}^- was also well resolved and displayed similarities to that of Sn_{40}^-, suggesting that the additional atom in Sn_{41}^- does not distort the Sn_{40}^- structure too much and providing strong evidence for the high stability of the Sn_{40}^- cluster.

E. EA and HOMO – LUMO Gap as a Function of Size: Semiconductor to Metal Transition. The EAs obtained for Sn_n from the current work are given in Table 6.1 and compared with previously reported values. For n = 4–8, our data are consistent with those by Moravec *et al*.,[218] but in the size range of n = 9–12, our data are much more accurate because Moravec *et al*. were only able to give a range of values. Kaya and co-workers[219] reported EAs for a large set of Sn_n clusters, but most of their EA values were underestimated because of the poor resolution and the hot band transitions that led to low binding energy tails. Their EAs were in general between 0.2–0.5 eV too low. For Sn_{12}, their EA was too low by 0.88 eV. Our EAs are plotted as a function of size in Figure 6.3a. Large size variations are observed for small clusters of $n \leq 12$. Distinct minima are seen in the EA vs. n curve at n = 4, 7, 17, 29, 36, and 40. Interestingly, these EA minima correspond to maxima in the HOMO–LUMO gaps (Figure 6.4), suggesting that the corresponding neutral clusters exhibit pronounced stability. In Figure 6.3b, we plotted the EAs as a function of $n^{-1/3}$, i.e., $1/r$, where r is the cluster radius and is proportional to $n^{1/3}$. It is seen that the EAs follow in general a straight line, which extrapolates to 4.4 eV

at infinite cluster size, very close to the bulk work function of tin (4.42 eV). The EAs for clusters above n = 42 fall on the straight line, suggesting that the large clusters can be described by the classical metallic droplet model.[224]

In Figure 6.4 we plotted the HOMO–HUMO gaps of Sn_n clusters as a function of size. All clusters up to n = 41 display a HOMO–LUMO gap, suggesting these clusters are semiconductor-like with a closed shell electronic configuration. The HOMO–LUMO gaps are strongly dependent on the cluster size. In addition to the unusually large gaps shown by Sn_4 and Sn_7, there are other pronounced maxima at n = 16–18, 22, 29, 36, and 40, which correspond to the EA minima, as mentioned above. The HOMO–HUMO gap disappeared precipitously for clusters with $n \geq 42$, suggesting that the larger clusters are metallic-like. The semiconductor to metallic transition at n = 42 is also accompanied by the abrupt change in the PES spectral pattern and the EA vs. $1/r$ curve (Figure 6.3b), which shows that the EAs of clusters above n = 42 can be described by the metallic droplet model.[224]

6.4 Conclusion

A photoelectron spectroscopy study was carried out for Sn_n^- (n = 4 – 45) clusters at two detachment photon energies, 193 and 266 nm, under well controlled experimental conditions to produce relatively cold cluster anions. Well resolved PES spectra were obtained for small clusters with n = 4–25 and surprisingly for two large clusters, Sn_{29}^- and Sn_{40}^-. The well resolved spectra can be used to compare with future theoretical calculations to elucidate the detailed structures of the tin clusters. The PES spectra of very small Sn_n^- clusters (n = 4–13) were compared with those of Si_n^- and Ge_n^- clusters,

and both similarities and differences were observed, depending on the size. More accurate electron affinities for tin clusters were obtained and the evolution of their electronic structure was systematically investigated. A HOMO–LUMO gap was observed in the PES spectra for clusters with $n \leq 41$, indicating the semiconductor nature of small tin clusters. A semiconductor-to-metallic transition was observed at $n = 42$, beyond which no energy gaps were observed and the PES spectra became featureless and continuous.

CHAPTER SEVEN

DISCOVERY OF STANNASPHERENE AND PLUMBASPHERENE

7.1 Sn_{12}^-: Stannashperene

7.1.1 Introduction

Different from its lighter congeners, silicon and germanium which are semiconductors, the normal allotrope of tin under ambient conditions (β-Sn) is a metal with a body-centered tetragonal lattice, but it also has a small band gap semiconducting phase (α-Sn) with a diamond lattice similar to Si and Ge that is stable at low temperatures.[208] Prior experimental[173,198,200,209,211] and theoretical[201,203,205,216] studies suggest that small tin clusters possess similar structures to those of Si and Ge. An interesting experimental observation was that small tin clusters exhibit melting temperatures exceeding that of the bulk,[200] consistent with the notion that small tin clusters have similar bonding configurations as those of the semiconductor Si and Ge clusters. Previous PES experiments[217-219] also suggested that the spectra of small Sn_n^- clusters are similar to those of the corresponding Ge_n^- clusters. However, these PES experiments were all done at low photon energies (below 4.661 eV) and under relatively low resolution. During our photoelectron spectroscopy (PES) experiments (using a photon energy of 6.424 eV) aimed at understanding the semiconductor to metal transition in tin clusters (see chapter six), the spectrum of Sn_{12}^- was observed to be remarkably simple and totally different from the corresponding Ge_{12}^- cluster, suggesting that Sn_{12}^- is a unique and highly symmetric cluster.

Structural optimization starting from an icosahedral (I_h) cluster led to a slightly distorted cage with C_{5v} symmetry. However, adding an electron to Sn_{12}^- resulted in a stable closed-shell I_h-Sn_{12}^{2-} cluster, which was synthesized in the form of KSn_{12}^- ($K^+[Sn_{12}^{2-}]$) with a similar PES spectrum as Sn_{12}^-. The I_h-Sn_{12}^{2-} cage is shown to be bonded by four delocalized radial π bonds and nine delocalized on-sphere tangential σ bonds from the 5p orbitals of the Sn atoms, whereas the $5s^2$ electrons remain largely localized and nonbonding. The bonding pattern in Sn_{12}^{2-} is similar to the well-known $B_{12}H_{12}^{2-}$ cage, with the twelve $5s^2$ localized electron pairs replacing the twelve B-H bonds. The Sn_{12}^{2-} cage has a diameter of 6.1 Å and can host most transition metal atoms in the periodic table.

7.1.2 Results and Discussion

We have obtained well resolved PES spectra of size-selected Sn_n^- clusters with high photon energies (up to 6.424 eV or 193 nm) and under well controlled experimental conditions (see chapter six). In the size range of n<20, we indeed observed that the PES spectra of Sn_n^- are similar to those of the corresponding Ge_n^- with the exception of Sn_{12}^- (Figure 6.5). Whereas the spectrum of Ge_{12}^- is rather congested with numerous poorly resolved features, and that of Sn_{12}^- is remarkably simple and well structured (Figure 6.5). Four bands were resolved in the binding energy range from 3 to 4 eV, followed by a large gap and two well resolved bands around 5 eV. The lowest energy band yielded an adiabatic detachment energy, i.e., the electron affinity of neutral Sn_{12}, to be 3.23 ± 0.05 eV and a vertical detachment energy (VDE) of 3.34 ± 0.03 eV. Although low symmetry structures similar to Ge_{12} have been proposed for Sn_{12}, the relatively simple and

characteristic PES spectrum of Sn_{12}^- immediately suggested that it should possess a high symmetry structure different from that of Ge_{12}^-.

In pondering the possible high symmetry structures for Sn_{12}^-, my collaborators started from the highest symmetry possible for a twelve-atom cluster, the icosahedral cage. However, the Jahn-Teller effect led to a slightly lower symmetry C_{5v} ($^2A_1$) species (Figure 7.2a), which is only slightly distorted from the I_h structure mainly by the depression of one apex atom. The computed first VDE (3.27 eV) of the C_{5v} Sn_{12}^- is in excellent agreement with the experimental value of 3.34 eV. By adding one electron to Sn_{12}^-, we found that the resulting Sn_{12}^{2-} species is a highly stable I_h cage with a closed electron shell (Figure 7.2b). Several other low symmetry structures, including those suggested for Ge_{12}, have also been calculated for Sn_{12}^{2-}, but they are all much higher in energy (Figure 7.3). We were able to make Sn_{12}^{2-} in the form of KSn_{12}^- ($K^+[Sn_{12}^{2-}]$) experimentally by laser vaporization of a tin target containing ~15% K. The photoelectron spectrum of KSn_{12}^- (Figure 7.1b) is very similar to that of Sn_{12}^-, suggesting that the Sn_{12}^{2-} motif is not distorted greatly due to the presence of K^+. Our calculations showed that the K^+ counter ion is outside the Sn_{12}^{2-} cage with a C_{3v} ($^1A_1$) symmetry (Figure 7.2c). Indeed, only relatively small structural perturbations were observed in the Sn_{12}^{2-} cage due to the K^+ coordination. The isomer with K^+ inside the Sn_{12}^{2-} cage is much higher in energy by 3.4 eV because of the large size of the K^+ ion, which expands the cage diameter from 6.07 Å (Figure 7.2b) to ~6.45 Å.

To help understand the stability of the I_h-Sn_{12}^{2-} cage, we analyzed its valence molecular orbitals. Sn has a valence electron configuration of $5s^25p^2$. We found that because of the large energy separation between the 5s and 5p shells there is little s-p

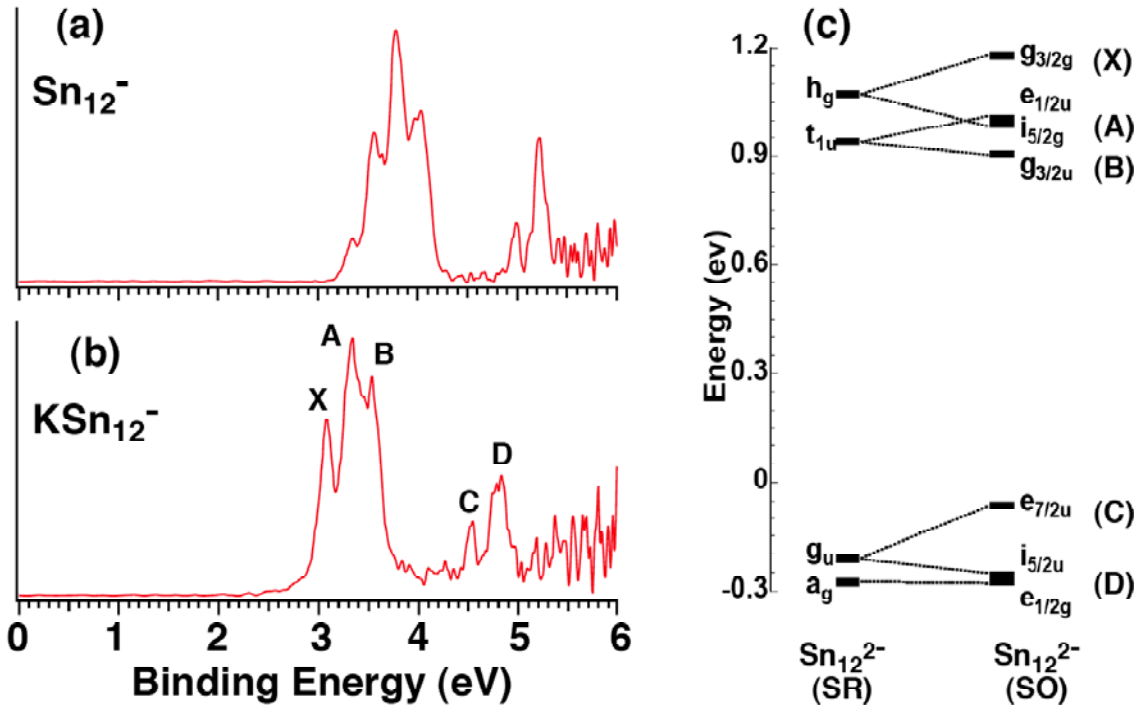

Figure 7.1 Photoelectron spectra of (a) Sn_{12}^- and (b) KSn_{12}^- at 193 nm (6.424 eV). (c) Scalar relativistic (SR) energy levels of the 5p-based valence molecular orbitals of the I_h Sn_{12}^{2-} and the correlation to the spin-orbit (SO) coupled levels of I_h* Sn_{12}^{2-}, where the asterisk indicates the double-group symmetry.

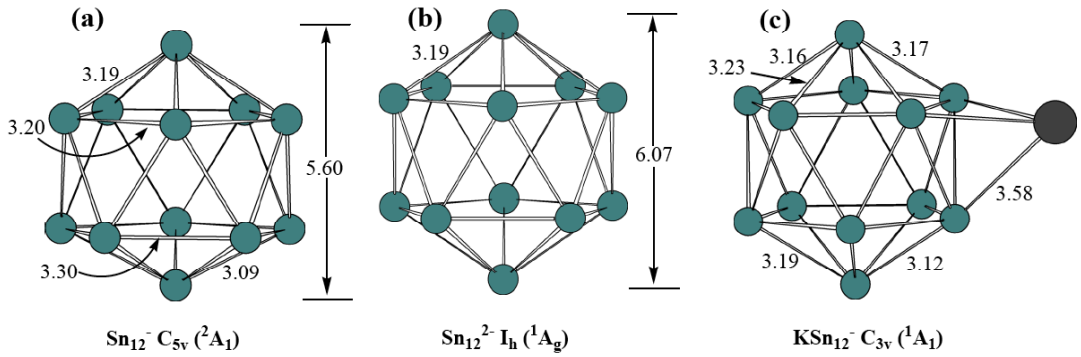

Figure 7.2. Optimized structures. (a) Sn_{12}^-. (b) Sn_{12}^{2-}. (c) KSn_{12}^-. The bond distances and cage diameters are in Å.

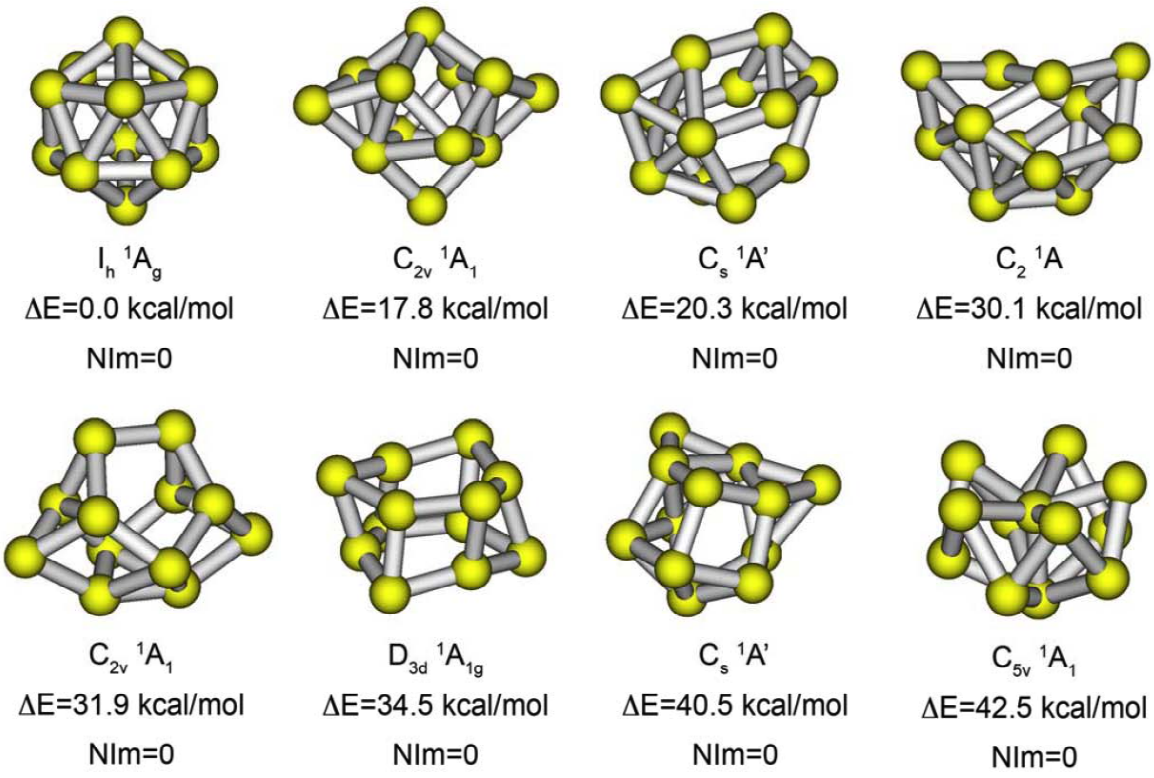

Figure 7.3 Alternative structures of Sn_{12}^{2-}. The energies are relative to the I_h cage. All structures are local minima (NIm = 0) and were calculated using Gaussion 03 at the B3LYP/3-21G level of theory.

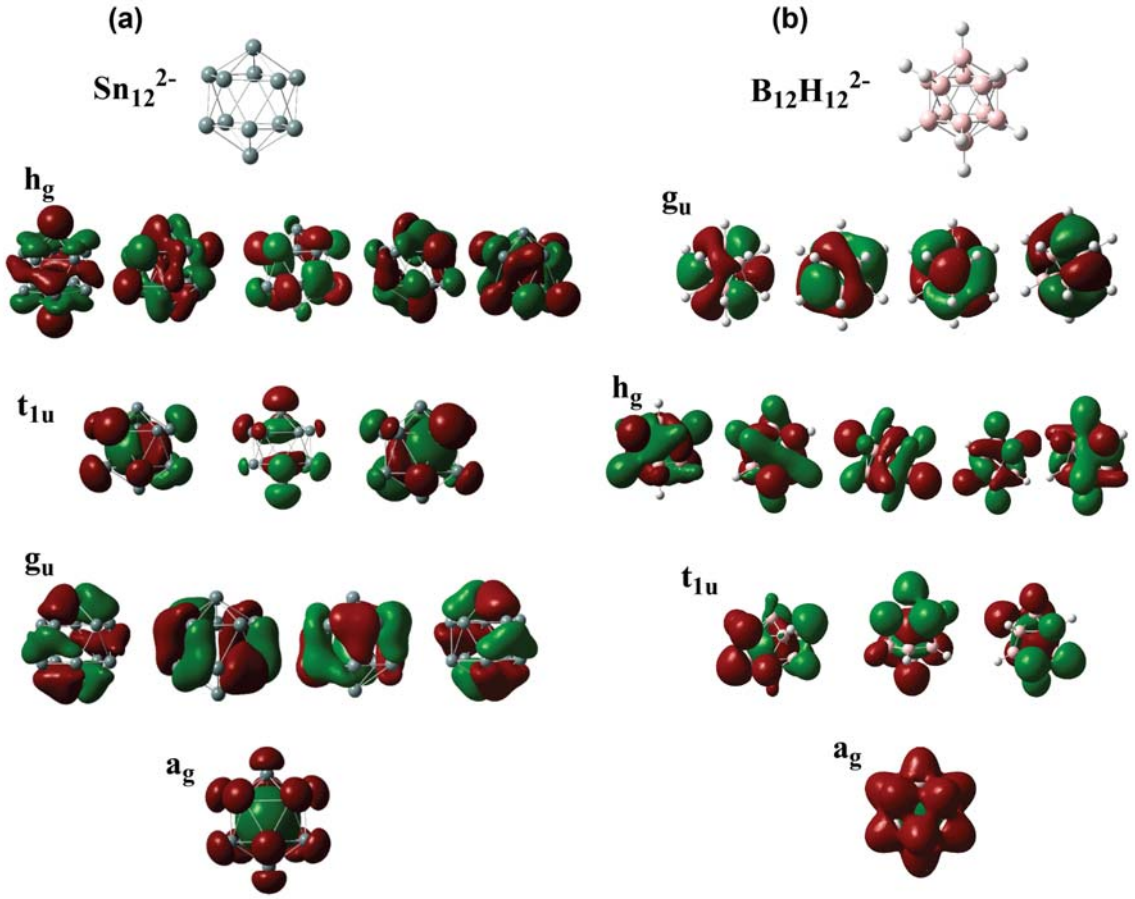

Figure 7.4 Comparison of the valence molecular orbitals of (a) Sn_{12}^{2-} and (b) $B_{12}H_{12}^{2-}$.

hybridization in Sn_{12}^{2-}. The $5s^2$ electron pair is largely localized on each Sn atom, leaving only the two 5p electrons responsible for the bonding on the Sn_{12}^{2-} cage. Figure 7.1c shows the valence molecular orbital diagram at the scalar relativistic (SR) and spin-orbit (SO) coupled levels. It is shown that the MO levels of Sn_{12}^{2-} with SO effect are in excellent agreement with the PES spectral pattern of $K^+[Sn_{12}^{2-}]$: the observed spectral features (X, A, B, C, D) are labeled in Figure 7.1c next to the SO-levels.

Among the thirteen valence orbitals, four are delocalized radial π bonding orbitals (a_g and t_{1u}) formed from the radial p_z atomic orbitals. The remaining nine orbitals (g_u and h_g) are delocalized in-sphere σ bonding orbitals from the tangential p_x and p_y atomic orbitals. The bonding pattern in Sn_{12}^{2-} is remarkably similar to that in the famous $B_{12}H_{12}^{2-}$ molecule (Figure 7.4), which was first predicted to be a stable molecule by molecular orbital theory[225] and subsequently synthesized.[226] The B_{12} cage in $B_{12}H_{12}^{2-}$ is also bonded similarly by four delocalized radial π bonding orbitals and nine in-sphere delocalized σ orbitals with 12 localized B-H bonds, which are equivalent to the $5s^2$ electrons in the Sn_{12}^{2-} cage. Because of the delocalized π bonding in Sn_{12}^{2-} and its spherical symmetry, a name, stannaspherene, is suggested for this highly stable and symmetric species.

Cage structures involving Sn are known in inorganic complexes and the Zintl phases.[227,228] However, the I_h-Sn_{12}^{2-} empty cage is not known before. The high stability of this cluster suggests that it may be synthesized in the solid state using suitable ligands or counter ions. More excitingly, the Sn_{12}^{2-} cage has a diameter of ~6.1 Å, only slightly smaller than that of C_{60}, and can host an atom inside much like the endohedral fullerenes. Indeed, theoretical calculations have shown that $Cd@Sn_{12}$ is a stable I_h cage[229] and

several endohedral Pb_{12} clusters, such as $Al@Pb_{12}^{+}$ and $Pt@Pb_{12}^{2-}$, have been synthesized.[230-232] A recent report revealed stable Cu-Sn cluster compositions from high-temperature annealing and suggested core-shell cage type of structures.[233] The stability of the stannaspherene and its large internal volume suggest that Sn_{12}^{2-} may trap many different types of endohedral atoms. Experimental and theoretical results[221] suggest that most transition metal atoms can be hosted inside the Sn_{12}^{2-} cage, yielding a large class of new endohedral stannaspherenes.

7.1.3 Conclusion

During photoelectron spectroscopy experiments aimed at understanding the semiconductor-to-metal transition in tin clusters, the spectrum of Sn_{12}^{-} was observed to be remarkably simple and different from that of Ge_{12}^{-}, suggesting that Sn_{12}^{-} is a unique and highly symmetric cluster. It was found to possess a slightly distorted cage structure with C_{5v} symmetry. However, adding an electron to Sn_{12}^{-} resulted in an I_h-Sn_{12}^{2-} cluster, which was synthesized as $K^{+}[Sn_{12}^{2-}]$. The I_h-Sn_{12}^{2-} cage is shown to be bonded by four delocalized radial π bonds and nine delocalized on-sphere tangential σ bonds from the 5p orbitals of the Sn atoms, whereas the $5s^2$ electrons remain largely localized and nonbonding. The bonding pattern in Sn_{12}^{2-} is similar to the well-known $B_{12}H_{12}^{2-}$ cage. The Sn_{12}^{2-} cage, for which a name "stannaspherene" is coined, has a diameter of 6.1 Å, suggesting it can trap a variety of atoms to for endohedral stannaspherenes.

7.2 Endohedral Stannaspherenes ($M@Sn_{12}^{-}$): A Rich Class of Stable Molecular Cage Clusters

7.2.1 Introduction

Since the discovery and bulk synthesis of fullerenes,[11,234] there have been great expectations in cluster science to uncover other stable atomic clusters that may be used as building blocks for cluster-assembled nanomaterials. The heavy congeners of C in group 14 are not known to form fullerene-like *empty* cage structures until very recently when it is discovered serendipitously that a 12-atom Sn cluster forms a highly stable *empty* cage (Sn_{12}^{2-} — stannaspherene)[207] with a large inner diameter (6.1 Å), only slightly smaller than that of C_{60}. Although polyhedral cages are common in inorganic compounds,[228,235] *empty* cage clusters with large internal volumes are rare.[236,237] Stannaspherene can be viewed as a real inorganic analog of the fullerenes because of its spherical π bonding,[207] similar to that in the $B_{12}H_{12}^{2-}$ cage molecule.[225,226] Several metal-encapsulated cage clusters from heavy group 14 elements are known,[229-231,233,238-245] but the metal-encapsulation was thought to be essential for the cage structure. Here we report that stannaspherene can trap an atom from any of the transition-metal series or the f-blocks in the periodic table, giving rise to a large class of new endohedral cage clusters. We have produced a selected set of $M@Sn_{12}^-$ (M = Ti, V, Cr, Fe, Co, Ni, Cu, Au, Pt, Nb, Ta, Hf, Y, Gd) using laser vaporization and characterized them using photoelectron spectroscopy. Both experimental and theoretical evidence shows that these clusters maintain perfect or pseudo-icosahedral symmetry with the central atom inducing very little distortion to the Sn_{12}^{2-} cage. The central atom in $M@Sn_{12}^-$ maintains its quasi-atomic nature analogous to that in the endohedral fullerenes[246,247], yielding a rich class of potential building blocks for new materials with tunable electronic, magnetic, or chemical properties.

7.2.2 Results and Discussion

Figure 7.5 displays the 193 nm photoelectron spectra of Sn_{12}^- doped with 3d transition metals and a few selected 4d and 5d dopants. More spectra with other dopants including rare earth elements are given in Figure 7.6. All the spectra are well resolved with numerous distinct electronic transitions. In general the spectra of $M@Sn_{12}^-$ become more complicated as one moves from Cu to the left of the transition series due to the open d shell and the relative orbital-energy variation of the 3d electrons, which are core-like in Cu, but become frontier levels in the early transition metals. Remarkably, there is a characteristic doublet feature around 5 eV (labeled g_u in Figure 7.5), which exist in all the spectra with little variation among the different doped $M@Sn_{12}^-$ species.

Previous section has shown that the stannaspherene Sn_{12}^{2-} possesses an inner diameter of 6.1 Å (Figure 7.2),[207] large enough to trap any transition metal, f-block atoms or certain main group atoms. The doublet spectral features around 5 eV in all the $M@Sn_{12}^-$ clusters bear considerable resemblance to similar spectral features primarily derived from the on-sphere g_u σ orbitals in stannaspherene (Figure 7.8), suggesting that all the doped $M@Sn_{12}^-$ clusters possess similar structures and that the Sn_{12} cage is intact in $M@Sn_{12}^-$. To confirm the endohedral nature of $M@Sn_{12}^-$ and understand their electronic structure, my collaborators performed extensive theoretical calculations. Here we focus on the $CuSn_{12}^-$ system (Figure 7.7). The theoretical results indicate that indeed the endohedral $Cu@Sn_{12}^-$ is overwhelmingly more stable than any of the exohedral isomers. The calculated adiabatic and vertical detachment energies and simulated photoelectron spectrum of the endohedral $Cu@Sn_{12}^-$ with spin-orbit coupling are in

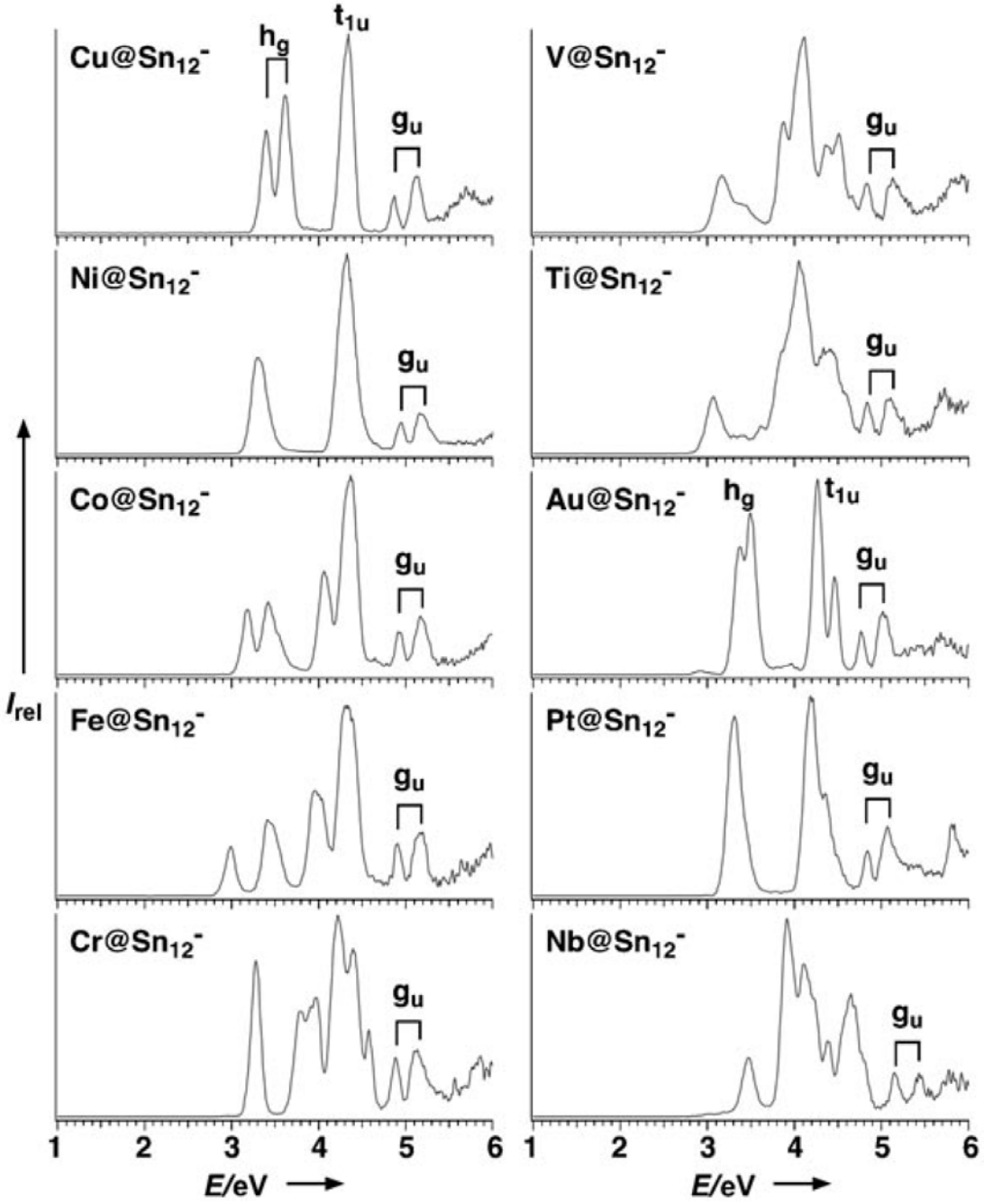

Figure 7.5 Photoelectron spectra of $M@Sn_{12}^-$ (M = Cu, Ni, Co, Fe, Cr, V, Ti, Au, Pt, and Nb) at 193 nm (6.424 eV).

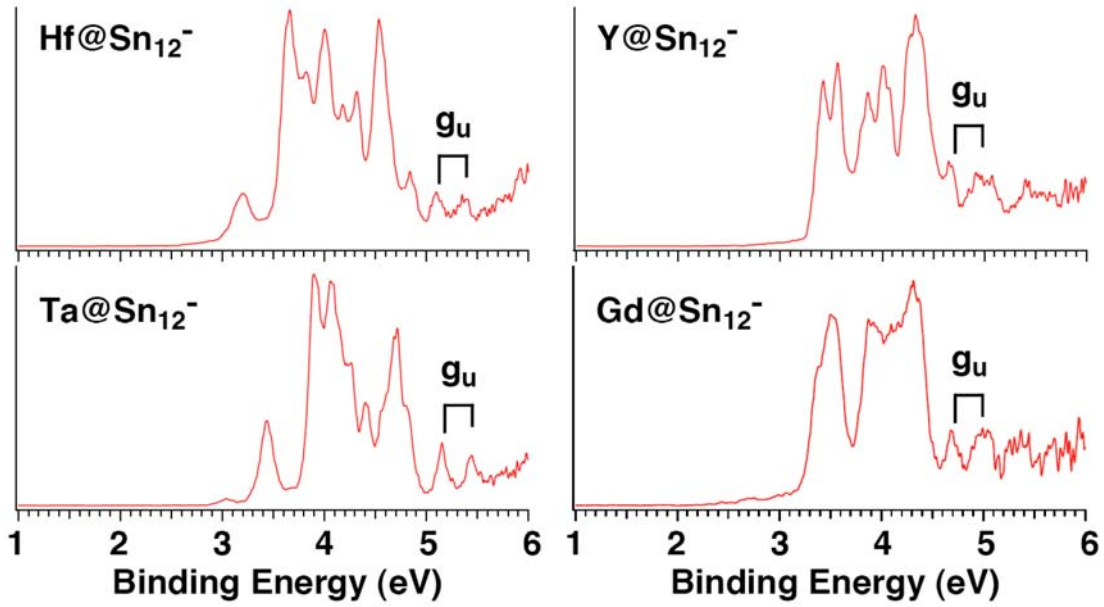

Figure 7.6 Photoelectron spectra of more endohedral stannaspherenes $M@Sn_{12}^-$ (M = Hf, Ta, Y,and Gd).

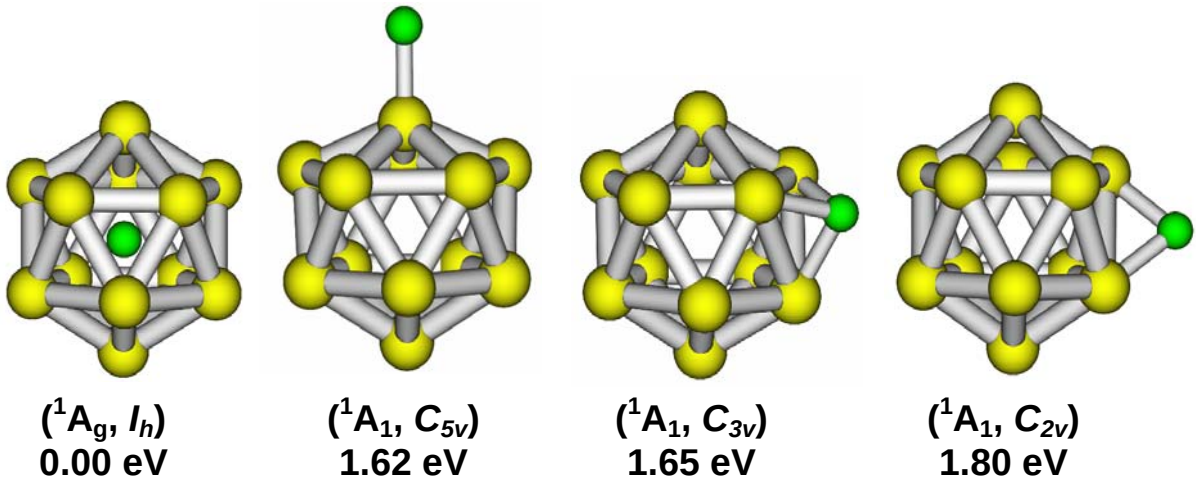

Figure 7.7 Optimized structures of the global minimum endohedral $Cu@Sn_{12}^-$ cluster and several exohedral $CuSn_{12}^-$ and their relative energies.

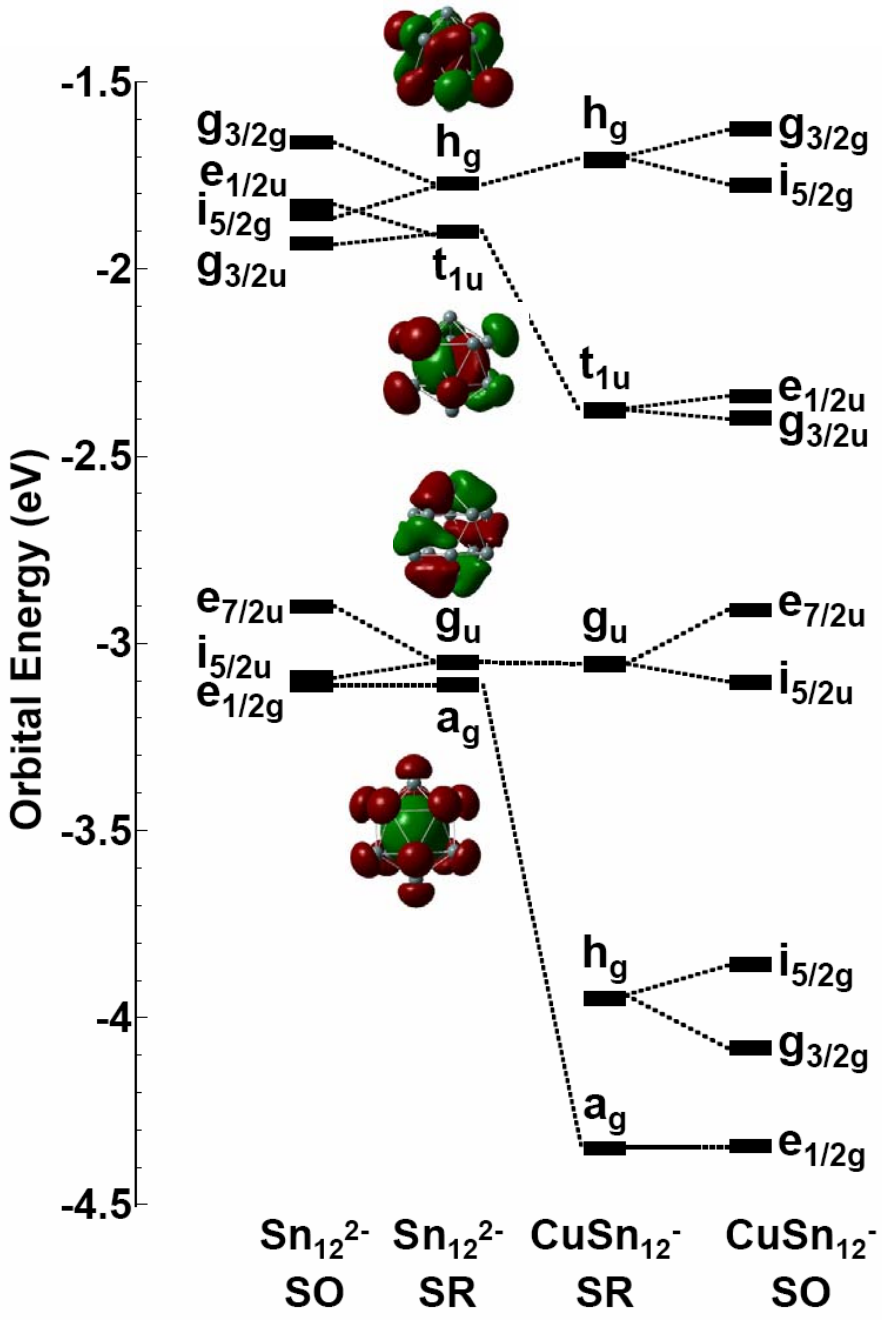

Figure 7.8 Correlation diagram between the scalar relativistic (SR) valence levels of Sn_{12}^{2-} and $Cu@Sn_{12}^{-}$ and their spin-orbit split levels. The SR molecular orbital contour surfaces of Sn_{12}^{2-} are also shown. The lower h_g orbital in $Cu@Sn_{12}^{-}$ is the Cu $3d^{10}$ shell.

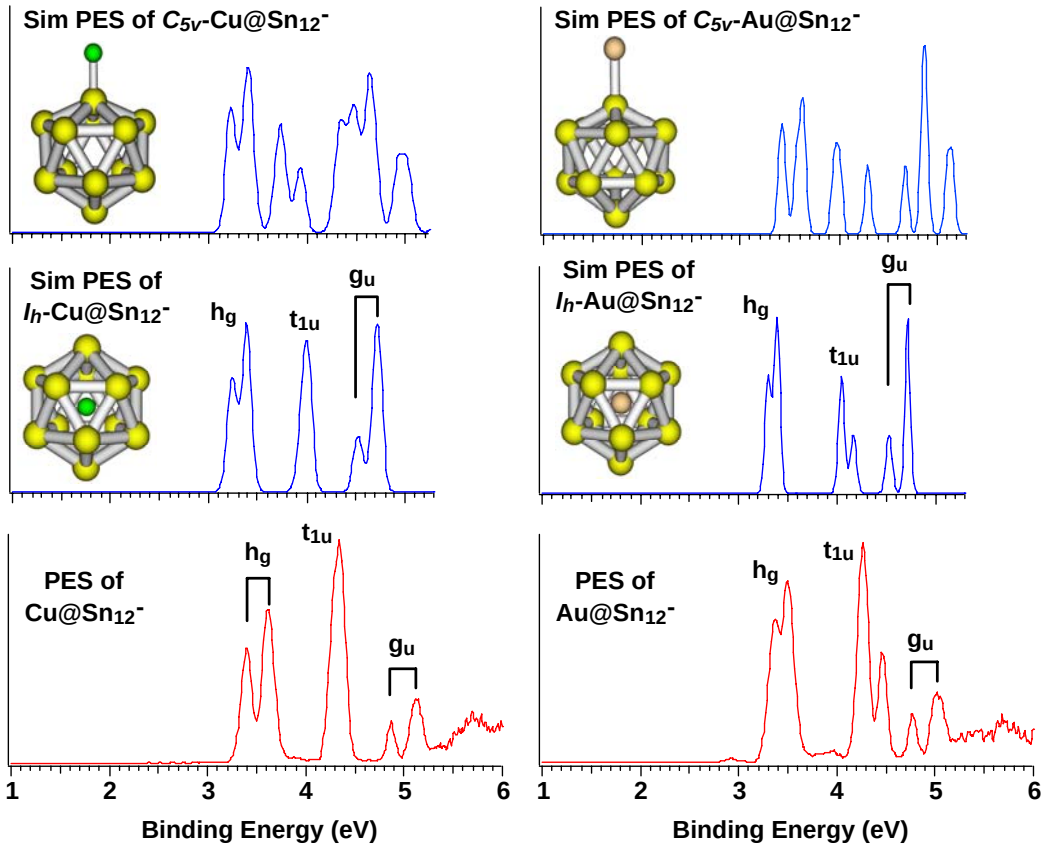

Figure 7.9 Comparison of the simulated spectra (blue) of the endohedral I_h $Cu@Sn_{12}^-$ and $Au@Sn_{12}^-$, and the exohedral C_{5v} $CuSn_{12}^-$ and $AuSn_{12}^-$ to the respective experimental photoelectron spectra (red). Note the dramatic difference between the simulated spectra for the global minima I_h endohedral cages and the C_{5v} exohedral isomers. The simulated spectra were obtained simply by fitting calculated spin-orbital energies with gaussion functions, whereas the intensities were not calculated explicitly.

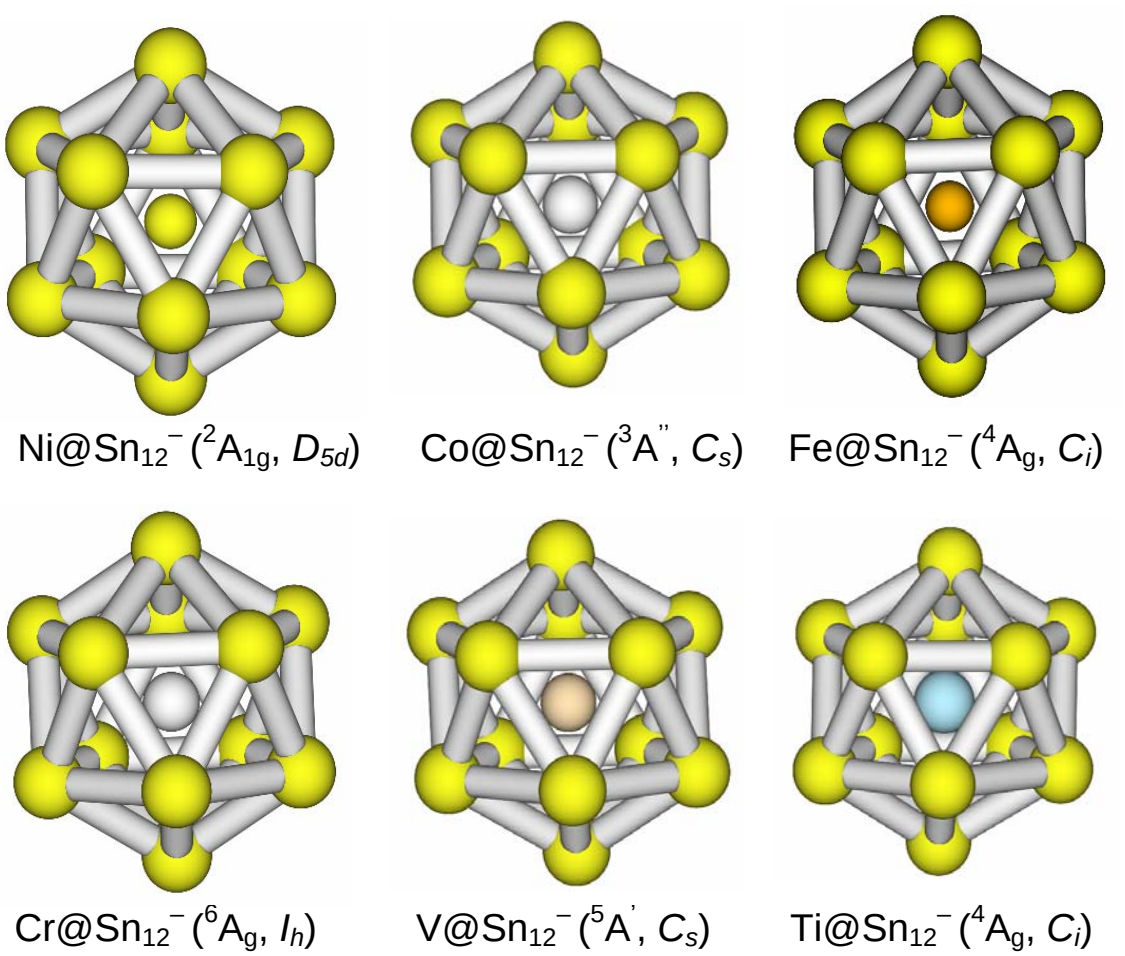

Figure 7.10 Optimized structures of the endohedral stannaspherenes $M@Sn_{12}^-$ with open shell 3*d* endohedral atoms (M = Ni, Co, Fe, Cr, V, and Ti).

Table 7.1 The first adiabatic (ADE) and vertical (VDE) electron detachment energies for $M@Sn_{12}^-$. The ADE also represents the electron affinity of the neutral $M@Sn_{12}$ clusters. All energies are in eV.

	ADE	VDE
$Ti@Sn_{12}^-$	2.95 ± 0.05	3.05 ± 0.04
$V@Sn_{12}^-$	3.03 ± 0.04	3.17 ± 0.03
$Cr@Sn_{12}^-$	3.21 ± 0.03	3.26 ± 0.03
$Fe@Sn_{12}^-$	2.92 ± 0.03	2.98 ± 0.02
$Co@Sn_{12}^-$	3.13 ± 0.03	3.19 ± 0.03
$Ni@Sn_{12}^-$	3.21 ± 0.03	3.26 ± 0.03
$Cu@Sn_{12}^-$	3.33 ± 0.03	3.40 ± 0.02
$Au@Sn_{12}^-$	3.32 ± 0.03	3.37 ± 0.02
$Pt@Sn_{12}^-$	3.24 ± 0.03	3.31 ±0.02
$Nb@Sn_{12}^-$	3.38 ± 0.06	3.47 ± 0.05

excellent agreement with the experimental data (Figure 5.9), confirming unequivocally its stability and structure.

$Cu@Sn_{12}^-$ is a perfect icosahedral (I_h) cluster (Figure 7.9) with a Sn-Sn distance (3.21 Å) very close to that in stannaspherene (3.19 Å), suggesting moderate interactions between the central Cu atom and the Sn_{12} cage. The Cu-Sn distance (3.05 Å) in $Cu@Sn_{12}^-$ is considerably longer than the Cu-Sn distance (2.6 Å) in diatomic CuSn,[248] consistent with the relatively weak covalent interactions between Cu and the Sn_{12} cage in $Cu@Sn_{12}^-$. In fact, $Cu@Sn_{12}^-$ can be described as a Cu^+ ion trapped inside stannaspherene, $Cu^+@Sn_{12}^{2-}$, similar to the charge transfer complexes formed in endohedral fullerenes.[222,246,247] Figure 7.8 compares the scalar relativistic (SR) and spin-orbit (SO) coupled energy levels of the valence molecular orbitals (MO) of $Cu@Sn_{12}^-$ and those of stannaspherene. As we showed previously, stannaspherene is bonded by the Sn 5p electrons only, which transform into h_g, t_{1u}, g_u, and a_g valence MOs (Figure 7.8), whereas the Sn 5s electrons are mainly non-bonding lone pairs. Upon insertion of Cu^+ into Sn_{12}^{2-}, the radial bonding MOs (a_g and t_{1u}) are stabilized because they are symmetry-allowed to interact with the d orbitals of the dopant, whereas the purely tangential g_u MO is not affected at all because of symmetry restrictions. The h_g HOMO, which has a small amount of mixing from the radial orbitals is slightly destabilized. The filled $3d^{10}$ shell of Cu transforms into an h_g orbital in $Cu^+@Sn_{12}^{2-}$, maintaining its fivefold degeneracy. When spin-orbit coupling is taken into account, each degenerate orbital is split into two levels. The SO coupling in the corresponding MOs in $Cu@Sn_{12}^-$ and Sn_{12}^{2-} are very similar (Figure 7.8). The spin-orbit split MO pattern of $Cu@Sn_{12}^-$ is in excellent agreement with the observed spectral pattern, as labeled in the spectrum of $Cu@Sn_{12}^-$

(Figure 7.5). The Cu $3d^{10}$ levels and the a_g orbitals have too high binding energies to be ionized at the photon energy used. The spin-orbit splittings in the h_g HOMO and the g_u orbitals are large enough to be clearly resolved experimentally. The spectrum of $Au@Sn_{12}^-$ is almost identical to that of $Cu@Sn_{12}^-$ except that the spin-orbit splitting in the t_{1u} orbital is enhanced in $Au@Sn_{12}^-$, which is also born out from our calculations (Figure 7.9), confirming the endohedral nature of $Au@Sn_{12}^-$. The first ADE and VDE of $Cu@Sn_{12}^-$ and $Au@Sn_{12}^-$ are identical within our experimental uncertainties (Table 7.1).

Although the $Cu@Sn_{12}^-$ cluster possesses perfect icosahedral symmetry, our calculations show that the other endohedral $M@Sn_{12}^-$ clusters with open d shells on the central dopant except $Cr@Sn_{12}^-$ (Figure 7.10) have slightly distorted structures. However, the structural distortions are very small and the actual cage structure of all the $M@Sn_{12}^-$ clusters are very close to the ideal I_h symmetry. The nearly identical doublet features around 5 eV in all the spectra of the $M@Sn_{12}^-$ clusters are due to the same g_u orbitals (Figure 7.5), which are purely on-sphere σ orbitals (Figure 7.8) and are not expected to be affected by the central atom. This spectral characteristic provides a fingerprint for the endohedral cage structures for all the $M@Sn_{12}^-$ clusters and reflects the robustness of the stannaspherene cage. The more complicated spectral features in the lower binding energy range in the open d-shell $M@Sn_{12}^-$ clusters are expected. For the late transition metal dopants (Ni, Fe, Co), our calculations show that the 3d electrons are still significantly lower in energy and cannot be detached at 193 nm. The extra spectral features in $Co@Sn_{12}^-$ and $Fe@Sn_{12}^-$ are likely due to spin polarization of the h_g HOMO and the t_{1u} orbitals. For the early transition metal dopants (Cr, V, Ti), the 3d electrons have similar binding energies as the Sn-derived frontier h_g and t_{1u} orbitals, resulting in

much more complex spectral patterns due to direct detachment from the 3d valence levels in the low binding energy region (Figure 7.5). The 4d and 5d dopants behave similarly as the 3d dopants, resulting in similar photoelectron spectra for the corresponding endohedral stannaspherenes. Our photoelectron spectra suggest that the rare earth atoms also form endohedral stannaspherenes, judged by the g_u doublet spectral fingerprint in the spectra of $Y@Sn_{12}^-$ and $Gd@Sn_{12}^-$ (Figure 7.6) and confirmed by our theoretical calculations.

All the $M@Sn_{12}^-$ anionic species can be described as $[M^+@Sn_{12}^{2-}]$, whereas the neutral endohedral stannaspherenes ($M@Sn_{12}$) can be described as $[M^{2+}@Sn_{12}^{2-}]$. For the 3d dopants, all the endohedral stannaspherenes are magnetic with high spins, characteristic of the atomic 3d electrons ranging from $3d^2$ in $[Ti^{2+}@Sn_{12}^{2-}]$ to $3d^8$ in $[Ni^{2+}@Sn_{12}^{2-}]$, giving rise to a new class of cage clusters with tunable magnetic and optical properties. In contrast to the encapsulated Si or Ge clusters, where the dopants are critical to stabilize the cage structures,[229,238-244] the stability of $M@Sn_{12}$ derives from the intrinsic stability of stannaspherene itself, much like the endohedral fullerenes. Our study indicates that all the transition metal or f-block atoms can be trapped inside stannaspherene. This is quite advantageous relative to the endohedral fullerenes, which can only trap the alkali, alkali earth, or rare earth atoms while the chemically more interesting transition metal atoms do not form endohedral fullerenes.[222]

Ni or Pt encapsulated Pb_{12} icosahedral clusters, similar to $Ni@Sn_{12}^-$ or $Pt@Sn_{12}^-$, have been synthesized in solution and characterized in bulk.[231,245] Even though the doped Ni or Pt atom was thought to be essential for the cage compounds, we have evidence that Pb_{12}^{2-} is also a highly stable *empty* cage cluster (see next section)[220] similar to Sn_{12}^{2-}, both

of which are isoelectronic with the well-known borane cage molecule $B_{12}H_{12}^{2-}$.[225,226] Hence, the previously observed $Pt@Pb_{12}^{2-}$ and $Ni@Pb_{12}^{2-}$, as well as $Al@Pb_{12}^{+}$ cation $[Al^{3+}@Pb_{12}^{2-}]$,[230] should belong to a whole family of endohedral plumbaspherenes, similar to the endohedral stannaspherene family. Icosahedral $M@Au_{12}$ types of cage clusters have also been predicted[249] and observed experimentally.[250] However, similar to the metal-encapsulated Si or Ge clusters,[229,238-244] the dopant is critical for the cage structure of $M@Au_{12}$ because the bare Au_{12} cluster does not possess a cage structure.[16] If flexible bulk synthetic methods can be found for the vast number of endohedral stannaspherenes, we anticipate the creation of novel cluster-assembled materials with continuously tunable electronic, magnetic, or optical properties across the entire transition series or the f-block elements.

7.2.3 Conclusion

Experimental and theoretical evidence is reported that the icosahedral stannaspherene Sn_{12}^{2-} cage can trap an atom from any of the transition-metal series or the f-elements, giving rise to a myriad of stable endohedral clusters. A selected set of $M@Sn_{12}^{-}$ cluster has been created using laser vaporization and characterized by photoelectron spectroscopy. It is shown that these clusters maintain perfect or pseudo-icosahedral symmetry with the central metal atom inducing very little distortion to the stannaspherene cage. The doped atom in $M@Sn_{12}^{-}$ keeps its quasi-atomic nature with large magnetic moments. The endohedral stannaspherenes might thus be viewed as "superatoms", yielding potentially a rich class of new building blocks for cluster-assembled materials with tunable magnetic, electronic, and chemical properties.

7.3 Pb_{12}^{2-}: Plumbaspherene

7.3.1 Introduction

During recent photoelectron spectroscopy (PES) experiments aimed at understanding the semiconductor-to-metal transition in tin clusters, we found the spectra of Sn_{12}^- to be remarkably simple and totally different from the corresponding Ge_{12}^- cluster.[207] This observation led to the discovery of a C_{5v} cage structure for Sn_{12}^-, which is only slightly distorted from the icosahedral (I_h) symmetry as a result of the Jahn-Teller effect. However, adding an electron to Sn_{12}^- resulted in a highly stable and closed-shell I_h-Sn_{12}^{2-} cage cluster. Owing to the large 5p-5s energy separation, the I_h-Sn_{12}^{2-} cage was found to be bound primarily by the $5p^2$ electrons forming four radial π bonds and nine in-sphere σ bonds with the $5s^2$ electrons behaving like lone pairs. The Sn_{12}^{2-} cage was shown to be isoelectronic to the well-known $B_{12}H_{12}^{2-}$ molecule[225,226] with the $5s^2$ lone pairs replacing the localized B-H bonds, and was named "stannaspherene" for its π bonding characteristics and high symmetry. In this section, we report a similar study that the corresponding Pb_{12}^{2-} cluster also exists as a highly stable I_h cage, which has an even larger interior volume than stannaspherene and can host most transition metal atoms in the periodic table to form a new class of endohedral cage clusters.

7.3.2 Results and Discussion

Figure 7.11 displays the PES spectra of Pb_n^- (x = 11-13) at 193 nm. Clearly, the Pb_{12}^- spectrum is special relative to those of its neighbors, showing only four bands (X, A, B, C), whereas much more complex spectral features were observed for Pb_{11}^- and

Pb_{13}^-. This observation suggested that Pb_{12}^- should possess a relatively high symmetry structure. We also obtained the spectrum of Pb_{12}^- at 266 nm, which is compared to the 193 nm spectrum in Figure 7.12, as well as to the corresponding spectra of KPb_{12}^-. The 355 nm spectrum of Pb_{12}^- (not shown) can only access the first detachment feature (X) around 3.1 eV. At 266 nm, the A and B bands of Pb_{12}^- between 3.5 and 4 eV are resolved into at least five spectral features. The spectra of KPb_{12}^- are nearly identical to those of Pb_{12}^- (Figure 7.12), except that they are shifted to lower binding energies due to charge transfer from K to the Pb_{12} moiety, $K^+[Pb_{12}^{2-}]$. At 266 nm, the first band (X) of KPb_{12}^- at 2.7 eV is resolved into a doublet, whereas a shoulder on the lower binding energy side is resolved in the B band at ~3.6 eV. The weak continuous signals beyond 5 eV in the 193 nm spectra for both Pb_{12}^- and KPb_{12}^- are due to a combination of imperfect background subtraction and possible multi-electron processes (shake-up processes). The electron affinities of Pb_{12} and KPb_{12} are measured from the threshold feature to be 3.09 ± 0.03 and 2.71 ± 0.03 eV, respectively. The vertical detachment energies for the ground state transitions for Pb_{12}^- and KPb_{12}^- are measured to be 3.14 ± 0.03 and 2.77 ± 0.03 eV, respectively. The PES spectra of Pb_{12}^- and other small Pb_n^- clusters have been measured previously at lower spectral resolution and lower photon energies.[217,219] The current experiment yielded better resolved spectra, more accurate electron binding energies, and more spectral features to cover the valence spectral range.

Geometry optimization for Pb_{12}^- from a high symmetry icosahedral cage led to a Jahn-Teller distorted lower symmetry C_{5v} ($^2A_1$) species (Figure 7.13a), analogous to Sn_{12}^- (section 7.1).[207] The computed first vertical detachment energy (3.08 eV) of the C_{5v} Pb_{12}^-

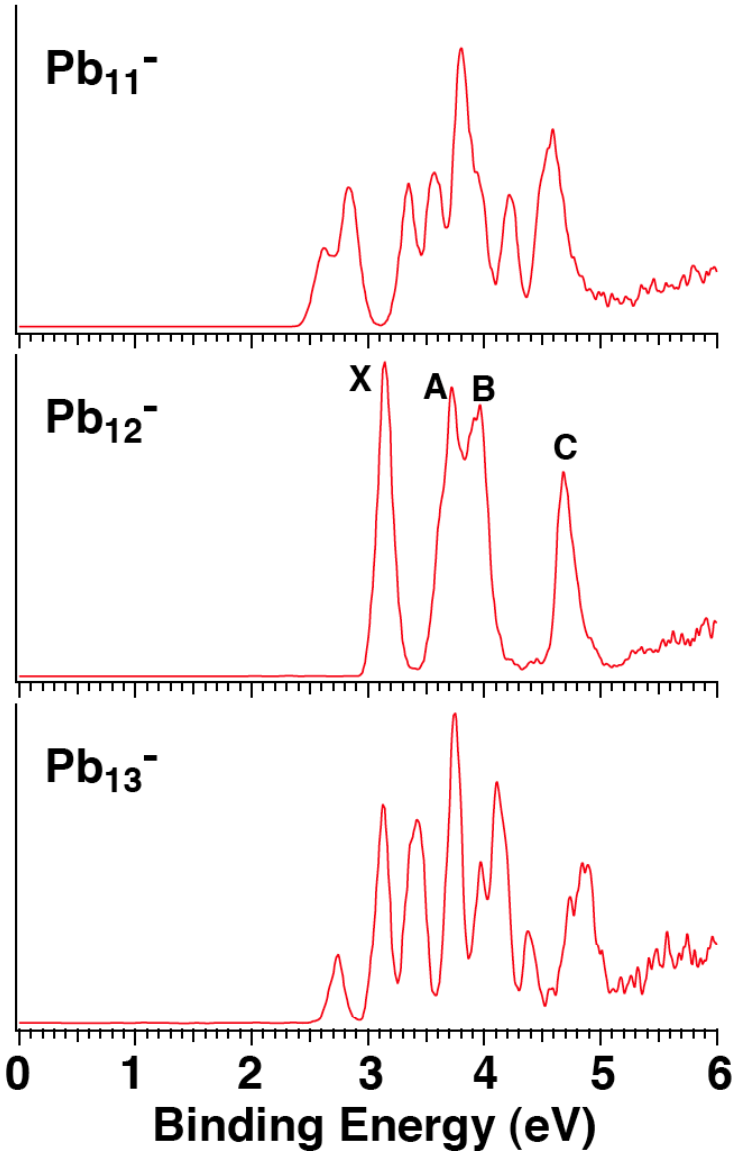

Figure 7.11 Photoelectron spectra of Pb_n^- (n = 11, 12, 13) at 193 nm (6.424 eV). Note the relatively simple spectral pattern of Pb_{12}^- with respect to those of Pb_{11}^- and Pb_{13}^-.

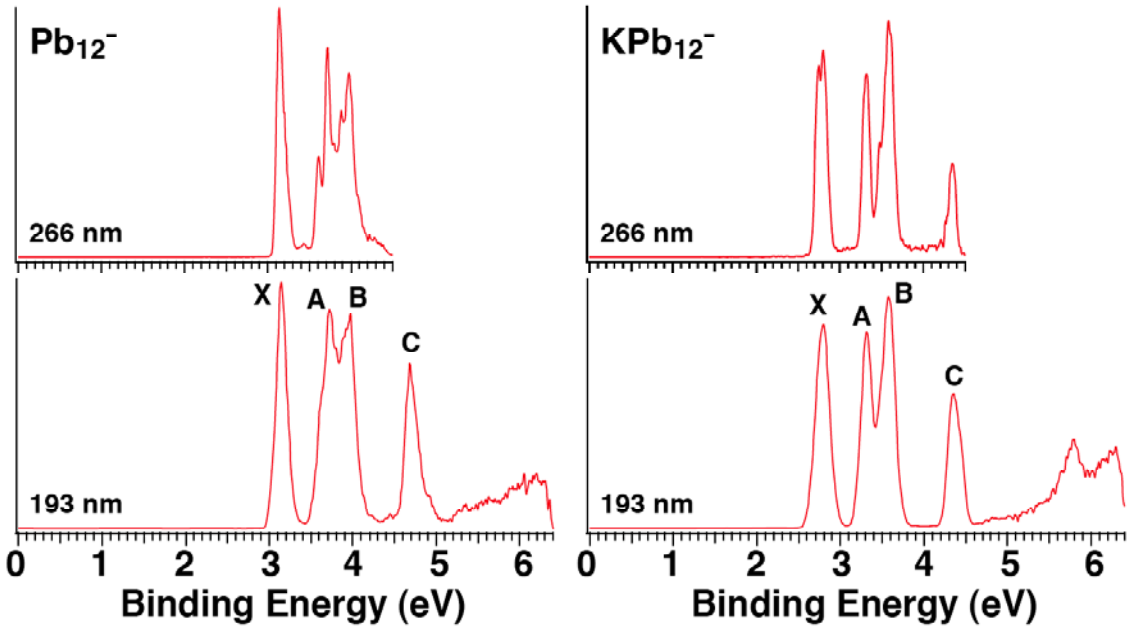

Figure 7.12 The photoelectron spectra of Pb_{12}^- at 266 and 193 nm compared to those of KPb_{12}^-.

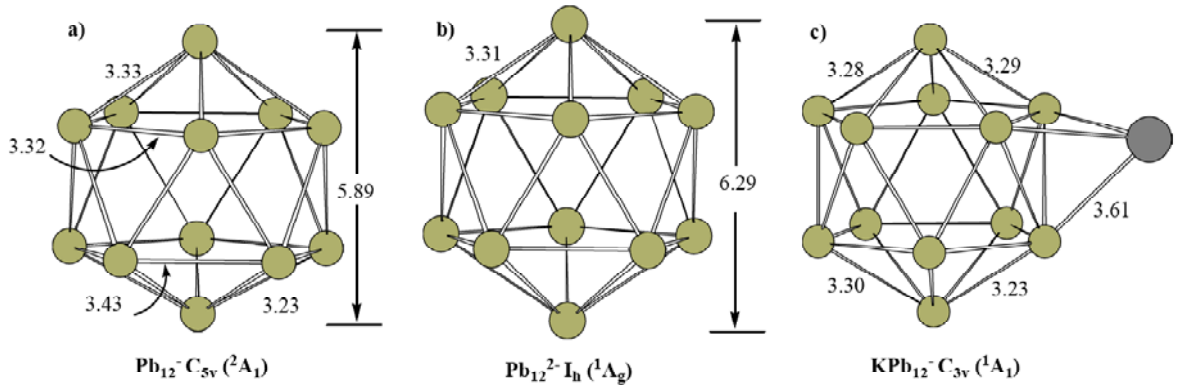

Figure 7.13 Optimized structures. (a) Pb_{12}^-. (b) Pb_{12}^{2-}. (c) KPb_{12}^-. The bond distances and cage diameters are in Å.

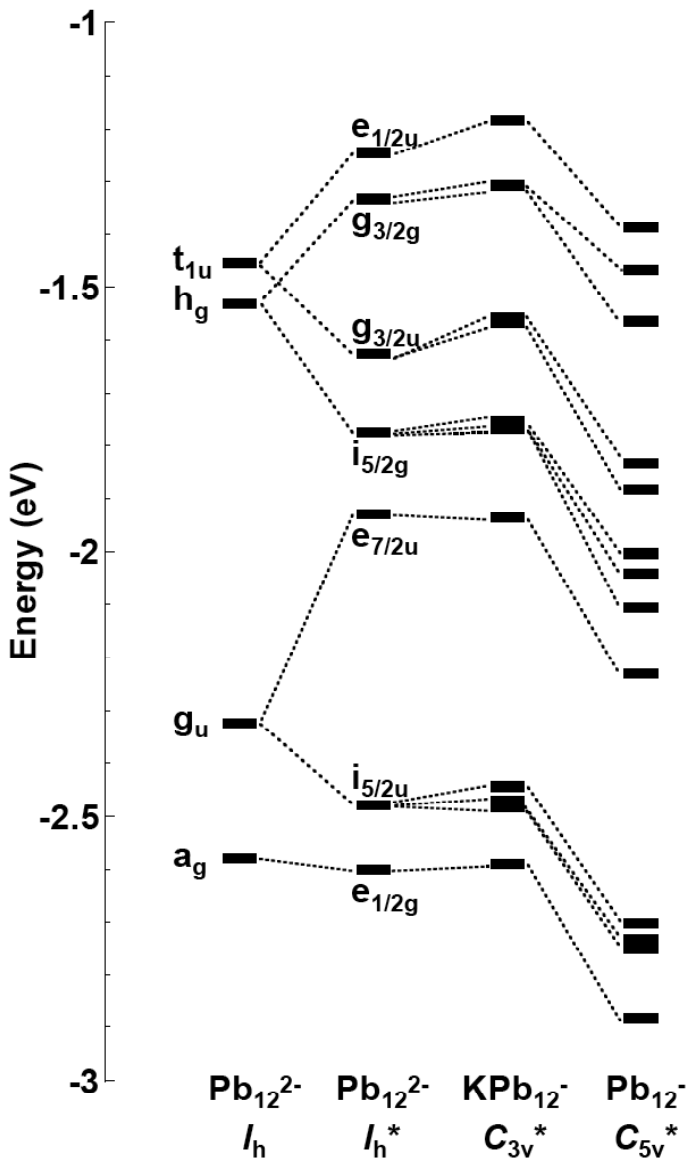

Figure 7.14 Scalar relativistic (SR) energy levels of the 6p-based valence molecular orbitals of the I_h Pb_{12}^{2-} and the correlation to the spin-orbit coupled levels of I_h^* Pb_{12}^{2-} and the lower symmetry C_{3v}^* $K^+[Pb_{12}^{2-}]$ and C_{5v}^* Pb_{12}^-, where the asterisk indicates the double-group symmetry. The 6s-based MOs are mainly localized on each atom and are separated from the bottom of the 6p band by more than 4 eV. The energy levels of Pb_{12}^{2-} are shifted down by 2.63 eV to compare with the monoanions.

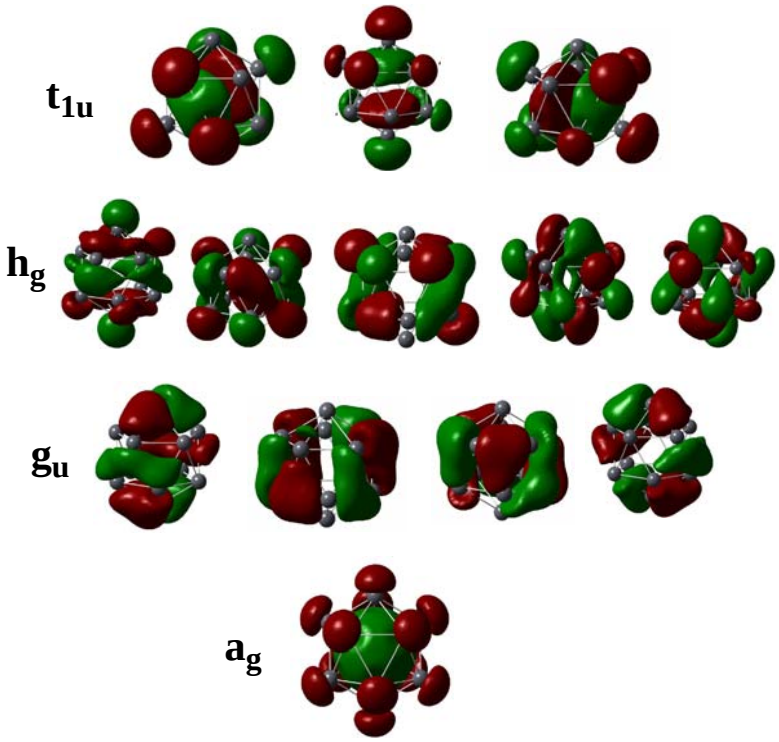

Figure 7.15 Pictures of the valence molecular orbitals of Pb_{12}^{2-}.

is in excellent agreement with the experimental value of 3.14 eV. Whereas ion mobility experiment suggests that Pb_n^+ clusters possess compact near-spherical morphologies,[199] several theoretical studies have given various structures for neutral Pb_{12}.[251-254] We note that the two most recent works by Wang *et al*.[253] and Rajesh *et al*.[254] suggested distorted cage structures for Pb_{12}. However, we find that the doubly charged Pb_{12}^{2-} species is a highly stable and perfect I_h cage with a closed electron shell (Figure 7.13b). We were able to synthesize Pb_{12}^{2-} stabilized by a counter ion in KPb_{12}^- ($K^+[Pb_{12}^{2-}]$), whose photoelectron spectra are compared to those of Pb_{12}^- in Figure 7.12. The similar photoelectron spectra between KPb_{12}^- and Pb_{12}^- suggests that the Pb_{12}^{2-} cage upon K^+ coordination is probably not distorted too much from the ideal I_h symmetry, which is born out from our calculated structure (Figure 7.13c). Our calculations showed that the K^+ counter ion prefers to stay outside the cage with a C_{3v} ($^1A_1$) symmetry, inducing very little perturbation to the Pb_{12}^{2-} cage relative to the ideal I_h symmetry. The isomer with K^+ inside the Pb_{12}^{2-} cage is much higher in energy by 2.37 eV because of the large size of the K^+ ion. The calculated vertical detachment energy (2.78 eV) of the C_{3v} KPb_{12}^- agrees very well with the experimental value of 2.77 eV, lending considerable credence to the identification of the I_h Pb_{12}^{2-} cage. In fact, we show next that the PES spectra of both Pb_{12}^- and KPb_{12}^- can be understood from the valence molecular orbitals (MOs) of the I_h Pb_{12}^{2-}, as shown in Figure 7.14.

Under the I_h symmetry, the 6p-based valence orbitals of Pb transform into MOs t_{1u}, h_g, g_u, and a_g in Pb_{12}^{2-}, which form two groups with a large energy gap at the scalar relativistic level of theory (Figure 7.14). The 6s-based MOs are much more stable due to the so-called "inert electron pair effect" arising from the relativistic effects;[255] they are

separated by more than 4 eV from the 6p-based MOs and cannot be accessed even at 193 nm in our PES experiments for Pb_{12}^- and KPb_{12}^-. However, when spin-orbit (SO) coupling effect, which is expected to be very large for Pb, is considered, the orbital pattern becomes quite different (Figure 7.14). The strong SO coupling transforms the MOs into three groups of energetically separated spinors: ($e_{1/2u}$, $g_{3/2g}$), ($g_{3/2u}$, $i_{5/2g}$, $e_{7/2u}$), and ($i_{5/2u}$, $e_{1/2g}$). This pattern of spinors is in remarkable qualitative agreement with the observed PES spectra for Pb_{12}^- and KPb_{12}^-, suggesting that further splittings of the MOs in the lower symmetry Pb_{12}^- and KPb_{12}^- are relatively small. This is indeed the case, as illustrated in the energy correlation diagrams in Figure 7.14. The small energy splitting is owing to the relatively small structural distortions from the I_h structure in Pb_{12}^- and KPb_{12}^-, indicating the structural robustness of the 12 atom Pb cage.

The canonical scalar-relativistic MOs of Pb_{12}^{2-} shown in Figure 7.15 are similar to those of the stannaspherene Sn_{12}^{2-},[1] which has been shown to be valent isoelectronic to the $B_{12}H_{12}^{2-}$ molecule.[225,226] Among the 13 valence MOs, there are 4 radial π orbitals (a_g and t_{1u}) and 9 in-sphere σ MOs (g_u and h_g). Analogous to Sn_{12}^{2-}, which has been named as stannaspherene for its π bonding character and its nearly spherical structure,[207] we suggest "plumbaspherene" for the highly stable and robust Pb_{12}^{2-} cage.

Plumaspherene has a computed diameter of 6.29 Å, slightly larger than that of stannaspherene (6.07 Å). Thus, it is expected that Pb_{12}^{2-} can trap an atom inside to form endohedral plumbaspherenes, $M@Pb_{12}$. In fact, two $M@Pb_{12}$ icosahedral cage clusters have been synthesized previously.[230,231] A remarkable endohedral compound, $[Pt@Pb_{12}]^{2-}$, has been synthesized in solution and crystalline form with K^+(2,2,2-crypt) as counter ions.[231] X-ray diffraction and NMR experiments have confirmed that this cluster

possesses I_h symmetry. It can be viewed as a zero-valent Pt atom trapped inside plumbaspherene, $Pt@Pb_{12}^{2-}$. In a laser vaporization experiment involving Pb and Al, a cluster with the composition $AlPb_{12}^{+}$ was observed to be unusually intense in the mass distribution.[230] Density functional calculations show that this cluster possesses an I_h structure with a closed electron shell. This cluster can be viewed as an Al^{3+} ion trapped inside plumbaspherene, $Al^{3+}@Pb_{12}^{2-}$, to give a total charge of +1. In another laser vaporization experiment involving Pb/Co, the $CoPb_{12}^{-}$ cluster was observed to be relatively intense in the mass distribution and was proposed to be an icosahedral $Co@Pb_{12}$ cage.[232] A very recent report describes the synthesis of an empty polyhedral Pb_{10}^{2-} cage, which is compared to the $B_{10}H_{10}^{2-}$ borane.[256] This result suggests that the Pb_{12}^{2-} plumaspherene should also be a stable species in solution and can be synthesized in the condensed phase. More importantly, the current work implies that the previously observed $M@Pb_{12}$ clusters were due to the intrinsic stability of *empty* plumbaspherene, rather than the effect of the doped atom. Hence, we can expect that a whole new family of stable $M@Pb_{12}$ endohedral clusters may exist, analogous to the endohedral fullerenes.[246,247]

7.3.3 Conclusion

Although Si or Ge is not known to form empty cage clusters like the fullerenes, we recently found a unique 12-atom icosahedral tin clusters, Sn_{12}^{2-} — stannaspherene. Here we report photoelectron spectroscopy and theoretical evidence that Pb_{12}^{2-} is also a highly stable icosahedral cage cluster and bonded by four delocalized radial π bonds and nine delocalized on-sphere σ bonds from the 6p orbitals of the Pb atoms. Following

Sn_{12}^{2-}, we coin a name, plumbaspherene, for the highly stable and nearly spherical Pb_{12}^{2-} cluster, which is expected to be stable in solution and solid state. Plumbaspherene has a diameter of ~6.3 Å with an empty interior volume large enough to host most transition metal atoms, affording a new class of endohedral clusters.

CHAPTER EIGHT

OBSERVATION OF CHEMISORPTION AND PHYSISORPTION OF DI-DEUTERIUM ON ALUMINUM CLUSTER ANIONS

8.1 Introduction

Small atomic clusters exhibit unique size-dependent properties. In the cluster regime, the change of a single atom can dramatically alter the structural, electronic, chemical, and magnetic properties of a cluster. The size-dependent chemical reactivity of clusters with simple molecules is important to understand catalysis by small particles and has been a critical part of cluster science. H_2 is the simplest molecule with great technological and biological importance. Studies of the interaction of H_2 with metal clusters may lead to new catalysts and to nanomaterials with good hydrogen storage capacity. Thus, the chemical reactivities of transition metal clusters with H_2 have been extensively studied.[257-264] Aluminum clusters are relatively simple electronic systems and have been intensively studied both theoretically[95,265-271] and experimentally.[95,195,271-276] Aluminum is a main group element with a $3s^2 3p^1$ electron configuration. In small aluminum clusters, the Al atom behaves as a monovalent atom because of the large energy separation between the 3*s* and 3*p* orbitals. With the increase of cluster size, the *s* and *p* bands start to overlap and the Al atom begins to behave as a trivalent atom.[276] Although the electronic structure of Al clusters has been well understood, their chemical properties have been investigated relatively scarcely,[277-280] in particular, the reactivity of Al clusters with H_2.[277-279]

Aluminum metal surface is relatively inert toward hydrogen and has a large activation energy barrier (about 1 eV) for the dissociation of molecular hydrogen.[281] It is well known that aluminum surface does not adsorb (extremely low sticking coefficient) molecular hydrogen under normal conditions.[282,283] It would be interesting to study the interaction of H_2 with aluminum clusters, which are expected to have different properties from the bulk surface. Indeed, Cox *et al*. found that for neutral Al clusters only Al_6 and Al_7 seemed to exhibit significant reactivity with D_2.[277] Using size-selected low-energy ion beam techniques, Jarrold and Bower showed that Al_n^+ cationic clusters exhibit large activation barriers toward D_2 and the activation barriers increase with cluster size from a little over 1 eV for Al_{10}^+ to around 2 eV for Al_{27}^+,[278] quite analogous to the bulk surfaces. At high collision energies, they did observe chemical reactions. They observed $Al_{n-1}D^+$ for n<10 and both Al_nD^+ and $Al_{n-1}D^+$ for larger clusters. More interestingly they also observed metastable $Al_nD_2^+$ adducts for larger n. Early theoretical calculations were carried out on the interactions between Al clusters and H_2 by Upton,[265] who computed Al_nH_2 (n = 2-6) and found that only Al_6H_2 is exothermic for the dissociation of H_2, consistent with the high reactivity of Al_6 observed by Cox *at al*. Khanna and Jena showed computationally that H_2 is more reactive toward the open shell icosahedral Al_{13} cluster than the closed shell icosahedral $Al_{12}C$ cluster.[284] More recently, extensive *ab initio* electronic structure calculations of hydrogenated aluminum clusters Al_nH_m (n = 1–8, m = 1, 2) and $Al_{13}H$ have been performed by Kawamura *et al.*,[285] who showed that the binding energies of the di-hydride forms of Al_nH_2 are all higher than 5 eV, i.e., higher than the dissociation energy of H_2, suggesting that H_2 should be dissociative on the smaller Al_n clusters.

It is important to understand the interactions of hydrogen with nanostructured aluminum because aluminum plays an important roll in many proposed hydrogen storage materials. Aluminum hydrides, alane (AlH_3) and di-alane (Al_2H_6), similar to the boranes, are known stable molecules with high hydrogen content.[286-290] Kawamura *et al.* performed theoretical calculations for higher alane clusters Al_nH_{3n} (n = 3-7) and proposed these species prefer cyclic or linear polymeric structures.[291] Alkali alanates, $MAlH_4$ [M = Li, Na, K], have also been studied as potential hydrogen storage materials.[292-294] Yarovsky and Goldberg[295] have theoretically suggested an $Al_{13}H_{12}$ species, where one H atom is adsorbed on each Al atom on the icosahedral Al_{13} surface. The $Al_{13}H_{12}$ cluster gives a hydrogen storage capacity of 3.3% by weight. A hypothetical $Al_{13}H_{42}$ cluster with much higher hydrogen storage capacity was also proposed by Yarovsky and Goldberg.

In this chapter, I describe an experimental study of aluminum di-deuteride cluster anions, $Al_nD_2^-$ (n = 3, 6-15), using photoelectron spectroscopy (PES). A similar PES work was reported by Burkart *et al*. for $Al_nH_m^-$ (n = 12-14; m = 1, 2) to confirm the high stability of $Al_{13}H$.[296] The current work provides a more extensive and systematic study and focuses on the nature of interaction between molecular hydrogen and small Al_n^- cluster anions. D_2 is used instead of H_2 for better mass resolution. We expect that the observation and conclusion should equally apply to H_2. Our PES results suggest that D_2 can either dissociate, chemisorb, or physisorb onto Al_n^- clusters, depending on the size and electronic structure of the Al_n^- clusters. The currents results provide new insight into the nature of the size-dependent interactions between hydrogen and aluminum clusters and should stimulate further theoretical studies.

8.2 Experimental Results

Figure 8.1 displays the PES spectra of $Al_nD_2^-$ (n = 3, 6-15) taken at 193 nm compared with those of pure aluminum cluster anions Al_n^-, which were reported previously.[276] Due to the very weak ion intensities of $Al_nD_2^-$ (n = 1, 2, 4 and 5), we were not able to obtain their PES spectra. Well-resolved electronic transitions were obtained for all the observed $Al_nD_2^-$ species. The adiabatic detachment energies (ADEs) or the electron affinities for the corresponding neutral clusters were measured from the lowest binding energy peaks. Since no vibrational structures were resolved, the ADEs were estimated by drawing a straight line along the leading edge of the threshold peaks and then adding the instrumental resolution to the intersect with the binding energy axis. The ADEs, given in Table 8.1 for both bare Al_n^- and the deuterated $Al_nD_2^-$ clusters and also plotted in Figure 8.2, were determined from the lower photon energy spectra, wherever available, due to the slightly better spectral resolution at the lower photon energies.

Comparison between the PES spectra of $Al_nD_2^-$ and Al_n^- can reveal information about the electronic interaction of D_2 with Al_n^-. Three general behaviors were observed in comparing the spectra between the deuterated and bare clusters. First, for the smaller clusters with n = 3, 6, 7, and 10, we observed that the spectra of $Al_nD_2^-$ are totally different from those of the corresponding Al_n^- clusters, both in terms of the spectral features and the ADEs. Second, for n = 9, 11, 13, and 15, the opposite was observed. The spectra of $Al_nD_2^-$ for these four clusters are almost identical to those of the bare Al_n^- clusters both in terms of the spectral features and ADEs. This is particularly true for $Al_9D_2^-$, $Al_{13}D_2^-$ and $Al_{15}D_2^-$. The ADEs of the deuterated species for these species are only slightly increased relative to the bare clusters (Table 8.1 and Figure 8.2). For n = 8,

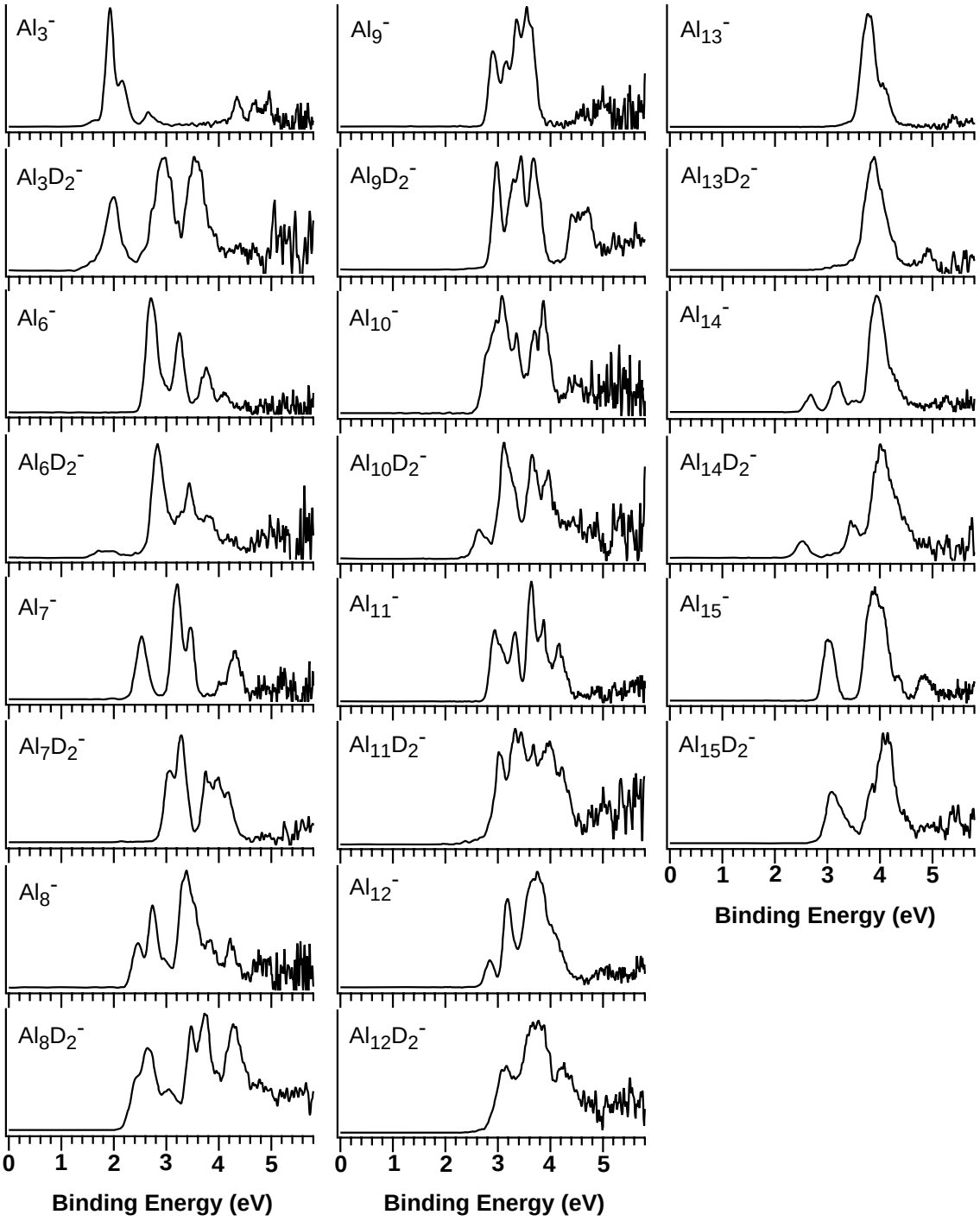

Figure 8. 1 Photoelectron spectra of Al_n^- and $Al_nD_2^-$ taken at 193 nm (6.424 eV).

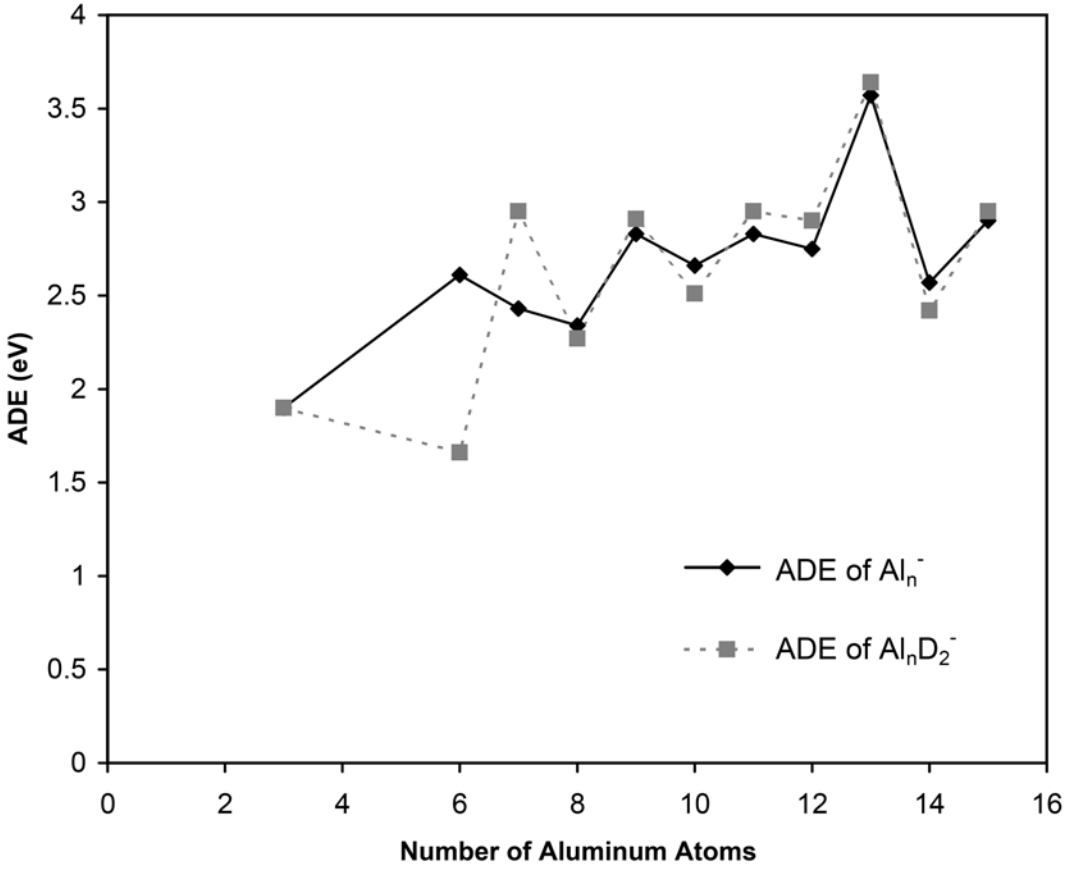

Figure 8. 2 The adiabatic detachment energies of Al_n^- and $Al_nD_2^-$ versus the number of aluminum atoms.

Table 8.1 Adiabatic detachment energies (ADE) for Al_n^- and $Al_nD_2^-$.

n	Al_n^- (eV)	$Al_nD_2^-$ (eV)
3	1.90 ± 0.03 [a]	1.90 ± 0.10
6	2.61 ± 0.05 [b]	1.66 ± 0.15
7	2.43 ± 0.06 [c]	2.95 ± 0.04
8	2.34 ± 0.05 [b]	2.27 ± 0.04
9	2.83 ± 0.05 [b]	2.91 ± 0.04
10	2.66 ± 0.05 [b]	2.51 ± 0.04
11	2.83 ± 0.05 [b]	2.95 ± 0.04
12	2.75 ± 0.06 [c]	2.90 ± 0.10
13	3.57 ± 0.05[d]	3.64 ± 0.08
14	2.57 ± 0.05 [b]	2.42 ± 0.10
15	2.90 ± 0.06 [c]	2.95 ± 0.10

[a]. From ref. [297].
[b]. Measured more accurately in this work at 266 nm.
[c]. From ref. [276].
[d]. From ref. [298].

12, and 14, an intermediate behavior was observed, in that, certain spectral similarities seem to exist between those of $Al_nD_2^-$ and Al_n^-. But there are also significant differences. In particular, the ADEs of $Al_nD_2^-$ for these three species generally exhibit more significant changes than the corresponding Al_n^- clusters.

As noted in the introduction, Burkart *et al.*[296] reported PES spectra for aluminum hydride clusters $Al_nH_m^-$ with n = 12 - 14 and m = 1, 2 previously. The current spectra of $Al_{12}D_2^-$ and $Al_{14}D_2^-$ are better resoled and consistent with those on the hydrogenated species reported by Burkart *et al*. However, our $Al_{13}D_2^-$ spectrum is different from that of $Al_{13}H_2^-$ by Burkart *et al*. The $Al_{13}H_2^-$ spectrum by Burkart *et al*. exhibited an extra lower binding energy band around 3.3 eV relative to the current spectrum of $Al_{13}D_2^-$. The $Al_{13}H_2^-$ spectrum reported by Burkart *et al.* had a rather low count rate and poorer resolution. We suspect that the extra band in the Burkart *et al*.' spectrum could be due to either a structural isomer or contaminations.

8.3 Discussion

The geometrical and electronic structures of small aluminum clusters have been well studied. Small clusters are expected to be more reactive due to the presence of large number of surface atoms with low coordination numbers. The EAs of the bare Al_n clusters display an even-odd effect for n>6 (Figure 8.2), where the odd-sized clusters possess higher EAs than their even-sized neighbors. This observation suggests that all odd-sized neutral Al_n clusters are open shell with an unpaired electron and their corresponding anions Al_n^- are all closed shell, giving rise to the enhanced electron binding energies in the anions. The even-sized neutral Al_n clusters are all closed shell

with a HOMO-LUMO gap, thus giving rise to the reduced electron binding energies for their anions. The enhanced EA of Al_6 is because it has a triplet ground state with two unpaired electrons,[269] instead of a closed shell configuration. This electronic structure information is revealed clearly in the PES spectra of the bare Al_n^- clusters,[276] as shown in Figure 8.1.

If D_2 chemisorbs on Al_n^-, the PES spectra and ADEs of $Al_nD_2^-$ are expected to be different from those of the corresponding bare Al_n^- clusters. This is because the electronic energy levels of Al_n^- is expected to be perturbed by D_2 or in cases of dissociative chemisorption di-deuterides are formed. If D_2 physisorbs on Al_n^-, one would expect that $Al_nD_2^-$ and Al_n^- should have similar PES spectra and similar ADE values since there is little electronic interaction between D_2 and Al_n^-. Based on our experimental data and the comparison between the spectra of $Al_nD_2^-$ and Al_n^-, we observed both dissociative and molecular chemisorption, as well as physisorption of D_2 on Al_n^- clusters in $Al_nD_2^-$, depending on the size and the electronic properties of the Al_n^- cluster.

A. Dissociative Chemisorption: $Al_nD_2^-$ (n = 3, 6, 7, 10). For these four species, their PES spectra are totally different from those of the corresponding bare Al_n^- clusters, i.e., their electronic structures are very different from those of the bare clusters. This observation suggests that D_2 is likely to be dissociatively chemisorbed on the Al_n^- clusters, forming two hydride bonds. There have been no theoretical calculations of hydrogen interacting with negatively charged Al_n^- clusters. But early calculations by Upton suggested that H_2 dissociates on neutral Al_6.[265] More recent calculations on neutral clusters by Kawamura *et al.*[285] showed that the total binding energies of two H atoms in Al_nH_2 ($n \leq 8$) are always larger than the dissociation energy of H_2, suggesting that H_2

prefers to dissociatively chemisorb onto the smaller Al clusters. Al_3H_2 is calculated to have a trigonal bipyramidal structure with each H atom coordinated to the three Al atoms. Al_6H_2 is shown to have a ground state structure, in which the two H atoms coordinate to two nearby faces on an octahedral Al_6, by both Upton and Kawamura *et al*. Al_7 has a ground state structure with an Al atom capping one face of the octahedral Al_6. Kawamura *et al*. showed that in Al_7H_2 one H atom is bonded atop the capping Al atom and the second H atom bridges the capping Al atom and another Al atom on the octahedral Al_6. In Al_3H_2, Al_6H_2, and Al_7H_2, the two hydride atoms are all next to each other on the cluster surface. Thus a low activation barrier is expected when H_2 approaches the cluster during chemisorption. On the other hand, Kawamura *et al*. showed that the most stable structure of Al_8H_2 involves two H atoms on the opposite site of the Al_8 clusters, suggesting a high activation barrier for H_2 dissociation on the Al_8 cluster surface. This is consistent with the molecular chemisorption of D_2 in $Al_8D_2^-$ (*vide infra*). Although there have been no calculations on $Al_{10}H_2$, the very different PES spectrum observed for $Al_{10}D_2^-$ compared to Al_{10}^- suggests that D_2 is very likely to be dissociatively chemisorbed on Al_{10}^-, analogous to that in $Al_6D_2^-$ or $Al_7D_2^-$.

B. Physisorption: $Al_nD_2^-$ (n = 9, 11, 13, 15). The PES spectra of these four deuterated species are nearly identical to those of their corresponding bare Al_n^- clusters and their ADEs are also similar to those of the corresponding bare clusters, particularly for n = 9, 13, 15. These observations imply that D_2 has very little effect on the electronic structure of these Al_n^- clusters, suggesting van der Waals interactions between D_2 and Al_n^- or physisorption of D_2 on Al_n^-. These species can essentially be characterized as van der Waals complexes, $(Al_n^-)D_2$. This is not surprising because these odd-sized Al_n^-

clusters are all closed shell electronic systems and they are expected to exhibit high activation barriers toward reaction with D_2. In particular, the electronic stability of Al_{13}^- is well known because it is a major shell closing in the jellium model. For example, it has the highest EA (3.57 eV) among the Al_n clusters,[276,278] as shown in Figure 8.2. Indeed, the electronic structure of the icosahedral Al_{13}^- is little perturbed in $Al_{13}D_2^-$, as evidenced in the nearly identical PES spectra of $Al_{13}D_2^-$ and Al_{13}^- (Figure 8.1). Al_{15}^- is known to have a structure, in which two Al atoms capping an icosahedral Al_{13}^- on the opposite site.[95] The nearly identical spectra of $Al_{15}D_2^-$ and Al_{15}^- suggest that D_2 is also very weakly bound to Al_{15}^-. Only the spectral features of $Al_{11}D_2^-$ show more variations from that of the bare Al_{11}^- cluster and a more significant ADE shift relative to Al_{11}^- as well, indicating a stronger interaction between D_2 and Al_{11}^- relative to the other three closed-shell clusters.

C. Chemisorption: $Al_nD_2^-$ (n = 8, 12, 14). For these three deuterated species, the PES spectra exhibit certain similarities, as well as visible difference from their corresponding bare clusters. The ADEs of these species also display more sizable shifts in general, compared to their corresponding bare clusters. These observations indicate that D_2 has stronger interactions with the underlying Al cluster anions, and should probably be characterized as chemisorption. The bare Al_n^- clusters are even-sized and they are all open shell species with one unpaired electron. Thus, it is understandable that D_2 would have stronger interactions with these open-shell clusters, compared to the closed-shell odd-sized clusters. Jarrold and Bower observed D_2 chemisorbed adduct onto Al_n^+ clusters in ion beam experiments at a collision energy of 3 eV.[278] It is interesting to note that even though they observed strong $Al_nD_2^+$ adducts for $n \geq 16$, in the smaller size

range only significant chemisorbed D_2 adduct were observed for $Al_{12}D_2^+$ and $Al_{14}D_2^+$. This is very likely due to the fact Al_{12}^+ and Al_{14}^+ are open shell with one unpaired electron, thus exhibiting stronger interactions with D_2, analogous to the open-shell anions, Al_8^-, Al_{12}^-, and Al_{14}^-. We further note that although Al_{13}^- is closed shell and chemically inert, theoretical calculations have suggested that the open shell neutral Al_{13} is more reactive toward H_2 and can dissociatively chemisorb H_2 with a moderate activation barrier.[284,295]

8.4 Conclusion

We performed a photoelectron spectroscopic investigation of $Al_nD_2^-$ (n = 3, 6-15), formed from laser vaporization of a pure aluminum target with a D_2-seeded helium carrier gas. Well-resolved photoelectron spectra were obtained for the $Al_nD_2^-$ clusters. Comparison of the photoelectron spectra of $Al_nD_2^-$ with those of Al_n^- yielded information about the nature of D_2 in the $Al_nD_2^-$ clusters. Dissociative chemisorption, molecular chemisorption, and physisorption were inferred from the spectral comparison, depending on the cluster size and their underlying electronic structure. For $Al_nD_2^-$ (n = 9, 11 13, 15), very similar PES spectra were observed with respect to the corresponding Al_n^- clusters, suggesting they are weakly bound van der Waals complexes $(Al_n^-)D_2$. For $Al_nD_2^-$ (n = 3, 6, 7, 10), the spectra of the deuterated species are completely different from the corresponding Al_n^- clusters, suggesting dissociative chemisorption to form di-deuterides. An intermediate behavior was observed for $Al_nD_2^-$ (n = 8, 12, 14), which were suggested to involve chemisorbed D_2. The deuteride $Al_nD_2^-$ clusters are consistent with the high reactivity expected for the very small clusters. The chemisorbed and physisorbed $Al_nD_2^-$

clusters are understood from the open-shell and closed-shell nature of the underlying Al_n^- clusters, respectively. The current PES data will be valuable to verify further theoretical calculations and contribute to elucidating the size-dependent chemical properties of Al clusters with H_2.

CHAPTER NINE

ALKALI-COINAGE METAL ALLOY CLUSTERS

9.1 Experimental and Computational Studies of Mixed Alkali and Coinage Metal Clusters

9.1.1 Introduction

Photoelectron spectroscopy (PES) in combination with *ab initio* calculations has recently been used to investigate a series of ring-shaped metal clusters consisting of planar four-membered molecular rings, which are shown to be stabilized by cyclic electron delocalization or aromaticity.[20,21,299-304] The aromatic nature of these ring-shaped metal clusters has been subsequently studied and confirmed.[305-310] The generally accepted notion is that ring-shaped metal clusters with $(4n + 2)\pi$ electrons such as Al_4^{2-} and Hg_4^{6-} can be aromatic and that they sustain ring currents when exposed to external magnetic fields, similar to ordinary aromatic molecules. Explicit calculations of the magnetically induced current densities have shown that for Al_4^{2-}, both σ and π orbitals sustain diatropic (aromatic) ring currents, whereas for Al_4^{4-} species the current is σ diatropic (aromatic) and the π current is paratropic (antiaromatic). This notion is also supported by earlier calculations of nucleus independent chemical shifts (NICS).[311] Thus, new concepts of multiple aromaticity for metal clusters, such as σ and π aromaticity, and σ aromaticity and antiaromaticity, have been introduced. A recent study of the magnetically induced currents of Al_4^{2-} and Al_4^{4-} using the Gauge-Including Magnetically Induced Current (GIMIC) method[312] yielded explicit values for the ring-current strengths, as well as the

diatropic (aromatic) and paratropic (antiaromatic) contributions to the ring current.[305] The ring-current study of the Al_4 clusters also provided accurate information about the shape of the magnetically induced ring currents and the aromaticity properties of the controversial case of Al_4^{4-} [313] can now be considered understood:[305] it is π-antiaromatic and σ-aromatic as originally suggested.[302]

Wannere *et al*.[314] recently studied computationally four-membered ring species of coinage metals, such as bipyramidal Cu_4Li_2, Ag_4Li_2, and Au_4Li_2 clusters of D_{4h} symmetry and used NICS calculations to assess their aromaticity. In these cases, Wannere *et al*. found that the largest diamagnetic (aromatic) contribution to the NICS value originates from the a_{1g} molecular orbital (MO), which is built mainly from the 4*s* atomic orbitals (AOs). However, the paramagnetic (antiaromatic) contribution from the highest occupied e_u orbitals, also formed mainly by the 4*s* AOs, cancels the a_{1g} contribution. Thus, the diamagnetic NICS value of -14.5 ppm seems to originate from the MOs with mainly 3*d* character. They considered therefore these coinage-alkali metal clusters as the first example of *d*-orbital aromatic molecules.[18]

We also mention here the recent density-functional theory (DFT) study by Fuentealba and Padilla-Campos[315] who calculated the molecular structures of neutral and positively charged bimetallic Cu_mLi_n (m, $n \leq 4$) clusters as well as the DFT studies by Tsipis *et al*.[316,317] who proposed a new class of molecules consisting of planar cyclic copper hydrides, Cu_nH_n.

In this chapter, I present the generation of Cu_4Na^- and Au_4Na^- clusters in the gas phase and their characterization experimentally using photoelectron spectroscopy and computationally at correlated *ab initio* levels by our collaborators. The singly charged

M_4Li^- (M = Cu, Ag, Au) and Ag_4Na^- species as well as the neutral Cu_4Li_2 and Cu_4Na_2 clusters have also been considered in the theoretical study. Photoelectron spectra of Cu_4Na^- and Au_4Na^- have been simulated by equation-of-motion coupled-cluster calculations of the low-lying electron detachment transitions and compared with the experimental data to identify the clusters observed in the PES experiment. The electron delocalization and aromaticity properties were studied by performing explicit calculations of the magnetically induced current densities using the newly developed GIMIC method.[312] Numerical integration of the magnetically induced current densities provided information about the ring-current strengths and the shape of the ring current. The GIMIC calculations clearly demonstrated that the square-planar coinage metal M_4^{2-} clusters are σ-aromatic systems primarily due to the *s* orbital bonding.

9.1.2 Experimental Results

The measured photoelectron spectra of Cu_4Na^- taken at two laser wavelengths, 532 nm (2.331 eV) and 266 nm (4.661 eV) are shown with the red curves in Figure 9.1. The photoelectron spectra of Au_4Na^- recorded at three laser wavelengths are analogously shown in Figure 9.2. The 266 nm spectrum of Cu_4Na^- displayed two weak bands (X, X') at lower binding energies and two strong bands (A, B) at higher energies. The X' band at 1.8 eV almost completely disappeared in the 532 nm spectrum and was most likely due to a mass contamination. The X band represents the transition from the ground state of Cu_4Na^- to that of Cu_4Na, yielding adiabatic (ADE) and vertical (VDE) detachment energies of 0.83 and 1.13 eV, respectively. The broad peak of the X band suggests a significant geometry change between the ground states of Cu_4Na^- and Cu_4Na. The A band

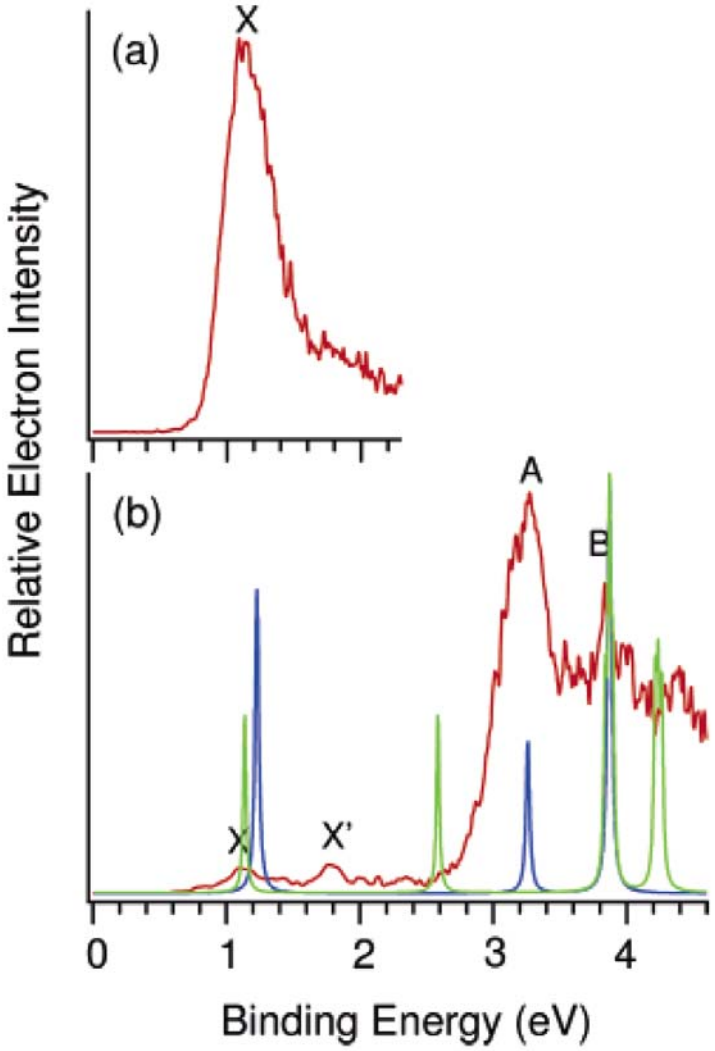

Figure 9.1 Comparison of calculated and measured photoelectron spectra of Cu_4Na^-. The measured spectra taken at (a) 532 nm (2.331 eV) and (b) 266 nm (4.661 eV) are shown in red. The calculated spectrum for the C_{4v} isomer is shown in blue and the spectrum of the planar C_{2v} isomer in green.

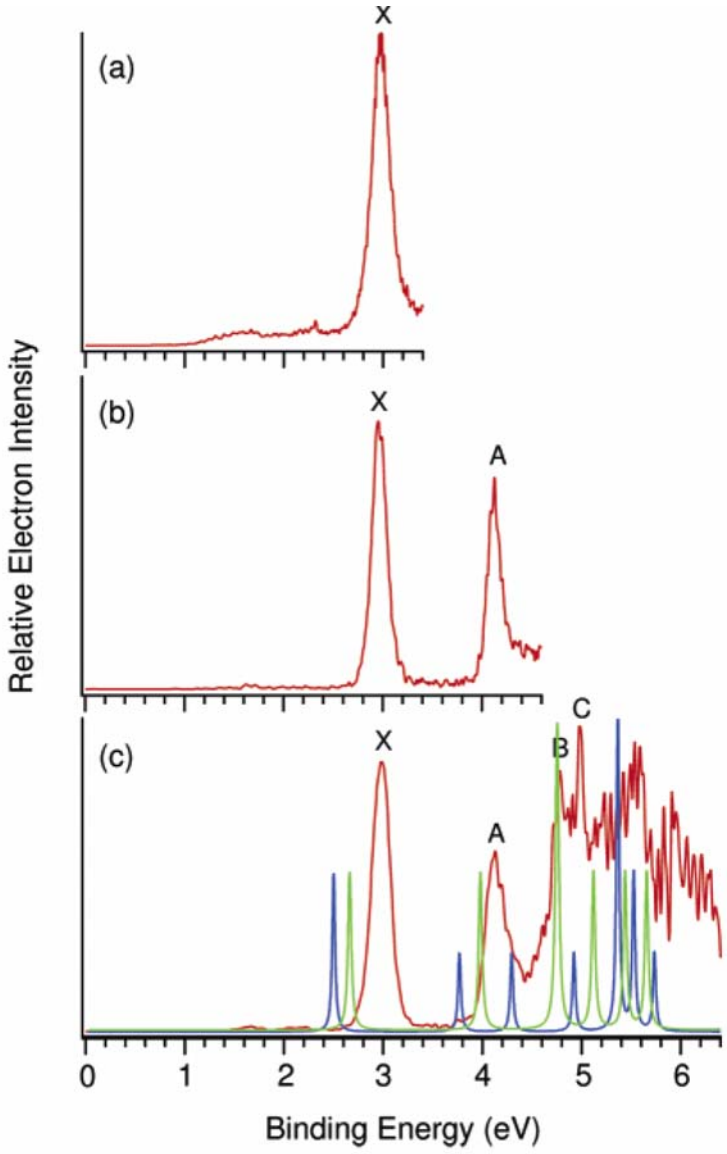

Figure 9.2 Comparison of calculated and measured photoelectron spectra of Au_4Na^-. The measured spectra taken at (a) 355 nm (3.496 eV), (b) 266 nm (4.661 eV), and (c) 193 nm (6.424 eV) are shown in red. The calculated spectrum for the C_{4v} isomer is shown in blue and the spectrum of the planar C_{2v} isomer in green.

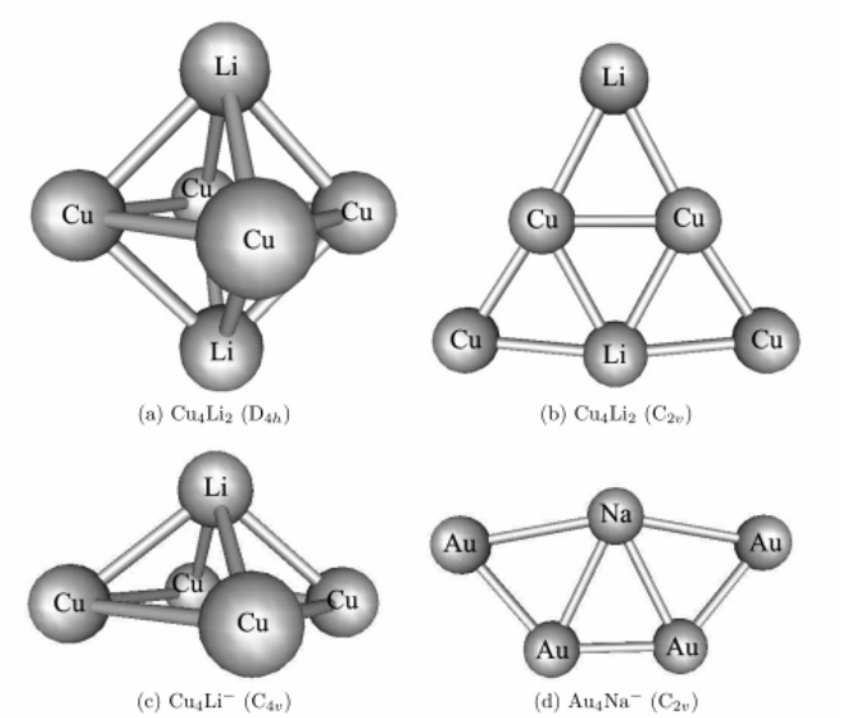

Figure 9.3 The molecular structure of (a) Cu_4Li_2 (D_{4h}), (b) Cu_4Li_2 (C_{2v}), (c) Cu_4Li^- (C_{4v}), and (d) Au_4Na^- (C_{2v}) optimized at the MP2 level using TZVPP (Cu, Li, Na) and 7*s*5*d*3*d*2*f* (Au) basis sets.

Figure 9.4 The HOMO (a) and HOMO-1 (b) molecular orbitals of Cu_4Li_2 calculated at the Hartree-Fock self-consistent field (HF SCF/TZVPP) level using the MP2/TZVPP molecular structure. The orbitals are spectated along the C_4 axis. The orbital energies (in eV) are given within parentheses.

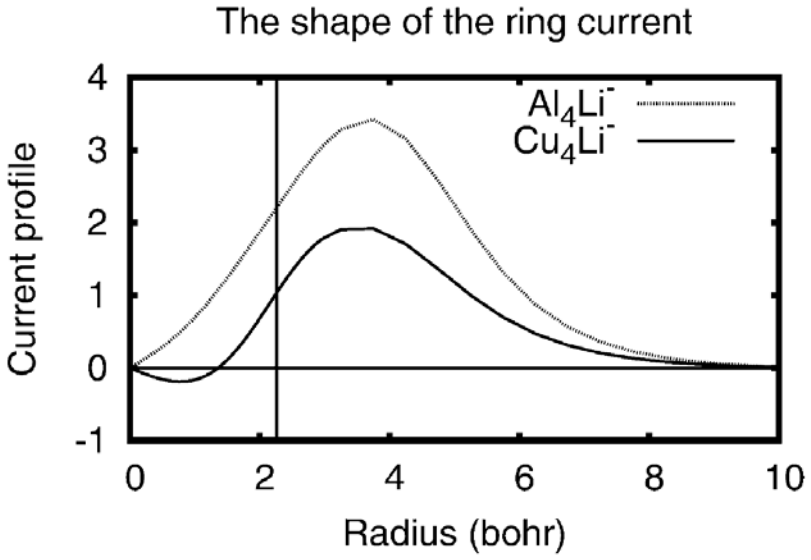

Figure 9.5 The shape of the ring current (in nA/T/bohr) for Cu_4Li^- calculated at the CCSD/TZVPP level using the MP2/TZVPP molecular structure is compared to the ring current profile of the Al_4^{2-} ring[305]. The vertical bar denotes the size of the Cu_4^{2-} ring. The size of the Al_4^{2-} ring is 0.2 bohr greater.

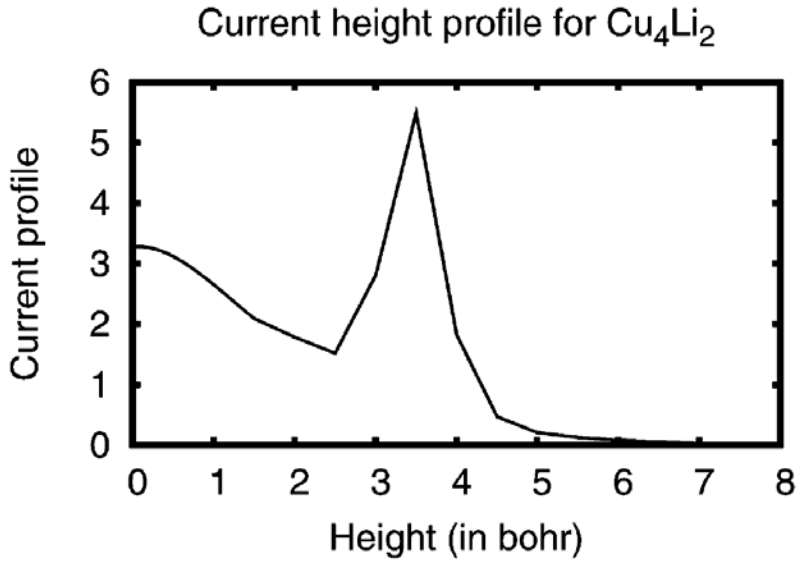

Figure 9.6 The current profile (in nA/T/bohr) as a function of the vertical distance from the Cu_4^{2-} ring in Cu_4Li_2 calculated at the CCSD/TZVPP level using the MP2/TZVPP structure.

Table 9.1 The observed vertical electron detachment energies (VDE in eV) from the photoelectron spectra of Cu_4Na^- in Figure 9.1 and Au_4Na^- in Figure 9.2. The uncertainty is ± 0.05 eV.

species	X[a]	A	B	C
Cu_4Na^-	1.13	3.26	3.84	
Au_4Na^-	2.98	4.12	4.79	4.98

[a] The adiabatic detachment energies for the X band or the electron affinities for the corresponding neutral Cu_4Na and Au_4Na are measured as 0.83 ± 0.04 and 2.82 ± 0.04 eV, respectively.

Table 9.2 The relative isomer energies (in kJ/mol) of the planar (C_{2v}) M_4A^- (M = Cu, Ag, and Au; A = Li and Na) isomers calculated at the MP2, CCSD, and CCSD(T) levels using the TZVPP (Li, Na, Cu, and Ag) and 7*s*5*p*3*d*2*f* (Au) basis sets[a]

species	MP2	CCSD	CCSD(T)	CCSD(T)[b]
Cu_4Li^-	11.7	-16.4	-3.1	30.9
Cu_4Na^-	-3.5	-31.0	-17.1	16.9
Ag_4Li^-	12.4	-11.3	-3.5	-
Ag_4Na^-	-3.0	-28.0	-18.8	-
Au_4Li^-	0.6	-41.3	-29.7	-
Au_4Na^-	-17.9	-63.1	-49.4	-

[a] The molecular structures were optimized at the MP2 level using the same basis sets. Negative isomer energies indicate that the planar isomer is the lowest one.[b] Extrapolated CCSD(T)/QZVPP value.

Table 9.3 The M-M and M-A bond distances (in pm) of the M_4A^- and M_4A_2 species (M = Cu, Ag, and Au; A = Li and Na) optimized at the MP2 level using the TZVPP (Li, Na, Cu, Ag) and 7*s*5*p*3*d*2*f* (Au) basis sets.

species	level	symmetry	M-M[a]	M-M[b]	M-A[c]	M-A[d]
Cu_4Li^-	MP2/TZVPP	C_{4v}	242.0		240.3	
Cu_4Na^-	MP2/TZVPP[e]	C_{4v}	242.0		275.0	
Cu_4Li^-	MP2/TZVPP	C_{2v}	243.6	235.8	248.5	244.5
Cu_4Na^-	MP2/TZVPP	C_{2v}	244.2	236.0	280.0	284.8
Ag_4Li^-	MP2/TZVPP	C_{4v}	270.6		253.6	
Ag_4Na^-	MP2/TZVPP	C_{4v}	270.1		288.9	
Ag_4Li^-	MP2/TZVPP	C_{2v}	269.6	260.6	260.8	261.7
Ag_4Na^-	MP2/TZVPP	C_{2v}	270.3	260.3	292.2	300.0
Au_4Li^-	MP2/7*s*5*p*3*d*2*f*	C_{4v}	264.3		249.1	
Au_4Na^-	MP2/7*s*5*p*3*d*2*f*	C_{4v}	263.6		282.3	
Au_4Li^-	MP2/7*s*5*p*3*d*2*f*	C_{2v}	261.1	251.4	257.5	255.7
Au_4Na^-	MP2/7*s*5*p*3*d*2*f*	C_{2v}	260.9	251.1	294.5	284.4
Cu_4Li_2	MP2/TZVPP	D_{4h}	246.1		242.8	
Cu_4Na_2	MP2/TZVPP	D_{4v}	243.8		280.8	
Cu_4Li_2	MP2/TZVPP	C_{2v}[f]	237.4	237.8	250.1	251.8
Cu_4Na_2	MP2/TZVPP	C_{2v}[g]	237.7	239.3	282.1	290.0

[a] For the planar clusters of C_{2v} symmetry, the distance between the inner and outer M atoms.[b] The distance between the two inner M atoms of the planar clusters.[c] For the planar clusters of C_{2v} symmetry, the distance between the A atom and the outer M atom of the planar clusters.[d] The distance between the A atom and the inner M atom of the planar clusters.[e] The corresponding distances obtained at the CCSD/TZVPP level are 251.7 and 280.4 pm.[f] The distance between the inner Cu atom and the Li atom at the cusp is 255.0 pm.[g] The distance between the inner Cu atom and the Na atom at the cusp is 282.0 pm.

Table 9.4 The vertical detachment energies (VDE in eV) for Cu_4Li^-, Cu_4Na^-, and Au_4Na^- calculated at the EOMIP CCSD level as compared to experimental data[a]

Cu_4Li^-	Cu_4Na^-			Au_4Na^-		
calcd	calcd			calcd		
(C_{4v})	(C_{4v})	(C_{2v})	exp	(C_{4v})	(C_{2v})	exp
1.313	1.229	1.137	1.13	2.501	2.662	2.98
3.193	3.259	2.586	3.26	3.769	3.980	4.12
3.636	3.864	3.840	3.84	4.295	4.751	4.79
4.062	3.876	3.871		4.923	4.758	4.98
		3.985		5.365	5.120	
		4.213		5.525	5.439	
				5.734	5.656	

[a] The molecular structures optimized at the MP2 level were used. The cluster symmetry is also indicated

Table 9.5 The integrated ring-current susceptibilities (in nA/T) for Cu_4Li^-, Cu_4Li_2, and Cu_4H_4 calculated at the CCSD/TZVPP level using the GIMIC method

	Al_4Li^- [a]	Cu_4Li^-	Cu_4Li_2	Cu_4H_4
diamagnetic current	32.4	19.4	23.2	2.1
paramagnetic current	0.0	-0.4	-0.4	-2.7
total current	32.4	19.0	22.8	-0.6
contribution from Li[b]	4.3	6.4	12.9	-
total ring current	28.1	12.6	10.0	-0.6

[a] From ref [305]. [b] The estimated net current circling the Li^+ cations.

in Figure 9.1b corresponding to a VDE of 3.26 eV and the B band (VDE: 3.84 eV) represent detachment transitions to two excited states of Cu_4Na. Other weak features are also present on the higher binding energy side of the 266 nm spectrum, giving the congested appearance in this spectral range. The weak features are also most likely due to the contaminant associated with band X'.

The experimental photoelectron spectra of Au_4Na^- in Figure 9.2 show no resemblance to those of Cu_4Na^-. Au_4Na^- seems to have much higher electron binding energies. Its ground state transition defined by band X yielded ADE and VDE of 2.82 and 2.98 eV, respectively. Three excited state transitions (A, B, C) were clearly resolved at VDEs of 4.12, 4.79, and 4.98 eV, respectively. Higher binding energy features in the 193 nm spectrum were observed but not well resolved. The Au_4Na^- spectra appear to have less contamination problems. The weak and broad features at lower binding energies (1.2 to 2.6 eV) in Figure 9.2a could be due to contamination or due to the presence of other low-lying isomers, but the 266 and 193 nm spectra shown in Figures 9.2b and 9.2c were quite clean.

The observed ADEs and VDEs are summarized in Table 9.1. To elucidate the structure and bonding of the two coinage alkali mixed clusters, the experimental data will be compared to calculated ionization potentials in Section 4.2.

9.1.3 Theoretical Results and Discussion

A. Molecular Structures. The energetically lowest structure obtained in the optimization at Møller-Plesset perturbation (MP2/TZVPP) level for Cu_4Li_2 is a bipyramidal cluster of D_{4h} symmetry (Figure 9.3a). At this computational level, it lies

77.0 kJ/mol below the planar one of C_{2v} symmetry (Figure 9.3b). The Cu atoms in Cu_4Li_2 seems to prefer to form a square with equidistant Cu-Cu bonds as previously reported.[314]

At the MP2/TZVPP level, the singly charged Cu_4Li^- cluster of C_{4v} in Figure 9.3c is found to be 11.7 kJ/mol below the planar C_{2v} isomer. The corresponding Au_4Na^- isomer of C_{2v} symmetry is shown in Figure 9.3d. However, the energy difference is small and by changing the counterion from Li^+ to Na^+ the pyramidal C_{4v} and the planar C_{2v} structures become almost degenerate with the planar structure 3.3 kJ/mol below the C_{4v} one. The planar isomer is stabilized further by inclusion of higher-order electron correlation effects. In single-point CCSD/TZVPP and CCSD(T)/TZVPP calculations using the MP2/TZVPP structures, the planar isomer of Cu_4Li^- is 16.4 and 3.1 kJ/mol below the pyramidal one. For Cu_4Na^-, the planar isomer is 3.4, 31.0, and 17.1 kJ/mol below the pyramidal structure calculated at the MP2, CCSD, and CCSD(T) levels. Zero-point energy corrections and entropy contributions do not change the order of the isomers since they reduce the energy difference between the planar and pyramidal isomers by only a few kJ/mol. However, at the MP2/QZVPP level the pyramidal Cu_4Li^- and Cu_4Na^- clusters are 45.7 and 30.2 kJ/mol below the planar isomers yielding extrapolated CCSD(T)/QZVPP isomer energies of 30.9 and 16.9 kJ/mol for Cu_4Li^- and Cu_4Na^-, respectively. Thus, we conclude that for the singly charged Cu_4Li^- and Cu_4Na^- clusters, the pyramidal isomers of C_{4v} symmetry are the energetically lowest ones.

The lowest isomer of Cu_4Na_2 is the bipyramidal cluster of D_{4h} symmetry. At the MP2/TZVPP level it is found to be only 15.4 kJ/mol below the planar structure of C_{2v} symmetry. As for Cu_4Na^-, the use of the QZVPP basis set favors the bipyramidal isomer, whereas high-order electron correlation contributions decrease the energy of the planar

isomer relative to the bipyramidal one. At the extrapolated CCSD(T)/QZVPP level, the bipyramidal Cu_4Li_2 and Cu_4Na_2 clusters are found to be 99.8 and 54.5 kJ/mol below the planar ones.

The relative isomer energies of the Ag_4^{2-} clusters are very similar to those of the corresponding Cu species. At the MP2/TZVPP level, pyramidal Ag_4Li^- is 12.4 kJ/mol below the planar one, whereas at the CCSD/TZVPP and CCSD(T)/TZVPP levels, the planar isomer is 11.3 and 3.5 kJ/mol below the C_{4v} structure. For the Ag_4Na^- cluster, the MP2/TZVPP, CCSD/TZVPP, and CCSD(T)/TZVPP isomer energy differences are 3.0, 28.0, and 18.8 kJ/mol with the planar isomer below the pyramidal one. The use of QZVPP quality basis sets would most likely switch the order yielding the lowest energy for the pyramidal isomers as for the corresponding Cu clusters.

The Au_4Li^- and Au_4Na^- clusters were optimized by our collaborators at the MP2 level using the 7*s*5*p*3*d*2*f* basis set for Au and the TZVPP basis sets for Li and Na. At the MP2 level, the planar Au_4Li^-, isomer of C_{2v} symmetry is only 0.6 kJ/mol above the pyramidal one, whereas CCSD and CCSD(T) calculations yielded the lowest energy for planar isomer. The isomer energy differences obtained at the CCSD and CCSD(T) levels are 41.3 and 29.7 kJ/mol. For Au_4Na^-, the planar isomer is significantly below the pyramidal structure at all computational levels. The isomer energy differences for Au_4Na^- obtained at the MP2, CCSD, and CCSD(T) levels are 17.9, 63.1, and 49.4 kJ/mol. The lowest isomers of both Au_4Li^- and Au_4Na^- clusters are the planar ones. The energy differences between the planar and pyramidal isomers are so large that the use of larger basis sets would hardly change the order of them.

The relative isomer energies obtained at MP2, CCSD, and CCSD(T) levels are given in Table 9.2, and the bond distances obtained in the structure optimizations in Table 9.3. The optimized cluster structures of Cu_4Li_2 (D_{4h}), Cu_4Li_2 (C_{2v}), Cu_4Li^- (C_{4v}), and Au_4Na^- (C_{2v}) are shown in Figures 9.3a-d.

B. Comparison Between Experimental and Calculated Photoelectron Spectra. The simulated photoelectron spectra of the pyramidal and planar Cu_4Na^- clusters shown as the blue and green curves in Figure 9.1 were calculated at the EOMIP CCSD level. The obtained VDEs for the pyramidal (C_{4v}) Cu_4Li^- and Cu_4Na^- clusters as well as the planar (C_{2v}) Cu_4Na^- cluster are given in Table 9.4. The calculated photoelectron spectra are rather independent of whether Li^+ or Na^+ is used as counterion, whereas the spectra for the planar and pyramidal Cu_4Na^- isomers differ significantly. The calculated spectra of the pyramidal Cu_4Li^- and Cu_4Na^- are very similar, except for the fourth detachment channel (Table 9.4). However, the peak patterns of the calculated spectra of the planar and pyramidal Cu_4Na^- clusters are completely different. This structural sensitivity of photoelectron spectra provides the basis for using PES and calculations to determine cluster structures. We were not able to measure the photoelectron spectra of Cu_4Li^- because of its complicated isotope pattern. Our measured photoelectron spectra of Cu_4Na^- (the red curves in Figure 9.1) are in good agreement with the simulated spectrum for the pyramidal structure (the blue curve) but disagree with the simulated spectrum for the planar structure (the green curve). In particular, the second detachment channel for the planar structure with a calculated VDE at 2.586 eV has no corresponding peak in the experimental spectrum. The comparison between the calculated and measured photoelectron spectra suggests that the experimental spectra are due to the Cu_4Na^- cluster

of C_{4v} symmetry, consisting of a planar four-membered Cu_4^{2-} ring. The planar Cu_4Na^- isomer of C_{2v} symmetry can be ruled out to be the main contributor to the experimental spectra since its second VDE deviates by 0.66 eV from the experimental value (Table 9.4) and the estimated uncertainty of the VDE calculated at the EOMIP CCSD/TZVPP level is significantly smaller.[318]

The calculated photoelectron spectra of the planar (C_{2v}) and pyramidal (C_{4v}) isomers of Au_4Na^- at the EOMIP CCSD level are shown in Figure 9.2, and the obtained ionization potentials are compared with the experimental VDEs in Table 9.4. Clearly, the calculated spectral pattern of the planar isomer (the green curve in Figure 9.2) agrees well with the experimental spectra (the red curves), although the calculated VDEs are somewhat smaller than the observed ones (Table 9.4). On the other hand, the pattern of the calculated photoelectron spectra for the pyramidal Au_4Na^- cluster (the blue curve in Figure 9.2) differs significantly from that of the experimental spectrum. These observations are consistent with the energetics of the two Au_4Na^- isomers and confirm that the planar Au_4Na^- isomer is indeed the global minimum.

C. The Nature of the Aromaticity of the Square-Planar Cu_4^{2-} Unit. Wannere *et al*.[314] calculated nucleus independent chemical shifts (NICS) for bipyramidal Cu_4Li_2, Ag_4Li_2, and Au_4Li_2. On the basis of the NICS contributions from different orbitals, they concluded that the aromatic properties of these clusters possess distinct differences from other square ring systems such as Al_4Li_2. According to their NICS calculations, the coinage four-membered rings are stabilized by *d* orbital aromaticity i.e., the cyclic electron delocalization is due to *d* electrons rather than *p* electrons as in ordinary aromatic molecules, because they found that the diamagnetic NICS value of -14.5 ppm at the

center of the cluster seems to originate from MOs with significant 3*d* character. The self-canceling orbital contributions in the NICS treatment is probably an artifact due to an unphysical orbital decomposition.[319] A comparison of the nuclear magnetic shielding constants for the Cu atoms, σ(Cu), calculated at *ab initio* and DFT levels of theory also indicates that generalized gradient (GGA) DFT methods should not be used to assess the aromaticity properties of the Cu_4^{2-} species. Calculations of the nuclear magnetic shielding constants (σ) for Cu_4Li_2 at the DFT level using Becke's three-parameter hybrid functional (B3LYP)[320,321] yield σ(Cu) values which are 600 ppm (67%) larger than the shielding constants obtained at the BP86 GGA level.[322-324] The σ(Cu) values calculated at the HF/TZVPP, MP2/TZVPP, and CCSD/TZVPP levels are 1838, 1675, and 1690 ppm, respectively, as compared to the B3LYP/TZVPP and BP86/TZVPP values of 1473 and 881 ppm. The small σ(Cu) value obtained in the BP86 GGA DFT calculation indicates that GGA DFT calculations are not recommended for studies of the magnetic shieldings of the Cu_4^{2-} clusters, whereas the Hartree-Fock-based *ab initio* correlation methods (MP2 and CCSD) seem to yield consistent nuclear magnetic shieldings.

The orbital plot in Figure 9.4 shows that the a_{1g} orbital has a large amplitude at the center of the Cu_4Li_2 cluster. The presence of a significant amount of electron charge at the cluster center shields the external magnetic field in the NICS point. Thus, the diamagnetic shielding contribution from the a_{1g} orbital in the NICS point is due to the presence of its electrons and not due to ring currents sustained by it. However, the highest occupied molecular orbital (HOMO) belonging to the e_u irreducible representation is ring-shaped and has a significant amplitude outside the Cu_4^{2-} ring. The orbital pictures

suggest that the HOMO is sustaining the current and therefore responsible for the aromaticity properties of the Cu_4^{2-} ring.

The first-order magnetically induced current density for Cu_4Li^- was calculated at the CCSD/TZVPP level using the GIMIC method.[312] In Figure 9.5, the shape of the magnetically induced ring current passing on the open side of the Cu_4Li^- ring is compared to the corresponding curve for Al_4Li^-. The current profiles of the two species are strikingly similar. The main difference between the Cu_4^{2-} and Al_4^{2-} currents is that for Cu_4^{2-} the current in the interior of the molecular ring is weak and dominantly paramagnetic, whereas for Al_4^{2-} the ring current is diatropic both inside and outside the ring. The a_{1g} orbital (HOMO-1) of Cu_4Li^- which has large amplitudes inside the ring does apparently not sustain any strong ring current. The large ring current appearing outside the Cu_4^{2-} ring suggests that the e_u orbital (HOMO) is mainly responsible for the transport of the electrons.

The integrated ring-current strengths passing a radial cross section are given in Table 9.5. The ring-current susceptibilities of 12.6 and 10.0 nA/T for Cu_4Li^- and Cu_4Li_2, respectively, are about as large as in benzene.[312,325] The ring-current susceptibility of the Cu_4^{2-} ring is thus 2-3 times weaker than for the Al_4^{2-} species.

The explicit orbital contributions to the magnetically induced currents cannot be obtained using the GIMIC method, because orbital currents are dependent on the choice of the gauge origin[319] and the unphysical current contributions from mixing of occupied orbitals cannot be eliminated in the GIMIC scheme. The contribution from valence *s* orbitals was therefore estimated by removing them from the basis set. In the current calculations without valence *s* orbitals, the ring-current susceptibility obtained at the MP2

level is 4.0 nA/T as compared to the MP2/TZVPP value of 12.2 nA/T; the Cu_4^{2-} ring sustains a weak ring current when the valence *s* basis functions are absent.

The GIMIC calculation of the vertical current profile in Figure 9.6 shows that the current in Cu_4Li_2 is not only sustained in the ring plane, but also between the ring and the Li^+ counterions. The sharp peak at 3.5 bohr is due to the Li^+ cations. The GIMIC calculations of the current density of Cu_4Li^- show that Cu_4^{2-} can be considered to be σ aromatic. In contrast to Wannere *et al*.,[314] we find no need to invoke the *d*-orbitals in order to explain the aromaticity of planar four-membered Cu_4^{2-} rings. In the case of Au_4Na^-, the calculations show that the planar isomer of C_{2v} symmetry is the energetically lowest one. This is also in agreement with experiment, since the measured photoelectron spectra indicates that the planar Au_4Na^- is also observed experimentally.

The magnetically induced current density was also calculated for Cu_4H_4, which is a planar molecule consisting of a square-shaped Cu_4 ring with the hydrogens bridging around it at the edges. As seen in Table 9.5, the Cu_4 ring in Cu_4H_4 does not sustain any strong magnetically induced ring current. The weak diatropic current circles inside and outside the Cu_4 ring, whereas the region in the vicinity of the H atoms and outside them are dominated by the paratropic ring current. The net ring-current susceptibility for Cu_4H_4 is only -0.6 nA/T.

9.1.4 Conclusion

Two coinage and alkali metal mixed clusters (Cu_4Na^- and Au_4Na^-) produced with laser vaporization have been characterized experimentally using photoelectron spectroscopy and computationally at correlated *ab initio* levels. The comparison of

measured and calculated photoelectron spectra shows that the observed Cu_4Na^- cluster is a pyramidal species with C_{4v} symmetry, whereas the observed Au_4Na^- cluster is planar with C_{2v} symmetry.

Ab initio electron correlation calculations also predict the pyramidal Cu_4Na^- and the planar Au_4Na^- isomers to be the energetically lowest ones. At the CCSD(T)/7*s*5*p*3*d*2*f* level, the planar Au_4Na^- isomer lies 49.4 kJ/mol below the pyramidal one, whereas at extrapolated CCSD(T)/QZVPP level, the pyramidal Cu_4Na^- cluster lies 16.9 kJ/mol below the planar one. *Ab initio* calculations on Ag_4Li^- and Ag_4Na^- show that the energetics of the Ag_4^{2-} clusters are similar to those of the Cu_4^{2-} species. The pyramidal Ag_4Li^- and Ag_4Na^- clusters are thus most likely the global minima.

Calculations of the magnetically induced current density in pyramidal Cu_4Li^- (C_{4v}) and bipyramidal Cu_4Li_2 (D_{4h}) clusters using the Gauge-Including Magnetically Induced Current (GIMIC) method show that the strong ring current is sustained mainly by the highest-occupied molecular orbital dominated by Cu 4*s* character. The Cu_4^{2-} ring is σ aromatic mainly from the 4*s* bonding interactions and the *d* orbitals do not sustain any strong ring current. The aromatic character of Cu_4^{2-} can thus be explained in terms of σ aromaticity. We found no evidence of any significant current density being sustained by the *d*-orbitals.

9.2 Photoelectron Spectroscopic and Computational Studies of Sodium Auride Clusters $Na_nAu_n^-$ (n = 1–3)

9.2.1 Introduction

Relativistic effects cause the stabilization of the 6s orbital of gold, giving rise to its anomalously high electron affinity comparable to that of iodine.[326-331] Analogies between gold and halogens have been proposed since gold readily forms ionic alkali-Au compounds, in which Au acts as an electron acceptor.[332-334] Ever since the discovery of CsAu and RbAu in 1959,[335] stoichiometric alkali-gold compounds (M/Au = 1) have attracted particular attention. All of these compounds are stable and their heat of formation decreases from LiAu to CsAu.[336] Proceeding through the series from LiAu to CsAu, a metal-insulator transition occurs between KAu and RbAu.[337] The insulating CsAu and RbAu crystallize in the cubic CsCl structure, whereas the structures of the metallic NaAu and KAu are more complicated and are still not fully elucidated.[335-339] Solid CsAu possesses an indirect band gap of 2.6 eV,[340] which can only be modeled when relativistic effects are included in band-structure calculations.[341,342] NaAu has been synthesized by precipitation from liquid ammonia solutions and observed in rapidly quenched alloys.[343-345] It has a metallic appearance and retains some gold color with the electrical conductivity lying in the metallic range.[335]

Some bimetallic gold-sodium clusters have been studied in the gas phase previously.[346-350] Neutral sodium-gold Na_mAu_n clusters (m = 0–10, n = 6–13) were produced by Hoshino *et al.*,[346] who measured the ionization potentials of Na_mAu_n. Heiz *et al.*[347] investigated gold-doped alkali-metal clusters Na_nAu and Cs_nAu; they measured the ionization potentials of these clusters and performed theoretical calculations at the relativistic density-functional level. Their results indicated that the electronic structures of Na_nAu clusters are jelliumlike, whereas Cs_nAu clusters show significant ionic characters. The diatomics KAu and NaAu were studied using resonant two-photon

ionization electronic spectroscopy by Duncan and co-workers,[349] who found ionic characters in both species.

The Wang group has been interested in the electronic structure and chemical bonding of bimetallic gold clusters both theoretically and experimentally using photoelectron spectroscopy (PES) of size-selected anions.[250,351-353] In Au-Si and Au-B mixed clusters, it was found that a single gold atom can behave like a H atom to form fairly strong Au-Si or Au-B covalent bonds.[354-358] Very recently, a combined PES and *ab initio* calculations on a series of sodium-coinage metal clusters of the form NaM_4^- (M = Cu, Ag, and Au) have been reported to determine their molecular structures and analyze their aromatic properties.[359] In this section, I present a study of the finite-size analogs of the NaAu compound – free anionic and neutral stoichiometric Na_nAu_n (n = 1–3) clusters. The anionic $Na_nAu_n^-$ species were produced by laser vaporization and PES was used to probe their electronic properties. *Ab initio* calculations were carried out to elucidate the electronic and geometrical structures of both the anionic and neutral Na_nAu_n clusters for n = 1-4. Since the energy differences between the isomers are small, the interplay between experiment and theory is necessary for making the correct identification of the most stable isomers observed experimentally. The present studies on the sodium auride clusters may lead to further understanding of the electronic and structural properties of intermetallic compounds and liquid alloys, such as their ionicity and local order.[347,360]

9.2.2 Experimental Results

A. $NaAu^-$. Figure 9.7 displays the photoelectron spectra of $NaAu^-$ at the four different photon energies. The 532 nm spectrum (Figure 9.7a) shows one relatively sharp

band (X), which is broader than the instrumental resolution, suggesting it contains unresolved vibrational features. The relatively sharp onset of the X band yields an ADE of 0.62 ± 0.03 eV, which also represents the electron affinity (EA) of neutral NaAu. The band maximum defines a VDE of 0.77 ± 0.03 eV for the ground state transition. At 355 nm (Figure 9.7b), a new band (A) is observed at a VDE of 3.42 eV, which defines the first excited state of neutral NaAu with an excitation of 2.65 eV above the ground state (X). The X-A energy separation also represents an approximate measure of the gap between the highest occupied molecular orbital (HOMO) and the lowest unoccupied molecular orbital (LUMO) of NaAu. At 266 nm (Figure 9.7c), two more bands (B and C) are observed at VDE's of 3.89 and 4.32 eV, respectively. The 193 nm spectrum (Figure 9.7d) reveals more transitions at higher binding energies, but they are less well defined due to the poor signal-to-noise ratio. A band D is tentatively labeled for the sake of discussion. The ADE and VDE's are given in Table 9.6, where they are compared with theoretical calculations at different levels of theory.

B. $Na_2Au_2^-$. The photoelectron spectra of $Na_2Au_2^-$ are shown in Figure 9.8 at the four photon energies. Both the 532 and 355 nm spectra display only one relatively sharp band (X) for the ground state transition, yielding a VDE of 1.54 ± 0.03 eV and an ADE of 1.46 ± 0.03 eV. At 266 nm (Figure 9.8c), a band (A) is observed at a VDE of 4.37 eV, which represents the first excited state of Na_2Au_2 with an excitation energy of 2.83 eV. At 193 nm, an intense and sharp band (B) is observed at a VDE of 4.76 eV. Weaker and almost continuous signals are observed between 5 and 6 eV in the 193 nm spectrum, suggesting a high density of electronic state in the higher binding energy region. Two bands (C and D) are labeled for the sake of discussion. The ADE and VDE's are given in

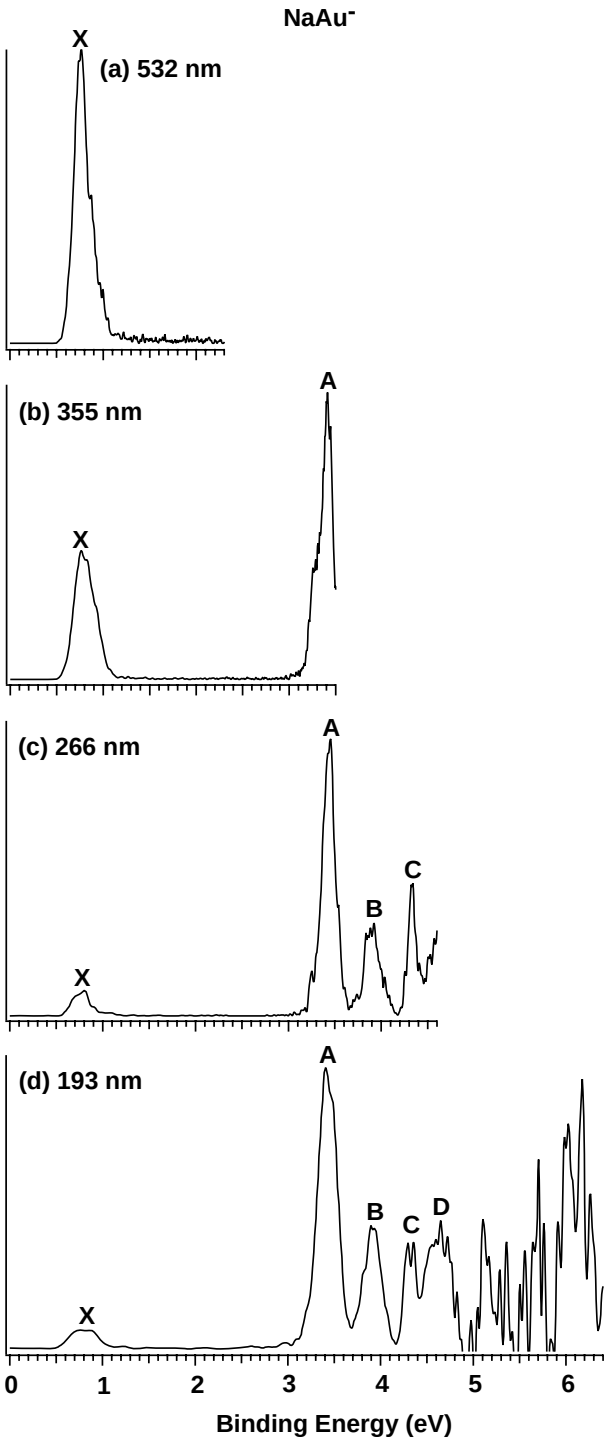

Figure 9.7 The photoelectron spectra of $NaAu^-$ measured at (a) 532 nm (2.331 eV), (b) 355 nm (3.496 eV), (c) 266 nm (4.661 eV), and (d) 193 nm (6.424 eV).

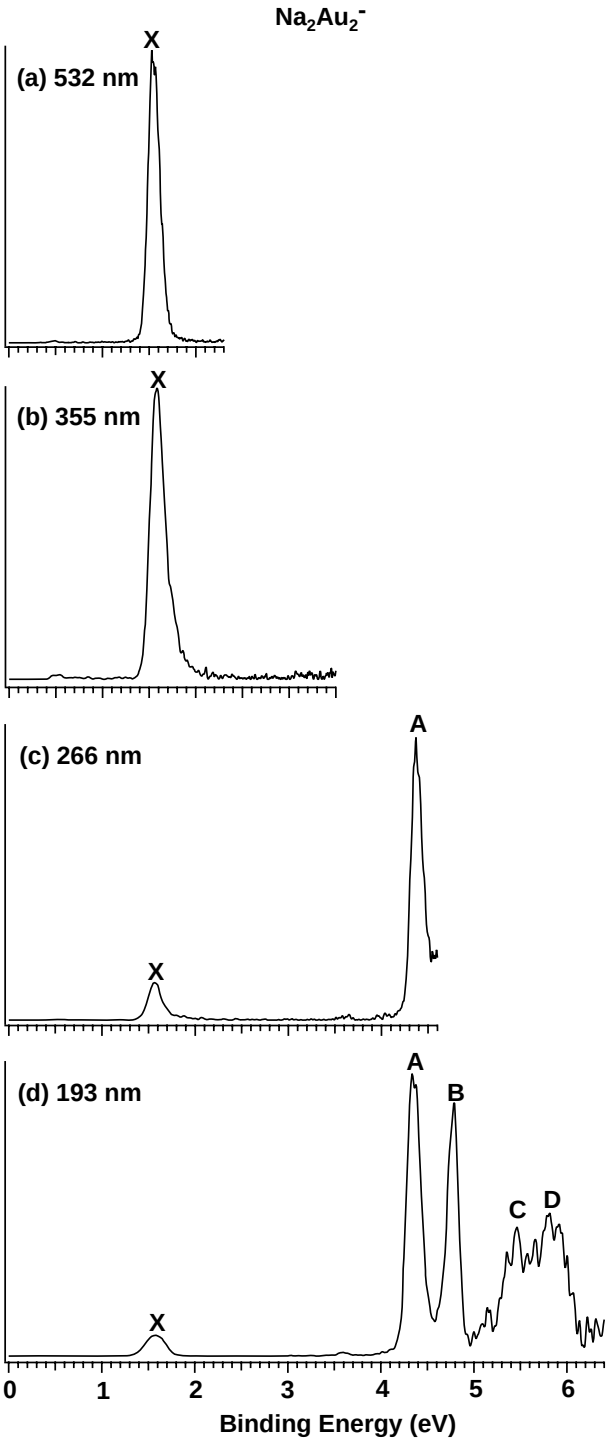

Figure 9.8 The photoelectron spectra of $Na_2Au_2^-$ measured at (a) 532 nm, (b) 355 nm, (c) 266 nm, and (d) 193 nm.

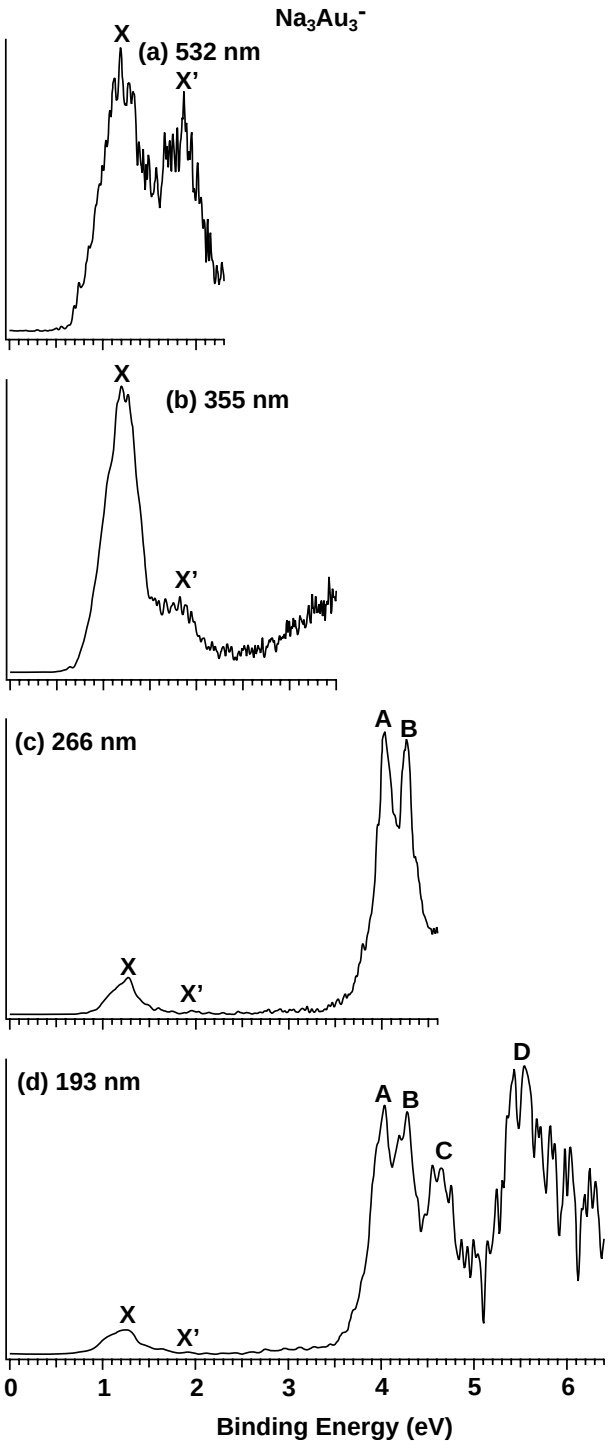

Figure 9.9 The photoelectron spectra of Na3Au3- measured at (a) 532 nm, (b) 355 nm, (c) 266 nm, and (d) 193 nm.

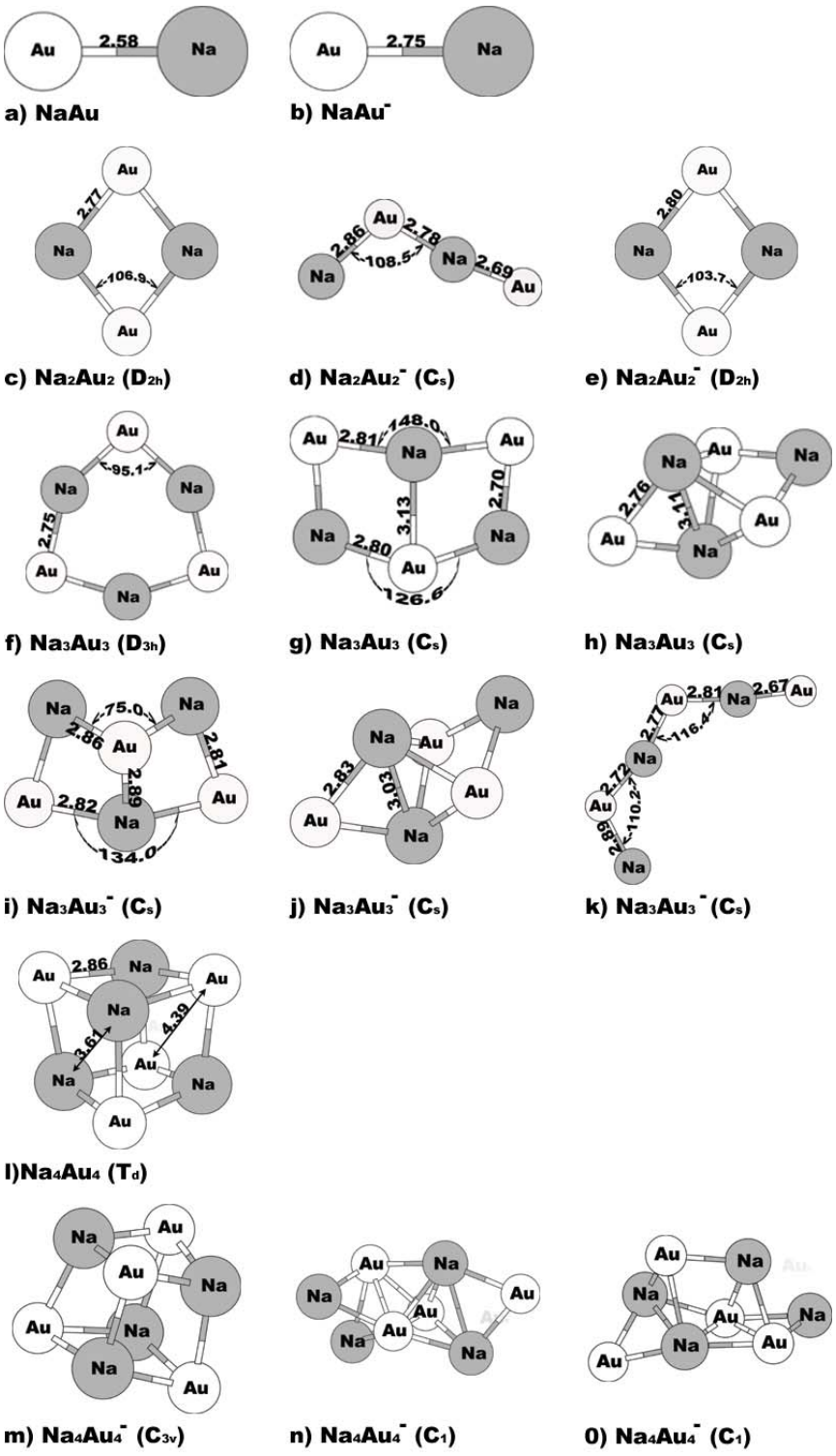

Figure 9.10 Molecular structures of Na_nAu_n and $Na_nAu_n^-$ (n = 1–4) optimized at the MP2 level. Selected bond lengths are in Å and the bond angles are in degree.

Table 9.6 Experimental ADE and VDE's of $NaAu^-$ ($C_{\infty v}$) compared with the calculated values. The VDE values were computed at the CC2/MP2 and EOMIP/CCSD levels. The singlet (S) and triplet (T) final states of NaAu were calculated at the RI-CC2 level using the $NaAu^-$ optimized structure. All energies are in eV.

	Experiment		Calculation		
	ADE	VDE	ADE (MP2)	VDE (CC2/MP2)	VDE (CCSD)
X	0.62 ± 0.03	0.77 ± 0.03	0.650	0.714	0.659
A		3.42 ± 0.03		3.417 (T)	3.572
B		3.89 ± 0.03		3.906 (S)	
C		4.32 ± 0.03		4.281 (T) 4.363 (T) 4.389 (S)	
D		~4.6		4.527 (T) 4.552 (S) 4.587 (T)	

Table 9.7 Experimental ADE and VDE's of $Na_2Au_2^-$ compared with the calculated values. The VDE values were computed at the CC2/MP2 level. The singlet (S) and triplet (T) final states of Na_2Au_2 were calculated at the RI-CC2 level using the $Na_2Au_2^-$ optimized structures. For $Na_2Au_2^-$ (C_s), the VDEs were also calculated at EOMIP/CCSD level. All energies are in eV.

	Experiment		Calculation			
			C_s		D_{2h}	
	ADE	VDE	VDE		ADE	VDE
			CC2/MP2	CCSD	MP2	CC2/MP2
X	1.46 ± 0.03	1.54 ± 0.03	1.536	1.465	0.284	0.298
A		4.37 ± 0.03	4.354 (T)	4.270		3.520 (T)
			4.401 (S)			3.902 (T)
B		4.76 ± 0.03	4.716 (T)	5.061		4.034 (S)
			4.837 (T)			4.108 (T)
C, D		~5-6	5.082 (T)	5.309		4.611 (T)
			5.145 (T)			4.651 (T)
			5.160 (S)			4.791 (T)
			5.186 (S)			4.720 (S)
			5.191 (T)			4.737 (T)
			5.200 (T)			4.818 (S)
			5.348 (S)			4.832 (S)
			5.388 (T)			4.835 (T)
			5.389 (S)			4.872 (S)
			5.390 (S)			4.891 (S)
			5.393 (T)			4.907 (T)
			5.444 (T)			
			5.458 (T)			
			5.516 (T)			
			5.555 (S)			
			5.570 (S)			
			5.650 (T)			
			5.651 (T)			
			5.679 (S)			
			5.680 (S)			
			5.698 (T)			

Table 9.8 Experimental ADE and VDE's of $Na_3Au_3^-$ compared with the calculated values. The VDE values were computed at the CC2/MP2 level. The singlet (S) and triplet (T) final states of Na_3Au_3 were calculated at the RI-CC2 level using the $Na_3Au_3^-$ optimized structures. All energies are in eV.

	Experiment		Calculation			
			C_s[a]		C_s[b]	
	ADE	VDE	ADE MP2	VDE CC2/MP2	ADE MP2	VDE CC2/MP2
X	0.79 ± 0.06	1.20 ± 0.05	0.696	1.138	0.631	0.885
X'		1.81 ± 0.05		1.862[c]		3.676 (T)
A		4.03 ± 0.03		4.023 (T)		3.989 (T)
B		4.25 ± 0.03		4.242 (T)		4.029 (S)
				4.342 (S)		4.255 (T)
C		4.61 ± 0.05		4.547 (S)		4.268 (S)
				4.684 (T)		4.348 (T)
				4.815 (T)		4.586 (T)
				4.827 (T)		4.615 (T)
				4.868 (T)		4.647 (S)
				4.956 (T)		
D		~5.4				

[a] The bent-flake isomer of C_s symmetry (Figure 9.10i).
[b] The compact isomer of C_s symmetry (Figure 9.10j).
[c] From the quasi-linear isomer (Figure 9.10k).

Table 9.9 Relative energies at RI-MP2 and CCSD levels for different isomers of $Na_nAu_n^-$ and Na_nAu_n (n = 2-4) presented in Figure 9.10. All energies are in eV.

Isomers	RI-MP2	CCSD
$Na_2Au_2^-$ (d-C_s)	0	0
(e-D_{2h})	-0.001	0.137
$Na_3Au_3^-$ (i-C_s)	0	0
(j-C_s)	-0.022	0.077
(k-C_s)	0.571	-
Na_3Au_3 (f-D_{3h})	0	0
(g-C_s)	0.007	0.089
(h-C_s)	-0.079	0.140
$Na_4Au_4^-$ (m-C_{3v})	0	-
(n-C_1)	-0.006	-
(o-C_1)	0.086	-

Table 9.7, where they are compared with theoretical calculations. Very weak signals are visible around 0.5 eV in the 532 and 355 nm spectra, as well as around 3.6 eV in the 266 and 193 nm spectra (Figure 9.8). These weak signals can be due to either impurities or weakly populated low-lying isomers. As will be shown below in the theoretical calculations (Table 9.7), these weak signals are consistent with the calculated VDE's of a low-lying D_{2h} isomer.

C. $Na_3Au_3^-$. The spectra of $Na_3Au_3^-$ become broad and more complicated, as shown in Figure 9.9 at the four photon energies. The 532 nm spectrum (Figure 9.9a) exhibits two very broad bands, labeled X and X' at VDE's of 1.20 and 1.81 eV, respectively. The ADE for band X is estimated to be 0.79 ± 0.06 eV. At 355 nm (Figure 9.9b), the band X' becomes much weaker and it is almost negligible in the 266 and 193 nm spectra, suggesting that it is due to a weakly populated isomer. The 266 nm spectrum (Figure 9.9c) reveals two overlapping bands at VDE's of 4.03 eV (A) and 4.25 eV (B), which should come from the main isomer that gives rise to band X. The X-A energy separation of 2.83 eV defines a very large HOMO-LUMO gap for Na_3Au_3, similar to that in NaAu and Na_2Au_2. In the 193 nm spectrum (Figure 9.9d), more transitions are observed, which are not well resolved. Two broad bands (C and D) can be identified, which probably contain many overlapping detachment transitions. The observed ADE and VDE's are given in Table 9.8, where they are compared with theoretical calculations.

9.2.3 Theoretical Results

A. $NaAu^-$, NaAu, $Na_2Au_2^-$, and Na_2Au_2. The molecular structures of the neutral and the anionic clusters were optimized by our collaborators at the second-order Møller-

Plesset perturbation level (MP2) using the resolution-of-the-identity approach (RI).[361] The Na-Au bond length in the neutral diatomic species is calculated to be 2.58 Å (Figure 9.10a), whereas that in the anion was found to increase to 2.75 Å (Figure 9.10b). The calculated VDE's from $NaAu^-$ are compared with the experiment in Table 9.6. For $Na_2Au_2^-$, we found two low-lying isomers: a quasi-linear structure of C_s symmetry (Figure 9.10d) and a rhombic structure of D_{2h} symmetry (Figure 9.10e). At the RI-MP2 level, the isomer of D_{2h} symmetry is 0.001 eV below the C_s one (Table 9.9). Electron correlation corrections obtained at the CCSD level shift the C_s isomer 0.137 eV below the D_{2h} one; by adding the zero-point energy corrections the splitting increases to 0.162 eV. In the RI-MP2 optimization of neutral Na_2Au_2, only one low-lying isomer was obtained, namely a rhombic species of D_{2h} symmetry (Figure 9.10c). In the structural optimization of neutral Na_2Au_2 starting from the quasi-linear C_s structure of $Na_2Au_2^-$ (Figure 9.10d) the molecular structure relaxes without any barrier towards the rhombic structure. The VDE's have been calculated for both the C_s and D_{2h} isomers of $Na_2Au_2^-$, as given in Table 9.7.

B. $Na_3Au_3^-$ and Na_3Au_3. For $Na_3Au_3^-$, the two lowest energy isomers (Figure 9.10i and 9.10j) consist of three-dimensional structures of C_s symmetry. At the RI-MP2 level, the more compact structure (Figure 9.10j) is 0.022 eV lower in energy (Table 9.9), but by considering higher-order correlation effects at the CCSD level, the bent-flake structure (Figure 9.10i) is found to be 0.077 eV below the compact one. A quasi-linear isomer for $Na_3Au_3^-$ (Figure 9.10k) was also obtained, which was found to be 0.571 eV above the lowest isomer at the RI-MP2 level (Table 9.9). For neutral Na_3Au_3, the lowest energy isomer was found to be a six-membered ring of D_{3h} symmetry (Figure 9.10f).

Another low-lying isomer (Figure 9.10g), which corresponds to the global minimum of the anion, lies only 0.089 eV higher in energy at the CCSD level. This isomer also possesses C_s symmetry, but is less bent. The compact isomer (Figure 9.10h) of Na_3Au_3 lies 0.140 eV above the D_{3h} structure at the CCSD level. The calculated ADE's and VDE's for the isomers of $Na_3Au_3^-$ are compared to the experimental data in Table 9.8.

C. $Na_4Au_4^-$ and Na_4Au_4. The molecular structures were optimized for $Na_4Au_4^-$ and Na_4Au_4 even though the anionic species was not observed in the current experiment. The lowest energy isomer of the neutral Na_4Au_4 cluster is a distorted cube with T_d symmetry (Figure 9.10l), whereas for the anion there are three nearly-degenerate isomers consisting of a slightly distorted tetrahedron of C_{3v} symmetry (Figure 9.10m) and two more irregular structures of C_1 symmetry (Figure 9.10n and 9.10o). Their relative energies at the RI-MP2 level are given in Table 9.9. The electron affinity for the Na_4Au_4 isomer with the T_d symmetry calculated at the RI-MP2 level is only 0.09 eV. The extremely low electron affinity indicates that the neutral cluster is very stable, but the anion would be very unstable, which might explain why $Na_4Au_4^-$ was not produced in the current experiment. The first VDE's for the C_{3v} and the two C_1 anionic clusters calculated at the RI-MP2 level are 0.34, 1.32 and 1.44 eV, respectively.

9.2.4 Discussion and PES Spectral Assignments

The VDE's of the energetically lowest $Na_nAu_n^-$ isomers were computed by our collaborators by adding (CC2)[361] singlet and triplet excitation energies of the neutral clusters to the first VDE of the anionic species calculated at the MP2 level. The characters of the first few excited states can be well described using single-electron

transitions. For comparison with the experimental results, the VDE's were also calculated at the equation-of-motion ionization-potential (EOMIP)/CCSD level[362] for $NaAu^-$ and $Na_2Au_2^-$. The VDE's calculated at different levels are close to each other (Tables 9.6 and 9.7). The first few VDE's calculated at the EOMIP/CCSD level agree within 0.2 eV with the experimental values, whereas the values obtained at CC2/MP2 level are in excellent agreement with the experiment. Transitions to the excited states lying at 3.5 eV or higher above the ground state are originated from electron detachments of the 5*d*-derived molecular orbitals and are highly congested, consistent with experimental observations.

A. $NaAu^-$. The ground state electron configuration of $NaAu^-$ at the Hartree-Fock level is calculated to be $6\sigma^2 3\pi^4 1\delta^4 7\sigma^2 8\sigma^1$ ($^2\Sigma$), where the 8σ orbital corresponds to the LUMO of neutral NaAu and is antibonding mainly of Na 3s character, the 7σ orbital is a bonding orbital mainly of Au 6s character, and the 1δ, 3π, and 6σ orbitals are of Au 5d character. The first band X in the PES spectra (Figure 9.7) results from the detachment of the extra electron in the 8σ orbital, resulting in the ground state of NaAu ($^1\Sigma$). The Na-Au bond length is decreased from 2.75 Å in the anion to 2.58 Å in the neutral (Figure 9.10a and 9.10b), consistent with the antibonding nature of the 8σ orbital and the unresolved vibrational progression in the X band of the PES spectra (Figure 9.7). As seen in Table 9.6, the calculated ADE (0.650 eV) at MP2 level and the VDE (0.714 eV) at the CC2/MP2 level for the ground state transition are in good agreement with the experimental data, although the calculated VDE (0.659 eV) at the CCSD level appears to be slightly underestimated.

The next detachment channel is from the doubly occupied 7σ orbital, which yields both a triplet $^3\Sigma$ ($6\sigma^2 3\pi^4 1\delta^4 7\sigma^1 8\sigma^1$) and a singlet final state $^1\Sigma$ ($6\sigma^2 3\pi^4 1\delta^4 7\sigma^1 8\sigma^1$). The

computed VDE's for these two states are in excellent agreement with the experimental values for bands A and B in the PES spectra, respectively (Table 9.6). Detachments from the Au 5d type orbitals lead to a complicated and congested set of excited states for neutral NaAu (Table 9.6), consistent with the less well resolved bands C and D. Overall, the calculated VDE's are in excellent agreement with the experimental data, verifying the validity of the theoretical methods for treating the Na-Au clusters.

B. $Na_2Au_2^-$. At the RI-MP2 level, the quasi-linear (C_s, Figure 9.10d) and the rhombic (D_{2h}, Figure 9.10e) $Na_2Au_2^-$ are almost degenerate, whereas at the CCSD level the C_s $Na_2Au_2^-$ is 0.137 eV lower in energy. The VDE calculated at the RI-MP2 level for the rhombic structure is only 0.298 eV, which is more than 1.2 eV smaller than the experimental value (Table 9.7). Therefore, the D_{2h} isomer can be firmly ruled out as the main $Na_2Au_2^-$ species observed experimentally. However, the low VDE for the D_{2h} isomer is consistent with the very weak signals observed around 0.5 eV (Figure 9.8a, b). Moreover, the calculated VDE for the second detachment channel for the D_{2h} isomer is 3.52 eV (Table 9.7), which is consistent with the weak feature at ~3.6 eV (Figure 9.8c, d). Thus, the D_{2h} isomer does seem to exist experimentally, albeit at very low abundance.

The calculated VDE for the C_s $Na_2Au_2^-$ at both the RI-MP2 (1.536 eV) and CCSD (1.465 eV) levels are in good agreement with the experimental value (Table 9.7), confirming unequivocally that the global minimum of $Na_2Au_2^-$ possesses the quasi-linear structure (Figure 9.10d). However, in our structural optimization for the neutral Na_2Au_2 starting from the C_s structure of $Na_2Au_2^-$, we found that it relaxes towards the rhombic D_{2h} structure, preventing us from computing the ADE for the C_s global minimum of $Na_2Au_2^-$. The ground state transition in the PES spectra of $Na_2Au_2^-$ yielded a fairly sharp

band (X, Figure 9.8), suggesting that the C_s structure should be a local minimum on the potential energy surface of neutral Na_2Au_2. Perhaps, the energy barrier between the C_s and C_{2h} structures are too small in the neutral for us to locate the C_s minimum in our calculation.

The ground state electron configuration of the C_s $Na_2Au_2^-$ at the Hartree-Fock level is calculated to be $8a''^2 20a'^2 21a'^2 22a'^2 23a'^1$ ($^2A'$). The 23a' orbital is primarily of Na 3s character, whereas the 22a' and 21a' orbitals are primarily of Au 6s character. Orbitals below 20a' are all of Au 5d character. The first band X in the PES spectra results from the detachment of the extra electron in the 23a' orbital. Detachment of an electron from the doubly occupied 22a' orbital produces both a triplet and a single final state with calculated VDEs at 4.354 and 4.401 eV, respectively, at the RI-MP2 level (Tables 9.7), which are in excellent agreement with the experimental VDE of the A band (4.37 eV). The calculated VDE's for the triplet final states of removing an electron from the 21a' and 20a' orbitals are very close and should correspond to the well-resolved B band in the PES spectra (Table 9.7 and Figure 9.8). Beyond 5 eV, an extremely high density of electronic states from detachment of the Au 5d type orbitals is obtained (Table 9.7), consistent with the experimental observation of nearly continuous signals between 5 and 6 eV in the 193 nm spectrum (Figure 9.8d).

C. $Na_3Au_3^-$. The global minimum of $Na_3Au_3^-$ has a bent-flake structure of C_s symmetry (Figure 9.10i). The calculated ground state VDE from this anion is 1.138 eV at RI-MP2 level, in good agreement with the first VDE of the main isomer (1.20 ± 0.05 eV) observed experimentally (Table 9.8). The calculated ADE at RI-MP2 level for the bent-flake global minimum is 0.696 eV, consistent with the experimental value of 0.79 ±

0.06 eV. For the more compact $Na_3Au_3^-$ isomer (Figure 9.10j), the calculated first VDE at RI-MP2 level is 0.885 eV. If we examine the PES spectra carefully in Figure 9.9, there seem to be a shoulder on the leading edge of the X band, which could hint the presence of this more compact isomer, which is only 0.077 eV above the global minimum (Table 9.9). However, the overlap of this transition with the dominating transition (X) from the global minimum prevents us from a definitive assignment.

The extra band (X') with a VDE of 1.81 eV observed more prominently in the 532 nm spectrum (Figure 9.9) must be due to another isomer, since no such VDE is obtained in the calculations from the two C_s isomers. The calculated first VDE from the quasi-linear isomer (Figure 9.10k) is 1.862 eV at RI-MP2 level, in excellent agreement with the X' band. The quasi-linear isomer is a minimum on the potential-energy surface since no imaginary vibrational frequencies are obtained in the calculation. However, it is surprising that this isomer is present at all because it lies 0.571 eV above the global minimum at the RI-MP2 level (Table 9.9). The observation of the quasi-linear isomer of $Na_3Au_3^-$ may be understood from a kinetic point of view because it can be viewed as simply adding a NaAu unit to the quasi-linear $Na_2Au_2^-$ (Figure 9.10d). There may exist a significant barrier preventing the quasi-linear $Na_3Au_3^-$ from completely converting to the global minimum bent-flake structure. In any case, the 266 and 193 nm spectra (Figure 9.9) suggest that the presence of the higher energy isomers is negligible since the X band from the global minimum dominates in the low binding energy range. Therefore, the main features in the higher binding energy range observed in the 266 and 193 nm spectra should all primarily come from the bent-flake isomer.

The ground state electron configuration of the bent-flake global minimum of $Na_3Au_3^-$ (Figure 9.10i) at the Hartree-Fock level is calculated to be $18a''^2 25a'^2 19a''^2 26a'^2 27a'^1$ ($^2A'$), where the 27a', 26a', 19a", and 25a' are mainly of Au 6s and Na 3s characters, and the 18a" orbital and deeper MO's are mainly due to the Au 5d. Detachment from the 27a' orbital with a calculated VDE of 1.138 eV yields the ground state band (X) in the PES spectra of $Na_3Au_3^-$ (Tables 9.8). The second detachment channel is from the 26a' orbital, which results in a triplet final state with a calculated VDE of 4.023 eV and a singlet final state with a calculated VDE of 4.342 eV (Table 9.8). The calculated VDE from the triplet final state is in excellent agreement with the VDE measured for the A band (4.03 eV), whereas the singlet state may contribute to the B band (VDE: 4.25 eV). The next detachment channel is from the 19a" orbital, which also leads to a triplet and singlet final state with calculated VDE's of 4.242 and 4.547 eV, respectively (Tables 9.8). The calculated VDE for the triplet final state of this detachment channel is in excellent agreement with the measured VDE of the B and (4.25 eV), whereas the singlet final state is in good agreement with band C. Our calculations show that beyond 4.5 eV there is a high density of electronic states, consistent with the congested spectral features in the high binding energy side in the 193 nm spectrum (Figure 9.9).

D. Chemical Bonding in the Na_nAu_n and $Na_nAu_n^-$ Clusters. The excellent agreement between the theoretical calculations and the experimental PES data provide significant credence for the identified global minimum structures for the $Na_nAu_n^-$ and Na_nAu_n clusters. We note that the potential energy surfaces of the anions and the neutral are quite different for the n = 2 and 3 cases. Small sodium auride clusters are expected to

have significant ionic characters because the electron affinity of gold is much larger than that of sodium. Our calculations suggest that Na and Au atoms in small neutral Na_nAu_n show significant ionic interactions and can be viewed as $(Na^+Au^-)_n$. For neutral NaAu, the numerical integration of the charge density shows that Na is positively charged with a net charge of about +0.7 |e|. Earlier studies on gold-alkali metal species also indicated that charge is transferred from the alkali metal to the gold atom.[347,349] The neutral Na_2Au_2 and Na_3Au_3 clusters adopt planar D_{2h} and D_{3h} ring structures and Na_4Au_4 possesses an almost cubic T_d structure, which are similar to those of the corresponding $(NaCl)_n$ clusters.[363] In the small anionic $Na_nAu_n^-$ clusters (n = 1, 2) the extra electron goes to the Na site and the sodium atoms remain practically neutral, whereas the extra charge is carried by the Au atoms. Addition of one extra electron to Na_2Au_2 produces a Na-Au-Na-Au^- quasi-linear structure. The Au atom at the end of the quasi-linear structure (Figure 9.10d) has a charge surplus of 0.3 electron and the net charge of the middle Au atom is -0.7 |e|. Our calculations show that $Na_3Au_3^-$ also has a low-lying quasi-linear isomer, which is observed experimentally and can be viewed as the extension of the global minimum of $Na_2Au_2^-$ by one NaAu unit.

9.2.5 Conclusion

Photoelectron spectroscopy has been combined with high-level *ab initio* calculations to examine the electronic and atomic structures of a series of stoichiometric sodium auride clusters, $Na_nAu_n^-$ (n = 1 - 3). Well-resolved photoelectron spectra have been obtained and are compared with *ab initio* calculations at several levels of sophistication to confirm the global minima of the anionic and neutral clusters. The

lowest energy isomer of $Na_2Au_2^-$ was identified as a quasi-linear molecule of C_s symmetry. A planar isomer of D_{2h} symmetry lies 0.137 eV higher in energy. The two lowest energy isomers of $Na_3Au_3^-$ consist of three-dimensional structures of C_s symmetry. The energetically lowest one has a bent-flake structure and lies only 0.077 eV below a compact cluster structure of C_s symmetry. A quasi-linear isomer was also observed for $Na_3Au_3^-$ experimentally and was born out from our calculations. The potential energy surfaces for the neutral clusters are found to be quite different from that of the anions for Na_2Au_2 and Na_3Au_3. Molecular structure calculations of neutral Na_2Au_2 yielded a planar four-membered ring of D_{2h} symmetry. For neutral Na_3Au_3, the lowest energy isomer consists of a planar six-membered ring of D_{3h} symmetry.

REFERENCES

[1] J. Jellinek, *Theory of Atomic and Molecular Clusters with a Glimplse at Experiments*, Springer Series in Cluster Physics (Springer, Berlin, 1999).

[2] *Metal Clusters at Surfaces*, edited by K.-H. Meiwes-Broer, Springer series in Cluster Physics (Springer, Berlin, 1999).

[3] W. A. Deheer, W. D. Knight, M. Y. Chou, and M. L. Cohen, *Solid State Physics-Advances in Research and Applications* **40**, 93 (1987).

[4] W. A. Deheer, *Reviews of Modern Physics* **65**, 611 (1993).

[5] W. D. Knight, K. Clemenger, W. A. Deheer, W. A. Saunders, M. Y. Chou, and M. L. Cohen, *Phys. Rev. Lett.* **52**, 2141 (1984).

[6] V. Bonacickoutecky, P. Fantucci, and J. Koutecky, *Chem. Rev.* **91**, 1035 (1991).

[7] W. Ekardt, *Physical Review B* **29**, 1558 (1984).

[8] M. L. Cohen, M. Y. Chou, W. D. Knight, and W. A. Deheer, *J. Phys. Chem.* **91**, 3141 (1987).

[9] S. H. Joo, S. J. Choi, I. Oh, J. Kwak, Z. Liu, O. Terasaki, and R. Ryoo, *Nature* **414**, 470 (2001).

[10] M. Valden, X. Lai, and D. W. Goodman, *Science* **281**, 1647 (1998).

[11] H. W. Kroto, J. R. Heath, S. C. Obrien, R. F. Curl, and R. E. Smalley, *Nature* **318**, 162 (1985).

[12] X. Li, L. S. Wang, A. I. Boldyrev, and J. Simons, *J. Am. Chem. Soc.* **121**, 6033 (1999).

[13] L. S. Wang, A. I. Boldyrev, X. Li, and J. Simons, *J. Am. Chem. Soc.* **122**, 7681 (2000).

[14] X. Li, H. J. Zhai, and L. S. Wang, *Chem. Phys. Lett.* **357**, 415 (2002).

[15] H. Hakkinen, M. Moseler, and U. Landman, *Phys. Rev. Lett.* **89** (2002).

[16] F. Furche, R. Ahlrichs, P. Weis, C. Jacob, S. Gilb, T. Bierweiler, and M. M. Kappes, *J. Chem. Phys.* **117**, 6982 (2002).

[17] H. Hakkinen, B. Yoon, U. Landman, X. Li, H. J. Zhai, and L. S. Wang, *J. Phys. Chem. A* **107**, 6168 (2003).

[18] H. J. Zhai, A. N. Alexandrova, K. A. Birch, A. I. Boldyrev, and L. S. Wang, *Angewandte Chemie-International Edition* **42**, 6004 (2003).

[19] H. J. Zhai, B. Kiran, J. Li, and L. S. Wang, *Nature Materials* **2**, 827 (2003).

[20] X. Li, A. E. Kuznetsov, H. F. Zhang, A. I. Boldyrev, and L. S. Wang, *Science* **291**, 859 (2001).

[21] A. E. Kuznetsov, A. I. Boldyrev, X. Li, and L. S. Wang, *J. Am. Chem. Soc.* **123**, 8825 (2001).

[22] J. Li, X. Li, H. J. Zhai, and L. S. Wang, *Science* **299**, 864 (2003).

[23] B. Kiran, S. Bulusu, H. J. Zhai, S. Yoo, X. C. Zeng, and L. S. Wang, *Proceedings of the National Academy of Sciences of the United States of America* **102**, 961 (2005).

[24] D. E. Bergeron, A. W. Castleman, T. Morisato, and S. N. Khanna, *Science* **304**, 84 (2004).

[25] *Advances in Metal and Semiconductor Clusters*, edited by M. A. Duncan, Volumes 1-4, Published by JAI Press Inc. (1993-1998).

[26] *Advances in Metal and Semiconductor Clusters*, edited by M. A. Duncan, Volume 5, Published by Elsevier Science Publishers (2001).

[27] J. H. D. Eland, *Photoelectron Spectroscopy* (Butterworths, London, 1984).

[28] D. G. Leopold, J. Ho, and W. C. Lineberger, *J. Chem. Phys.* **86**, 1715 (1987).

[29] C. L. Pettiette, S. H. Yang, M. J. Craycraft, J. Conceicao, R. T. Laaksonen, O. Cheshnovsky, and R. E. Smalley, *J. Chem. Phys.* **88**, 5377 (1988).

[30] G. Gantefor, M. Gausa, K. H. Meiwesbroer, and H. O. Lutz, *Journal of the Chemical Society-Faraday Transactions* **86**, 2483 (1990).

[31] T. P. Lippa, S. J. Xu, S. A. Lyapustina, J. M. Nilles, and K. H. Bowen, *J. Chem. Phys.* **109**, 10727 (1998).

[32] K. R. Asmis, N. L. Pivonka, G. Santambrogio, M. Brummer, C. Kaposta, D. M. Neumark, and L. Woste, *Science* **299**, 1375 (2003).

[33] D. H. Paik, I. R. Lee, D. S. Yang, J. S. Baskin, and A. H. Zewail, *Science* **306**, 672 (2004).

[34] G. Markovich, R. Giniger, M. Levin, and O. Cheshnovsky, *J. Chem. Phys.* **95**, 9416 (1991).

[35] A. Nakajima, T. Taguwa, K. Hoshino, T. Sugioka, T. Naganuma, F. Ono, K. Watanabe, K. Nakao, Y. Konishi, R. Kishi, and K. Kaya, *Chem. Phys. Lett.* **214**, 22 (1993).

[36] H. B. Wu, S. R. Desai, and L. S. Wang, *Phys. Rev. Lett.* **77**, 2436 (1996).

[37] M. A. Hoffmann, G. Wrigge, B. von Issendorff, J. Muller, G. Gantefor, and H. Haberland, *European Physical Journal D* **16**, 9 (2001).

[38] H. Prinzbach, A. Weller, P. Landenberger, F. Wahl, J. Worth, L. T. Scott, M. Gelmont, D. Olevano, and B. von Issendorff, *Nature* **407**, 60 (2000).

[39] G. Gantefor and W. Eberhardt, *Phys. Rev. Lett.* **76**, 4975 (1996).

[40] L. S. Wang, H. S. Cheng, and J. W. Fan, *J. Chem. Phys.* **102**, 9480 (1995).

[41] D. M. Neumark, *High Resolution Photodetachment Studies of Molecular Negative Ions*, in "Ion and Cluster Ion Spectroscopy and Structure" (Elsevier, Amsterdam, 1989).

[42] S. G. Li, J. F. Fuller, X. Wang, B. R. Sohnlein, P. Bhowmik, and D. S. Yang, *J. Chem. Phys.* **121**, 7692 (2004).

[43] A. H. Zewail, *J. Phys. Chem. A* **104**, 5660 (2000).

[44] B. J. Greenblatt, M. T. Zanni, and D. M. Neumark, *Science* **276**, 1675 (1997).

[45] N. Pontius, P. S. Bechthold, M. Neeb, and W. Eberhardt, *Phys. Rev. Lett.* **84**, 1132 (2000).

[46] *Cluster of Atoms and Molecules* ***I***, edited by H. Haberland, Springer Series in Chemical Physics 52 (Springer, Berlin, 1995).

[47] M. B. Knickelbein, *Philosophical Magazine B-Physics of Condensed Matter Statistical Mechanics Electronic Optical and Magnetic Properties* **79**, 1379 (1999).

[48] D. M. Cox, D. J. Trevor, R. L. Whetten, E. A. Rohlfing, and A. Kaldor, *Physical Review B* **32**, 7290 (1985).

[49] J. P. Bucher, D. C. Douglass, and L. A. Bloomfield, *Phys. Rev. Lett.* **66**, 3052 (1991).

[50] I. M. L. Billas, A. Chatelain, and W. A. Deheer, *Science* **265**, 1682 (1994).

[51] M. B. Knickelbein, *J. Chem. Phys.* **115**, 1983 (2001).

[52] M. B. Knickelbein, *Phys. Rev. Lett.* **86**, 5255 (2001).

[53] E. K. Parks, B. J. Winter, T. D. Klots, and S. J. Riley, *J. Chem. Phys.* **94**, 1882 (1991).

[54] R. H. Schultz, K. C. Crellin, and P. B. Armentrout, *J. Am. Chem. Soc.* **113**, 8590 (1991).

[55] T. E. Gough, M. Mengel, P. A. Rowntree, and G. Scoles, *J. Chem. Phys.* **83**, 4958 (1985).

[56] G. V. Chertihin and L. Andrews, *J. Chem. Phys.* **106**, 3457 (1997).

[57] Z. D. Hu, B. Shen, J. R. Lombardi, and D. M. Lindsay, *J. Chem. Phys.* **96**, 8757 (1992).

[58] G. von Helden, D. van Heijnsbergen, and G. Meijer, *J. Phys. Chem. A* **107**, 1671 (2003).

[59] M. E. A and M. E. W., *Transport Properties of Ions in Gases* (Wiley, New York, 1988).

[60] P. R. Kemper and M. T. Bowers, *J. Phys. Chem.* **95**, 5134 (1991).

[61] J. Hunter, J. Fye, and M. F. Jarrold, *Science* **260**, 784 (1993).

[62] M. F. Jarrold and J. E. Bower, *J. Chem. Phys.* **96**, 9180 (1992).

[63] P. Dugourd, R. R. Hudgins, D. E. Clemmer, and M. F. Jarrold, *Rev. Sci. Instrum.* **68**, 1122 (1997).

[64] T. P. Martin, T. Bergmann, H. Gohlich, and T. Lange, *J. Phys. Chem.* **95**, 6421 (1991).

[65] E. K. Parks, L. Zhu, J. Ho, and S. J. Riley, *J. Chem. Phys.* **102**, 7377 (1995).

[66] E. K. Parks, L. Zhu, J. Ho, and S. J. Riley, *J. Chem. Phys.* **100**, 7206 (1994).

[67] E. K. Parks, L. Zhu, J. Ho, and S. J. Riley, *Zeitschrift Fur Physik D-Atoms Molecules and Clusters* **26**, 41 (1993).

[68] E. K. Parks, B. J. Winter, T. D. Klots, and S. J. Riley, *J. Chem. Phys.* **96**, 8267 (1992).

[69] T. D. Klots, B. J. Winter, E. K. Parks, and S. J. Riley, *J. Chem. Phys.* **95**, 8919 (1991).

[70] B. J. Winter, T. D. Klots, E. K. Parks, and S. J. Riley, *Zeitschrift Fur Physik D-Atoms Molecules and Clusters* **19**, 375 (1991).

[71] M. F. Jarrold and J. E. Bower, *J. Phys. Chem.* **97**, 1746 (1993).

[72] M. F. Jarrold and J. E. Bower, *J. Chem. Phys.* **98**, 2399 (1993).

[73] J. Lerme, C. Bordas, M. Pellarin, B. Baguenard, J. L. Vialle, and M. Broyer, *Physical Review B* **48**, 12110 (1993).

[74] B. Baguenard, M. Pellarin, C. Bordas, J. Lerme, J. L. Vialle, and M. Broyer, *Chem. Phys. Lett.* **205**, 13 (1993).

[75] M. Pellarin, B. Baguenard, C. Bordas, M. Broyer, J. Lerme, and J. L. Vialle, *Zeitschrift Fur Physik D-Atoms Molecules and Clusters* **26**, S137 (1993).

[76] K. Rademann, M. Ruppel, and B. Kaiser, *Berichte Der Bunsen-Gesellschaft-Physical Chemistry Chemical Physics* **96**, 1204 (1992).

[77] B. Baguenard, M. Pellarin, J. Lerme, J. L. Vialle, and M. Broyer, *J. Chem. Phys.* **100**, 754 (1994).

[78] G. Vonhelden, M. T. Hsu, N. Gotts, and M. T. Bowers, *J. Phys. Chem.* **97**, 8182 (1993).

[79] M. F. Jarrold and V. A. Constant, *Phys. Rev. Lett.* **67**, 2994 (1991).

[80] J. M. Hunter, J. L. Fye, M. F. Jarrold, and J. E. Bower, *Phys. Rev. Lett.* **73**, 2063 (1994).

[81] M. F. Jarrold, *Science* **252**, 1085 (1991).

[82] E. C. Honea, A. Ogura, C. A. Murray, K. Raghavachari, W. O. Sprenger, M. F. Jarrold, and W. L. Brown, *Nature* **366**, 42 (1993).

[83] J. Muller, B. Liu, A. A. Shvartsburg, S. Ogut, J. R. Chelikowsky, K. W. M. Siu, K. M. Ho, and G. Gantefor, *Phys. Rev. Lett.* **85**, 1666 (2000).

[84] G. R. Burton, C. S. Xu, and D. M. Neumark, *Surf. Rev. Lett.* **3**, 383 (1996).

[85] K. M. Ho, A. A. Shvartsburg, B. C. Pan, Z. Y. Lu, C. Z. Wang, J. G. Wacker, J. L. Fye, and M. F. Jarrold, *Nature* **392**, 582 (1998).

[86] W. C. Wiley and I. H. McLaren, *Rev. Sci. Instrum.* **26**, 1150 (1955).

[87] W. A. Deheer and P. Milani, *Rev. Sci. Instrum.* **62**, 670 (1991).

[88] L. S. Wang and H. Wu, *Cluster Materials, Advances in Metal and Semiconductor Clusters, Vol. **4**, edited by M. A. Duncan* (Jai Press, Greenwich, 1998).

[89] L. S. Zheng, C. M. Karner, P. J. Brucat, S. H. Yang, C. L. Pettiette, M. J. Craycraft, and R. E. Smalley, *J. Chem. Phys.* **85**, 1681 (1986).

[90] S. H. Yang, C. L. Pettiette, J. Conceicao, O. Cheshnovsky, and R. E. Smalley, *Chem. Phys. Lett.* **139**, 233 (1987).

[91] G. Markovich, S. Pollack, R. Giniger, and O. Cheshnovsky, *J. Chem. Phys.* **101**, 9344 (1994).

[92] P. Kruit and F. H. Read, *Journal of Physics E-Scientific Instruments* **16**, 313 (1983).

[93] O. Cheshnovsky, S. H. Yang, C. L. Pettiette, M. J. Craycraft, and R. E. Smalley, *Rev. Sci. Instrum.* **58**, 2131 (1987).

[94] C. E. Moor, *Atomic Energy Levels, Vol II* (US GPO, Washington D. C., 1971).

[95] J. Akola, M. Manninen, H. Hakkinen, U. Landman, X. Li, and L. S. Wang, *Physical Review B* **60**, 11297 (1999).

[96] W. L. Brown, R. R. Freeman, K. Raghavachari, and M. Schluter, *Science* **235**, 860 (1987).

[97] Q. L. Zhang, Y. Liu, R. F. Curl, F. K. Tittel, and R. E. Smalley, *J. Chem. Phys.* **88**, 1670 (1988).

[98] K. Raghavachari and C. M. Rohlfing, *J. Chem. Phys.* **89**, 2219 (1988).

[99] M. F. Jarrold and E. C. Honea, *J. Phys. Chem.* **95**, 9181 (1991).

[100] B. Marsen, M. Lonfat, P. Scheier, and K. Sattler, *Physical Review B* **62**, 6892 (2000).

[101] M. Maus, G. Gantefor, and W. Eberhardt, *Applied Physics a-Materials Science & Processing* **70**, 535 (2000).

[102] N. Binggeli, J. L. Martins, and J. R. Chelikowsky, *Phys. Rev. Lett.* **68**, 2956 (1992).

[103] N. Binggeli and J. R. Chelikowsky, *Phys. Rev. Lett.* **75**, 493 (1995).

[104] S. Ogut, J. R. Chelikowsky, and S. G. Louie, *Phys. Rev. Lett.* **79**, 1770 (1997).

[105] G. Meloni, M. J. Ferguson, S. M. Sheehan, and D. M. Neumark, *Chem. Phys. Lett.* **399**, 389 (2004).

[106] L. Mitas, J. C. Grossman, I. Stich, and J. Tobik, *Phys. Rev. Lett.* **84**, 1479 (2000).

[107] I. Rata, A. A. Shvartsburg, M. Horoi, T. Frauenheim, K. W. M. Siu, and K. A. Jackson, *Phys. Rev. Lett.* **85**, 546 (2000).

[108] K. A. Jackson, M. Horoi, I. Chaudhuri, T. Frauenheim, and A. A. Shvartsburg, *Phys. Rev. Lett.* **93** (2004).

[109] S. Yoo, J. J. Zhao, J. L. Wang, and X. C. Zeng, *J. Am. Chem. Soc.* **126**, 13845 (2004).

[110] J. Zhao, J. Wang, J. Jellinek, S. Yoo, and X. C. Zeng, *European Physical Journal D* **34**, 35 (2005).

[111] S. H. Yoo and X. C. Zeng, *Angewandte Chemie-International Edition* **44**, 1491 (2005).

[112] R. R. Hudgins, M. Imai, M. F. Jarrold, and P. Dugourd, *J. Chem. Phys.* **111**, 7865 (1999).

[113] D. Tomanek and M. A. Schluter, *Phys. Rev. Lett.* **56**, 1055 (1986).

[114] U. Rothlisberger, W. Andreoni, and M. Parrinello, *Phys. Rev. Lett.* **72**, 665 (1994).

[115] S. Yoo, X. C. Zeng, X. L. Zhu, and J. Bai, *J. Am. Chem. Soc.* **125**, 13318 (2003).

[116] C. C. Arnold, T. N. Kitsopoulos, and D. M. Neumark, *J. Chem. Phys.* **99**, 766 (1993).

[117] A. I. Boldyrev and L. S. Wang, *J. Phys. Chem. A* **105**, 10759 (2001).

[118] P. H. Acioli and J. Jellinek, *Phys. Rev. Lett.* **89** (2002).

[119] D. J. Wales and H. A. Scheraga, *Science* **285**, 1368 (1999).

[120] S. Goedecker, *J. Chem. Phys.* **120**, 9911 (2004).

[121] J. Hutter, A. Alavi, T. Deutsch, M. Bernasconi, S. Goedecker, D. Marx, M. Tuckerman, and M. Parrinello, *CPMD*; Max-Planck-Institue fur Festkorperforschung; Stuttart; Version 3.9.1 (1997-2001).

[122] D. Porezag, T. Frauenheim, T. Kohler, G. Seifert, and R. Kaschner, *Physical Review B* **51**, 12947 (1995).

[123] M. J. Frisch *et al.*, *Gaussian 03*, Revision C.02; Gaussian, Inc.: Wallingford, CT, (2004).

[124] T. N. Kitsopoulos, C. J. Chick, A. Weaver, and D. M. Neumark, *J. Chem. Phys.* **93**, 6108 (1990).

[125] C. S. Xu, T. R. Taylor, G. R. Burton, and D. M. Neumark, *J. Chem. Phys.* **108**, 1395 (1998).

[126] O. Cheshnovsky, S. H. Yang, C. L. Pettiette, M. J. Craycraft, Y. Liu, and R. E. Smalley, *Chem. Phys. Lett.* **138**, 119 (1987).

[127] S. Li, R. J. Vanzee, W. Weltner, and K. Raghavachari, *Chem. Phys. Lett.* **243**, 275 (1995).

[128] A. A. Shvartsburg, B. Liu, M. F. Jarrold, and K. M. Ho, *J. Chem. Phys.* **112**, 4517 (2000).

[129] M. Menon and K. R. Subbaswamy, *Physical Review B* **51**, 17952 (1995).

[130] D. K. Yu, R. Q. Zhang, and S. T. Lee, *Physical Review B* **65** (2002).

[131] Q. Sun, Q. Wang, P. Jena, B. K. Rao, and Y. Kawazoe, *Phys. Rev. Lett.* **90** (2003).

[132] E. D. Jemmis, B. V. Prasad, S. Tsuzuki, and K. Tanabe, *J. Phys. Chem.* **94**, 5530 (1990).

[133] F. A. Cotton, G. Wilkinson, C. A. Murillo, and M. Bochmann, *Advanced Inorganic Chemistry, 6th ed.;* (Wiley-Interscience, New York, 1999).

[134] D. Y. Zubarev and A. I. Boldyrev, *Unpublished results*.

[135] J. M. Goicoechea and S. C. Sevov, *J. Am. Chem. Soc.* **126**, 6860 (2004).

[136] R. Kishi, H. Kawamata, Y. Negishi, S. Iwata, A. Nakajima, and K. Kaya, *J. Chem. Phys.* **107**, 10029 (1997).

[137] S. D. Li, Q. L. Guo, X. F. Zhao, H. S. Wu, and Z. H. Jin, *J. Chem. Phys.* **117**, 606 (2002).

[138] S. D. Li, G. M. Ren, and Z. H. Jin, *J. Chem. Phys.* **119**, 10063 (2003).

[139] L. Kronik, R. Fromherz, E. Ko, G. Gantefor, and J. R. Chelikowsky, *European Physical Journal D* **24**, 33 (2003).

[140] A. Tekin and B. Hartke, *PCCP* **6**, 503 (2004).

[141] C. Pouchan, D. Begue, and D. Y. Zhang, *J. Chem. Phys.* **121**, 4628 (2004).

[142] C. Majumder and S. K. Kulshreshtha, *Physical Review B* **69** (2004).

[143] N. N. Nair, T. Bredow, and K. Jug, *J. Comput. Chem.* **25**, 1255 (2004).

[144] K. Raghavachari, *Zeitschrift Fur Physik D-Atoms Molecules and Clusters* **12**, 61 (1989).

[145] B. X. Li, P. L. Cao, B. Song, and Z. Z. Ye, *Phys. Lett. A* **307**, 318 (2003).

[146] K. Raghavachari and V. Logovinsky, *Phys. Rev. Lett.* **55**, 2853 (1985).

[147] H. X. Wang and R. P. Messmer, *Physical Review B* **41**, 5306 (1990).

[148] C. H. Patterson and R. P. Messmer, *Physical Review B* **42**, 7530 (1990).

[149] R. B. King, T. Heine, C. Corminboeuf, and P. V. Schleyer, *J. Am. Chem. Soc.* **126**, 430 (2004).

[150] W. N. Lipscomb, *Boron Hydrides* (Benjamin, New York, 1963).

[151] E. L. Muetterties, *Boron Hydride Chemistry* (Academic Press, New York, 1975).

[152] K. Wade, *Journal of the Chemical Society D-Chemical Communications*, 792 (1971).

[153] Z. F. Chen, H. J. Jiao, A. Hirsch, and W. Thiel, *J. Mol. Model.* **7**, 161 (2001).

[154] A. Hirsch, Z. F. Chen, and H. J. Jiao, *Angewandte Chemie-International Edition* **40**, 2834 (2001).

[155] R. B. King and D. H. Rouvray, *J. Am. Chem. Soc.* **99**, 7834 (1977).

[156] J. Aihara, *J. Am. Chem. Soc.* **100**, 3339 (1978).

[157] S. Q. Wei, R. N. Barnett, and U. Landman, *Physical Review B* **55**, 7935 (1997).

[158] B. X. Li and P. L. Cao, *Physical Review B* **62**, 15788 (2000).

[159] L. A. Bloomfield, M. E. Geusic, R. R. Freeman, and W. L. Brown, *Chem. Phys. Lett.* **121**, 33 (1985).

[160] W. D. Reents and V. E. Bondybey, *Chem. Phys. Lett.* **125**, 324 (1986).

[161] D. E. Bergeron and A. W. Castleman, *J. Chem. Phys.* **117**, 3219 (2002).

[162] E. C. Honea, A. Ogura, D. R. Peale, C. Felix, C. A. Murray, K. Raghavachari, W. O. Sprenger, M. F. Jarrold, and W. L. Brown, *J. Chem. Phys.* **110**, 12161 (1999).

[163] C. Y. Zhao and K. Balasubramanian, *J. Chem. Phys.* **116**, 3690 (2002).

[164] A. I. Boldyrev and L. S. Wang, *Chem. Rev.* **105**, 3716 (2005).

[165] H. J. Zhai, A. E. Kuznetsov, A. I. Boldyrev, and L. S. Wang, *Chemphyschem* **5**, 1885 (2004).

[166] D. Y. Zubarev, A. I. Boldyrev, X. Li, L. F. Cui, and L. S. Wang, *J. Phys. Chem. A* **109**, 11385 (2005).

[167] A. A. Shvartsburg, B. Liu, Z. Y. Lu, C. Z. Wang, M. F. Jarrold, and K. M. Ho, *Phys. Rev. Lett.* **83**, 2167 (1999).

[168] G. Kohl, *Zeitschrift Fur Naturforschung Section a-a Journal of Physical Sciences* **9**, 913 (1954).

[169] A. Kant and B. H. Strauss, *J. Chem. Phys.* **45**, 822 (1966).

[170] J. E. Kingcade, U. V. Choudary, and K. A. Gingerich, *Inorg. Chem.* **18**, 3094 (1979).

[171] K. A. Gingerich, I. Shim, S. K. Gupta, and J. E. Kingcade, *Surf. Sci.* **156**, 495 (1985).

[172] J. R. Heath, Y. Liu, S. C. Obrien, Q. L. Zhang, R. F. Curl, F. K. Tittel, and R. E. Smalley, *J. Chem. Phys.* **83**, 5520 (1985).

[173] T. P. Martin and H. Schaber, *J. Chem. Phys.* **83**, 855 (1985).

[174] J. E. Kingcade, H. M. Nagarathnanaik, I. Shim, and K. A. Gingerich, *J. Phys. Chem.* **90**, 2830 (1986).

[175] T. M. Miller, A. E. S. Miller, and W. C. Lineberger, *Physical Review A* **33**, 3558 (1986).

[176] C. C. Arnold, C. S. Xu, G. R. Burton, and D. M. Neumark, *J. Chem. Phys.* **102**, 6982 (1995).

[177] G. R. Burton, C. S. Xu, C. C. Arnold, and D. M. Neumark, *J. Chem. Phys.* **104**, 2757 (1996).

[178] Y. Negishi, H. Kawamata, T. Hayase, M. Gomei, R. Kishi, F. Hayakawa, A. Nakajima, and K. Kaya, *Chem. Phys. Lett.* **269**, 199 (1997).

[179] K. Kaya, H. Kawamata, Y. Negishi, T. Hayase, R. Kishi, and A. Nakajima, *Zeitschrift Fur Physik D-Atoms Molecules and Clusters* **40**, 5 (1997).

[180] Y. Negishi, H. Kawamata, F. Hayakawa, A. Nakajima, and K. Kaya, *Chem. Phys. Lett.* **294**, 370 (1998).

[181] D. Feldmann, R. Rackwitz, E. Heinicke, and H. J. Kaiser, *Zeitschrift Fur Naturforschung Section a-a Journal of Physical Sciences* **32**, 302 (1977).

[182] J. Thogersen, L. D. Steele, M. Scheer, C. A. Brodie, and H. K. Haugen, *Journal of Physics B-Atomic Molecular and Optical Physics* **29**, 1323 (1996).

[183] M. Scheer, R. C. Bilodeau, C. A. Brodie, and H. K. Haugen, *Physical Review A* **58**, 2844 (1998).

[184] S. Li, R. J. Vanzee, and W. Weltner, *J. Chem. Phys.* **100**, 7079 (1994).

[185] S. D. Li, Z. G. Zhao, H. S. Wu, and Z. H. Jin, *J. Chem. Phys.* **115**, 9255 (2001).

[186] S. Ogut and J. R. Chelikowsky, *Physical Review B* **55**, R4914 (1997).

[187] J. L. Wang, G. H. Wang, and J. J. Zhao, *Physical Review B* **64**, 205411 (2001).

[188] B.-X. Li, P.-L. Cao, B. Song, and Z.-Z. Ye, *Phys. Lett. A* **307**, 318 (2003).

[189] S. Bulusu, S. Yoo, and X. C. Zeng, *J. Chem. Phys.* **122**, 164305 (2005).

[190] S. Yoo and X. C. Zeng, *J. Chem. Phys.* **124** (2006).

[191] S. Eisebitt, J. Luning, J. E. Rubensson, T. vanBuuren, S. N. Patitsas, T. Tiedje, M. Berger, R. ArensFischer, S. Frohnhoff, and W. Eberhardt, *Solid State Commun.* **97**, 549 (1996).

[192] T. Vanbuuren, T. Tiedje, J. R. Dahn, and B. M. Way, *Appl. Phys. Lett.* **63**, 2911 (1993).

[193] M. BenChorin, B. Averboukh, D. Kovalev, G. Polisski, and F. Koch, *Phys. Rev. Lett.* **77**, 763 (1996).

[194] F. W. Froben and W. Schulze, *Surf. Sci.* **156**, 765 (1985).

[195] G. Gantefor, K. H. Meiwesbroer, and H. O. Lutz, *Physical Review A* **37**, 2716 (1988).

[196] J. Bai, L. F. Cui, J. L. Wang, S. H. Yoo, X. Li, J. Jellinek, C. Koehler, T. Frauenheim, L. S. Wang, and X. C. Zeng, *J. Phys. Chem. A* **110**, 908 (2006).

[197] L. F. Cui, L. M. Wang, and L. S. Wang, *J. Chem. Phys.*, in press (2007).

[198] A. A. Shvartsburg and M. F. Jarrold, *Physical Review A* **60**, 1235 (1999).

[199] A. A. Shvartsburg and M. F. Jarrold, *Chem. Phys. Lett.* **317**, 615 (2000).

[200] A. A. Shvartsburg and M. F. Jarrold, *Phys. Rev. Lett.* **85**, 2530 (2000).

[201] C. Majumder, V. Kumar, H. Mizuseki, and Y. Kawazoe, *Physical Review B* **64**, 233405 (2001).

[202] C. Majumder, V. Kumar, H. Mizuseki, and Y. Kawazoe, *Physical Review B* **71**, 035401 (2005).

[203] K. Joshi, D. G. Kanhere, and S. A. Blundell, *Physical Review B* **67**, 235413 (2003).

[204] S. Krishnamurty, K. Joshi, D. G. Kanhere, and S. A. Blundell, *Physical Review B* **73**, 045419 (2006).

[205] F. C. Chuang, C. Z. Wang, S. Ogut, J. R. Chelikowsky, and K. M. Ho, *Physical Review B* **69**, 165408 (2004).

[206] G. A. Breaux, C. M. Neal, B. P. Cao, and M. F. Jarrold, *Physical Review B* **71**, 073410 (2005).

[207] L. F. Cui, X. Huang, L. M. Wang, D. Y. Zubarev, A. I. Boldyrev, J. Li, and L. S. Wang, *J. Am. Chem. Soc.* **128**, 8390 (2006).

[208] W. G. Burgers and L. J. Groen, *Discussions of the Faraday Society* **23**, 183 (1957).

[209] K. Laihing, R. G. Wheeler, W. L. Wilson, and M. A. Duncan, *J. Chem. Phys.* **87**, 3401 (1987).

[210] M. Watanabe, Y. Saito, S. Nishigaki, and T. Noda, *Japanese Journal of Applied Physics Part 1-Regular Papers Short Notes & Review Papers* **27**, 344 (1988).

[211] S. Yoshida and K. Fuke, *J. Chem. Phys.* **111**, 3880 (1999).

[212] A. B. Anderson, *J. Chem. Phys.* **63**, 4430 (1975).

[213] D. G. Dai and K. Balasubramanian, *J. Chem. Phys.* **96**, 8345 (1992).

[214] D. G. Dai and K. Balasubramanian, *J. Phys. Chem.* **100**, 19321 (1996).

[215] B. Wang, L. M. Molina, M. J. Lopez, A. Rubio, J. A. Alonso, and M. J. Stott, *Annalen Der Physik* **7**, 107 (1998).

[216] Z. Y. Lu, C. Z. Wang, and K. M. Ho, *Physical Review B* **61**, 2329 (2000).

[217] G. Gantefor, M. Gausa, K. H. Meiwesbroer, and H. O. Lutz, *Zeitschrift Fur Physik D-Atoms Molecules and Clusters* **12**, 405 (1989).

[218] V. D. Moravec, S. A. Klopcic, and C. C. Jarrold, *J. Chem. Phys.* **110**, 5079 (1999).

[219] Y. Negishi, H. Kawamata, A. Nakajima, and K. Kaya, *J. Electron. Spectrosc. Relat. Phenom.* **106**, 117 (2000).

[220] L. F. Cui, X. Huang, L. M. Wang, J. Li, and L. S. Wang, *J. Phys. Chem. A* **110**, 10169 (2006).

[221] L. F. Cui, X. Huang, L. M. Wang, J. Li, and L. S. Wang, *Angewandte Chemie-International Edition* **46**, 742 (2007).

[222] T. Guo, R. E. Smalley, and G. E. Scuseria, *J. Chem. Phys.* **99**, 352 (1993).

[223] C. C. Arnold and D. M. Neumark, *J. Chem. Phys.* **99**, 3353 (1993).

[224] D. M. Wood, *Phys. Rev. Lett.* **46**, 749 (1981).

[225] H. C. Longuet-Higgins and M. d. V. Roberts, *Proc. Roy. Soc. A* **230**, 110 (1955).

[226] A. R. Pitochelli and M. F. Hawthorne, *J. Am. Chem. Soc.* **82**, 3228 (1960).

[227] N. Wiberg and P. Power, *Molecular Clusters of the Main Group Elements* (WILEY-VCH Verlag, Weinheim, 2004).

[228] J. D. Corbett, *Angewandte Chemie-International Edition* **39**, 670 (2000).

[229] V. Kumar and Y. Kawazoe, *Appl. Phys. Lett.* **80**, 859 (2002).

[230] S. Neukermans, E. Janssens, Z. F. Chen, R. E. Silverans, P. V. Schleyer, and P. Lievens, *Phys. Rev. Lett.* **92**, 163401 (2004).

[231] E. N. Esenturk, J. Fettinger, Y. F. Lam, and B. Eichhorn, *Angewandte Chemie-International Edition* **43**, 2132 (2004).

[232] X. Zhang, G. L. Li, X. P. Xing, X. Zhao, Z. C. Tang, and Z. Gao, *Rapid Commun. Mass Spectrom.* **15**, 2399 (2001).

[233] G. A. Breaux, D. A. Hillman, C. M. Neal, and M. F. Jarrold, *J. Phys. Chem. A* **109**, 8755 (2005).

[234] W. Kratschmer, L. D. Lamb, K. Fostiropoulos, and D. R. Huffman, *Nature* **347**, 354 (1990).

[235] S. Alvarez, *Dalton Transactions*, 2209 (2005).

[236] J. F. Bai, A. V. Virovets, and M. Scheer, *Science* **300**, 781 (2003).

[237] S. Bulusu, X. Li, L. S. Wang, and X. C. Zeng, *Proceedings of the National Academy of Sciences of the United States of America* **103**, 8326 (2006).

[238] S. M. Beck, *J. Chem. Phys.* **87**, 4233 (1987).

[239] H. Hiura, T. Miyazaki, and T. Kanayama, *Phys. Rev. Lett.* **86**, 1733 (2001).

[240] V. Kumar and Y. Kawazoe, *Phys. Rev. Lett.* **8704** (2001).

[241] S. N. Khanna, B. K. Rao, and P. Jena, *Phys. Rev. Lett.* **89** (2002).

[242] K. Koyasu, M. Akutsu, M. Mitsui, and A. Nakajima, *J. Am. Chem. Soc.* **127**, 4998 (2005).

[243] V. Kumar, A. K. Singh, and Y. Kawazoe, *Nano Lett.* **4**, 677 (2004).

[244] C. Schrodt, F. Weigend, and R. Ahlrichs, *Z. Anorg. Allg. Chem.* **628**, 2478 (2002).

[245] E. N. Esenturk, J. Fettinger, and B. Eichhorn, *Chem. Commun.*, 247 (2005).

[246] D. S. Bethune, R. D. Johnson, J. R. Salem, M. S. Devries, and C. S. Yannoni, *Nature* **366**, 123 (1993).

[247] Y. Chai, T. Guo, C. M. Jin, R. E. Haufler, L. P. F. Chibante, J. Fure, L. H. Wang, J. M. Alford, and R. E. Smalley, *J. Phys. Chem.* **95**, 7564 (1991).

[248] W. Plass, H. Stoll, H. Preuss, and A. Savin, *Theochem-Journal of Molecular Structure* **339**, 67 (1995).

[249] P. Pyykko and N. Runeberg, *Angewandte Chemie-International Edition* **41**, 2174 (2002).

[250] X. Li, B. Kiran, J. Li, H. J. Zhai, and L. S. Wang, *Angewandte Chemie-International Edition* **41**, 4786 (2002).

[251] S. K. Lai, P. J. Hsu, K. L. Wu, W. K. Liu, and M. Iwamatsu, *J. Chem. Phys.* **117**, 10715 (2002).

[252] J. P. K. Doye and S. C. Hendy, *European Physical Journal D* **22**, 99 (2003).

[253] B. L. Wang, J. J. Zhao, X. S. Chen, D. N. Shi, and G. H. Wang, *Physical Review A* **71** (2005).

[254] C. Rajesh, C. Majumder, M. G. R. Rajan, and S. K. Kulshreshtha, *Physical Review B* **72** (2005).

[255] P. Pyykko, *Chem. Rev.* **88**, 563 (1988).

[256] A. Spiekermann, S. D. Hoffinann, and T. F. Fassler, *Angewandte Chemie-International Edition* **45**, 3459 (2006).

[257] M. E. Geusic, M. D. Morse, and R. E. Smalley, *J. Chem. Phys.* **82**, 590 (1985).

[258] R. L. Whetten, M. R. Zakin, D. M. Cox, D. J. Trevor, and A. Kaldor, *J. Chem. Phys.* **85**, 1697 (1986).

[259] J. L. Elkind, F. D. Weiss, J. M. Alford, R. T. Laaksonen, and R. E. Smalley, *J. Chem. Phys.* **88**, 5215 (1988).

[260] P. Fayet, A. Kaldor, and D. M. Cox, *J. Chem. Phys.* **92**, 254 (1990).

[261] J. L. Persson, M. Andersson, and A. Rosen, *Zeitschrift Fur Physik D-Atoms Molecules and Clusters* **26**, 334 (1993).

[262] J. Ho, L. Zhu, E. K. Parks, and S. J. Riley, *J. Chem. Phys.* **99**, 140 (1993).

[263] J. Conceicao, R. T. Laaksonen, L. S. Wang, T. Guo, P. Nordlander, and R. E. Smalley, *Physical Review B* **51**, 4668 (1995).

[264] S. Burkart, N. Blessing, and G. Gantefor, *Physical Review B* **60**, 15639 (1999).

[265] T. H. Upton, *Phys. Rev. Lett.* **56**, 2168 (1986).

[266] R. O. Jones, *J. Chem. Phys.* **99**, 1194 (1993).

[267] O. Dolgounitcheva, V. G. Zakrzewski, and J. V. Ortiz, *J. Chem. Phys.* **111**, 10762 (1999).

[268] J. Akola, H. Hakkinen, and M. Manninen, *Physical Review B* **58**, 3601 (1998).

[269] B. K. Rao and P. Jena, *J. Chem. Phys.* **111**, 1890 (1999).

[270] R. Ahlrichs and S. D. Elliott, *PCCP* **1**, 13 (1999).

[271] J. Akola, M. Manninen, H. Hakkinen, U. Landman, X. Li, and L. S. Wang, *Physical Review B* **62**, 13216 (2000).

[272] D. M. Cox, D. J. Trevor, R. L. Whetten, E. A. Rohlfing, and A. Kaldor, *J. Chem. Phys.* **84**, 4651 (1986).

[273] W. A. Deheer, P. Milani, and A. Chatelain, *Phys. Rev. Lett.* **63**, 2834 (1989).

[274] K. E. Schriver, J. L. Persson, E. C. Honea, and R. L. Whetten, *Phys. Rev. Lett.* **64**, 2539 (1990).

[275] A. Nakajima, K. Hoshino, T. Naganuma, Y. Sone, and K. Kaya, *J. Chem. Phys.* **95**, 7061 (1991).

[276] X. Li, H. B. Wu, X. B. Wang, and L. S. Wang, *Phys. Rev. Lett.* **81**, 1909 (1998).

[277]D. M. Cox, D. J. Trevor, R. L. Whetten, and A. Kaldor, *J. Phys. Chem.* **92**, 421 (1988).

[278] M. F. Jarrold and J. E. Bower, *J. Am. Chem. Soc.* **110**, 70 (1988).

[279] M. F. Jarrold and J. E. Bower, *Chem. Phys. Lett.* **144**, 311 (1988).

[280] B. D. Leskiw and A. W. Castleman, *Chem. Phys. Lett.* **316**, 31 (2000).

[281] J. Harris, *Applied Physics a-Materials Science & Processing* **47**, 63 (1988).

[282] J. Paul, *Physical Review B* **37**, 6164 (1988).

[283] A. Winkler, G. Pozgainer, and K. D. Rendulic, *Surf. Sci.* **251**, 886 (1991).

[284] S. N. Khanna and P. Jena, *Chem. Phys. Lett.* **218**, 383 (1994).

[285] H. Kawamura, V. Kumar, Q. Sun, and Y. Kawazoe, *Materials Transactions* **42**, 2175 (2001).

[286] P. Breisacher and B. Siegel, *J. Am. Chem. Soc.* **86**, 5023 (1964).

[287] K. Lammertsma and J. Leszczynski, *J. Phys. Chem.* **94**, 2806 (1990).

[288] M. Shen and H. F. Schaefer, *Mol. Phys.* **76**, 467 (1992).

[289] V. Barone, L. Orlandini, and C. Adamo, *J. Phys. Chem.* **98**, 13185 (1994).

[290] L. Andrews and X. Wang, *Science* **300**, 741 (2003).

[291] H. Kawamura, V. Kumar, Q. Sun, and Y. Kawazoe, *Physical Review A* **67** (2003).

[292] J. A. Dilts and E. C. Ashby, *Inorg. Chem.* **11**, 1230 (1972).

[293] R. T. Walters and J. H. Scogin, *J. Alloys Compd.* **379**, 135 (2004).

[294] H. Morioka, K. Kakizaki, S. C. Chung, and A. Yamada, *J. Alloys Compd.* **353**, 310 (2003).

[295] I. Yarovsky and A. Goldberg, *Molecular Simulation* **31**, 475 (2005).

[296] S. Burkart, N. Blessing, B. Klipp, J. Muller, G. Gantefor, and G. Seifert, *Chem. Phys. Lett.* **301**, 546 (1999).

[297] H. B. Wu, X. Li, X. B. Wang, C. F. Ding, and L. S. Wang, *J. Chem. Phys.* **109**, 449 (1998).

[298] X. Li and L. S. Wang, *Physical Review B* **65**, 153404 (2002).

[299] T. Heine, C. Corminboeuf, and G. Seifert, *Chem. Rev.* **105**, 3889 (2005).

[300] A. I. Boldyrev and L. S. Wang, *Chem. Rev.* **105**, 3716 (2005).

[301] X. Li, H. F. Zhang, L. S. Wang, A. E. Kuznetsov, N. A. Cannon, and A. I. Boldyrev, *Angewandte Chemie-International Edition* **40**, 1867 (2001).

[302] A. E. Kuznetsov, J. D. Corbett, L. S. Wang, and A. I. Boldyrev, *Angewandte Chemie-International Edition* **40**, 3369 (2001).

[303] A. E. Kuznetsov, K. A. Birch, A. I. Boldyrev, X. Li, H. J. Zhai, and L. S. Wang, *Science* **300**, 622 (2003).

[304] A. I. Boldyrev and A. E. Kuznetsov, *Inorg. Chem.* **41**, 532 (2002).

[305] Y. C. Lin, J. Juselius, D. Sundholm, and J. Gauss, *J. Chem. Phys.* **122** (2005).

[306] R. W. A. Havenith, P. W. Fowler, E. Steiner, S. Shetty, D. Kanhere, and S. Pal, *PCCP* **6**, 285 (2004).

[307] Z. F. Chen, C. Corminboeuf, T. Heine, J. Bohmann, and P. V. Schleyer, *J. Am. Chem. Soc.* **125**, 13930 (2003).

[308] C. G. Zhan, F. Zheng, and D. A. Dixon, *J. Am. Chem. Soc.* **124**, 14795 (2002).

[309] P. W. Fowler, R. W. A. Havenith, and E. Steiner, *Chem. Phys. Lett.* **342**, 85 (2001).

[310] J. Juselius, M. Straka, and D. Sundholm, *J. Phys. Chem. B* **105**, 24A (2001).

[311] P. V. Schleyer, C. Maerker, A. Dransfeld, H. J. Jiao, and N. Hommes, *J. Am. Chem. Soc.* **118**, 6317 (1996).

[312] J. Juselius, D. Sundholm, and J. Gauss, *J. Chem. Phys.* **121**, 3952 (2004).

[313] S. K. Ritter, *Chemical & Engineering News* **81**, 23 (2003).

[314]C. S. Wannere, C. Corminboeuf, Z. X. Wang, M. D. Wodrich, R. B. King, and P. V. R. Schleyer, *J. Am. Chem. Soc.* **127**, 5701 (2005).

[315] P. Fuentealba and L. Padilla-Campos, *Int. J. Quantum Chem* **102**, 498 (2005).

[316] A. C. Tsipis and C. A. Tsipis, *J. Am. Chem. Soc.* **125**, 1136 (2003).

[317] C. A. Tsipis, E. E. Karagiannis, P. F. Kladou, and A. C. Tsipis, *J. Am. Chem. Soc.* **126**, 12916 (2004).

[318] J. F. Stanton, K. W. Sattelmeyer, J. Gauss, M. Allan, T. Skalicky, and T. Bally, *J. Chem. Phys.* **115**, 1 (2001).

[319] E. Steiner and P. W. Fowler, *PCCP* **6**, 261 (2004).

[320] C. T. Lee, W. T. Yang, and R. G. Parr, *Physical Review B* **37**, 785 (1988).

[321] A. D. Becke, *J. Chem. Phys.* **98**, 5648 (1993).

[322] A. D. Becke, *Physical Review A* **38**, 3098 (1988).

[323] J. P. Perdew, *Physical Review B* **33**, 8822 (1986).

[324] S. H. Vosko, L. Wilk, and M. Nusair, *Can. J. Phys.* **58**, 1200 (1980).

[325] M. P. Johansson, J. Juselius, and D. Sundholm, *Angewandte Chemie-International Edition* **44**, 1843 (2005).

[326] P. Pyykko, *Angewandte Chemie-International Edition* **43**, 4412 (2004).

[327] H. Schwarz, *Angewandte Chemie-International Edition* **42**, 4442 (2003).

[328] P. Schwerdtfeger, *Heteroat. Chem* **13**, 578 (2002).

[329] P. Schwerdtfeger, *Angewandte Chemie-International Edition* **42**, 1892 (2003).

[330] H. Schmidbaur, *Gold. Progress in Chemistry, Biochemistry and Technology* (Wiley, Chichester, UK, 1999).

[331] J. P. Desclaux and P. Pyykko, *Chem. Phys. Lett.* **39**, 300 (1976).

[332] M. Jansen and A. V. Murding, *Gold. Progress in Chemistry, Biochemistry and Technology* (Wiley, New York, 1999).

[333] P. Pyykko, *Angewandte Chemie-International Edition* **41**, 3573 (2002).

[334] L. Gagliardi, *J. Am. Chem. Soc.* **125**, 7504 (2003).

[335] W. E. Spicer, A. H. Sommer, and J. G. White, *Physical Review* **115**, 57 (1959).

[336] C. Koenig, N. E. Christensen, and J. Kollar, *Physical Review B* **29**, 6481 (1984).

[337] G. Kienast, J. Verma, and W. Klemm, *Z. Anorg. Allg. Chem.* **310**, 143 (1961).

[338] U. Zachwieja, *Z. Anorg. Allg. Chem.* **619**, 1095 (1993).

[339] R. J. Batchelor, T. Birchall, and R. C. Burns, *Inorg. Chem.* **25**, 2009 (1986).

[340] W. E. Spicer, *Physical Review* **125**, 1297 (1962).

[341] N. E. Christensen and J. Kollar, *Solid State Commun.* **46**, 727 (1983).

[342] A. Hasegawa and M. Watabe, *Journal of Physics F-Metal Physics* **7**, 75 (1977).

[343] A. D. Pelton, *Bulletin of Alloy Phase Diagrams* **7**, 136 (1986).

[344] E. Zintl, J. Gonbeau, and W. Dullenkopf, *Zeitschrift Fur Physikalische Chemie-Abteilung a-Chemische Thermodynamik Kinetik Elektrochemie Eigenschaftslehre* **154**, 1 (1931).

[345] W. Haucke, *Zeitschrift Fur Elektrochemie Und Angewandte Physikalische Chemie* **43**, 712 (1937).

[346]K. Hoshino, T. Naganuma, K. Watanabe, A. Nakajima, and K. Kaya, *Chem. Phys. Lett.* **211**, 571 (1993).

[347] U. Heiz, A. Vayloyan, E. Schumacher, C. Yeretzian, M. Stener, P. Gisdakis, and N. Rosch, *J. Chem. Phys.* **105**, 5574 (1996).

[348] U. Heiz, A. Vayloyan, and E. Schumacher, *J. Phys. Chem.* **100**, 15033 (1996).

[349] A. Stangassinger, A. M. Knight, and M. A. Duncan, *J. Phys. Chem. A* **103**, 1547 (1999).

[350] T. Baruah, S. A. Blundell, and R. R. Zope, *Physical Review A* **64**, 043202 (2001).

[351] H. J. Zhai, J. Li, and L. S. Wang, *J. Chem. Phys.* **121**, 8369 (2004).

[352] H. J. Zhai, B. Kiran, and L. S. Wang, *J. Chem. Phys.* **121**, 8231 (2004).

[353] X. Li, B. Kiran, L. F. Cui, and L. S. Wang, *Phys. Rev. Lett.* **95** (2005).

[354] B. Kiran, X. Li, H. J. Zhai, L. F. Cui, and L. S. Wang, *Angewandte Chemie-International Edition* **43**, 2125 (2004).

[355] X. Li, B. Kiran, and L. S. Wang, *J. Phys. Chem. A* **109**, 4366 (2005).

[356] H. J. Zhai, L. S. Wang, D. Y. Zubarev, and A. I. Boldyrev, *J. Phys. Chem. A* **110**, 1689 (2006).

[357] D. Y. Zubarev, J. Li, L. S. Wang, and A. I. Boldyrev, *Inorg. Chem.* **45**, 5269 (2006).

[358] B. Kiran, X. Li, H. J. Zhai, and L. S. Wang, *J. Chem. Phys.* **125** (2006).

[359] Y. C. Lin, D. Sundholm, J. Juselius, L. F. Cui, X. Li, H. J. Zhai, and L. S. Wang, *J. Phys. Chem. A* **110**, 4244 (2006).

[360] M. L. Saboungi, W. Geertsma, and D. L. Price, *Annu. Rev. Phys. Chem.* **41**, 207 (1990).

[361] F. Weigend and M. Haser, *Theoret. Chem. Acc.* **97**, 331 (1997).

[362] J. F. Stanton and J. Gauss, *J. Chem. Phys.* **101**, 8938 (1994).

[363] M. Hargittai, *Chem. Rev.* **100**, 2233 (2000).